Tunable Ordered Assembly of MXene and Related Nanomaterials for Scalable Energy Applications

A thesis submitted to Indian Institute of Technology Guwahati for the degree of

Doctor of Philosophy

By

Pronoy Dutta

Under the supervision of

Dr. Uday Narayan Maiti

Department of Physics

Indian Institute of Technology Guwahati

Guwahati-781039, India

February 2023

Dedicated to

My Father……

Your dreams, my execution.

Department of Physics
Indian Institute of Technology Guwahati
Guwahati-781039
Assam, India

Declaration

I hereby declare that the thesis work entitled **"Tunable Ordered Assembly of MXene and Related Nanomaterials for Scalable Energy Applications"** has been entirely carried out by me at Department of Physics, Indian Institute of Technology Guwahati under the supervision of **Dr. Uday Narayan Maiti** and neither this work nor any part of it has been submitted elsewhere for any degree/diploma or any other academic award.

Pronoy Dutta
Roll no: 176121016
Senior research fellow
Department of Physics
Indian Institute of Technology
Guwahati
Guwahati-781039, India

Department of Physics
Indian Institute of Technology Guwahati
Guwahati-781039
Assam, India

Certificate

It is certified that the work contained in the thesis titled **"Tunable Ordered Assembly of MXene and Related Nanomaterials for Scalable Energy Applications"** has been carried out by Mr. Pronoy Dutta (Roll no: 176121016) at Indian Institute of Technology Guwahati under my supervision and neither this work nor any part of it has been submitted elsewhere for any degree/diploma or other academic award.

Uday Narayan Maiti

Dr. Uday Narayan Maiti

Associate Professor
Department of Physics
Indian Institute of Technology
Guwahati
Guwahati-781039, India

Acknowledgements

The materialization of this thesis is a reflection of all the learnings and blessings that I have accumulated over the course of my life, and now I would like to express my gratitude to those without whom this journey would not have become a reality.

First and foremost, I would like to express my greatest appreciation to my supervisor Dr. Uday Narayan Maiti for his constant motivation, guidance and encouragement. I owe my sincerest gratitude to him for giving me the opportunity to work under his supervision. His passion, deep scientific understanding along with his persistence to excellence have immensely helped me shape the perception of research. Most importantly, the confidence he showed in me throughout these years and the freedom he provided to perform my research while arranging for all the necessities in the lab is beyond any expectations.

I am really grateful to my doctoral committee members, Prof. Dobbidi Pamu, Dr. Pankaj Kumar Mishra and Prof. Lal Mohan Kundu for regular evaluation of my work. I deeply acknowledge their constructive advice and invaluable suggestions. I would like to thank Head of the Department of Physics, our faculty members, Central Instrumental Facility (CIF) and Indian Institute of Technology Guwahati for providing me the laboratory and the state-of-the-art instrumental facilities. I would also like to acknowledge IIT Guwahati for providing me with the fellowship and accommodation in this beautiful campus. I am also thankful to our Central Workshop, Department of Mechanical Engineering for allowing me to fabricate research items through their facility.

The ambience of any place can be as good as its people and in this regard I am really grateful to my seniors and my labmates. I express my sincere gratitude to Dr. Anirban Sikdar and Dr. Abhisek Majumdar for their constant support and valuable guidance to help me glide through the initial days of learning. I am extremely greatful to my labmates Golam, Sujit, Amalika, Snehasish, Priyam, Pranab and Hemant for their support, discussions and endless advice that shaped this thesis. I would like to specially thank Sujit and Amalika for their extraordinary support; it is always a ‘YES’ whenever I reach out for any help from you people. My appreciation to my hostel mates and neighbours Arghyajit, Samit and Riajul for all those happy hostel moments and the long night walks that I will always remember. Special thanks to my dear friends, seniors and juniors Surojit, Sanket, Devabrat, Devendar, Swarup, Samit, Soumen,

Sayan da, Pranjna, Sourav, Pushpesh, Rakesh, Rajesh for making my stay in the campus enjoyable and for being a part of this journey.

I am really blessed to have a loving family with me. I am greatly indebted to my parents Late Pulak Chandra Dutta and Anjali Dutta for their unconditional love and blessings. My mother is instrumental in building my character and my father is the one who decorated that character with all the real-life skills that I have. The lessons I learned from you while accompanying you on your projects have served me well throughout these Ph.D. days and will continue to guide me always. I am deeply thankful to my girlfriend and now wife Debasree Dey for supporting me through my ups and downs and for being a constant in my life. The faith you have shown in me is invaluable. I would also like to thank my childhood buddy Amit Kumar Dey for his support and motivation. Last but not least, my sister Eshita, grandmother Bakul Bala Dutta, my uncle and aunts Subir mama, Prabir mama, Chaitali masi, Tapas meso; I am greatly indebted for your support towards my family in the crucial days.

Pronoy Dutta
IIT Guwahati

CONTENTS

Abstract

Electrochemical energy storage, be it in the form of batteries or supercapacitors, are the frontrunners when it comes to storing the green energy generated from intermittent renewable energy sources. Since the discovery of graphene, supercapacitive electrode development and research have gained much attraction due to its long cycle life and excellent power density. Although materials like graphene provided enhanced capacitance through its high surface area induced increased electrochemical double layer capacitance (EDLC), the capacitance and energy density were still fairly limited. Pseudocapacitive materials, which in addition to EDLC also store charge through redox reactions, show a great potential in improving the above metrics. In this regard, MXene, a transition metal carbide and or nitride based two-dimensional material have recently been the first choice as electrode material for its outstanding conductivity, pseudocapacity and hydrophilic properties. However, like any other 2D nanomaterial, the thin nanoscale sheets of MXene are needed to be assembled in a macrostructural form in order to develop supercapacitive electrodes. Such assembly of nanosheets are always associated with face-to-face restacking challenges that mitigate the true performance of the pristine material. Loss of electroactive surface area, increased ion-diffusion resistance and ohomic losses are some of the fundamental challenges that originates from severe restacking of nanosheets. Attaining high mass loading with high specific capacitance, excellent energy and power density is majorly restricted by these issues. The present thesis aims to comprehensively address these fundamental challenges through the development of MXene and MXene based macrostructure that are developed for efficient energy storage with optimised electrode architecture. Specifically, achieving commercial scale mass loading while retaining state-of-the-art capacitance metrics with a sustainable, low-cost, highly scalable strategy is the primary goal of this work. For instance, a room temperature spontaneous interfacial assembly for MXene and graphene as a gelator is introduced which results in a highly scalable hybrid hydrogel structure. Hydrogels, a highly suitable electrode macrostructure, are a hydrated porous architecture developed from interlinked nanosheets that provides ample ion-transport channels with high surface accessibility. The resulting electrodes delivered an excellent capacitance of 653.7 F g^{-1} at 2 mV s^{-1} in three-electrode setup and 460 F g^{-1} in symmetric two electrode mode. Further, at commercial loadings (~ 10 mg cm^{-2}) we retained up to 320 F g^{-1} at 2 mV s^{-1} with an electrode mass loading of 9.3 mg cm^{-2}. Importantly, by electrolyte assisted mechanical compression, the hydrogels can be easily modified to

develop compact thin electrodes with a density of 2.44 g cm^{-3} where a high volumetric performance of 1522 F cm^{-3} (at 2 mV s^{-1}) was attained with 50% retention of capacitance at 100 mV s^{-1}. Having achieved a hybrid hydrogel of MXene and graphene with such high capacitive performance, the importance of developing a pristine MXene hydrogel without the addition of graphene like gelator or binder was essential. However, with the small sheet size and intrinsic stiffness in the MXene material, it was necessary to drastically improve the intersheet interaction through controlled orientation and increased van der Waals interaction. In this regard, we introduced a critical density controlled spontaneous assembly of MXene with liquid crystallinity induced long range ordered MXene dispersion. It is established that self-supporting pristine hydrogels of MXene is only possible over a certain critical concentration which is dependent on the MXene sheet size. By simply tuning the gelation time, the mass loading of the electrodes was increased up to 14.9 mg cm^{-2} where an areal capacitance of 5043 mF cm^{-2} and gravimetric capacitance of 337 F g-1 was simultaneously achieved. However, the high density requirement and high gelation time of spontaneous assembly were the major challenges of pristine hydrogel development. In order to mitigate such high dependency, a forced assembly of MXene is proposed with the aid of an externally applied electric field. The field assisted guided gelation not only allowed the freestanding MXene hydrogel development from MXene dispersions as low as 5 mg mL^{-1}, but also reduced the gelation time to seconds from hours. This optimised strategy is also capable of facile controllability over MXene sheet orientation in hydrogels, providing parallel or vertically oriented macrostructures of MXene. The electric-field assisted MXene hydrogels show a gravimetric capacitance of 395 F g^{-1} with an excellent rate performance of 42% at 5000 mV s^{-1}. Moreover, the hydrogel electrodes were dried in ambient condition to develop MXene films which deliver 1251 F cm^{-3} of volumetric capacitance which is 77% higher than commonly used vacuum filtered films. Compared to hydrogels, controlling the restacking in a compact film structure adds further challenge due to the high volumetric density in film electrodes. To address this issue, we introduced bio-waste derived cellulose nanofibers as a spacer into the MXene through electric-field assisted forced gelation. Due to the mutual interaction among the functionalised MXene and cellulose nanofibers, the nanowires were dragged along with MXene into a hydrogel structure which was then dried to produce a flexible electrode. Such restacking controlled assembly had a huge impact in simultaneously achieving all the three important metrics, i.e. gravimetric, volumetric and areal capacitance with an ultrahigh mass loading electrode. With a multi-stacked electrode design, we achieved a mass loading of 73.4 mg cm^{-2} with an areal, volumetric and gravimetric capacitance of 16 F cm^{-2}, 1356 F cm^{-3} and 216 F g^{-1} respectively. In addition, the negative

MXene/cellulose electrodes were paired with a pseudocapacitive rGO/CNT/PANI to develop an asymmetric device with operating voltage window of 1.5 V which resulted in an energy density of 27.8 Wh kg^{-1} at a power density of 501 W kg^{-1}. The ability to fabricate such MXene hybrids over a number of substrates like conducting or non-conducting cloth is also demonstrated which allows developing wearable capacitors. The excellent retention of energy storage and delivery during bending conditions opens a lot of possibilities in portable energy applications. Thus, the major accomplishments of the current thesis can be summarised as ambient condition synthesis, facile scalability, excellent controllability over nanosheets orientations, achievement of exceptionally high mass loading electrode with excellent storage metrics. We believe that the present thesis work can provide a strong guideline to develop MXene and MXene based hybrid hydrogels and films not only for energy storage applications but for a wide range of application fields while maintaining state-of-the-art performance in the respective domains.

List of Abbreviations

EES	Electrochemical energy storage
2D	Two-dimensional
EDLC	Electrochemical double layer capacitors
IHP	Inner Helmholtz plane
OHP	Outer Helmholtz plane
CV	Cyclic voltammetry
GCD	Galvanostatic charge-discharge
EIS	Electrochemical Impedance Spectroscopy
0D	Zero-dimensional
1D	One-dimensional
GO	Graphene oxide
rGO	Reduced graphene oxide
CNT	Carbon nanotubes
AC	Activated carbon
HF	Hydrofluoric acid
HCl	Hydrochloric acid
LiF	Lithium fluoride
MILD	Minimally intensive layer delamination
MWCNT	Multi walled carbon nanotubes
PANI	Polyaniline
ECSA	Electrochemical surface area
EDS	Energy dispersive X-ray spectroscopy
FESEM	Field emission scanning electron microscopy
FETEM	Field emission transmission electron microscopy
STEM	Scanning transmission electron microscopy
BET	Brunauer–Emmett–Teller
XRD	X-ray diffraction
XPS	X-ray photoelectron spectroscopy

List of Publications

Journal Publications:

1. **Pronoy Dutta**, Anirban Sikdar, Abhisek Majumdar, Munu Borah, N. Padma, Subhradip Ghosh, Uday Narayan Maiti, "Graphene aided gelation of MXene with oxidation protected surface for supercapacitor electrodes with excellent gravimetric performance", **Carbon**, 2020, 169, 225.

2. **Pronoy Dutta**, Amalika Patra, Sujit Kumar Deb, Anirban Sikdar, Abhisek Majumdar, Golam Masud Karim, Uday Narayan Maiti, "Freestanding MXene-hydrogels prepared via critical density-controlled self-assembly: high-performance energy storage with ultrahigh capacitive vs. diffusion-limited contribution", **J. Mater. Chem A**, 2021, 9, 25013-25023

3. **Pronoy Dutta**, Sujit Kumar Deb, Amalika Patra, Abhisek Majumdar, Golam Masud Karim, C.K. Parashar, M.K. Mohanta, M. Qureshi, Uday Narayan Maiti, Electric Field Guided Fast and Oriented Assembly of MXene into Scalable Pristine Hydrogels for Customized Energy Storage and Water Evaporation Applications, **Adv. Funct. Mater.** 2204622 (2022) 2204622.

4. **Pronoy Dutta,** Sujit Kumar Deb, Amalika Patra, Golam Masud Karim, Snehasish Das, Uday Narayan Maiti, Guided co-assembly of MXene and cellulose nanofibers: Simultaneous achievement of all three energy metrics with ultrahigh loading electrodes, (Communicated).

5. Abhisek Majumdar, **Pronoy Dutta**, Anirban Sikdar, Heehyeon Lee, Debasis Ghosh, Sambhu Nath Jha, Shilpa Tripathi, Yongtak Oh, Uday Narayan Maiti, "Impact of Atomic Rearrangement and Single Atom Stabilization on MoSe2@NiCo2Se4 Heterostructure Catalyst for Efficient Overall Water Splitting", **Small**, 2022, 18, 220062

6. Anirban Sikdar, **Pronoy Dutta**, Sujit Kumar Deb, Abhisek Majumdar, N Padma, Subhradip Ghosh, Uday Narayan Maiti, "Spontaneous three-dimensional self-assembly of MXene and graphene for impressive energy and rate performance pseudocapacitors", **Electrochimica Acta**, 2021, 391, 138959

7. Golam Masud Karim, **Pronoy Dutta**, Abhisek Majumder, Amalika Patra, Sujit Kumar Deb, Snehasish Das, Neha V Dambhare, Arup K Rath, Uday Narayan Maiti, "Ultra-fast electro-reduction and activation of graphene for high energy density wearable supercapacitor asymmetrically designed with MXene", **Carbon**, 2023, 203, 191.

8. Abhisek Majumdar, **Pronoy Dutta**, Yunho Kang, Golam Masud Karim, Sang Ouk Kim, Uday Narayan Maiti, "Microwave-Assisted Rapid Fabrication of Highly Catalytic Active In-Plane Heterostructure for Efficient Oxygen Evolution Reaction", **Appl. Surf. Sci.** 2023, 617, 156622.

9. Anirban Sikdar, Abhisek Majumdar, **Pronoy Dutta**, Munu Borah, Sang Ouk Kim, Uday Narayan Maiti, "Ultra-large area graphene hybrid hydrogel for customized performance

supercapacitors: High volumetric, areal energy density and potential wearability", **Electrochimica Acta**, 2020, 332, 135492.

10. Anirban Sikdar, Sujit Kumar Deb, Abhijit Gogoi, Abhisek Majumdar, **Pronoy Dutta**, K. Anki Reddy, Uday Narayan Maiti, "Polyaniline-Graphene Hydrogel Hybrids via Diffusion Controlled Surface Polymerization for High Performance Supercapacitor", **ACS Appl. Nano Mater.** 2020, 3, 12, 12278.

11. Anirban Sikdar, Abhisek Majumdar, Abhijit Gogoi, **Pronoy Dutta**, Munu Borah, Soumen Maiti, Chiranjib Gogoi, K. Anki Reddy, Youngtak Oh, Uday Narayan Maiti, "Diffusion driven nanostructuring of metal-organic frameworks (MOFs) for graphene hydrogel based tunable heterostructures: Highly active electrocatalyst for efficient water oxidation", **J. Mater. Chem A**, 2021, 9, 7640-7649.

12. Abhisek Majumdar, Golam Masud Karim, **Pronoy Dutta**, Heehyeon Lee, Sujit Kumar Deb, Anirban Sikdar, Yongtak Oh, Uday Narayan Maiti, "Microwave Induced Rapid Surface Amorphization of Metal Oxide Nanowire into Sulfides Shell for Electronically Modulated Efficient Hydrogen Evolution Catalyst", **Catal. Today**, 2022

Works presented in conference:

1. International Conference on Advanced Nanomaterials and Nanotechnology (ICANN-2021) at IIT Guwahati**.**
2. International Conference on Nano Science and Technology (ICONSAT 2020), SNBNCBS, Kolkata
3. Optoelectronic and Nano Materials for Advanced Technology (ICONMAT 2019), Cochin University

Chapter 1

Introduction

Chapter 1

Introduction

Rapid global development and economic growth have exponentially increased our dependency on the fossil fuels over the last few decades.[1] Such reliance over the limited reserves of the natural resource not only questions the sustainability of our continuous development, but also raises concerns over the global climate change that is altering the natural course of Earth.[2] Therefore, the development of alternative green energy solutions that not only ease the fossil fuel dependency but also ensures a green sustainable future is one of the prime challenges of today's researchers. In this regard, solar energy, wind energy, hydropower has shown considerable development over these years.[3,4] However, the intermittent nature of most of these renewable energy sources demand suitable energy storage systems to enable round the clock supply of such green energies. Batteries and supercapacitors lies in the forefront of such energy storage solutions.[5,6] Recently, with the introduction of two-dimensional (2D) materials, supercapacitors have gained great attention due to their instantaneous power delivery and high cycle life.[7]

The advancement of supercapacitive research gained new heights with the introduction of graphene.[8–10] However, its limited double layer capacitance greatly limits the energy density of graphene based supercapacitive devices.[11] Development of pseudocapacitive materials, i.e., materials with faradaic reactions at the electrode-electrolyte interface, is believed to bridge the gap between high power density supercapacitors and high energy density batteries.[12–14] MXenes, a newly discovered 2D material, have recently attracted immense research attraction in this aspect in recent times.[15] Unlike graphene and other 2D materials, these possess a rare combination of metal like conductivity, hydrophilicity and pseudocapacity which enables extraordinary performance in several fields of applications like electromagnetic interface shielding, gas sensing, catalysis, sensors and energy storage.[16–23]

Nanoscale materials are often assembled in macroscopic structures with 2D materials serving as building blocks to develop materials for practical applications.[24,25] However, face-to-face restacking and different assembling conditions mitigate the complete potential of these materials to a large extent. Loss of surface and active site accessibility, greater hindrance to electrolyte transport into the bulk of electrode material, instability of the macrostructure under charge-discharge cycles are some of the bottlenecks often introduced in macrostructural

forms.[26,27] Further, developing highly scalable assembly techniques and an optimized structure that enable commercial scale mass loadings, i.e., the mass of electrode per unit area are the most crucial parameters in supercapacitive electrode development.

In this chapter, we briefly present the supercapacitive energy storage, its fundamental techniques and corresponding materials for supercapacitive electrode development. Introduction of MXene, its properties and recent advances in MXene based energy storage is also discussed in this chapter. Existing bottlenecks in the development of MXene and MXene based macrostructures, their structural advantages and disadvantages are also discussed briefly. Different energy storage characterization techniques and methodologies like proper identification and quantification techniques of pseudocapacitive materials are also presented. Motivation and the prime objectives of the thesis are also discussed at the end of this chapter.

1.1. Electrochemical supercapacitors: Fundamentals

Among various methods to store energy for on-demand controlled supply, electrochemical energy storage (EES) remains the most lucrative approach due to its highest conversion efficiency. Fuel cells, batteries, supercapacitors, flow cells are a few such popular examples of chemical to electrical energy conversion systems.[28,29] Although batteries have largely dominated the EES systems, low cycle life, severe safety challenges and low power density are the few pieces of the puzzle needed to fulfill the ultimate energy storage solution. Here, in this regard, supercapacitive energy storage has gained much attraction with the introduction of new two-dimensional (2D) materials. While supercapacitors have a rather modest energy density when compared to batteries, it makes up for it with its ultrahigh power densities, large cycle life, increased safety and overall lower cost of synthesis.[29]

Classical capacitors consist of two parallel plates separated by an insulating dielectric medium that stores charge electrostatically. When an external bias is applied across the parallel plates, charges move from one plate to another creating deficiency and excess of equal and opposite charges at the metal plates. The capacity of such a device is defined as,

$$C = \frac{\varepsilon A}{d} \tag{1}$$

where, ε, A and d are the dielectric constant, area of the electrode and distance between the metal plates respectively. As evident from the equation, the capacitance of a capacitor largely depends on the geometrical area and the distance between the plates of the device. As a result,

the limited geometrically limited area and plate separation results in small capacitance as also shown in the Regone plot in Fig. 1.1.

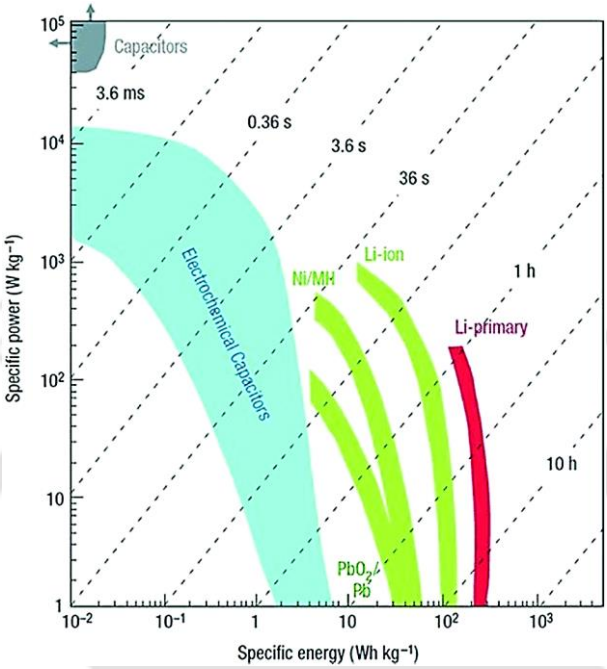

Figure 1.1. Regone plot indicating the power and energy densities of popular commercial electrochemical energy storage systems. Adopted from Ref. [30]

On the other hand, the principle of the electrochemical supercapacitors are based on the separation of solvated ions at the electrode-electrolyte interface along with the transfer of charge at the interface medium upon application of an external bias. Generally, when the two electrodes are polarized, solvated ions of opposite charge move towards the opposite polarity electrodes creating a layer of dielectric water between the polarized electrode and the column of solvated charges.[29] Thus the atomistic separation generated via the water layer increases the capacitance several folds. On the other hand, the surface area of the devices is increased by several folds by utilizing 2D materials over conventional metal plates used in capacitors. As an example, the surface area of graphene can be as high as 2660 $m^2 g^{-1}$.[31]

Depending on the interfacial charge storage mechanism electrochemical capacitors are generally categorized into three different categories, a) Electrochemical double layer capacitors (EDLC), b) pseudocapacitors and c) hybrid capacitors.[32–34]

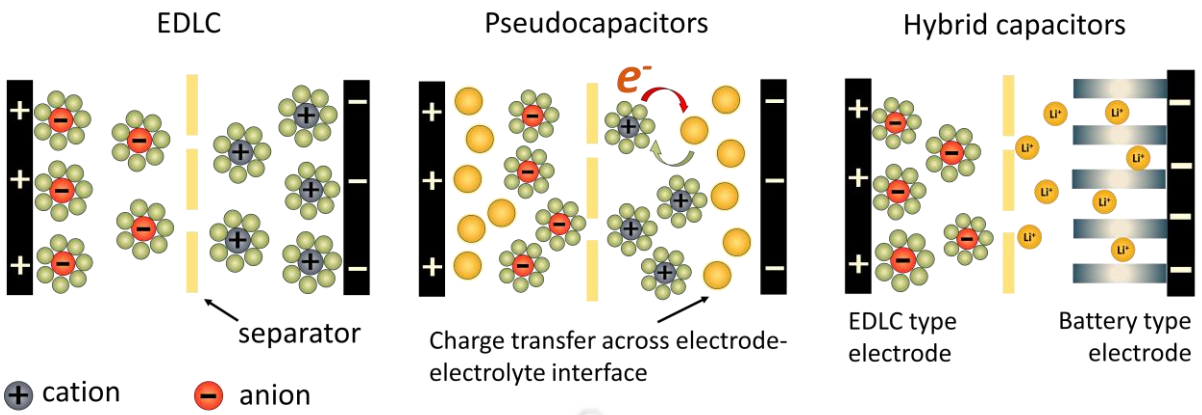

Figure 1.2. Schematic representation of different electrochemical capacitors.

1.1.1. Electrochemical double layer capacitors

Electrochemical double layer capacitors or EDLCs store charges only via adsorption of solvated ionic molecules, i.e., the electrodes in EDLC are electrochemically inactive and do not take part in charge transfer across the electrode and electrolyte interface. Due to the simple adsorption mechanism, the process is highly reversible with remarkable charge-discharge capability which leads to high power densities and also possesses long cycle life due to the non-reactive nature of the process.

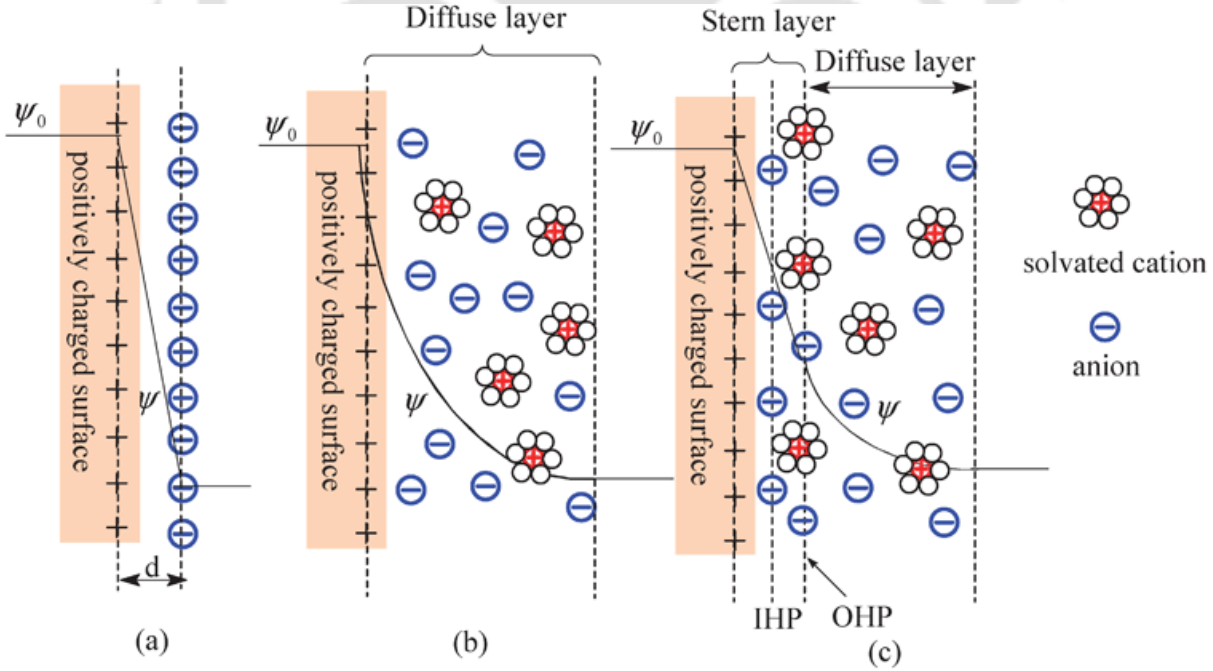

Figure 1.3. Different models describing the EDLC formation at the positive surface: (a) Helmholtz model, (b) Gouy-Chapman model and (c) Stern model respectively. Adapted from Ref. [35]

EDLC formation at the electrode-electrolyte interface can be described through several models starting from the first description ever proposed in 1853 by Helmholtz.[34] This model describes the formation of EDL as simple distribution of opposite charges at the supercapacitor interface and proposed that the capacitance will only depend on the applied potential having a linear relationship. However, it was later observed that capacitance not only depends on the potential but also varies with the ionic concentration of the electrolyte. Gouy and Chapman later proposed that instead of an oppositely polarized columnar plane, a rather continuous distribution of anions and cations can be considered which was driven by the thermal motion.[36,37] This is referred as the diffuse layer. However, as this model often overestimated the double layer capacitance, Otto Stern in 1924 further modified this by combining the two previous descriptions of EDLC.[38] Stern proposed two distinct regions in the charge accumulation near the electrode surface. The inner compact immobile layer consists of strongly adsorbed ions as proposed by Helmholtz which is also known as the inner Helmholtz plane (IHP) followed by a diffused layer of mobile ions called the outer Helmholtz plane or OHP. The total double layer capacitance of this arrangement can be considered as two capacitors in series such that,

$$\frac{1}{C_{dl}} = \frac{1}{C_{IHP}} + \frac{1}{C_{OHP}} \qquad (2)$$

Due to the absence of any physical electron transfer at the interface, EDLC based supercapacitors can instantaneously (within 10^{-8} s) store charge which results in characteristic high power densities of the devices.

1.1.2. Pseudocapacitors

Pseudocapacitors store charges via fast reversible redox reactions occurring on the interface of solid electrode and electrolyte. The term 'pseudo' in pseudocapacitors originates from the fact that although such a process appears or contributes to capacitance but in fact the accumulation of charges in the electrode takes place via faradaic processes. Such additional kinetics at the electrode allows pseudocapacitive materials to overcome the capacity of EDLCs and actually hold the potential to bridge the gap between supercapacitors and batteries. Ruthenium dioxide (RuO_2),[39,40] polyaniline (PANI),[41,42] MXenes,[18,43] layered double hydroxides (LDH),[44–46] spinel oxides[47–51] are some of the popular materials representing such category of materials.

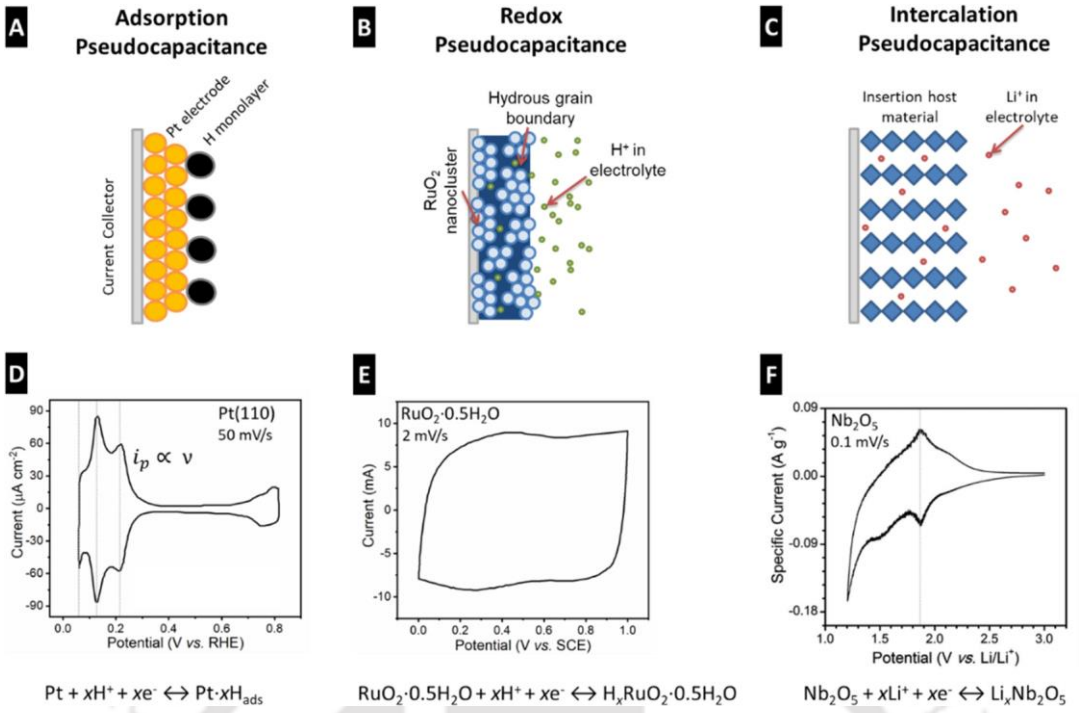

Figure 1.4. (a-c) Schematic illustration of three different types of pseudocapacitive mechanisms occurring at the solid-electrolyte interface; (d-f) examples of corresponding cyclic voltammetry (CV) curves corresponding to adsorption type, redox and intercalation type pseudocapacitance respectively. Adapted with permission from Ref. [14].

Usually pseudocapacitors can be characterized in three distinct categories depending on their charge storage [13].

a) Adsorption pseudocapacitance: Such pseudocapacitance occurs when electrochemical species get adsorbed over the electrode surface. Examples of such processes include the adsorption of H on Pt surface or O and OH over the surface of nickel oxides.

b) Redox pseudocapacitance: Here the adsorbed species from the electrolyte gets involved in reversible faradaic reactions. For example, adsorption and successive the faradaic reaction of H^+ ions over $Ti_3C_2T_x$ MXene surface, redox reaction of RuO_2 in hydrous electrolyte.

c) Intercalation pseudocapacitance: In this case, the electrochemical ions get intercalated into the bulk of the electrode through pores and channels which is then followed by a faradaic reaction. However, unlike batteries, here no phase change of the active material takes place. The intercalation of Li^+ ions into Nb_2O_5 is an example of such intercalation type pseudocapacitance.

1.1.3. Hybrid supercapacitors

Hybrid supercapacitors usually have an asymmetric configuration where both the electrodes can be of capacitive or capacitive and battery type. Such devices are considered as a middle ground between capacitors and battery type energy storage systems. Depending on the configuration hybrid capacitors can be of two types. The first one is the capacitor/capacitor type where the anode and cathode either be EDLC or pseudocapacitive type. Whereas, the second type can be a one capacitive i.e., EDLC or pseudocapacitive and the other being battery type electrode. Here as the positive cathode and negative anodes are different, they can work independently in a device configuration. Due to this, the electrodes have their independent potential windows. This enables one to increase the operating potential of the device higher than a usual symmetric device which results in much higher energy densities and overall stability.

1.2. Performance metrics and figure of merits of supercapacitors

1.2.1. Capacitance

Capacitance or the amount of charge stored in a material when a certain potential is applied is the prime figure of merit for any supercapacitive material. Capacitance of a material primarily depends upon its surface area, structural features like porosity, electrolyte, type of faradaic reactions in the material, the thickness of the electrostatic EDLC layer *etc.* There are several electrochemical methods through which the capacitance of an electrode can be determined. Some of such methods are discussed below:

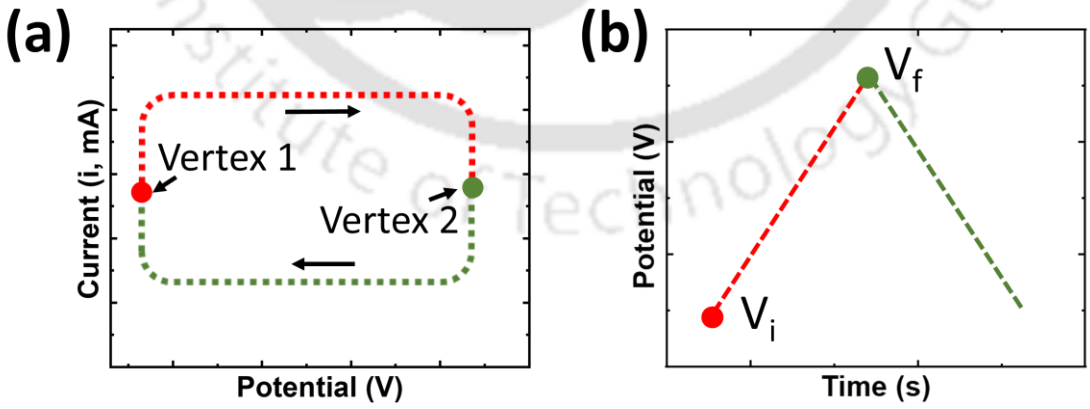

Figure 1.5. Schematic illustration of (a) cyclic voltammetry (CV) and (b) galvanostatic charge-discharge (GCD) curves.

1.2.1.1. Cyclic voltammetry

Cyclic voltammetry (CV) is an electrochemical technique that records the current response of a material when it is polarized within a certain potential range starting from a starting potential (vertex 1) to the final potential (vertex 2) at a particular scan rate (mV s^{-1}) as shown in Fig 1.5.a. The current response is measured with the help of an electrochemical workstation in which the potential is swept cyclically for a desired amount of times and hence the name cyclic voltammetry. The polarization curves obtained from CV provide crucial information about the amount of charge stored, presence or absence of redox-reactions, charge storage mechanism and also the rate performance of the material.

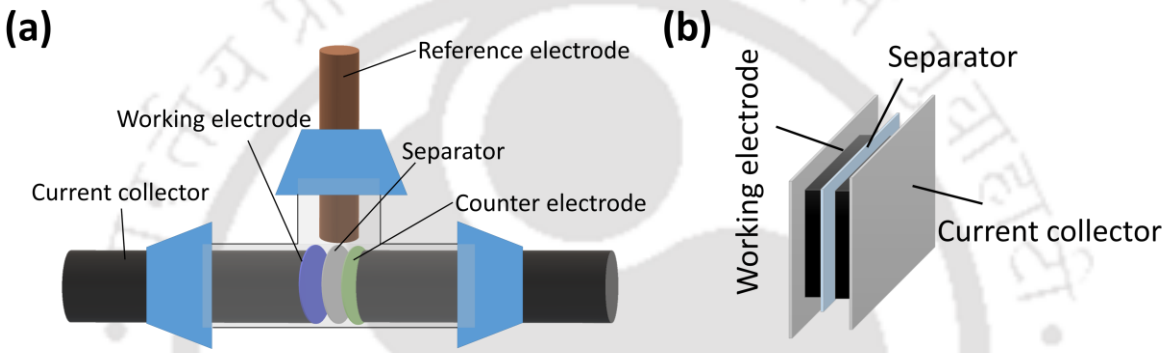

Figure 1.6. Schematic illustration of (a) three-electrode Swagelok type cell and (b) two-electrode setup for electrochemical characterization of supercapacitors.

Measurements of CV can be done in three-electrode or two-electrode configurations. In three-electrode method, the working electrode is the material under investigation, which is accompanied by a suitable reference electrode as well as a counter electrode as shown in Fig. 1.6.a. In two-electrode method, both the reference and counter electrodes are the active material and the reference electrode is connected with the counter electrode itself (Fig.1.6.b). Three-electrode measurements are suitable to determine the exact potential response of a material, its specific capacitance and the type of capacitive response offered by the material. On the other hand, two-electrode methods are more practical as they simulate a practical device for commercial applications. Two-electrode devices can be considered as two supercapacitors connected in series. Therefore, the total capacitance of a two-electrode device is defined as,

$$\frac{1}{C_{cell}} = \frac{1}{C_+} + \frac{1}{C_-} \quad (3)$$

Where, C_{cell}, C_+ and C_- are the capacitance of the device, positive electrode and negative electrode respectively. For a symmetric type configuration $C_+ = C_- = C_{single}$. In this case from *Eq.* 3, $C_{cell} = C_{single}/2$.

The capacitance of a material or device can be normalized with its mass, area or volume of the material which then gives specific capacitance like gravimetric (C_s, F g^{-1}), areal (C_{area}, F cm^{-2}) and volumetric (C_{Vol}, F cm^{-3}) capacitance respectively. The capacitance of the material or device can be determined by calculating the area of the CV profile from which the capacitance is defined as,

$$C_s = \frac{1}{mv\Delta V}\int_{V_i}^{V_f} idV \tag{4}$$

$$C_{Area} = \frac{1}{Av\Delta V}\int_{V_i}^{V_f} idV \tag{5}$$

$$C_{Vol} = \frac{1}{Vol \cdot v\Delta V}\int_{V_i}^{V_f} idV \tag{6}$$

where i is the current density (A), ΔV is the potential window (V) of the supercapacitor, v is the scan rate (mV s^{-1}), m is the total mass of the electrodes (g), A is the geometrical area of the electrode (cm^2), Vol is the volume of the supercapacitor (cm^3), V_i and V_f are the initial and final potentials respectively. In the case of three-electrode configuration, mass or volume is considered for the active material only and for two electrode devices, mass and volume of both the electrodes are taken into consideration.

1.2.1.2. Galvanostatic charge-discharge

Galvanostatic charge-discharge or GCD is another characterization method where first, the active material or supercapacitor device is charged up to its allowed potential under the application of a constant current density and then discharged completely with the same current density (Fig. 1.5.b). Similar to CV, GCD curves can also provide insightful information about the charge storage mechanism in the electrodes. In the case of pure EDLC devices, the GCD profiles show a linear triangular nature. Whereas, the presence of redox reactions induces non-linearity in the curves which results in slightly deviated triangular GCD profiles. Other than the discharge mechanism, GCD curves can also indicate the resistive loss in an electrode which can be determined by the resistive drop at the start of the discharge curve of the electrode.

While determining the capacitance from GCD curves, one has to be aware about the type of capacitive storage mechanism first. For linear relationships, the relations governing the capacitance can be expressed as,

$$C_s = \frac{I}{m\left(\frac{\Delta V}{\Delta t}\right)} \tag{7}$$

$$C_{Area} = \frac{I}{A\left(\frac{\Delta V}{\Delta t}\right)} \tag{8}$$

$$C_{Vol} = \frac{I}{Vol\left(\frac{\Delta V}{\Delta t}\right)} \tag{9}$$

here also, *m* represents the mass of the working electrode for three-electrode studies and the mass of both the electrodes for two-electrode measurements. Δt represents the total discharge time. However, when we have non-linear relationship, it is wiser to express the relation as an integration of the current and time as,

$$C = I\int_{V_i}^{V_f} \frac{1}{V(t)}\,dt \tag{10}$$

which then can be normalised with the respective mass, area or volume to obtain the specific capacitance.

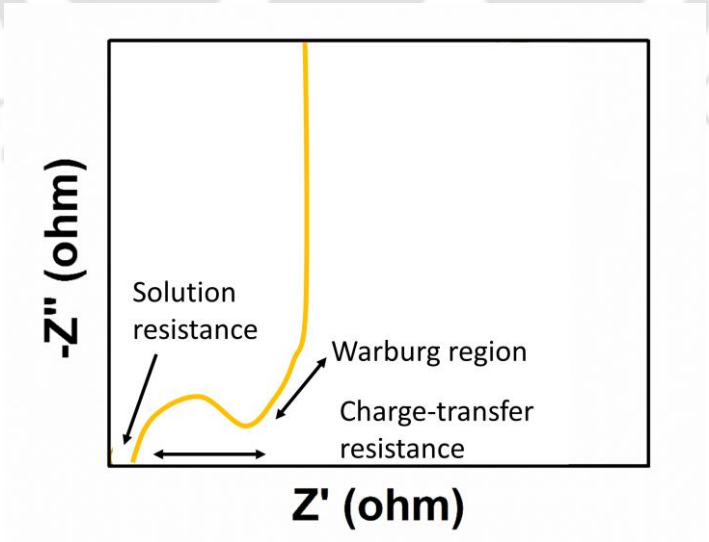

Figure 1.7. Typical Nyquist plot showing EIS spectra and its different regions of interest.

1.2.2. Impedance analysis

Impedance analysis or electrochemical impedance spectroscopy (EIS) is a powerful tool that can provide insightful information about all the electrochemical procedures that are taking place at the electrified electrode-electrolyte interface. Generally, several processes like adsorption, mass-transfer, internal resistive losses, charge-transfers simultaneously take place in a supercapacitive material as soon as it is moved from its equilibrium. EIS can identify all such processes uniquely by applying an AC signal of small amplitude (generally 5-10 mV) having varying frequencies (100 kHz to 0.1 Hz). The fact that all of the above-mentioned processes have certain time dependency, allows EIS to distinguish these processes at once at different frequency regions of the spectra.[52–54] EIS analysis can be expressed in several ways depending on the required analysis. Out of these, the Nyquist plot (imaginary impedance Z" vs real impedance Z') and bode plot (phase angle vs frequency) are the most popular ones. A typical example of a Nyquist plot is shown in Fig. 1.7. The plot can be decided in three regions, namely high frequency, mid-frequency and low frequency regions. The plot starts from high frequency response indicating the points on the right side of the spectra in the graph. The point of intersection in the real resistance (Z') in Nyquist plot indicates the solution resistance. This is often followed by a semicircle which is typical in processes involving faradaic processes. In the mid-frequency region, a 45° line is observed which indicates the semi-infinite diffusion resistance of the material. The intersection of the extrapolated semicircle on the real impedance axis gives the charge-transfer resistance at the electrode-electrolyte interface. After the Warburg impedance region, the low frequency region starts where a vertical rise of the spectra is observed which indicates that in this region the electrodes act as pure capacitive type only. It is to be noted that an ideal capacitor device would provide a completely vertical line in the Nyquist plot whereas a pure resistive component would add a line parallel to the X-axis having zero imaginary value.

1.2.3. Energy and power density

Energy and power density are two of the major characteristics of any energy storage device. These parameters are usually expressed in a Ragone plot as shown in Fig. 1.1. These density metrics are usually normalised with the mass or volume of the electrodes. Both of these values can be determined from both CV and GCD techniques.

From CV profiles determination of specific energy (E_s, Wh kg^{-1} and E_{Vol}, Wh L^{-1}) and power densities (P_s, W kg^{-1} and P_{Vol}, W L^{-1}) of the material or devices is performed using the following equations:

$$E_s = \frac{\Delta V}{3600 \cdot mv} \int_{V_i}^{V_f} idV \tag{11}$$

$$E_{Vol} = \frac{\Delta V}{3600 \cdot Vol \cdot v} \int_{V_i}^{V_f} idV \tag{12}$$

and,

$$P_s = \frac{1}{m} \int_{V_i}^{V_f} idV \tag{13}$$

$$P_{Vol} = \frac{1}{Vol} \int_{V_i}^{V_f} idV \tag{14}$$

For GCD technique,

$$E_s = \frac{1}{m} \int iVdt \tag{15}$$

$$E_{Vol} = \frac{1}{Vol} \int iVdt \tag{16}$$

and,

$$P_s = \frac{E_s}{\Delta t} \tag{17}$$

$$P_{Vol} = \frac{E_{Vol}}{\Delta t} \tag{18}$$

1.2.4. Long term stability and cycle life

The long term operational stability of any supercapacitive device or electrode is crucial for its widespread commercial applicability. As mentioned earlier, purely EDLC devices, due to their simple adsorption based mechanism, displays great cycle life (>50,000 cycles).[55,56] However, the same cannot be ensured for pseudocapacitive materials as certain degradability in the reversible charge transfer process is usually observed after a few thousand cycles.[57] Therefore, proper long term characterization of such electrode materials is extremely necessary for the complete evaluation of the electrode materials. Such experiments can be performed by performing CV or GCD tests for a large number of cycles. The coulombic efficiency *w.r.t.*

cycle number can also be determined to evaluate any change in energy loss in the long term operation of such devices.

1.2.5. Determination of capacitance type and quantification techniques

The distinction between supercapacitive and battery materials was clear until Conway in the 1970s discovered new metal oxides like RuO_2 and MnO_2 that display redox reactions that were dominantly surface limited and exhibit EDLC like characteristics. Later, with the introduction of 2D materials like conductive polymers, metal oxides, transition metal carbides and nitrides, the line between battery and supercapacitors began to fade away rapidly. Simultaneous achievement of supercapacitor like power density and battery like energy density, which was long considered as the 'holy grail' of energy storage research, seemed achievable with pseudocapacitive energy storage. However, as supercapacitors slowly closed the energy storage metrics through strategic material design and additional redox reactions i.e., pseudocapacitance, the proper distinction between these materials became harder and demands further attention. Some of such characteristic techniques for the proper identification of energy storage materials are discussed in the following section.

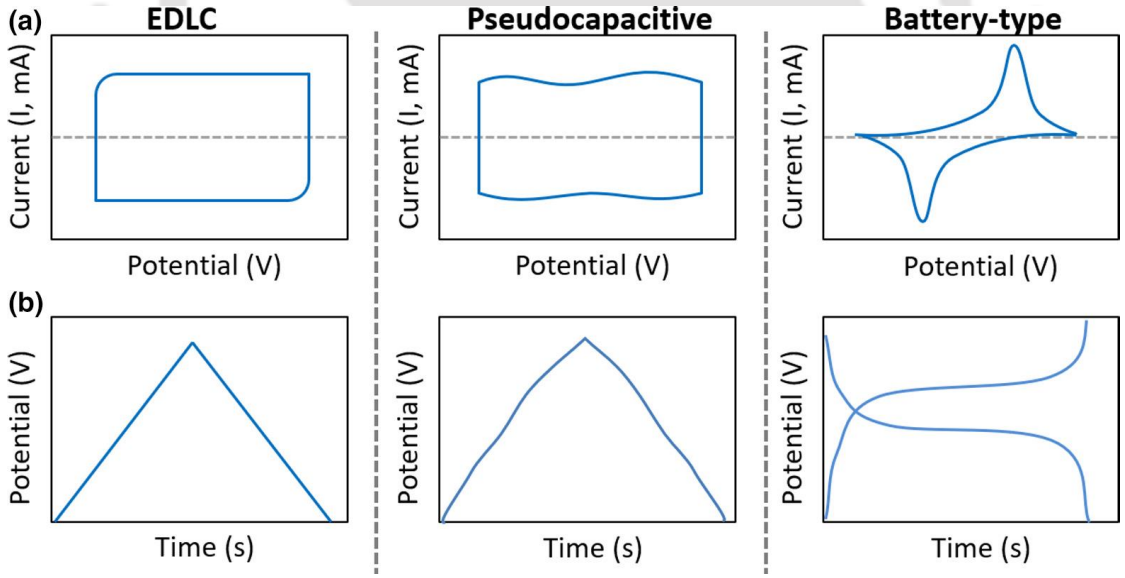

Figure 1.8. Electrochemical methods for energy storage materials: (a) examples of different CV curves for different energy storage types; (b) corresponding GCD curves with battery materials showing significant differences in the polarisation curve compared to EDLC and pseudocapacitive materials. Adopted from Ref. [12]

While designing energy storage electrodes, improper designation of storage type can potentially lead to conflicting results. In order to ensure proper classification, first, the

galvanostatic charge-discharge (GCD) and cyclic voltammetry (CV) should be analysed. The capacitance type can be uniquely distinguished from CV curves as normal EDLC type curves are featureless rectangular type whereas for pseudocapacitive materials, an increase of currents and certain potentials can be observed. The difference in the CV profiles can be seen in Fig. 1.8.a.

Things start to be confusing in the case of pseudocapacitors and batteries. The CV curves of both the pseudocapacitors and battery include current peaks at certain potentials, which is shown in Fig. 1.8.a. Correspondingly, the GCD curves of both the battery materials and pseudocapacitors can show varying degrees of deviation from the usual linear charge-discharge behaviours with deviations visible at potentials where redox or intercalation peaks are observed in the corresponding CV curves (Fig. 1.8.b). A simple yet effective approach for distinguishing pseudocapacitive materials is to identify whether the anodic and cathodic curves of the scan are the mirror image of one another. This implies fast redox reactions with minimal separation between redox peaks in both the scans, whereas the peaks for battery like material will often have a large separation. However, it should be noted that this approach is to be used with care as diffusion limitation of the electrolyte can also give rise to 'extrinsic pseudocapacitance', which can also show peak separation in the CV profiles. In such cases, distinction between these two kinetics becomes even more blurred and in-situ or ex-situ characterizations are required to understand whether the electrode material has gone through significant phase change or mass transfer, which would indicate toward a battery type material.

Another simple tool is the linear relationship of supercapacitor materials with varying scan rates. On the other hand, for semi-infinite diffusion controlled or battery type intercalation behaviour the current is often proportional to the square root of the scan rate. Thus, in general, $i(V) = av^b$, where $i(V)$ is the current at specific potential, a and b are constants and v represent the scan rate. In a logarithmic plot of current vs scan rate, b value of 1 indicates pure EDLC material whereas a value of 0.5 directs towards diffusion limitations which is predominant in battery like electrodes. Pseudocapacitive materials with symmetric reversible signature, that is no separation between their peaks reflect b value close to 1.[58,59]

For materials that have b value between 0.5 to 1, the energy storage kinetics is a combination of both surface capacitive and semi-infinite diffusion type. Ideally, for a pseudocapacitor,

although the b value should be near 1, this can depend on electrode material and architecture; specially the available porosity and thickness of the electrode.

Now to quantify the charge storage contributions, Trassati and Dunn have formalised a cyclic voltammetry based procedure with the help of the equation,

$$i(V,v) = k_1(V)v + k_2(V)v^{\frac{1}{2}} \quad (19)$$

Here the total CV current at a particular potential and scan rate is represented as a sum of the surface-limited process ($i \propto v$) and diffusion-limited process ($i \propto v^{\frac{1}{2}}$) with $k_1(V)$ and $k_2(V)$ being constants. Re-arranging this equation gives,

$$\frac{i(V,v)}{v^{\frac{1}{2}}} = k_1(V)v^{\frac{1}{2}} + k_2(V) \quad (20)$$

Solving this equation for $k_1(V)$ and $k_2(V)$ gives a linear equation where the slope and the intercept represent the $k_1(V)$ and $k_2(V)$ respectively.[60] This in turn provides the surface controlled and diffusion-limited processes as mentioned earlier. It is important to note that this equation does not account for the ohmic losses, which are responsible for peak shifts especially at higher scan rates.

With the above discussion in mind, in summery a EDLC or a pseudocapacitive material will have a current that is almost linear to the scan rate, consists of peaks that are highly reversible with little separation in their positions and do not indicate a phase change of the materials. On the other hand, battery type electrodes exhibit large separation in peaks with current being proportional to the square root of the scan rate along with large mass transfer with phase change of the electrodes.

1.3. Supercapacitive materials for energy storage

1.3.1. EDLC type materials

Carbon based materials are the prime candidates for purely EDLC type energy storage. Their extremely high surface area, scalable production, defined pore structure makes them highly suitable for electrodes for EDLC type supercapacitive electrodes.[61] Furthermore, the excellent electrochemical stability of carbon based materials in a wide range of electrolytes makes them a truly pH independent EDLC type electrode material.

The success of graphene attracted a lot of research in the field of material science which resulted in the discovery of a plethora of carbon based materials. From zero-dimensional (0D)

carbon dots to one-dimensional (1D) carbon nanotubes (CNT) or three-dimensional porous activated carbons; carbon based materials unveiled some of the most promising results in the fields of energy storage.

Graphene, a two-dimensional hexagonal array of sp^2 hybridized carbon atoms, remains as one of the most studied two-dimensional material in the world.[62–64] Due to the two-dimensional arrangement of atoms, graphene exhibits an exceptionally high surface area of 2,630 $m^2\ g^{-1}$ which immediately fulfills one of the major criterion as a superior EDLC material.[65] Furthermore, due to the delocalized electrons in the plane of graphene that originates from the π bonds of 2p orbitals enable exceptional electronic conductivity for the material which can greatly reduce the ohmic losses in a supercapacitive device.[65] Even then all such attributes often do not reflect in practical applications. The fact that single layer graphene is not suitable for commercial applications, these nanomaterials are assembled in a microstructural form by using these 2D materials as a building block. To enable large scale economical production of graphene, Hummers method is used to chemically exfoliate the stacked layers of graphite via decorating several functional groups over the basal planes of graphene.[66] These are known as graphene oxide or GO. Due to the presence of these functional groups the conductivity of GO is usually far less than graphene. Therefore, GO is often chemically reduced after assembly to develop macrostructures of reduced graphene-oxide (rGO). Li *et al.* achieved with such reduced graphene electrodes where they used chemical reduction to produce chemically converted graphene (CCG) and successively utilized vacuum filtration for the development of rGO film electrode.[67] However, during such assembly these nanosheets tend to restack in a face-to-face manner which greatly reduces their surface area. To overcome such challenges other materials like 0D or 1D materials can be incorporated within the macrostructures to overcome some of the critical restacking in the structure.[64] In another approach, pores can be introduced in the basal structure of graphene which can enable facile ion-transport into the bulk of the material to make a larger surface area available for supercapacitive applications.

1D carbon nanotubes (CNT) are cylindrical tubular structure of graphene like hexagonally arranged carbon atoms. CNTs are formed by basically rolling a graphene sheet in tubular structures.[68] Depending on the number of graphene layers, these structures can be single-walled (SWCNT) or multi-walled (MWCNT).[69] CNTs are usually developed form chemical vapor deposition (CVD), laser aberration and arc discharge processes.[70] Due to the intrinsic porous architecture paired with the graphene like high conductivity and stability, CNTs have shown extraordinary performance in high power applications. However, the lower specific surface

area of CNT (< 500 m^2 g^{-1}) bottlenecks the overall energy density and specific capacitance to a great extent.[71] Generally, the gravimetric capacitance of CNT based electrode lies within 110 F g^{-1}.[72]

Activated carbon (AC) is one of the most popular form of sp^2 bonded amorphous carbon that is used for supercapacitive applications. High surface area, porous structure, good conductive properties and moderately costly yet highly scalable development procedure make them highly suitable for commercial applications.[72] These carbon allotropes are usually developed from natural carbon containing materials like wood, coal, husk through thermal or chemical activation. The surface area of AC can be as high as 3000 m^2 g^{-1} which is mainly due to the numerous pores that are originated from the activation process of ACs.[73] On behalf of such attributes, ACs can deliver a specific capacitance of 100-300 F g^{-1} depending on the pore size distribution and quality of ACs. Furthermore, the life cycle of AC electrodes can be as high as 10^6 cycles due to its high stability in EDLC charge-discharge process.[74–76] However, the bottleneck with AC lies in its low energy densities and its dependence on capacitance over the quality of AC which is highly dependent on the carbon source and preparation method.

Carbon templating offers a unique and effective way to produce nanostructured carbon with large surface area, uniform and ordered pore size distribution with interconnected porous channels.[77] Templated carbons are usually prepared by inflation of an initial carbon containing precursor followed by high temperature carbonization. Such an approach allows for application specific controlled development of carbon materials with defined structural properties. For example, templated carbon obtained through zeolite Y as a template yielded a specific capacitance of 340 F g^{-1} which has high stability in long-term cycling (>10,000 cycles).[78] While zeolite Y as a template gives rise to microporous carbon, silica sphere and SBA-15 can provide with macroporous and mesoporous carbon respectively.[77] Such controllability over pore size allows facile ion transport channels in the structure and enables development of commercial scale mass loading of electrodes. However, such fabrication of carbons is often associated with high development cost of materials.

1.3.2. Pseudocapacitive materials

Pseudocapacitive materials are often regarded as a bridge between high power density EDLC supercapacitors and high energy density batteries. Fig. 1.1 indicates the specific energy vs. time of charging pl of EDLC devices and batteries where the difference between these two systems can be clearly identified. Where batteries like Li-ions have high energy densities with charging

time of nearly hours, this energy value rapidly decreases at lower time scales. On the other hand, EDLC devices have constant energy density at nearly all time scales, but at the cost of low stored energy. Thus, pseudocapacitive materials find their application in between these two extremes with timescale lying between ~10s to minutes.

Pseudocapacitance first surfaced with the investigation electrochemical properties of RuO_2 in 1971.[79,80] However, initial studies indicated towards low gravimetric values due to the inaccessibility of the bulk of the structures. Subsequently, the importance of hydrated structure was identified and the specific capacitance value increased up to 700 F g^{-1} with $RuO_2 \cdot nH_2O$, where n = 0.5.[81] The pseudocapacitive mechanism of the process can be identified as,

$$RuO_x(OH)_y + \delta H^+ + \delta e^- \leftrightarrow RuO_{x-\delta}(OH)_{y+\delta} \quad (21)$$

here, theoretically, specifically $\delta = 2$ results in a maximum capacitance of ~ 1450 F g^{-1}.[82]

The benefits of hydrated RuO_2 primarily result from four unique structural and chemical features, a) redox behavior of Ru^{4+} cation allows fast redox reactions for pseudocapacitance; b) presence of structural water allows protons from electrolyte to fast access the "inner surface" of the electrode; c) metallic conductivity of RuO_2 decreases the ohmic losses; d) a porous "outer surface" area decreases the diffusion path of electrolytes. In spite of these significant advances, widespread commercialization of ruthenium based electrodes have still not been realized due to the high cost of the transition metal oxides.

In this regard, MnO_2 emerges as a great alternative to RuO_2 due to its low cost, greater abundance and overall higher theoretical capacitance.[47] In aqueous medium the charge storage mechanism of MnO_2 occurs through the reversible change in the oxidation state of Mn from +4 and +3[83]:

$$MnO_2 + xA^+ + xe^- \leftrightarrow A_xMnO_2 \quad (22)$$

The pseudocapacitive performance of MnO_2 was first investigated by Lee and Goodenough in 1999.[84] A large theoretical capacitance of 1233 F g^{-1} was predicted for the material for a potential window of 0.9.[85] Whereas this predicted capacitance is very much achieved (>1000 F g^{-1}) for ultrathin film electrodes, the performance drops drastically as the electrode thickness increases (~ 200-250 F g^{-1}).[86–88] This is due to the relatively low conductivity of MnO_2 (10^{-7} to 10^{-3} S cm^{-1}) structures compared to RuO_2 (10^4 S cm^{-1}). Therefore, significant advancement

needed to be done in order to achieve greater conductivity to enable the development of commercial scale mass loading electrodes.

Several metal oxide spinel structures having the formula AB_2O_4, offers excellent theoretical pseudocapacitive properties, low cost and a structural three dimensional porous pathways for faster ion diffusion of electrolytes. Co_3O_4,[89] Fe_3O_4,[90] Mn_3O_4[91] are some of the popular spinel structure oxides that are used for electrochemical energy storage systems. Mn_3O_4 particularly exhibits excellent capacitive performance having 314 F g^{-1}.[92] However, the low conductivity of the material impedes the rate performance. Thus it is often paired with a conductive scaffold like graphene to improve the rate performance at the cost of some capacitance loss. $NiCo_2O_4$ is another spinel oxide that shows excellent capacitive performance with gravimetric capacitance as high as 2000 F g^{-1} for an 0.6 V operational window.[93] However, it is to be noted that while working with spinel oxide, special care has to be taken as these materials often include battery like chemistry along with the pseudocapacitive processes. Thus to avoid any phase change of these materials, the potential window has to be considered carefully. Further preparation of spinel oxide electrode for supercapacitive applications have to be carefully performed to keep these structures ultrathin at nanoscale form to emphasize the pseudocapacitive reactions only.

Layered transition metal oxides (e.g., $Ni(OH)_2$, $Co(OH)_2$) are also receiving much attention due to their intrinsic nm scale interlayer spacing which allows fast diffusion and intercalation/de-intercalation of ionic species into the structure. However, similar to spinel oxides, layered hydroxides also involve at least one phase change during the charging-discharging process.[94] This makes using such materials as extrinsic pseudocapacitors as the bulk of the material incorporates battery like chemistry. Thus, these electrodes are prepared thin enough to make the pseudocapacitance dominant over the battery like kinetics.

In addition to these above mentioned materials, several transition metal based chalcogenides provide pseudocapacitive properties at nanostructured form which is not otherwise observed in their bulk structure. Materials like MoS_2, TiS_2 have pseudocapacitance when they are developed as nanoparticles or 2D sheet like structures. Furthermore, very recently MXene materials have emerged as a major pseudocapacitive candidate due to their several physiochemical properties that attracted a lot of research in the few recent years.

1.4. MXene and MXene based composites for energy storage

1.4.1. Introduction to MXene

MXenes are the latest addition to the family of pseudocapacitive materials that recently attracted a lot of attention in the field of energy storage. Discovered in 2011 by Gogotsi *et al.*, MXene wields some rare combination of metallic conductivity while simultaneously having pseudocapacitance and hydrophilicity.[95] Due to its extraordinary physiochemical properties MXenes have attracted a lot of research in various applications such as energy storage,[96,97] sensing,[98,99] electromagnetic interface shielding,[100,101] solar water evaporation,[102] catalysis[21] *etc.* Till now more than 150 types of MXene materials have been successfully predicted and new members are being discovered routinely.

MXenes are derived from MAX phase materials which have the general formula $M_{n+1}AX_n$ where M represents the transition metals, A is group IIIA or IV A elements, X denotes carbon and/or nitrogen and *n* can have the value 1-3. For MXene synthesis, these A atoms are removed from the MAX phase with the help of chemical etching treatments.

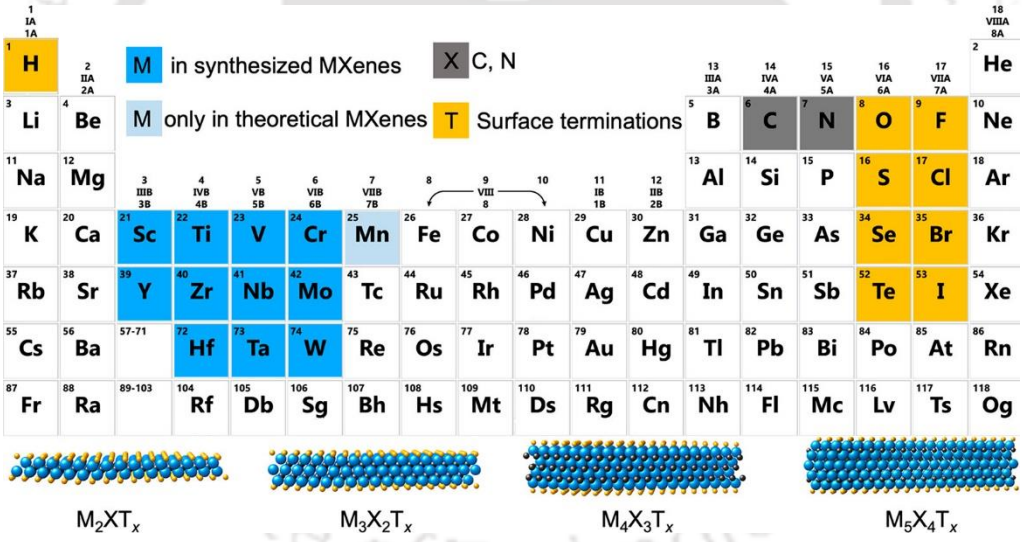

Figure 1.9. Periodic table indicating the possible compositions of MXene. Schematics at the bottom represent the four possible structures of MXene materials. Adopted with permission from Ref. [12]

1.4.2. Preparation methods

Most 2D materials like graphene are stacked one over another in their bulk structure and held together via the action of the van der Waals force. This allows simple delamination of the building blocks from the bulk structure. However, for MXene, M and X atoms are connected with the group III and IV A atoms via strong metallic bonds, which makes the etching much

more cumbersome. However, the basic idea behind chemical etching lies in weakening the relatively weaker M-A bonds in the MAX structure. In the pioneering effort by Naguib and Gogotsi, they included hydrofluoric acid (HF) to etch MAX phase Ti_3AlC_2.[95] As a result of the strong reaction the with the MAX phase, $Ti_3C_2T_x$ MXene was produced where the basal plane of the material was decorated with several functional groups. Thus, MXenes have the formula $M_{n+1}X_nT_x$ where T_x represents several functional groups like –OH, –Cl, –F, –O etc. The basal plane coverage and the type of functional groups very much depend on the type of etchants used and etchant time. The above mentioned reaction follows the path,

$$Ti_3AlC_2 + 3HF \rightarrow Ti_3C_2 + AlF_3 + \frac{3}{2H_2} \quad (23)$$

$$Ti_3C_2 + 2H_2O \rightarrow Ti_3C_2(OH)_2 + H_2 \quad (24)$$

$$Ti_3C_2 + 2HF \rightarrow Ti_3C_2F_2 + H_2 \quad (25)$$

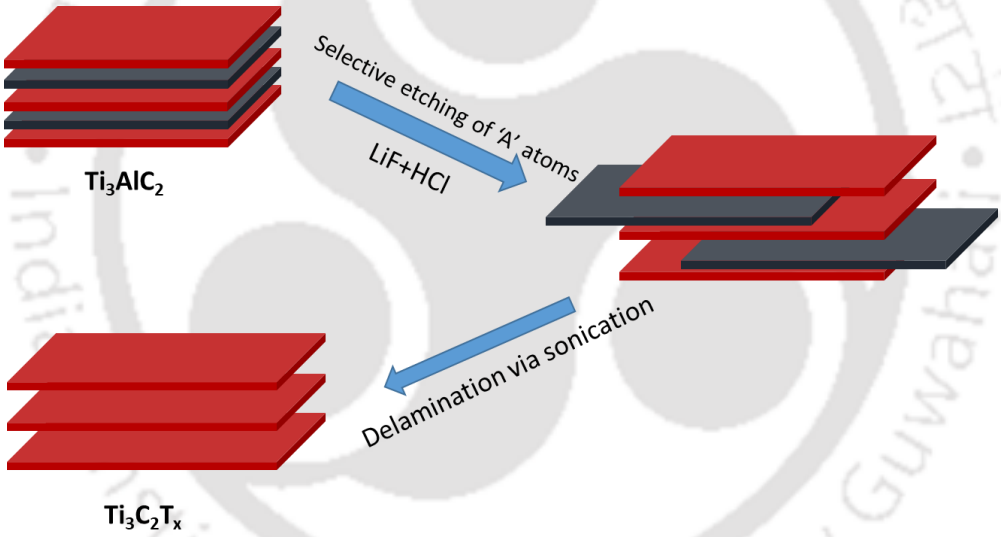

Figure 1.10. Schematic illustration of the acid etching process of MAX material Ti_3AlC_2 to develop $Ti_3C_2T_x$ MXene.

The resultant *A* atom etched multilayer MXenes are then further delaminated with several delamination methods like ultrasonication and cation intercalation to synthesize single or few layer MXene flakes. Although this method was highly successful, HF based etching is now being slowly replaced with milder hydrochloric acid (HCl) and fluoride salt (LiF) based in-situ HF techniques as introduced by Ghidiu *et al.*[97] Not only this procedure is a much safer approach to etching but it also improves the yield, lowers the sonication times and overall better quality MXene with less defects and vacancies. Furthermore, it was shown that with careful selection

of LiF and HCl concentration in the etching solution, the delamination can actually be accomplished only with handshaking which resulted in large sheet MXene. This procedure is known as minimally intensive layer delamination method or MILD.[103]

1.4.3. Structural and electronic properties of MXene

Structure of MXene cannot be defined without considering the position of its functional groups. The position of these functional groups is considered to be over the hollo sites between two adjacent C atoms. As an example, position of the structural model for M_2X MXenes predicts four different positions for functional groups in combinations of different positions over the A and B sites as shown in Fig. 1.11.[104] These are (a) functional group atoms over the hollow site A where no X is present below; (b) both the functional groups on the B site that is in line with the underlying X atoms; (c) both the functional groups directly over the transition metal atoms and (d) one functional group over A and B site each.

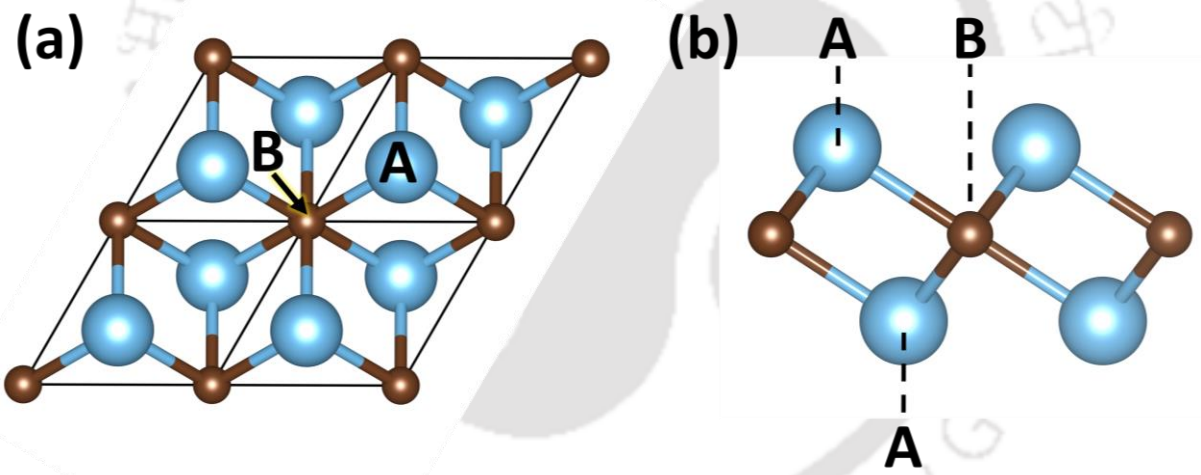

Figure 1.11. (a) Top and (b) side view of M_2X with A and B sites indicating the possible positions of functional groups over the structure. Blue and brown balls indicate the M and X atoms respectively.

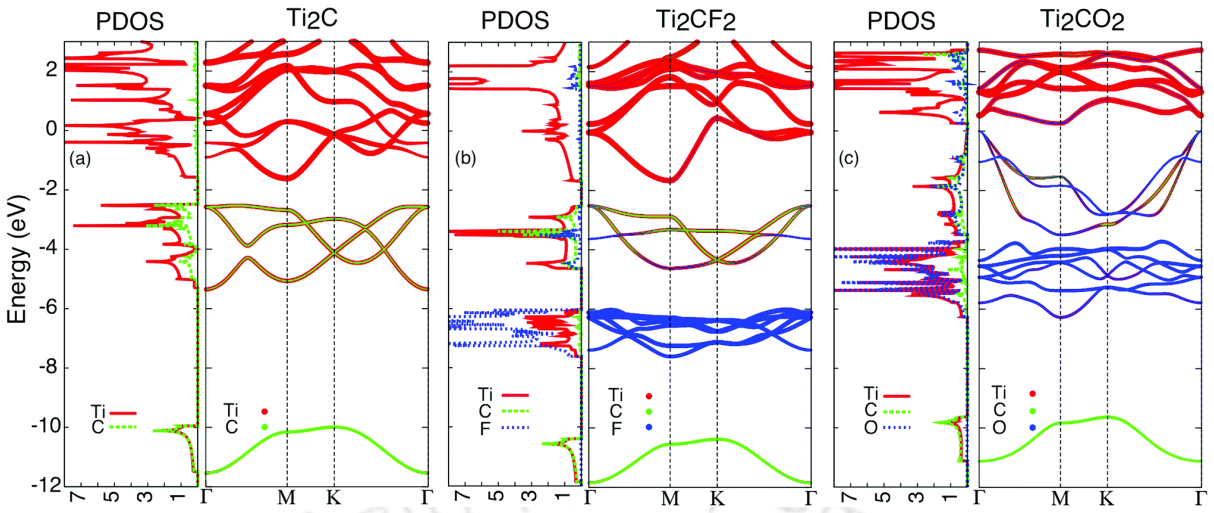

Figure 1.12. Projected density of states and corresponding band structures for (a) Ti_2C, (b) Ti_2CF_2, (c) Ti_2CO_2. Fermi level is located at 0 eV in all the diagrams. Adapted from Ref. [104]

Numerous experimental and theoretical studies conclude that the MXene too, similar to MAX phase materials, has a metallic electronic structure. Such metallic property arises due to the d orbital of transition metals that extends over the Fermi level, whereas, the p bands of C and N lie slightly below the d band with a band gap. The electronic structure of MXene varies significantly once the functional groups are introduced to the structure. For example, several model structures predict that MXenes with F and OH terminations have electronic structures similar to pure MXene, i.e., metallic.[105] On the other hand, MXenes with O terminations tend to have a band gap and thus have a semiconducting nature. $Ti_2C_2O_2$ shows a semiconducting electronic structure with a bandgap of 0.24 eV while $Ti_2C_2F_2$ and $Ti_2C(OH)_2$ are both metallic in nature. This trend is further observed in Zr_2CO_2 and Hf_2CO_2 MXenes with 0.88 and 1 eV bandgaps.[105] The semiconducting nature of O terminations arises from the fact that O requires two electrons from the basal plane of MXene to stabilize whereas F and OH terminations require only one such electron. This moves the Fermi level of the system much lower for O groups than for OH and F terminations. In Fig. 1.12 the medication in electronic structure with different surface terminations is shown. It can be seen that both F and O groups introduce new bands in the structure. After hybridization, although F receives an electron from the basal plane, the downshifted Fermi level still lies amidst the d band and thus keeps the system metallic. On the other hand, because of two electron contribution to O terminations the Fermi level moves further down lying in the center of Ti d and C p bands which results in the semiconducting nature of the material.[104]

1.5. Challenges in nanomaterial assembly and energy storage

Development of a highly scalable and low cost assembly technique, which is not only adaptable to application specific needs but also preserves the intrinsic qualities of a nanomaterial even in its macrostructural form, is the key to their grand success in real world scenarios. The nanoscale dimensions of 2D materials inherently require them to be assembled into macrostructural forms for their use in most practical applications. However, while designing an ideal 3D structure out of these nanomaterials, several structural parameters should be realized specially when using them as electrodes for supercapacitive applications. For example, while developing electrode structures, face-to-face restacking of nanosheets remains one of the major challenges which not only reduces the accessible surface area of the electrodes but also impedes the unrestricted flow of electrolyte into the bulk of the structure. This restricts the development of high mass loading electrodes as the diffusion resistance of electrolyte increases rapidly. In the recent years, as MXene based materials have shown extraordinary performance metrics in the field of supercapacitive energy storage, several strategies have emerged to address these challenges through controlled assembly and structural modifications of electrodes. In this section we review the recent advances of such techniques mainly applied for $Ti_3C_2T_x$ MXene and their applications in supercapacitive energy storage applications.

All the macrostructures of MXene that are utilized in supercapacitive applications can be categorized mainly into three different forms: a) dried thin films b) aerogels and c) solvated MXene frameworks. Dried films of MXene are mainly developed through spray coating,[106,107] rolling of MXene 'clay' and vacuum filtration techniques.[108,109] This is one of the frequently used macrostructural forms for researchers mainly for its simplicity in the development of MXene and MXene based electrodes. In the early years, Ghidiu *et al.* developed MXene based 'clay' electrodes via rolling of clay like $Ti_3C_2T_x$ MXene and then subsequently died the pressed MXene to develop thin film electrodes. These MXene materials provided a volumetric and gravimetric capacitance of 900 F cm^{-3} and 245 F g^{-1} respectively in acidic 1M H_2SO_4 electrolytes.[110] Further, vacuum filtration methods, due to its facile development procedure, is often the first choice of researchers for nanomaterial assembly. In vacuum filtration, a stable MXene dispersion is passed through a porous membrane with the help of a suction device. Vacuum filtered MXene electrodes display around 280 F g^{-1} of gravimetric capacitance which decreases rapidly as the thickness of electrodes increases.[111] However, due to the high pressure gradient in the vacuum filtration method, the MXene nanosheets get highly restacked in a face-to-face manner which reduces the electrochemical performance of the material. Further, due to

restacking, the ion transport channels get blocked which affects the rate performance and this problem enhances as the mass loading of the electrode increases. Several other 2D materials are often introduced along with MXene to mitigate this restacking in the electrode. Zhao *et al.* incorporated multi walled CNT (MWCNT) in the MXene dispersion and successively vacuum filtered the dispersion to develop MXene/CNT composite electrode. X-ray diffraction spectroscopy (XRD) indicated an increase in the distance between $Ti_3C_2T_x$ interlayers due to the incorporation of CNTs. As a result, these composite electrodes showed much higher capacitance and rate performance in 1M $MgSO_4$ electrolyte compared to the pristine MXene films. A gravimetric capacitance of 150 F g^{-1} was achieved in the neutral electrolyte which remained at 117 F g^{-1} at 200 mV s^{-1}, reportedly providing 130% more capacitance than pure MXene film.[112] Later, Huang et al. introduced MnO_2 along with the MXene and CNT composite to further increase the specific capacity of MXene composite (221 F g^{-1}).[113] Graphene is also widely used to control the restacking in MXene VF electrodes. Introduction of merely 5 *wt*% graphene in the VF MXene electrode can result in an impressive volumetric performance of 1040 F cm^{-3}. More importantly, the rate performance of these electrodes witness an impressive improvement over the pure $Ti_3C_2T_x$ MXene, providing 30% capacitance retention at a scan rate of 10 V s^{-1} compared to just 6% retention in pure MXene counterpart. Such improvement in capacitive performance can be attributed to the graphene sheets that impedes the severe face-to-face restacking of the nanosheets and thus preserves the ion channels to improve the rate performance.[114] The surface accessibility and ions transport channels were further improved by incorporating holey graphene which further increased the volumetric capacitance up to 1445 F cm^{-3} at 2 mV s^{-1}.[115] Furthermore, several conducting polymers like polyaniline (PANI), polyvinyl alcohol (PVA), poly(diallyldimethylammonium chloride) (PDDA) are also introduced with MXenes to produce flexible, robust, conducting, restacking controlled electrodes.[116–118] In the first ever report of such MXene/polymer composite, Gogotsi *et al.* added PVA with MXene dispersion to develop a flexible, free-standing conducting film of MXene.[119] The resulting film achieved a volumetric capacitance up to 530 F cm^{-3} which was a crucial result to promote polymer MXene composite research. However, although these methods mitigated the restacking problem to some extent, most of these additive materials have low conductivity, hydrophilicity and pseudocapacitive properties compared to MXene. Thus the introduction of such foreign materials, specially polymers, lowers the true potential of the MXenes in supercapacitive energy storage applications.

Other than the development of hybrid electrodes with MXene, structural modification of electrodes through interlayer distance control, porosity modification during assembly also drastically affect the supercapacitive performance in MXene materials. Effect of shortened ion pathways in supercapacitive energy storage especially in restacked MXene films was studied in detail by Tang *et al.* They not only studied the effect of sheet size in ion transport but also introduced partial etching in the MXene sheets via controlled oxidation with concentrated sulfuric acid (H_2SO_4).[120] It was observed that MXene vacuum filtered electrodes with smaller MXene flake sizes have a much better rate performance than large MXene film electrode. The average flake size in this study was 1.28µm and 150 nm for large and small flake MXene respectively. The rate performance of these electrodes improved drastically when they were partially etched with H_2SO_4 to introduce pores in the structure. The acid induced etching restricted the oxidation of Ti atoms in $Ti_3C_2T_x$ which was confirmed from XPS analysis. The porous interconnected electrodes achieved a capacitance of 324 F g^{-1} at 5 mV s^{-1}. Interestingly, the specific capacitance of etched-MXenes increases for both large and small flake MXene which can be attributed to the increased access to active sites in MXene electrodes. Also, the rate performance of the small etched-MXene electrode increased dramatically as it retained 39% of capacitance at 10,000 mV s^{-1} compared to just 5.9% retention in pristine electrodes. In another report, macroporosity within the electrode structure was introduced by using polymethyl methacrylate (PMMA) spheres during vacuum filtration to induce an open structure in the electrode. Later, the composite was annealed at 400 ºC under an inert atmosphere to anneal the PMMA spheres which led to a 1-2 µm macropores with submicron wall thicknesses.[121] Such an electrode delivered a specific capacitance of 310 F g^{-1} at 10 mV s^{-1} and up to 100 F g^{-1} at an ultrahigh scan rate of 40,000 mV s^{-1} for a 13 µm film. Although, the rate performance looks promising for a pseudocapacitive material, the mass loading of these electrodes were limited to < 1 mg cm^{-2}, which may not be suitable for the commercialization of MXene electrodes and the performance of such electrodes at commercial scale mass loadings (~ 10 mg cm^{-2}) is yet to be investigated.

Solvated MXene frameworks are cross-linked 3D macrostructure of MXene and MXene composites which retains a defined shape while being solvated in a solvent. For example, MXene porous structure which has intercalated water into the entire framework is known as MXene hydrogels. These hydrogels or SMFs are usually critically died to form aerogels of these materials. Hydrogels provide numerous advantages for applications that involve a liquid solid interface like supercapacitive applications. Due to the intercalated water or solvent, these

macrostructures retain numerous ion transport channels in the structure which allow for faster ion transport and rate performance of the electrodes. Further, the porous network allows higher active site accessibility than dried films which tend to result in higher specific capacitance in electrodes. Now, although hydrogels and aerogels look similar as aerogels are derived from hydrogels through critical drying, due to the freezing of SMFs the nanosheets in the pore walls tend to restack in thicker walls which again reduces the surface area of electrodes. One of the usual routes to create 3D hydrogel monoliths of MXene is graphene assisted hydrothermal process. Yang *et al.* utilized the hydrothermal method to introduce chemical bonds between rGO and MXene nanosheets with the help of ethylenediamine (EDA). The resultant structure had an interconnected porous 3D hydrogel structure having specific capacity of 370 F g^{-1} at 2 mV s^{-1}.[122] Although this method provides a facile approach to develop 3D monolithical hydrogels, the use of high temperatures in the development process oxidizes the MXene which reduces the electrochemical performance of the material. In another approach, the negatively charged MXene nanosheets were crosslinked by using divalent cations like Fe^{2+}, Ni^{2+}, Co^{2+}, Mg^{2+}. These ions neutralize the electrostatic repulsion between MXene sheets to create microgels of the material. Deng *et al*. were able to achieve 272 F g^{-1} with high capacitance retention of 226 F g^{-1} at 1 V s^{-1}. However, although this process works efficiently to develop pristine MXene hydrogels, the effect of binding ions in the acidic electrolyte is not yet studied. Further, due to the local microgel assembly, these structure lacks structural integrity compared to previously mentioned hydrothermal monoliths. Unfortunately, the development of hydrogels of MXene is mostly limited to the above mentioned approaches which greatly suffer from synthesis induced degradation of MXene, scalability and structural integrity of these structures. Given the inherent beneficial properties of hydrogels in energy storage, immediate research attention into such macrostructure is very much required.

Unidirectional freeze drying followed by thawing in protic acids or drying in lypolizer is another approach to develop three dimensional hydrogel or aerogel monolith respectively. In such a method, a certain concentration of MXene solution in a metal base Teflon mold is put in contact with liquid nitrogen to freeze rapidly. The unidirectional freezing (down to top) arranges the nanosheets vertically in a monolithic structure. After freeze drying, these monolithical aerogels were used as supercapacitive electrodes where the excellent specific capacitance of 380 F g^{-1} was achieved. Furthermore, due to the vertical orientation in the structure, the diffusion of electrolyte ions into the bulk of the structure was eased which allows good retention of capacitance even at high mass loadings of 13 mg cm^{-3}.[123] In order to vertically

orient the MXene sheets in the electrode structure, Yang *et al.* reported an interesting approach utilizing the liquid crystalline phase and suitable surfactant induced controlled orientation in MXene. MXene dispersion in discotic nematic phase was obtained by strategically increasing the dispersion concentration up to 200 mg mL^{-1}. A non-ionic surfactant hexaethylene glycol monododecyl ether ($C_{12}E_6$) was then added with the solution to increase the molecular interaction among the nanosheets. The gel like dispersion was then sandwiched between two glass slides followed by uniaxial mechanical shearing to align the MXene sheets. [124] Due to the controlled orientation, these MXene electrodes showed consistently high scan rates for electrode thickness up to 200 µm. Furthermore, these electrodes retain almost 100% of their initial capacitance even after 20,000 charge-discharge cycles which indicates their excellent stability in the long run. Although this method undoubtedly provides quite promising results, the complexity in the development process and its scalability remains a challenge.

1.6. Objective of this thesis work

As evident from the previous discussion, MXene materials are a highly promising candidate as a supercapacitive electrode material for energy storage. Specially, the pseudocapacitive properties along with its hydrophilicity and metallic conductivity establish this material in a league of its own. However, although several alternative approaches have been taken to develop an ideal macrostructure of MXene suitable for supercapacitive electrodes, almost all of these techniques have their own disadvantages. Scalability and loss of performance at high mass loading or thickness are the most prominent ones that can bottleneck the widespread adaptation and industrial realization of this wonder material. To address these challenges, the primary motivation and the main objective of this thesis are as follows:

a) Development of a highly porous, hydrated hydrogel structure of MXene and graphene in a complete ambient condition synthesis strategy. The minimal quantity of graphene will act as gelator while the supercapacitive performance will mainly be contributed from pseudocapacitive MXene.
b) Development of pristine MXene hydrogels via strategic tuning of inter-sheet interaction and controlled sheet orientation via investigating the liquid crystalline properties of MXene dispersion.
c) Integration of MXene with bio-inspired agricultural waste derived cellulose nanofibers in a restacking controlled flexible film structure to achieve ultrahigh mass loading while retaining state-of-the-art capacitive performance.

d) Investigating the effect of an externally applied electric-field over the negatively charged MXene sheets to induce gelation in MXene while restricting the MXene oxidation in the anodic environment.

e) To achieve commercial scale mass loadings and scalability with 'second scale MXene dispersion to macrostructure development' protocol with greater controllability over MXene sheet orientation in the macrostructure.

1.7. Thesis contents and organization

This thesis work has been presented in six different chapters starting from a brief introduction of state-of-the-art technologies and challenges in MXene and energy storage research, specially supercapacitive devices. The rest of the thesis discusses about approaches to overcome the challenges while maintaining state-of-the-art energy storage metrics. This thesis ends with concluding remarks with future prospects in the field of energy storage. A brief description of the chapters is detailed below.

Chapter 1: This chapter provides a brief discussion about the current state-of-the-art energy storage technologies and characterization techniques particularly focusing on supercapacitive applications. Introduction to MXene based materials, recent progress of MXene in the field of energy storage and the current challenges over the development of MXene based electrodes have been included. Design principles of different MXene electrodes to attain commercial applicability and their corresponding experimental procedures have also been incorporated. At the end of the chapter, the objectives and motivation behind the present work are illustrated briefly.

Chapter 2: Hydrogels, a unique macrostructure developed from nano-building blocks, offers multidimensional advantage in a plethora of applications due to their hydrophilic porosity and restacking controlled high surface area. The excellent pseudocapacitive and conducting properties of MXene, interlinked in hydrogel network with one of the most studied supercapacitive material graphene, is expected to deliver outstanding supercapacitive performance. Here, in this chapter, we introduce a complete ambient condition gelation protocol to develop hybrid hydrogels of MXene and graphene, which not only protects MXene from any synthesis induced oxidation, but also provides state-of-the-art hybrid hydrogels that display excellent energy storage properties. Aided by a small quantity of graphene, this layer-by-layer gelation strategy prohibits complete face-to-face restacking of the two-dimensional nanosheets due to the intercalated water that ensures numerous ion-transport channels in the

hydrogel network. The as-developed MXene-graphene macrostructure displays excellent energy storage with 654 F g^{-1} in a three-electrode setup. Interestingly, simultaneous achievement of high areal (1442 F cm^{-2}) and volumetric (1522 F cm^{-3}) capacitance was ensured via simple tuning of gelation conditions. Furthermore, due to the numerous ion transport channels in the hydrogel structure, commercial scale mass loading (~ 10 mg cm^{-2}) of electrodes were successfully realized without sacrificing the rate performance. Due to their excellent rate performance, supercapacitive devices of MXene-graphene electrodes ensures power densities as high as 10 kW kg^{-1} with an equally impressive maximum energy density of 11 Wh kg^{-1} while being capable of retaining 98% capacitance at the end of 8000 charge-discharge cycles.

Chapter 3: In the last chapter, graphene was utilized as a gelator to link the MXene nanosheets in a network of porous hydrogel structures. However, the possibility of developing self-supporting pristine MXene hydrogel without the addition of any gelator or binder remains unanswered. In this chapter, freestanding hydrogels of pristine MXene have been successfully realized via liquid crystalline phase induced quasi-ordered self-assembly of MXene sheets over a metal plate. In order to address the weak interaction of MXene nanosheets in a hydrogel network, the dispersion properties of MXene are strategically tuned via density induced local orientational ordering and sheet size optimization to successfully develop the self-supporting macrostructure. In this work, we have identified that self-supporting hydrogels of MXene can only be formed above a critical dispersion concentration (C_{ct}) which is highly dependent on the MXene sheet size. The C_{ct} is determined to be 60 mg mL^{-1} and 40 mg mL^{-1} respectively for MXene sheets with an average dimension of 1.4 µm and 340 nm respectively. When utilized as electrodes for energy storage applications, these critical-density controlled self-assembled hydrogels exhibit excellent performance as supercapacitive electrodes with a gravimetric capacitance of 391 F g^{-1}. Furthermore, on behalf of the restacking controlled porous architecture, the mass loading of the hydrogels can be extended up to ~15 mg cm^{-2} while retaining a gravimetric capacitance of 337 F g^{-1}. The origin of this excellent retention of energy metrics at high mass loadings can be attributed to the predominant surface capacitive contribution (>94%) compared to the performance limiting diffusion limited processes. Further, a detailed analysis of energy storage kinetics depending on the MXene nanosheet size is illustrated in this chapter.

Chapter 4: Development of pristine MXene hydrogels with spontaneous assembly of MXene nanosheets over metal plate is highly dependent on dispersion concentration and requires hours of gelation time. In this chapter, an electric field assisted forced assembly method is introduced

to overcome the critical concentration requirement for self-supporting MXene hydrogel development. Not only the forced assembly technique can develop free-standing MXene hydrogels from dispersion concentrations as low as 5 mg ml^{-1}, but also drastically reduces the gelation time enabling MXene hydrogel development in 30 seconds only. An externally applied electric field in association with suitable choice of high reduction potential metal anode enables successful development of MXene hydrogels in seconds with minimal dispersion concentrations. Directional electrophoretic drag along with potential controlled in-situ interfacial release of ions gives rise to highly tunable sheet orientations in the hydrogel structure. This highly controllable strategy enables facile development of two-dimensional sheet like or three-dimensional monolithic structures of vertically oriented MXene hydrogel. Furthermore, a suitable range of applied bias is estimated through density functional theory estimations to restrain the possible oxidation of MXene at the anodic interface. The electrochemical performance of the electric-field guided MXene hydrogels were then studied in both three-electrode and two-electrode configurations to evaluate their performance. The as developed hydrogels exhibit an excellent performance of 395 F g^{-1} at 2 mV s^{-1} while retaining 42% of capacitance at high scan rates of 5000 mV s^{-1}. This field-guided assembly can also be utilized to develop flexible dried films of MXene which exhibits an excellent volumetric performance of 1251 F cm^{-3} with an excellent cyclic stability of 95% at the end of 15000 charge-discharge cycles.

Chapter 5: Development of compact high mass loading electrodes while simultaneously achieving excellent gravimetric, volumetric and areal capacitance still remains a fundamental challenge to be addressed till this date. In this chapter, bio-inspired co-assembly of cellulose nanofiber (CNF) and MXene is demonstrated with electric field guided forced assembly followed by successive ambient drying. Interestingly, due to the interfacial assembly method, MXene-CNF hybrid structures can be developed over any ion-permeable conducting or non-conducting substrate place in the anode-MXene dispersion interface. The benefits of CNF integration in MXene film structure is two-fold: first, the CNF structures in the interlayers of MXenes restrain critical restacking of nanosheets during drying by introducing ion-transfer veins throughout the structure and second, cross-linking of the strong cellulose fibers with MXene provides much higher structural strength compared to pristine MXene films, improving its flexibility and durability. Desired concentrations of CNF in the hybrid structure can easily be tuned with field-guided co-gelation, which is also confirmed through X-ray photoelectron studies along with thermo-gravimetric analysis. The MXene-CNF hybrid films provide

excellent gravimetric capacity of 360 F g^{-1} which is almost 30% higher than similarly produced vacuum filtered films. Further, the rate performance of the electrode can be readily tuned via simple CNF concentration tuning which enables 56% of capacitance retention at 10000 mV s^{-1} with a 50 *wt*% CNF electrode. Interestingly, due to the controlled restacking in the electrodes, a mass loading as high as 74 mg cm^{-2} was reached while maintaining an areal, volumetric and gravimetric capacitance of 16 F cm^{-2}, 1356 F cm^{-3} and 221 F g^{-1} respectively. Such unprecedented high mass loading with all-round capacitance metrics are rarely reported in literature. The MXene-CNF (MXCF) electrodes were also paired with reduced graphene-polyaniline-carbon nanotube (rGO-PANI-CNT) hybrid positive electrode to increase the operation potential to 1.5 V. This enables the device to deliver a high energy density of 28 Wh kg^{-1} with a maximum power density of 123 kW kg^{-1}. As a proof of concept of the transferability of the hybrids over different substrates, the MXene-CNF films were developed over carbon cloth, which was then analyzed as a wearable device. The stability of the wearable device over 5000 bending cycles at different angle is also illustrated in this chapter.

Chapter 6: Chapter 6 highlights the key findings of this work with concluding remarks. The future prospects of the MXene and MXene based hybrid electrodes in energy storage is also discussed at the end of this thesis.

References

1. IEA. Assessing the effects of economic recoveries on global energy demand and CO2 emissions in 2021. *Glob. Energy Rev. 2021* 1–36 (2021).
2. Perera, F. Pollution from Fossil-Fuel Combustion is the Leading Environmental Threat to Global Pediatric Health and Equity: Solutions Exist. *Int. J. Environ. Res. Public Health* **15**, (2018).
3. *Renewable-Energy-Driven Future*. *Renewable-Energy-Driven Future* (Elsevier, 2021). doi:10.1016/C2019-0-01298-8.
4. David, T. M., Silva Rocha Rizol, P. M., Guerreiro Machado, M. A. & Buccieri, G. P. Future research tendencies for solar energy management using a bibliometric analysis, 2000–2019. *Heliyon* **6**, e04452 (2020).
5. Winter, M. & Brodd, R. J. What are batteries, fuel cells, and supercapacitors? *Chem. Rev.* **104**, (2004).
6. Battery-Supercapacitor Energy, F., Astaneh, M., Andric, J., Lemian, D. & Bode, F. Battery-Supercapacitor Energy Storage Systems for Electrical Vehicles: A Review. *Energies 2022, Vol. 15, Page 5683* **15**, 5683 (2022).
7. Libich, J., Máca, J., Vondrák, J., Čech, O. & Sedlaříková, M. Supercapacitors: Properties and applications. *J. Energy Storage* **17**, 224–227 (2018).
8. Lemine, A. S., Zagho, M. M., Altahtamouni, T. M. & Bensalah, N. Graphene a promising electrode material for supercapacitors—A review. *Int. J. Energy Res.* **42**, 4284–4300 (2018).
9. Ke, Q. & Wang, J. Graphene-based materials for supercapacitor electrodes – A review. *J. Mater.* **2**, 37–54 (2016).
10. Yang, C. Review of Graphene Supercapacitors and Different Modified Graphene Electrodes. *Smart Grid Renew. Energy* **12**, (2021).
11. Bokhari, S. W. *et al.* Advances in graphene-based supercapacitor electrodes. *Energy Reports* **6**, 2768–2784 (2020).
12. Jiang, Y. & Liu, J. Definitions of Pseudocapacitive Materials: A Brief Review. *ENERGY Environ. Mater.* **2**, 30–37 (2019).
13. Augustyn, V., Simon, P. & Dunn, B. Pseudocapacitive oxide materials for high-rate electrochemical energy storage. *Energy Environ. Sci.* **7**, 1597–1614 (2014).
14. Fleischmann, S. *et al.* Pseudocapacitance: From Fundamental Understanding to High Power Energy Storage Materials. *Chemical Reviews* vol. 120 6738–6782 (2020).
15. Naguib, M. *et al.* Two-dimensional nanocrystals produced by exfoliation of Ti 3AlC 2. *Adv. Mater.* **23**, 4248–4253 (2011).
16. Hart, J. L. *et al.* Control of MXenes' electronic properties through termination and intercalation. *Nat. Commun.* **10**, 522 (2019).
17. Zhan, X., Si, C., Zhou, J. & Sun, Z. MXene and MXene-based composites: Synthesis, properties and environment-related applications. *Nanoscale Horizons* vol. 5 235–258 (2020).

18. Zhan, C. *et al.* Understanding the MXene Pseudocapacitance. *J. Phys. Chem. Lett.* **9**, 1223–1228 (2018).

19. Anasori, B., Lukatskaya, M. R. & Gogotsi, Y. 2D metal carbides and nitrides (MXenes) for energy storage. *Nat. Rev. Mater. 2017 22* **2**, 1–17 (2017).

20. Shahzad, F. *et al.* Electromagnetic interference shielding with 2D transition metal carbides (MXenes). *Science (80-.).* **353**, 1137–1140 (2016).

21. Ran, J. *et al.* Ti3C2 MXene co-catalyst on metal sulfide photo-absorbers for enhanced visible-light photocatalytic hydrogen production. *Nat. Commun.* **8**, (2017).

22. Lee, E., Vahidmohammadi, A., Yoon, Y. S., Beidaghi, M. & Kim, D. J. Two-Dimensional Vanadium Carbide MXene for Gas Sensors with Ultrahigh Sensitivity Toward Nonpolar Gases. *ACS Sensors* **4**, (2019).

23. Zhang, C. (John) *et al.* High capacity silicon anodes enabled by MXene viscous aqueous ink. *Nat. Commun.* **10**, (2019).

24. Lee, M. S., Yee, D. W., Ye, M. & Macfarlane, R. J. Nanoparticle Assembly as a Materials Development Tool. (2022) doi:10.1021/jacs.1c12335.

25. Amadi, E. V., Venkataraman, A. & Papadopoulos, C. Nanoscale self-assembly: concepts, applications and challenges. *Nanotechnology* **33**, 132001 (2022).

26. Raj, B., Padhy, A. K., Basu, S. & Mohapatra, M. Review—Futuristic Direction for R&D Challenges to Develop 2D Advanced Materials Based Supercapacitors. *J. Electrochem. Soc.* **167**, 136501 (2020).

27. Li, J. & Östling, M. Prevention of Graphene Restacking for Performance Boost of Supercapacitors—A Review. *Cryst. 2013, Vol. 3, Pages 163-190* **3**, 163–190 (2013).

28. Sagadevan, S. *et al.* Fundamental electrochemical energy storage systems. *Adv. Supercapacitor Supercapattery Innov. Energy Storage Devices* 27–43 (2021) doi:10.1016/B978-0-12-819897-1.00001-X.

29. Abbas, Q., Mirzaeian, M., Hunt, M. R. C., Hall, P. & Raza, R. Current State and Future Prospects for Electrochemical Energy Storage and Conversion Systems. *Energies* **13**, 5847 (2020).

30. Simon, P. & Gogotsi, Y. Materials for electrochemical capacitors. *Nature Materials* vol. 7 (2008).

31. Zhang, S., Wang, H., Liu, J. & Bao, C. Measuring the specific surface area of monolayer graphene oxide in water. *Mater. Lett.* **261**, 127098 (2020).

32. Jalal, N. I., Ibrahim, R. I. & Oudah, M. K. A review on Supercapacitors: Types and components. in *Journal of Physics: Conference Series* vol. 1973 12015 (IOP Publishing, 2021).

33. Lee, S. H., Kim, J. H. & Yoon, J. R. Laser Scribed Graphene Cathode for Next Generation of High Performance Hybrid Supercapacitors. *Sci. Reports 2018 81* **8**, 1–9 (2018).

34. Noori, A., El-Kady, M. F., Rahmanifar, M. S., Kaner, R. B. & Mousavi, M. F. Towards establishing standard performance metrics for batteries, supercapacitors and beyond. *Chem. Soc. Rev.* **48**, 1272–1341 (2019).

35. Zhang, L. & Zhao, X. S. Carbon-based materials as supercapacitor electrodes. *Chem. Soc. Rev.* **38**, 2520–2531 (2009).

36. Gouy, M. Sur la constitution de la charge électrique à la surface d'un électrolyte. *J. Phys. Théorique Appliquée* **9**, (1910).

37. Chapman, D. L. LI. A contribution to the theory of electrocapillarity . *London, Edinburgh, Dublin Philos. Mag. J. Sci.* **25**, (1913).

38. Stern, O. On the theory of the electrolytic double layer. *J. Electrochem. Appl. Phys. Chem.* **30**, (1924).

39. Ardizzone, S., Fregonara, G. & Trasatti, S. 'Inner' and 'outer' active surface of RuO2 electrodes. *Electrochim. Acta* **35**, 263–267 (1990).

40. Jiang, Q. *et al.* All Pseudocapacitive MXene-RuO2 Asymmetric Supercapacitors. *Adv. Energy Mater.* **8**, 1703043 (2018).

41. Mahdavi, H. & Shahalizade, T. Investigation of the pseudocapacitive properties of polyaniline nanostructures obtained from scalable chemical oxidative synthesis routes. *Ionics (Kiel).* **25**, 1331–1340 (2019).

42. Wang, H., Lin, J. & Shen, Z. X. Polyaniline (PANi) based electrode materials for energy storage and conversion. *J. Sci. Adv. Mater. Devices* **1**, 225–255 (2016).

43. Lukatskaya, M. R. *et al.* Probing the Mechanism of High Capacitance in 2D Titanium Carbide Using In Situ X-Ray Absorption Spectroscopy. *Adv. Energy Mater.* **5**, 1500589 (2015).

44. Prevot, V. *et al.* A templated electrosynthesis of macroporous NiAl layered double hydroxides thin films. *Chem. Commun.* **47**, 1761–1763 (2011).

45. Faour, A. *et al.* Correlation among structure, microstructure, and electrochemical properties of NiAl-CO 3 layered double hydroxide thin films. *J. Phys. Chem. C* **116**, 15646–15659 (2012).

46. Wang, Y., Yang, W. & Yang, J. A Co-Al layered double hydroxides nanosheets thin-film electrode. *Electrochem. Solid-State Lett.* **10**, A233 (2007).

47. Wei, W., Cui, X., Chen, W. & Ivey, D. G. Manganese oxide-based materials as electrochemical supercapacitor electrodes. *Chem. Soc. Rev.* **40**, 1697–1721 (2011).

48. Xu, H. *et al.* Flexible Asymmetric Micro-Supercapacitors Based on Bi2O3 and MnO2 Nanoflowers: Larger Areal Mass Promises Higher Energy Density. *Adv. Energy Mater.* **5**, 1401882 (2015).

49. Zhu, Y. G. *et al.* Phase Transformation Induced Capacitance Activation for 3D Graphene-CoO Nanorod Pseudocapacitor. *Adv. Energy Mater.* **4**, 1301788 (2014).

50. Yuan, C., Zhang, X., Su, L., Gao, B. & Shen, L. Facile synthesis and self-assembly of hierarchical porous NiO nano/micro spherical superstructures for high performance supercapacitors. *J. Mater. Chem.* **19**, 5772–5777 (2009).

51. Zhang, F. *et al.* Facile growth of mesoporous Co3O4 nanowire arrays on Ni foam for high performance electrochemical capacitors. *J. Power Sources* **203**, 250–256 (2012).

52. Heinze, J. Allen J. Bard and Larry F. Faulkner: Electrochemical Methods -

Fundamentals and Applications. Wiley, New York 1980, 718 + XVIII S. *Berichte der Bunsengesellschaft für Phys. Chemie* **85**, 1085–1086 (1981).

53. Wang, S. *et al.* Electrochemical impedance spectroscopy. *Nat. Rev. Methods Prim.* **1**, 41 (2021).

54. Taberna, P. L., Simon, P. & Fauvarque, J. F. Electrochemical Characteristics and Impedance Spectroscopy Studies of Carbon-Carbon Supercapacitors. *J. Electrochem. Soc.* **150**, A292 (2003).

55. Forouzandeh, P., Kumaravel, V. & Pillai, S. C. Electrode Materials for Supercapacitors: A Review of Recent Advances. *Catal. 2020, Vol. 10, Page 969* **10**, 969 (2020).

56. Ibrahim, T., Stroe, D., Kerekes, T., Sera, D. & Spataru, S. An overview of supercapacitors for integrated PV-energy storage panels. *Proc. - 2021 IEEE 19th Int. Power Electron. Motion Control Conf. PEMC 2021* 828–835 (2021) doi:10.1109/PEMC48073.2021.9432540.

57. Liu, T. & Li, Y. Addressing the Achilles' heel of pseudocapacitive materials: Long-term stability. *InfoMat* **2**, 807–842 (2020).

58. Augustyn, V. *et al.* High-rate electrochemical energy storage through Li + intercalation pseudocapacitance. *Nat. Mater.* **12**, 518–522 (2013).

59. Lindström, H. *et al.* Li+ ion insertion in TiO2 (anatase). 2. Voltammetry on nanoporous films. *J. Phys. Chem. B* **101**, 7717–7722 (1997).

60. Wang, J., Polleux, J., Lim, J. & Dunn, B. Pseudocapacitive contributions to electrochemical energy storage in TiO 2 (anatase) nanoparticles. *J. Phys. Chem. C* **111**, 14925–14931 (2007).

61. Miller, J. R. & Simon, P. Electrochemical Capacitors for Energy Management. *Science (80-.).* **321**, 651–652 (2008).

62. Ferrari, A. C. *et al.* Science and technology roadmap for graphene, related two-dimensional crystals, and hybrid systems. *Nanoscale* **7**, 4598–4810 (2015).

63. El-Kady, M. F., Shao, Y. & Kaner, R. B. Graphene for batteries, supercapacitors and beyond. *Nat. Rev. Mater. 2016 17* **1**, 1–14 (2016).

64. Geim, A. K. Graphene: Status and prospects. *Science (80-.).* **324**, 1530–1534 (2009).

65. Kamedulski, P. *et al.* High surface area micro-mesoporous graphene for electrochemical applications. *Sci. Rep.* **11**, 1–12 (2021).

66. Hummers, W. S. & Offeman, R. E. Preparation of Graphitic Oxide. *J. Am. Chem. Soc.* **80**, 1339 (1958).

67. Wang, Y., Yang, X., Pandolfo, A. G., Ding, J. & Li, D. High-Rate and High-Volumetric Capacitance of Compact Graphene–Polyaniline Hydrogel Electrodes. *Adv. Energy Mater.* **6**, 1600185 (2016).

68. Yang, Z. *et al.* Carbon nanotube- and graphene-based nanomaterials and applications in high-voltage supercapacitor: A review. *Carbon N. Y.* **141**, 467–480 (2019).

69. Baughman, R. H., Zakhidov, A. A. & De Heer, W. A. Carbon nanotubes - The route

toward applications. *Science (80-.).* **297**, 787–792 (2002).

70. Kolahdouz, M. *et al.* Carbon-Related Materials: Graphene and Carbon Nanotubes in Semiconductor Applications and Design. *Micromachines 2022, Vol. 13, Page 1257* **13**, 1257 (2022).

71. Peigney, A., Laurent, C., Flahaut, E., Bacsa, R. R. & Rousset, A. Specific surface area of carbon nanotubes and bundles of carbon nanotubes. *Carbon N. Y.* **39**, 507–514 (2001).

72. Simon, P. & Gogotsi, Y. Capacitive Energy Storage in Nanostructured Carbon–Electrolyte Systems. *Acc. Chem. Res.* **46**, 1094–1103 (2013).

73. Dwiyaniti, M. *et al.* Extremely high surface area of activated carbon originated from sugarcane bagasse. *IOP Conf. Ser. Mater. Sci. Eng.* **909**, 012018 (2020).

74. Wei, L., Sevilla, M., Fuertes, A. B., Mokaya, R. & Yushin, G. Polypyrrole-Derived Activated Carbons for High-Performance Electrical Double-Layer Capacitors with Ionic Liquid Electrolyte. *Adv. Funct. Mater.* **22**, 827–834 (2012).

75. Gamby, J., Taberna, P. L., Simon, P., Fauvarque, J. F. & Chesneau, M. Studies and characterisations of various activated carbons used for carbon/carbon supercapacitors. *J. Power Sources* **101**, 109–116 (2001).

76. Shi, H. Activated carbons and double layer capacitance. *Electrochim. Acta* **41**, 1633–1639 (1996).

77. Nishihara, H., Kyotani, T., Nishihara, H. & Kyotani, T. Templated Nanocarbons for Energy Storage. *Adv. Mater.* **24**, 4473–4498 (2012).

78. Ania, C. O., Khomenko, V., Raymundo-Piñero, E., Parra, J. B. & Béguin, F. The Large Electrochemical Capacitance of Microporous Doped Carbon Obtained by Using a Zeolite Template. *Adv. Funct. Mater.* **17**, 1828–1836 (2007).

79. Trasatti, S. & Buzzanca, G. Ruthenium dioxide: A new interesting electrode material. Solid state structure and electrochemical behaviour. *J. Electroanal. Chem. Interfacial Electrochem.* **29**, A1–A5 (1971).

80. Langmuir ; Bardos, J., Attard, D. C., Miklavcic, P. J., Miklavcic, S. J. & Attard, S. J. Voltammetric Characterization of Ruthenium Oxide-Based Aerogels and Other RuO2 Solids: The Nature of Capacitance in Nanostructured Materials. *Langmuir* **19**, 2532 (2003).

81. Yoshida, N. *et al.* Unveiling the origin of unusual pseudocapacitance of RuO 2· n H2O from its hierarchical nanostructure by small-angle x-ray scattering. *J. Phys. Chem. C* **117**, 12003–12009 (2013).

82. Wang, J. *et al.* Pseudocapacitive materials for electrochemical capacitors: from rational synthesis to capacitance optimization. *Natl. Sci. Rev.* **4**, 71–90 (2017).

83. Toupin, M., Brousse, T. & Bélanger, D. Charge storage mechanism of MnO2 electrode used in aqueous electrochemical capacitor. *Chem. Mater.* **16**, 3184–3190 (2004).

84. Lee, H. Y. & Goodenough, J. B. Supercapacitor Behavior with KCl Electrolyte. *J. Solid State Chem.* **144**, 220–223 (1999).

85. Liu, J. *et al.* MnO2-based materials for supercapacitor electrodes: challenges,

strategies and prospects. *RSC Adv.* **12**, 35556–35578 (2022).

86. Devaraj, S. & Munichandraiah, N. Effect of crystallographic structure of MnO2 on its electrochemical capacitance properties. *J. Phys. Chem. C* **112**, 4406–4417 (2008).

87. Ghodbane, O., Pascal, J. L. & Favier, F. Microstructural effects on charge-storage properties in MnO 2-based electrochemical supercapacitors. *ACS Appl. Mater. Interfaces* **1**, 1130–1139 (2009).

88. Peng, L. *et al.* Ultrathin two-dimensional MnO2/graphene hybrid nanostructures for high-performance, flexible planar supercapacitors. *Nano Lett.* **13**, 2151–2157 (2013).

89. Rabani, I. *et al.* Highly dispersive Co3O4 nanoparticles incorporated into a cellulose nanofiber for a high-performance flexible supercapacitor. *Nanoscale* **13**, 355–370 (2021).

90. Wang, S.-Y., Ho, K.-C., Kuo, S.-L. & Wu, N.-L. Investigation on Capacitance Mechanisms of Fe[sub 3]O[sub 4] Electrochemical Capacitors. *J. Electrochem. Soc.* **153**, A75 (2006).

91. Lee, J. W., Hall, A. S., Kim, J. D. & Mallouk, T. E. A facile and template-free hydrothermal synthesis of Mn 3O 4 nanorods on graphene sheets for supercapacitor electrodes with long cycle stability. *Chem. Mater.* **24**, 1158–1164 (2012).

92. Dubal, D. P., Dhawale, D. S., Salunkhe, R. R., Pawar, S. M. & Lokhande, C. D. A novel chemical synthesis and characterization of Mn3O4 thin films for supercapacitor application. *Appl. Surf. Sci.* **256**, 4411–4416 (2010).

93. Wu, Z., Zhu, Y. & Ji, X. NiCo2O4-based materials for electrochemical supercapacitors. *J. Mater. Chem. A* **2**, 14759–14772 (2014).

94. Augustyn, V., Simon, P. & Dunn, B. Pseudocapacitive oxide materials for high-rate electrochemical energy storage. *Energy Environ. Sci.* **7**, 1597–1614 (2014).

95. Anasori, B. *et al.* Two-Dimensional, Ordered, Double Transition Metals Carbides (MXenes). **12**, 34 (2021).

96. Lukatskaya, M. R. *et al.* Cation Intercalation and High Volumetric Capacitance of Two-Dimensional Titanium Carbide. *Science (80-.).* **341**, 1502–1505 (2013).

97. Ghidiu, M., Lukatskaya, M. R., Zhao, M.-Q., Gogotsi, Y. & Barsoum, M. W. Conductive two-dimensional titanium carbide ‘clay’ with high volumetric capacitance. *Nature* **516**, (2014).

98. Zhang, Y.-Z. *et al.* MXenes stretch hydrogel sensor performance to new limits. *Sci. Adv.* **4**, eaat0098 (2018).

99. Kim, S. J. *et al.* Metallic Ti3C2Tx MXene Gas Sensors with Ultrahigh Signal-to-Noise Ratio. *ACS Nano* **12**, 986–993 (2018).

100. Zhao, S. *et al.* Highly Electrically Conductive Three-Dimensional Ti3C2Tx MXene/Reduced Graphene Oxide Hybrid Aerogels with Excellent Electromagnetic Interference Shielding Performances. *ACS Nano* **12**, 11193–11202 (2018).

101. Liu, J. *et al.* Hydrophobic, Flexible, and Lightweight MXene Foams for High-Performance Electromagnetic-Interference Shielding. *Adv. Mater.* **29**, 1702367 (2017).

102. Dutta, P. *et al.* Electric Field Guided Fast and Oriented Assembly of MXene into Scalable Pristine Hydrogels for Customized Energy Storage and Water Evaporation Applications. *Adv. Funct. Mater.* **2204622**, 2204622 (2022).

103. Alhabeb, M. *et al.* Guidelines for Synthesis and Processing of Two-Dimensional Titanium Carbide (Ti3C2Tx MXene). *Chem. Mater.* **29**, 7633–7644 (2017).

104. Khazaei, M., Ranjbar, A., Arai, M., Sasaki, T. & Yunoki, S. Electronic properties and applications of MXenes: a theoretical review. *J. Mater. Chem. C* **5**, 2488–2503 (2017).

105. Khazaei, M. *et al.* Novel Electronic and Magnetic Properties of Two-Dimensional Transition Metal Carbides and Nitrides. *Adv. Funct. Mater.* **23**, 2185–2192 (2013).

106. Montazeri, K. *et al.* Beyond Gold: Spin-Coated Ti3C2-Based MXene Photodetectors. *Adv. Mater.* **31**, 1903271 (2019).

107. Zhang, C. *et al.* Transparent, Flexible, and Conductive 2D Titanium Carbide (MXene) Films with High Volumetric Capacitance. *Adv. Mater.* **29**, 1702678 (2017).

108. Ling, Z. *et al.* Flexible and conductive MXene films and nanocomposites with high capacitance. *Proc. Natl. Acad. Sci. U. S. A.* **111**, 16676–16681 (2014).

109. Rasool, K. *et al.* Efficient Antibacterial Membrane based on Two-Dimensional Ti3C2Tx (MXene) Nanosheets. *Sci. Reports 2017 71* **7**, 1–11 (2017).

110. Ghidiu, M., Lukatskaya, M. R., Zhao, M.-Q., Gogotsi, Y. & Barsoum, M. W. Conductive two-dimensional titanium carbide 'clay' with high volumetric capacitance. *Nat. 2014 5167529* **516**, 78–81 (2014).

111. Chen, H. *et al.* Carbon nanotubes enhance flexible MXene films for high-rate supercapacitors. doi:10.1007/s10853-019-04003-8.

112. Zhao, M. Q. *et al.* Flexible MXene/carbon nanotube composite paper with high volumetric capacitance. *Adv. Mater.* **27**, 339–345 (2015).

113. Huang, Y. L. & Bian, S. W. Vacuum-filtration assisted layer-by-layer strategy to design MXene/carbon nanotube@MnO2 all-in-one supercapacitors. *J. Mater. Chem. A* **9**, 21347–21356 (2021).

114. Yan, J. *et al.* Flexible MXene/Graphene Films for Ultrafast Supercapacitors with Outstanding Volumetric Capacitance. *Adv. Funct. Mater.* **27**, 1701264 (2017).

115. Fan, Z. *et al.* Modified MXene/Holey Graphene Films for Advanced Supercapacitor Electrodes with Superior Energy Storage. *Adv. Sci.* **5**, 1800750 (2018).

116. Rasool, K. *et al.* Efficient Antibacterial Membrane based on Two-Dimensional Ti3C2Tx (MXene) Nanosheets. *Sci. Rep.* **7**, 1–11 (2017).

117. Yu, W., Li, Y., Xin, B. & Lu, Z. MXene/PVA Fiber-based Supercapacitor with Stretchability for Wearable Energy Storage. *Fibers Polym.* **23**, 2994–3001 (2022).

118. Vahidmohammadi, A. *et al.* Thick and freestanding MXene/PANI pseudocapacitive electrodes with ultrahigh specific capacitance. *J. Mater. Chem. A* **6**, 22123–22133 (2018).

119. Ling, Z. *et al.* Flexible and conductive MXene films and nanocomposites with high capacitance. *Proc. Natl. Acad. Sci. U. S. A.* **111**, 16676–16681 (2014).

120. Tang, J. *et al.* Optimizing Ion Pathway in Titanium Carbide MXene for Practical High-Rate Supercapacitor. *Adv. Energy Mater.* 2003025 (2020) doi:10.1002/aenm.202003025.

121. Lukatskaya, M. R. *et al.* Ultra-high-rate pseudocapacitive energy storage in two-dimensional transition metal carbides. **2**, 17105 (2017).

122. Shang, T. *et al.* 3D Macroscopic Architectures from Self-Assembled MXene Hydrogels. *Adv. Funct. Mater.* **29**, (2019).

123. Bayram, V. *et al.* MXene Tunable Lamellae Architectures for Supercapacitor Electrodes. **10**, 16 (2021).

124. Xia, Y. *et al.* Thickness-independent capacitance of vertically aligned liquid-crystalline MXenes. *Nature* **557**, 409–412 (2018).

Chapter 2

Oxidation Protected Co-Assembly of MXene and Graphene for Supercapacitive Energy Storage Applications with Excellent Gravimetric Capacity

Chapter 2

Oxidation Protected Co-Assembly of MXene and Graphene for Supercapacitive Energy Storage Applications with Excellent Gravimetric Capacity

Gravimetric and volumetric capacitance are the two important matrices for any supercapacitor device, but only moderate achievement has been realized till date on the first figure-of-merit for MXene based electrodes. In this study, aided by a small quantity (5 wt%) of graphene, an interfacial layer-by-layer self-assembly of MXene has been employed to develop hydrogel based supercapacitor electrodes that display excellent gravimetric capacitance of 653.7 F g^{-1} at 2 mV s^{-1} in three-electrode setup. Very high areal (1442 mF cm^{-2}) and volumetric capacitance (~1522 F cm^{-3}) were also achieved by simple tuning of respective conditions like gelation time and electrolyte protected mechanical compression. Considering the fact that MXene is prone to oxidation at elevated gelation temperatures, this purely ambient gelation protocol is established to protect its redox active titanium sites. MXene-graphene hybrid hydrogel structures consisting of network of 2D-sheets can allow full utilization of metallic surfaces and redox active sites on MXene basal plane, and thereby display outstanding performance metrics. These hybrid hydrogels also show excellent cyclic stability even with commercial scale mass loading which can pave the way to their application in practical devices.

2.1. Introduction

Led by the discovery of graphene,[1] the last decade saw a tremendous advancement in nanotechnology bringing in a plethora of novel two-dimensional materials all decorated with its own unique material properties — MXene being the latest of them all.[2] Unlike other two-dimensional materials like graphene or transition metal dichalcogenides/oxides,[3,4] MXene possesses a rare combination of redox enabled Faradic surface paired with excellent metallic conductivity and hydrophilicity.[5,6] Combination of such properties makes it a perfect candidate as an energy storage material that can simultaneously display electrical double layer capacity (EDLC) and pseudocapacity.[7-9]

Due to the exquisite structural and material properties, nanomaterials show remarkable potential in several applications which inspired a lot of research in exploring new families of these nanostructures.[10-13] MXenes belong to a family of transition metal carbides and nitrides

and have the formula $M_{n+1}X_nT_x$, where M is transition metal, n = 1, 2 or 3, X is carbon and/or nitrogen and T_x represents the surface terminal groups. These 2D layered materials are a derivative of their MAX ($M_{n+1}AX_n$, where A is group III A or IV A element) phase precursors prepared through selective etching of the A group elements.[14] Recently, MXene have attracted considerable attention in the fields of supercapacitors,[15,16] catalysis,[17] electromagnetic interface shielding,[18] gas sensing[19] and Li ion batteries.[20] However, similar to all other 2D materials, MXene too is associated with their intrinsic tendency of face-to-face restacking and random aggregation, which severely limits the accessibility and the utilization of surfaces for electrochemical energy storage.[21] Several strategies have been adopted to address the restacking challenge, and particularly the introduction of other nanomaterials as spacers in MXene films has been practiced to date.[22,23] For example, conducting polymers (polyaniline, polypyrrole),[24] carbon nanotube (CNT) and graphene[25,26] have been incorporated in MXene thin films to attain high volumetric capacity (390-1700 F cm^{-3}). However, the gravimetric value remains in the moderate range (80-450 F g^{-1}), possibly due to limited ion transport capabilities and insufficient accessibility of electrochemically active surfaces.[27,28] Recently, vacuum filtration method has been widely used in fabricating MXene and MXene hybrid films.[29,30] But due to the tightly packed structures of the electrodes, the basal planes of the nanosheets are not fully utilized in energy storage due to the face-to-face restacking and pore blockage. In this regard, hydrogels produced via controlled self-assembly of 2D nanosheets can serve as an excellent choice. These hydrogels can offer large exposed surfaces and continuous ion transporting channels owing to their intrinsic hydrated structures with continuous pores.[31] Moreover, MXene in a hydrogel structure can benefit from the intercalated water which enables more hydrogen ions to access the redox active sites and thus can show dramatically enhanced gravimetric performance.[32] Unfortunately, the gelation strategy, which is highly successful for analogous material graphene, is hard to mimic in MXene due to its more rigid ceramic surface, intrinsic hydrophilicity, and its small sheet size. Very recently, a lot of research has been directed to develop MXene based hydrogels with graphene additive as the gelator which is highly beneficial due to its surface accessibility and delivery of excellent rate capability,[29,30] but still little improvements were observed with gravimetric value being confined in the range 300-450 F g^{-1} (in three-electrode configuration). Given the fact that at elevated temperatures titanium based metallic MXene ($Ti_3C_2T_x$) converts to the corresponding insulating metal oxide (TiO_2) in water medium at an accelerated rate,[33] such conversion is highly expected during hydrothermal gelation processes.[34] The signature of this partial oxidation in MXene during hydrogel processing was evident from the increased relative intensity of the XPS peak

corresponding to TiO_2 phase (458.9 eV) in the Ti2p core level spectra of MXene.[35-37] In this scenario, it is natural to expect that the advantage of highly exposed surfaces of MXene in their hydrogel structure may get partially neutralized by the loss of metallic and redox properties at the sites of oxidation, resulting in moderate gravimetric results. Thus, the current status urges to develop an alternative gelation strategy where the gelation induced oxidation can be avoided and significant breakthrough in gravimetric performance can be realized.

Herein, we demonstrate a facile, layer-by-layer gelation strategy of MXene over metallic substrate aided by only 5 wt% graphene without the involvement of any heat energy, thereby eliminating the possibility of processing induced surface oxidation. Such controlled co-assembly of oxidation-free MXene and graphene, in the form of porous hydrogel allowed an excellent gravimetric capacitance of 653.7 F g^{-1} at 2 mV s^{-1} in three-electrode configuration. Further, by electrolyte assisted mechanical compression we have achieved a high volumetric capacitance of 1522 F cm^{-3}, which is among the highest reported thus far. It is worthwhile to mention that as compared to three-electrode counterpart the performance in a two-electrode cell represents the most realistic figure-of-merit of a supercapacitor for practical application. Unfortunately, only a few reports on MXene research have demonstrated the complete two-electrode cell performance, and further the existing values are not only moderate but also were realized with a mass loading (<1.8 mg cm^{-2}) far from the commercial requirement of ~10 mg cm^{-2}. Our electrodes in two-electrode cell experiments exhibit very high gravimetric value of 459 F g^{-1} at 10 mV s^{-1} with 1.93 mg cm^{-2} areal mass loading and continue to display excellent gravimetric value (315 F g^{-1}) combined with an aerial capacitance of 1485.5 mF cm^{-2} when the loading is increased (9.26 mg cm^{-2}) to a practical scale.

2.2. Experimental section

2.2.1. Preparation of MXene and graphene oxide aqueous dispersion:

The MXene aqueous solution was prepared by selective etching of aluminum (Al) from multilayered Ti_3AlC_2 as described elsewhere.[16] Fluoride based salt, LiF (1g) was dissolved in 20 mL HCl (9M) and stirred until the solution became clear. This was followed by very slow addition of 1g Ti_3AlC_2 powder. The reaction was allowed for 24 hours at 35°C under continuous stirring. The resulting solution was then centrifuged at 3500 rpm several times. After each centrifugation, the supernatant was discarded and the solid residue was mixed with deionized water until the pH of the supernatant reached 6-7. The mixture was then sonicated in a sonication bath for one hour under continuous Ar bubbling followed by centrifugation for

one hour at 3500 rpm. The few-layered delaminated MXene was then collected as supernatant and used without any further modifications. Graphene Oxide (GO) was prepared from natural graphite flakes using well known modified Hummers method.[38-39]

2.2.2. Preparation of MXene-rGO hydrogel:

A facile room temperature synthesis strategy through electrostatic self-assembly was employed in preparation of MXene hydrogels in presence of small amount of GO as co-assembling agent. In a glass vial, the MXene colloidal suspension (20 mg mL^{-1}) and GO aqueous solution (7 mg mL^{-1}) in different weight ratios were mixed via manual hand shaking to prepare a homogenous solution. A polished Zn foil (1.2 cm × 3.5 cm) was subsequently kept within the solution for 20-120 min. During this period reduction of GO into graphene (reduced graphene oxide, rGO) and simultaneous co-assembly of MXene-graphene takes place over the metal plate to form a continuous hydrogel. The zinc plate along with the hydrogel was then transferred into another fresh water vial for 90 min to allow proper reduction of graphene oxide and removal of unreacted GO. Afterwards the MXene-graphene hydrogel (MXene-rGO hydrogel) was separated from zinc plate by etching in 6M KOH to obtain the freestanding hydrogel film which was then washed several times in water to restore the pH neutrality. The MXene to graphene weight ratio in the hydrogels were 95:5 denoted as $M_{95}G_5$-X (here the subscripts denote the proportion of MXene and graphene in the hydrogel and X represents the assembly time over the metal foil), 90:20 ($M_{90}G_{20}$-X), 85:15 ($M_{85}G_{15}$-X) and 80:20 ($M_{80}G_{20}$-X).

For electrolyte assisted compression, the hydrogels were first saturated with 3M H_2SO_4 by dipping them in the acidic solution for 3 hours. It was then placed above a butter paper and kept overnight in ambient condition to allow partial drying of the hydrogel followed by mechanical compression in a hydraulic press. The pressed thin samples were then again dipped in 3M H_2SO_4 for hours before using them as electrodes for electrochemical measurements.

2.2.3. Material Characterization:

The structural and morphological studies of the MXene-graphene hydrogels were characterized using FESEM (Zeiss, Sigma 300) and FETEM (JEM 2100, JEOL) operated at an accelerating voltage of 200 kV. X-ray diffraction patterns were observed by X-ray diffractometer (Rigaku, Japan). Oxford make Cypher was used for AFM images. The Raman vibrational studies of the samples were measured using Horiba LabRam HR with a 514 nm laser source operated for 30 s exposure time. For compositional studies, Energy Dispersive X-ray Spectroscopy was

performed with EDAX by AMETEK mounted on FESEM and an ESCALAB Xi+, Thermo Fisher Scientific Pvt. Ltd. was used for X-ray photoelectron spectroscopy (XPS).

The core level peak fitting of XPS spectra was performed using XPS Peak 4.1 and Shirley functions were used to carry out the background correction. To obtain a reasonable and physically correct peak fit, few restrictions were imposed, following the suggested protocol of Gogotsi et al.[40,41] First, all the intensity ratios of $2p_{3/2}$ and $2p_{1/2}$ components were constrained at 2:1. In addition, the binding energies were allowed to shift ±0.5 eV from their initial position. Finally, the full width at half maximum (FWHM) for a component of particular spectrum was allowed very small variation, if any, when fitted for different samples.

2.2.4. Electrochemical Characterizations:

Electrochemical performance of all the prepared samples were measured in both three and two-electrode configurations using PERSTAT 3000A-DX (Princeton Applied Research) electrochemical workstation, in 3M H_2SO_4 aqueous electrolyte. For three-electrode measurements, freestanding hydrogels (area 1 cm^2), a platinum wire and Ag/AgCl in 1M KCl were used as working, counter and reference electrodes respectively, with an active potential of -0.5 to 0.3 V vs Ag/AgCl. For two-electrode symmetric cell capacitors, two MXene-rGO hydrogels (area 1 cm^2) separated by Celgard 3400 membrane were sandwiched between two Platinum foils. All the cyclic voltammetry (CV) measurements were performed in a potential window of 0.8 V to avoid anodic oxidation and protect the stability of MXene as reported previously.[42] The electrochemical impedance spectroscopy (EIS) measurements, in the 10 mHz to 100 kHz frequency range, were performed at open circuit potential with an amplitude of 10 mV. The electrodes used in electrochemical measurements were dialyzed for 2 days before drying in freeze dryer and their weights were measured in a microbalance for calculation of specific capacitance.

The gravimetric specific capacitance C_g (F g^{-1}) was calculated from the CV curves using the following equation,

$$C_g = \frac{1}{\Delta V m v} \int i \, dV \qquad (1)$$

where i is the current density, ΔV being the potential window, m is the mass of the active material and v is the scan rate. For volumetric capacitance C_v,

$$C_v = \rho C_g \qquad (2)$$

where ρ is the density of the material calculated using the formula,

$$\rho = \frac{m}{Ad} \tag{3}$$

with A and d being the geometrical area and the thickness of the hydrogel electrode respectively.

For symmetric capacitors,

$$\text{Gravimetric capacitance, } C_g = \frac{1}{\Delta V M v}\int i\, dV \tag{4}$$

where i is the current density, ΔV is the potential window, M is the mass of the active material in both electrodes and v is the scan rate. The gravimetric capacitance of single electrodes (C_s) in symmetric cells was calculated according to the following equation,

$$C_s = 4C_g \tag{5}$$

$$\text{Areal capacitance, } C_A = \frac{M}{A}C_g \tag{6}$$

where M is the mass of both electrodes in symmetric cell and A is the geometrical area. The gravimetric energy density (E_g) and power density (P_g) were calculated as,

$$E_g = \frac{C_g \times (\Delta V)^2}{2 \times 3.6} \tag{7}$$

$$P_g = \frac{E_g \times v \times 3600}{\Delta V} \tag{8}$$

The real (C') and imaginary (C'') part of the capacitance were calculated using the following formula,

$$C'(\omega) = \frac{-Z''(\omega)}{\omega|Z(\omega)|^2} \tag{9}$$

$$C''(\omega) = \frac{Z'(\omega)}{\omega|Z(\omega)|^2} \tag{10}$$

where $Z'(\omega)$, $Z''(\omega)$ and $|Z(\omega)|^2$are the real, imaginary and absolute values of complex impedance from the EIS measurement. The angular frequency ω is defined as $\omega = 2\pi f$ with frequency f in Hz.

2.3. Results and discussion

MXene hydrogel with graphene content 5-20% is produced at ambient conditions via a simple layer-by-layer assembly of nanosheets over metallic zinc foil as shown schematically in Fig. 2.1. The gelation happens via successive stages: at the first stage, due to the lower reduction potential of zinc compared to graphene oxide (GO), GO nanosheets in contact with metal surface gets reduced to graphene (reduced graphene oxide, rGO) via spontaneous electron transfer from zinc ($Zn \rightarrow Zn^{2+} + 2e^-$). This first stage of gelation results in a thin layer of rGO over zinc plate and simultaneous generation of zinc ions (Zn^{2+}) at the interface.[43]

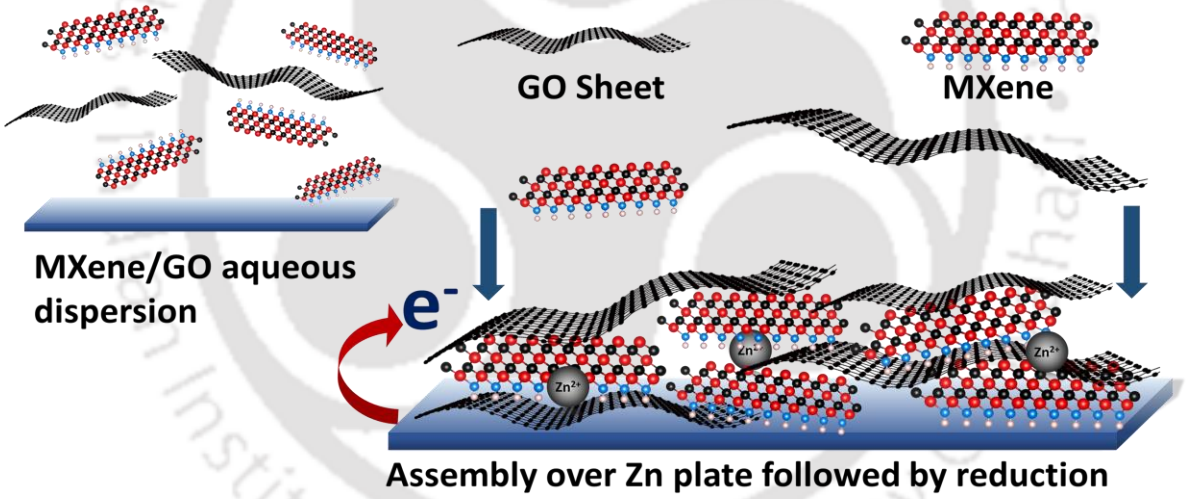

Figure 2.1. Schematic illustration of layer-by-layer gelation via spontaneous assembly and successive reduction.

These *in-situ* generated positively charged Zn^{2+}ions slowly diffuse away from the metal surface and force negatively charged MXene and GO sheets to assemble via electrostatic interaction over the foil. Here the assembled GO layers get reduced by further electron transfer from zinc through the conducting graphene surfaces already formed in the first stage. This maintains the ionization of zinc plate which again helps in further attraction of other layers of MXene and GO. Thus, the successive Zn ionization, attraction and subsequent reduction results in a layer-by-layer assembly of MXene-graphene nanosheets.[44,45] Continuation of this process

leads to a continuous hydrogel sheet in which the network structure gets stabilized by van der Waals interaction among the sheets of MXene, MXene-graphene and the $\pi - \pi$ interaction among graphene sheets. The face-to-face restacking is prohibited by intercalated water that remains hydrogen bonded with the oxygen/fluorine functional groups over the basal planes of MXene (—O,—OH,—F) and reduced graphene (—O,—COOH,—OH).

2.3.1. Morphological and structural analysis:

FESEM image of the freeze-dried hybrid hydrogel reveals its highly porous structure, where continuous macro-pores in the size range 5-50 micron is obvious (Fig. 2.2.a). The uniform distribution of MXene and graphene throughout the hydrogel structure is evident from cross sectional EDS elemental mapping corresponding to constituent Ti, C, F and O atoms that show a uniform profile (Fig. 2.2.b). MXene used for this gelation are exfoliated monolayers as

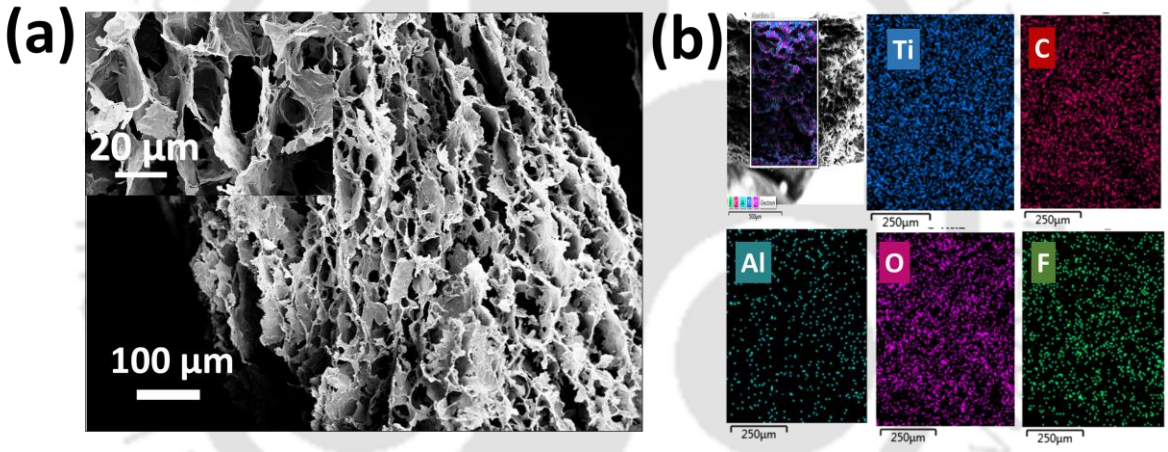

Figure 2.2. (a) Cross sectional FESEM image of freeze-dried hydrogel ($M_{95}G_5$-60) and its higher magnification image in the inset; (b) Cross sectional elemental mapping for MXene graphene hydrogel.

evident from its AFM image (Fig. 2.3.a), and was produced from its parent MAX phase (Ti_3AlC_2) by successful removal of interlayer aluminum which is confirmed by the absence of aluminium in the EDS elemental mapping in TEM (Fig. 2.3.b). BET analysis by N_2 adsorption/desorption reveals that the hydrogel possesses a considerably high specific surface area of 55 m^2 g^{-1} benefitting from the network interlinked structure which is much better than other MXene and MXene based materials (Fig. 2.4.a).[46,47] Pore structure analysis from BET further reveals that in addition to the macro-pores the hydrogel also possesses nano-pores with an average pore diameter of 3.45 nm (Fig. 2.4.a inset). Furthermore, the XRD analysis indicates a shift in (002) diffraction peak of MXene in the graphene incorporated hydrogels

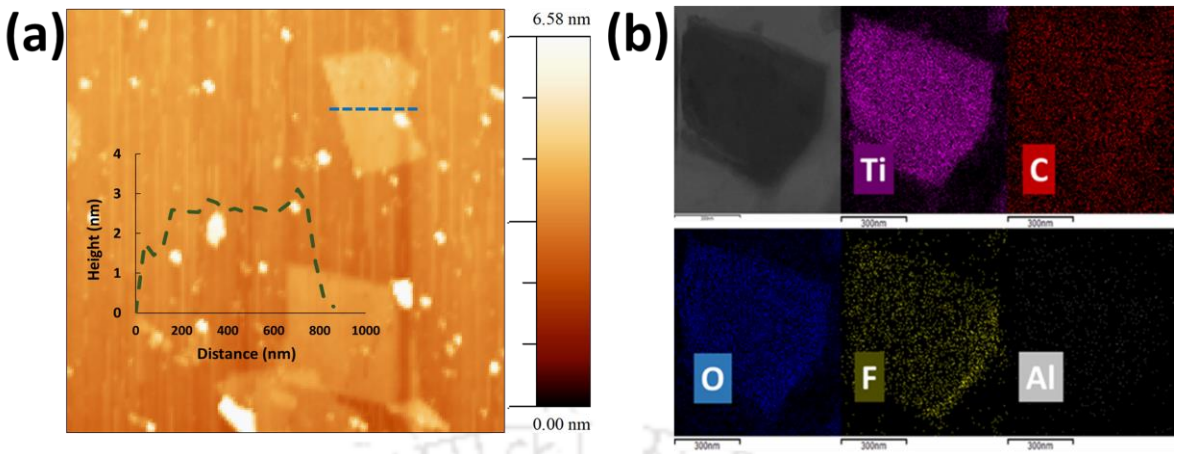

Figure 2.3. (a) AFM image shows the flat morphology of MXene flakes with a thickness of 2.5 nm; (b) TEM-EDS mapping of MXene, conforming successful removal of Al.

along with an increased broadness of the same (Fig. 2.4.b). The broadness of the peaks can be associated with the porous disordered structure of the nanosheets in the hydrogel. The diffraction peak at 6.5° for 5% graphene ($M_{95}G_5$-60), shifted to 6.22° when the graphene content is increased to 15% ($M_{85}G_{15}$-60), which corresponds to an interlayer spacing of 1.35 nm to 1.42 nm respectively. However, due to the broadness, the small shift of peak in XRD alone cannot be fully associated with graphene incorporation in the hydrogel structure. We have further discussed and confirmed the graphene incorporation in hydrogels through Raman and XPS investigation later.

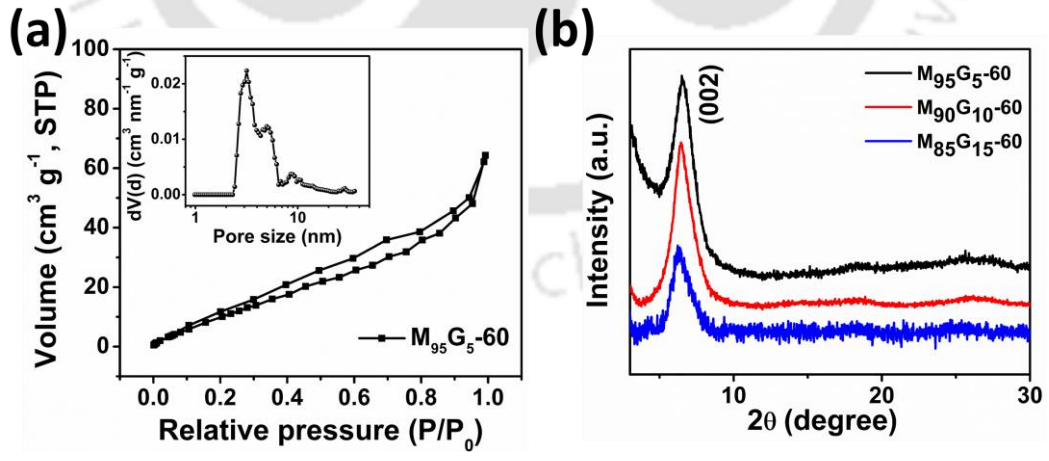

Figure 2.4. (a) N_2 adsorption/desorption isotherms with pore size distribution in the inset for $M_{95}G_5$-60 hydrogel; (b) XRD patterns of hydrogels with different MXene:GO wt%.

Selected area diffraction pattern, taken from the rectangular sheet as observed in TEM image (Fig. 2.5.a), shows well resolved hexagonal pattern that matches with MXene crystal structure

(Fig. 2.5.b).[48] Unlike the bigger graphene sheet at the background, MXene sheet does not show any wrinkles on its surface denoting the stiffness of this ceramic material (Fig. 2.5.a).[49] Together with the presence of characteristic Raman peaks of MXene, namely, A_{1g} (198 & 716 cm^{-1}) and E_g (286, 389 and 613 cm^{-1}), the presence of peaks corresponding to reduced graphene oxide at 1350 cm^{-1} (D) and 1580 cm^{-1} (G) signifies effective incorporation of graphene into the MXene structure (Fig. 2.5.c).[50]

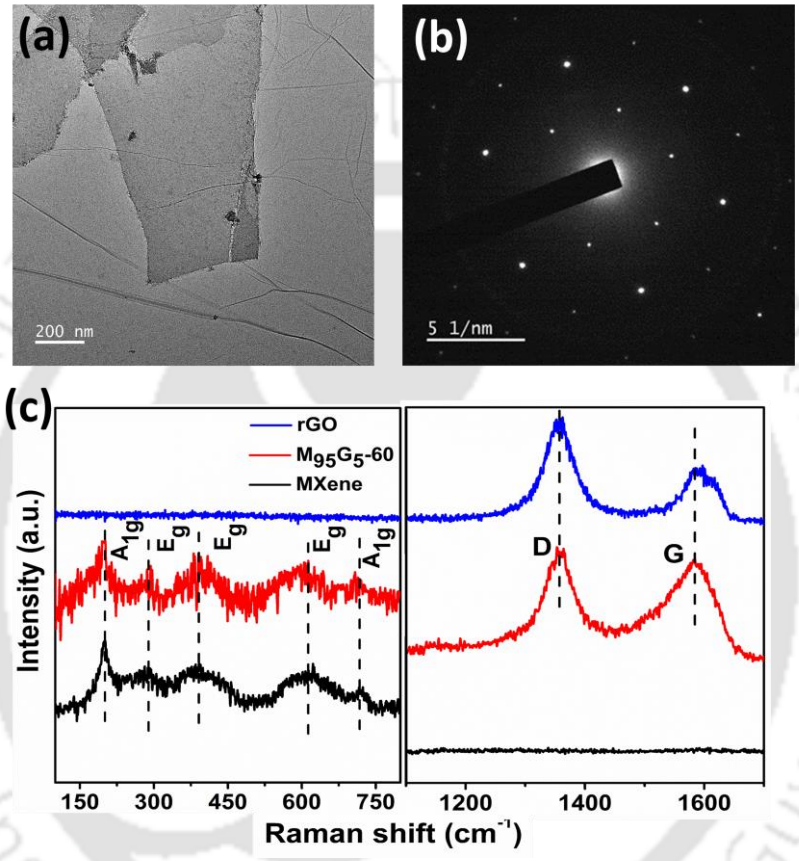

Figure 2.5. (a) TEM image of MXene flakes over large sheets of GO; (b) SAED pattern corresponding to MXene sheet; (c) Comparative Raman spectra of rGO, $M_{95}G_5$-60 and MXene.

2.3.2. Chemical analysis of MXene-graphene hydrogels:

Composition of pure MXene and MXene-graphene hydrogel ($M_{95}G_5$-60) were further analysed with XPS investigation. In the survey spectra of MXene (and hence also in $M_{95}G_5$-60) no peak at 76.07 eV related to aluminium was found which signifies its effective removal from parent MAX phase material (Fig. 2.6.a). High-resolution C1s XPS spectra for both MXene and $M_{95}G_5$-60 can be fitted with five component peaks related to C—Ti (282.44 eV), Ti—C—O (283.22 eV), C—C (284.8 eV), C—O (286.02 eV) and O=C—O (287.56 eV). Effective incorporation of graphene in $M_{95}G_5$-60 is obvious from its higher carbon content as evident

from increased atomic percentage of C—C (31% to 37%) and C—O (15% to 19%) (Fig. 2.6.b). High-resolution XPS spectra corresponding to Ti 2p can be fitted with four doublets (Ti $2p_{3/2}$ and Ti $2p_{1/2}$) out of which three are related to Ti (I, II or III) (455.1 and 461.2 eV), Ti^{2+} (I, II or III) (455.8 and 461.4 eV) and Ti^{3+} (I, II or III) (457.1 and 462.4 eV) ionic states of titanium of MXene whereas the forth doublet is related to Ti^{4+} (458.9 and 464.5 eV) state of TiO_2 (Fig. 2.6.c).[40,41] Here I, II and III corresponds to the three moieties in MXene referring to $Ti_3C_2O_x$, $Ti_3C_2(OH)_x$ and $Ti_3C_2F_x$ respectively. It is important to note that the peak profile of XPS Ti2p of MXene is not affected by room temperature gelation as is evident from Fig. 2.6.d

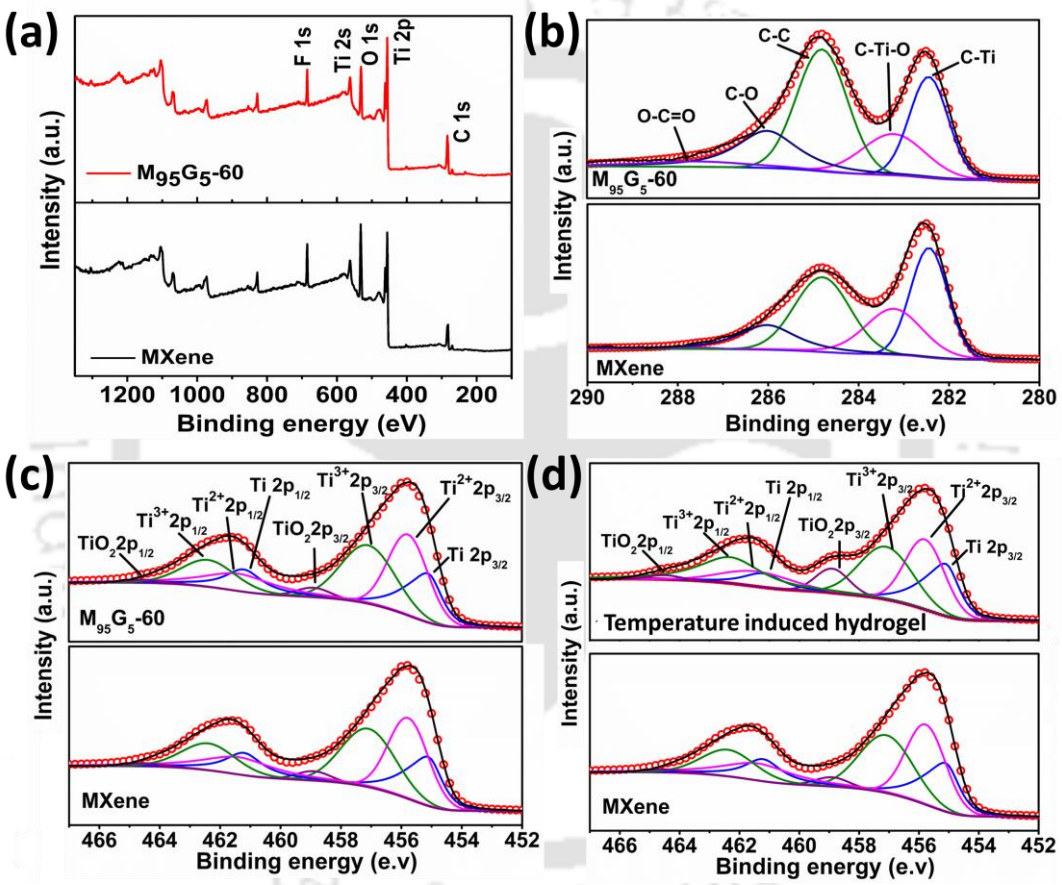

Figure 2.6. XPS analysis of MXene-graphene hydrogels: (a) survey spectra; (b) high resolution XPS spectrum of C 1s and (c) Ti 2p between MXene and MXene-graphene hydrogel; (d) corresponding Ti 2p spectra between MXene and temperature induced MXene-graphene hydrogel.

To further inspect any possible oxidation of MXene during gelation, atomic percentage (at.%) of oxygenated titanium site (TiO_2) before and after gelation is compared. The atomic percentage of TiO_2 in as-synthesized MXene is 2.5% and the value remained nearly unaltered (2.7%) in the MXene-graphene hydrogel, ruling out the possibility of any surface oxidation

which is very common in any other gelation method involving temperature.[34,37] To validate our conjecture about MXene oxidation in gelation conditions involving heat, XPS spectrum of MXene-graphene hydrogel developed by typical temperature induced protocol is analysed (Table 2.1). As evident from the XPS spectrum (Fig. 2.6.d), gelation involving temperature significantly increases the relative intensity of peak related to secondary TiO_2 phase and its atomic percentage significantly increases (8.8%) as compared to MXene (Table 2.1). This observation confirms that in any other process to obtain MXene based hydrogel, partial oxidation of MXene is likely to happen, whereas our ambient condition gelation strategy is free from this critical concern.

Table 2.1. High-resolution peak fitting of Ti 2p for MXene, MXene-graphene hybrid hydrogel (this report) and MXene-graphene hydrogel developed via temperature induced protocol.

Materials	**Ti (at.%)**	**Ti^{2+} (at.%)**	**Ti^{3+} (at.%)**	**TiO_2 (at.%)**
MXene	27.7	35.6	34.2	2.5
$M_{95}G_5$-60	31.5	34	31.8	2.7
Temperature induced MXene-graphene hydrogel	29.8	30.5	30.9	8.8

2.3.3. Electrochemical analysis:

Abundant multi-dimensional porous framework is expected to enable excellent surface accessibility with easy ion diffusion, whereas oxidation restricted gelation can preserve all the intrinsic properties of MXene. Such novel characteristics in an electrode can allow effective utilization of surface limited EDLC and pseudocapacity for supercapacitive energy storage. At first, nature of charge storage mechanism and energy storage performance were analysed in three-electrode configuration by directly using freestanding MXene-graphene hydrogels as working electrode without any additional current collector (see experimental section for details). Fig. 2.7.a shows the cyclic voltammetry (CV) profiles of the hydrogels with varying MXene content at a scan rate of 5 mV s^{-1}. The curves are dominated by two symmetric peaks at -0.31 V and -0.38 V (vs Ag/AgCl) in the cathodic and anodic currents respectively, corresponding to the redox activity of Ti site. During discharge, the electrolyte ions gets intercalated into the oxygen terminated Ti sites ($Ti_3C_2O_2$) and gradually transforms into $Ti_3C_2O(OH)$ terminations through redox reaction in presence of H_2SO_4 electrolyte. This reversible process again converts back to oxygen terminated Ti sites during the charging

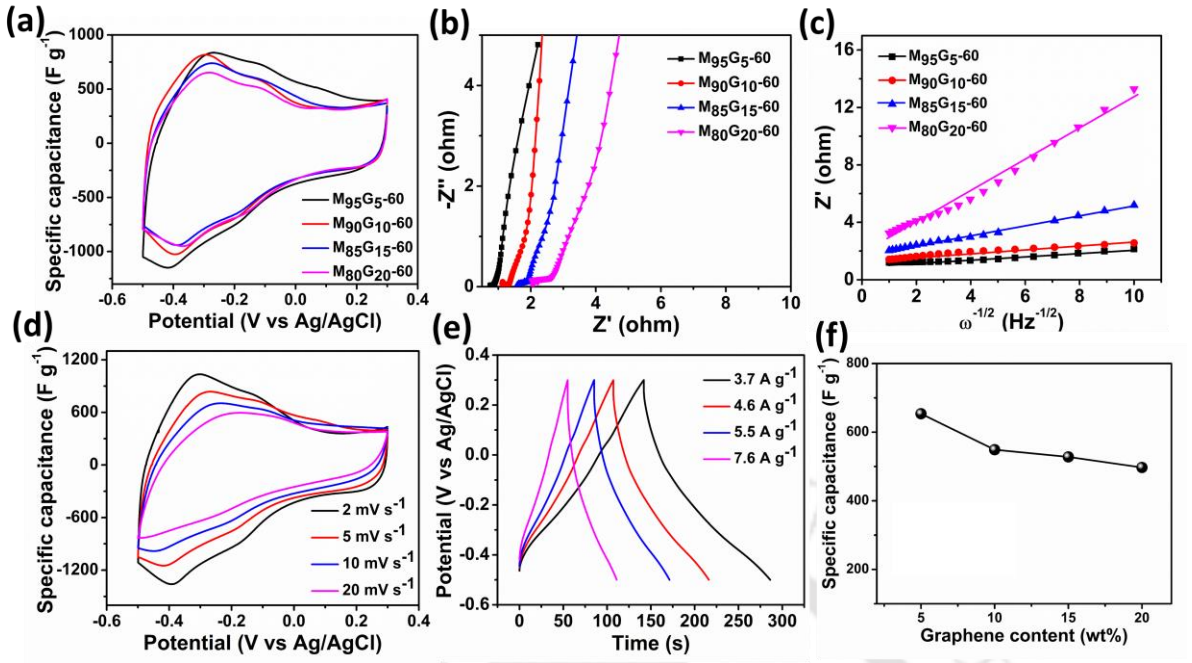

Figure 2.7. Energy storage performance of MXene-graphene hybrid hydrogel in three-electrode configuration**:** (a) CV curves at 5 mV s^{-1} for different graphene percentage; (b) EIS spectra and (c) linear fit representing the relationship between Z' and $\omega^{-1/2}$ of MXene-graphene hydrogels; (d) CV curves at different scan rates and (e) GCD curves at different current densities for $M_{95}G_5$-60 electrode; and (f) Gravimetric capacitance of MXene-graphene hydrogels at different graphene content at 2 mV s^{-1}.

process and thus creates the redox peaks observed in the CV profile.[50] The small separation of 70 mV between the two redox peaks confirms the high reversibility of the intercalation and de-intercalation of protons at the Ti atomic sites. Fig. 2.7.a also shows that, the area of CV profiles follow the order $M_{80}G_{20}$-60< $M_{85}G_{15}$-60< $M_{90}G_{10}$-60< $M_{95}G_5$-60, implying superior capacitive performance with lower graphene content. To understand the origin of this typical variation, equivalent-series-resistance (ESR) of the samples have been calculated from Nyquist plot that increases from 0.7Ω for the $M_{95}G_5$-60 to up to 2Ω for $M_{80}G_{20}$-60 (Fig. 2.7.b). Larger ESR with relative increase of graphene content signifies decrease of overall conductivity and ion transportability which can be attributed to the much larger size of graphene sheets (tens of microns as compared to sub-micron MXene sheets) and its lower conductivity as compared to the highly metallic conductivity of MXene. Moreover, the linear fit between the real impedance (Z') and $\omega^{-1/2}$ (where $\omega=2\pi f$) indicates lowest slope for $M_{95}G_5$-60, thus further validating the above argument (Fig. 2.7.c).[51] Based on the aforementioned discussion, we can conclude that better performance of samples with minimal graphene content is related to: (i) the higher

proportion of MXene which can contribute in capacitance through both EDLC and Faradic reaction, and (ii) lower diffusion resistance with higher metallic conductivity. The CV curves for $M_{95}G_5$-60 maintains a similar profile without much deviation as the scan rates are increased from 2 mV s^{-1} to 20 mV s^{-1} (Fig. 2.7.d). The galvanostatic charge-discharge (GCD) curves of the best performing sample ($M_{95}G_5$-60) at different current densities between -0.5 to 0.3 V (vs Ag/AgCl) is shown in Fig. 2.7.e. The symmetric GCD curves deviate from the usual triangular nature which is expected from MXene samples that store charge not only via charge double layer (EDLC) but also through pseudocapacitive mechanism on behalf of redox active surface. The specific gravimetric capacitance calculated from the CV is found to be 653.7 F g^{-1} for the $M_{95}G_5$-60 at a scan rate of 2 mV s^{-1} followed by 549 F g^{-1},528 F g^{-1},497.1 F g^{-1} for $M_{90}G_{10}$-60, $M_{85}G_{15}$-60 and $M_{80}G_{20}$-60 electrodes respectively (Fig. 2.7.f). Such gravimetric capacitance is much higher than other reported values at the same scan rate on MXene or MXene-graphene hybrids based electrodes (Table 2.2).

Table 2.2: Electrochemical performance comparison of MXene and MXene hybrid materials.

Material	Electrolyte	C_g (F g^{-1})	C_v (F cm^{-3})	Mass loading (mg cm^{-2})	Electrode thickness (µm)	Ref.
$Ti_3C_2T_x$	1 M Li_2SO_4	191.5	633	1.60	-	52
$Ti_3C_2T_x$-PVA	KOH	167	528	1.23	3.9	53
$Ti_3C_2T_x$-ZnO	1 M KOH	120	200	-	20	54
$Ti_3C_2T_x$-SWCNT	1M $MgSO_4$	134	390	0.73	2.5	55
$Ti_3C_2T_x$-rGO	6M KOH	405	370	0.74	8	56
$Ti_3C_2T_x$ Clay	1M H_2SO_4	245	900	1.85	5	57
$Ti_3C_2T_x$-PPY	1M H_2SO_4	416	1000	0.93	3.9	58
$Ti_3C_2T_x$	1M H_2SO_4	325	520	1.3	8	59
MXene hydrogel	3M H_2SO_4	380	1500	1.2	3	60
Holey GO-$Ti_3C_2T_x$	3M H_2SO_4	438	1445	1.3	~4	61
$Ti_3C_2T_x$-rGO	3M H_2SO_4	335	1040	-	3-4	62
$M_{95}G_5$-60 pressed at 10MPa	**3M H_2SO_4**	**624**	**1522**	**3.9**	**16**	**This work**

For any new material with potential supercapacitive application though three-electrode measurements are indeed valuable for initial assessment of electrode redox and surface activities at a well-defined potential, these values should not be considered reliable when it

comes to real world devices.[63] Till date, only few reports on MXene based supercapacitor have mentioned the performance in two-electrode cell, and nearly in all the cases the values of energy storage metric remains very moderate (50 -321 F g^{-1}).[30,64] We have done detailed characterization in two-electrode cell and have obtained state-of-the-art performance metric.

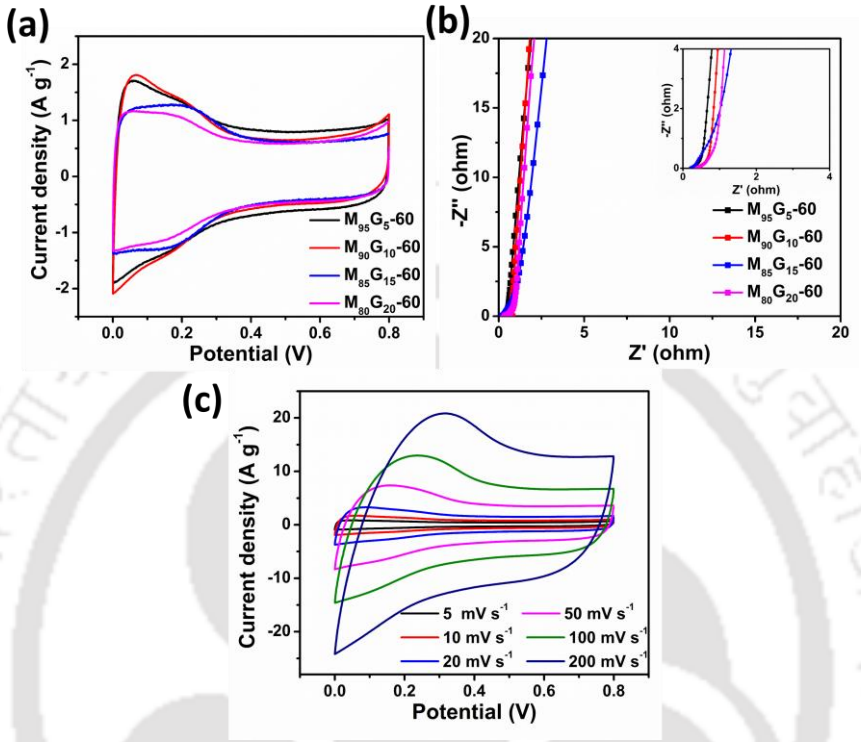

Figure 2.8. Two-electrode electrochemical measurements of hybrid hydrogels with different MXene: GO wt%. (a) CV curves of the hydrogels at a scan rate of 10 mV s^{-1}. (b) EIS plots with inset showing the magnified high frequency region. (c) CV curves of $M_{95}G_5$-60 at different scan rates from 5 mV s^{-1} to 200 mV s^{-1}.

Similar to the three-electrode test, the charge storage capacity of MXene based hydrogels in two-electrode test for different MXene: GO weight ratio follow the same order. The $M_{95}G_5$-60 electrode offers the highest capacitive performance which is obvious from the monotonically increased area of CV profiles (Fig. 2.8.a, Table 2.3). Easy diffusion of the electrolyte in all these samples is also obvious from steep vertical rise of EIS plots measured in symmetric cell configuration (Fig. 2.8.b). High specific capacitance values were registered for all the samples and a typical value of 384.2 F g^{-1} at 2 mV s^{-1} is displayed by the hydrogel $M_{95}G_5$-60, and further the capacitance still retains 78% at a higher scan rate of 100 mV s^{-1} (Fig. 2.8.c).

Table 2.3. List of electrodes measured in symmetric cells and their capacitive performance at 10 mV s^{-1} compared to some recent reports.

Material	Mass loading (mg cm^{-2})	Gravimetric capacitance per electrode (F g^{-1})	Areal capacitance (mF cm^{-2})
$M_{95}G_5$-20	1.93	459.9	443.8
$M_{95}G_5$-40	2.58	418.9	540.38
$M_{95}G_5$-60	4.15	377	782.27
$M_{95}G_5$-120	9.26	315	1458.45
$M_{90}G_{10}$-60	2.88	356.5	513.36
$M_{85}G_{15}$-60	2.22	312.37	346.73
$M_{80}G_{20}$-60	1.57	294	230.79

To examine the effect of areal mass loading, hydrogels of different thickness were produced by varying the gelation time (20-120 min). The area of the voltammogram and hence the specific capacitance of $M_{95}G_5$-20 (mass loading 1.93 mg cm^{-2}) is largest (460 F g^{-1} at 2 mV s^{-1}) as compared to other hydrogels with higher gelation time (Fig. 2.9.a). Although the areal mass loading of $M_{95}G_5$-20 is relatively lower as compared to other samples but the loading is comparable or better than the recent reports.[64,65] The gravimetric capacitance of $M_{95}G_5$-20 is higher as compared to other MXene or MXene-graphene hybrids reported thus far in two-electrode configuration. Additionally, as the scan rates are increased, the $M_{95}G_5$-20 electrode maintains a similar shape of the CV curves indicating better rate performance (Fig. 2.9.b) while the GCD curves of the same at different current densities are shown in Fig. 2.9.c. Because of the serious ion transport limitations, often currently reported supercapacitive materials are presented with mass loadings far lower than the commercially recommended values (~10 mg cm^{-2}) (Table 2.2).[66,67] But in the present study, due to controlled interfacial interlinking and superior electrolyte accessibility of MXene surfaces, an excellent specific gravimetric capacitance of 320 F g^{-1} (at 2 mV s^{-1}) in symmetric two-electrode cell is achieved even with a high mass loading of 9.26 mg cm^{-2} ($M_{95}G_5$-120). Further, electrodes of different areal loading display good capacitance retention at higher scan rates and $M_{95}G_5$-20 exhibit best rate performance with retention of 46% at high scan rate of 500 mV s^{-1} (Fig. 2.9.d). Fig. 2.10 demonstrates the areal and gravimetric capacitance of the hybrid hydrogels in symmetric cell full device configuration as a function of mass loading. A very high areal capacitance of 1485.5 mF cm^{-2} at 2 mV s^{-1} with a good gravimetric value of 320 F g^{-1} can simply be achieved by increasing the gelation time ($M_{95}G_5$-120), i.e., essentially increasing the areal mass loading to commercial level (9.26 mg cm^{-2}). In spite of the high mass loading it holds up good rate performance maintaining an areal capacitance of 1015 mF cm^{-2} even at 100 mV s^{-1}.

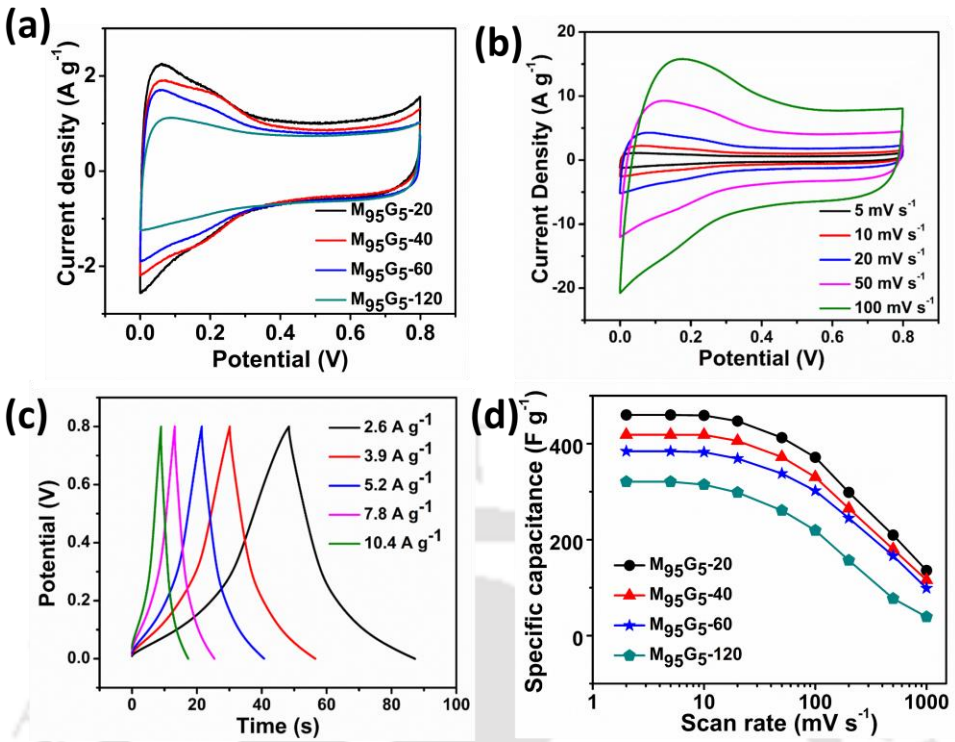

Figure 2.9. Energy storage performance of hybrid hydrogels developed with different gelation time in symmetric two-electrode device configuration: (a) CV curves at 10 mV s^{-1}; (b) CV curves at different scan rates in two-electrode configuration, (c) GCD curves for the $M_{95}G_5$-20 electrode; (d) gravimetric capacitance of MXene-graphene hybrid electrodes at different scan rates.

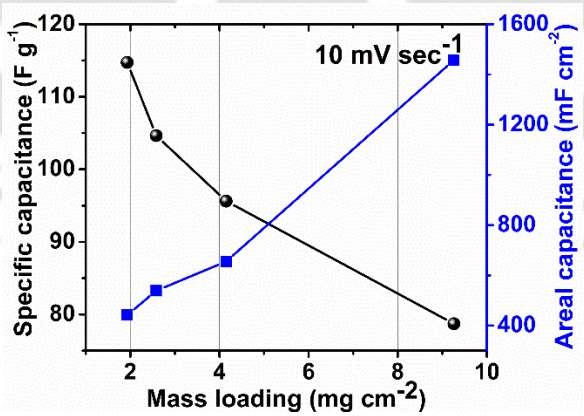

Figure 2.10. Comparison of device gravimetric and areal capacitance at different mass loading of electrodes.

Ragone plot shows that the MXene hydrogel electrodes can achieve high energy density at a high power density, typically $M_{95}G_5$-20 can deliver energy density of 10.23 Wh kg^{-1} at a power density of 460.35 W kg^{-1} and maintains upto 4.65 Wh kg^{-1} at an increased power density of

10.4 kW kg^{-1} (Fig. 2.11.a). Stability of the $M_{95}G_5$-20 electrode was investigated for 8000 charge-discharge cycles at a constant current density of 3 A g^{-1} and an excellent capacity retention of 98% was recorded which is very promising for their long term durable use (Fig. 2.11.b).

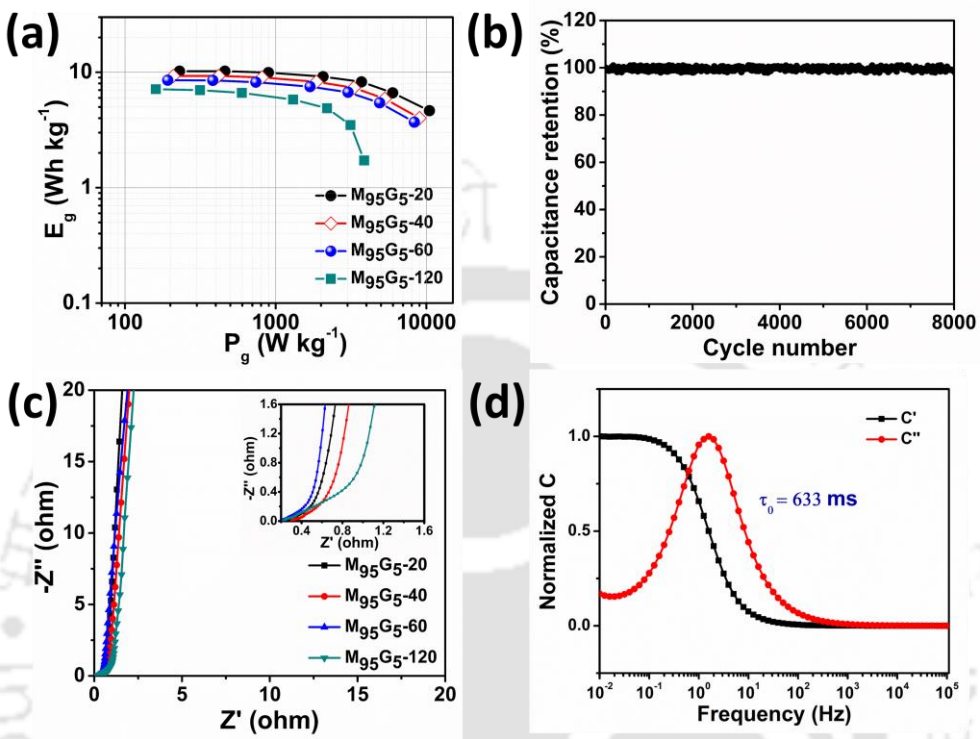

Figure 2.11. (a) Ragone plot showing gravimetric energy and power densities; (b) Cycling stability of $M_{95}G_5$-20 measured at constant current charge discharge with a current density of 3 A g^{-1} for 8000 cycles; (c) EIS spectra, inset shows the zoomed high frequency domain; (d) Normalised real and imaginary capacitance for $M_{95}G_5$-20.

Steep rise of the imaginary electrical impedance at low frequencies in Nyquist plot and low ESR (0.2-0.3Ω) signifies low resistance to ion diffusion in electrodes of different thicknesses (Fig. 2.11.c). Notably, the electrode with highest areal loading ($M_{95}G_5$-120) retains almost similar profile as compared to lower areal loading counterparts, confirming the presence of continuous ion transport channels irrespective of areal loading. As a consequence, the electrodes continue to display high gravimetric values with the increase of mass loading per unit footprint. High ion transportation efficiency with high areal mass loading is also evident from the low relaxation time (0.633 s) for the $M_{95}G_5$-20 which is obtained by analysing frequency dependent real and imaginary capacitance (C′(ω) and C″(ω) respectively) via complex capacitance modeling (Fig. 2.11.d).[68]

Volumetric energy density, an important metric often required, can also be achieved by compacting the hydrogel via electrolyte assisted mechanical compression to preserve the ion accessible pores. Hydrogels were first saturated with 3M H_2SO_4 before they were compressed at 5 and 10 MPa pressure (see experimental section for details). Fig. 2.12.a-c shows the cross sectional FESEM images of hydrogel electrode ($M_{95}G_5$-60) before and after mechanical compression, which indicates a 38-fold reduction in thickness due to 10 MPa pressure.

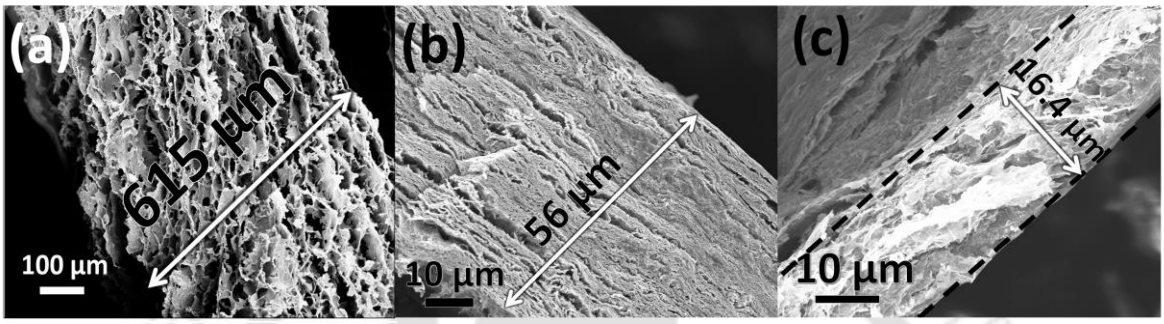

Figure 2.12. Thickness of gel electrodes obtained with cross-sectional FESEM images (a) before, and (b) & (c) after compression with 5 MPa and 10 MPa pressure respectively.

As a result, electrode density of 0.9 g cm^{-3} and 2.44 g cm^{-3} can be achieved with compression pressure of 5 MPa and 10 MPa respectively. It is worth noting that the mass loading (3.9 mg cm^{-2}) and thickness (>15 µm) of the compressed electrodes remain much higher compared to those mentioned in most recent reports (~0.7-3 mg cm^{-2} and ~3-8 µm) (Table 2.2). From the CV curves, the compact yet thick $M_{95}G_5$-60 electrode pressed at 10 MPa reached an outstanding volumetric capacitance of 1522 F cm^{-3} in three-electrode setup at 2 mV s^{-1} (Fig. 2.13.a), much higher than the electrodes pressed at 5 MPa (541.71 F cm^{-3}) and without pressing (45.79 F cm^{-3}). This volumetric capacitance of 1522 F cm^{-3} is one of the highest values reported on MXene or MXene-graphene hybrids based supercapacitor in the same three-electrode configuration (Table 2.2). Nonetheless, when tested in symmetric cell, the 10 MPa electrode can deliver 751.3 F cm^{-3} at 2 mV s^{-1} (Fig. 2.13.b). As the scan rate is increased it still maintains 698.9 F cm^{-3} at 10 mV s^{-1} and retains upto 50% of the capacitance at 100 mV s^{-1}. Importantly, the compact electrodes still maintain good gravimetric capacity together with high volumetric value in two-electrode measurements (Fig. 2.13.c). To highlight the role of electrolyte intercalation in preserving ion accessible channels even after mechanical compression, EIS spectrum of compacted samples is compared with naturally dried sample (Fig. 2.13.d). EIS spectra of the pressed ones are near vertical at low frequency region whereas it is more

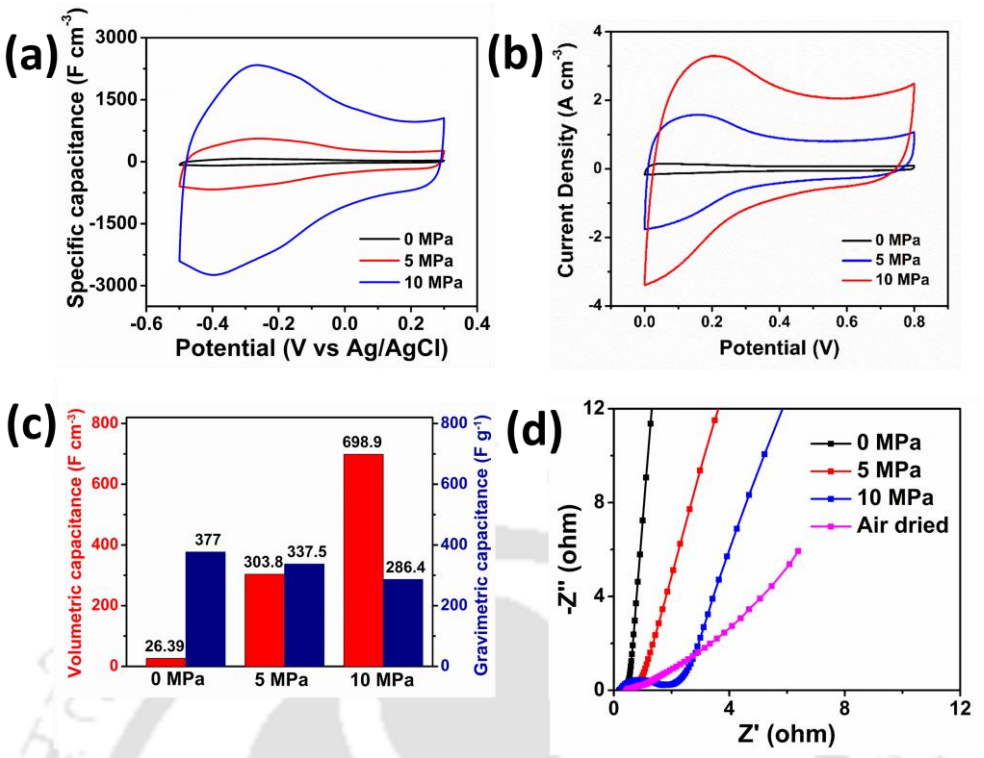

Figure 2.13. Volumetric energy storage performance by electrolyte assisted mechanically compacted hydrogel: (a) comparative CV curves in three-electrode setup at 2 mV s^{-1}; (b) CV curves of the $M_{95}G_5$-60 electrode pressed at different pressures measured in symmetric cell setup at 10 mV s^{-1}; (c) comparison of volumetric and gravimetric capacitance vs compression pressure at 10 mV s^{-1} in two-electrode configuration; (d) comparative EIS spectra of the compressed and air dried electrodes in symmetric cell setup.

inclined towards the real impedance axis for the air dried sample, signifying much better electrolyte ion diffusion and hence effective utilization of MXene surfaces in the former as presented schematically in Fig. 2.14. Thus, high compactness together with ensured accessibility of oxidation restricted MXene surface via preserved ion channels lead to high volumetric performance.

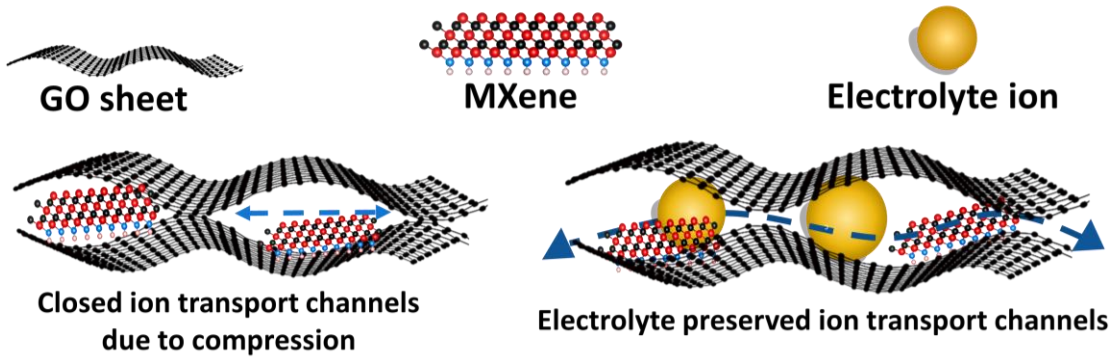

Figure 2.14. Schematic illustration of the electrolyte assisted mechanical compression process protecting the ion-transport channels in a compressed electrode.

In summary, simple oxidation restricted MXene based hydrogel development and most importantly tuneable and very high supercapacitive performance in all three aspects (gravimetric, areal and volumetric) make this hybrid hydrogel a potential candidate for future energy storage applications.

2.4. Conclusions

Briefly, supercapacitors with state-of-the-art performance metric have been realized with MXene based hybrid hydrogel electrodes developed via interfacial assembly. The as developed hydrogel with only 5% graphene as gelator can achieve exceptionally high gravimetric capacitance of 653.7 F g^{-1} at 2 mV s^{-1} in three-electrode test and 460 F g^{-1} in symmetric two-electrode configuration with long term cycling stability (< 2% decay over 8000 charge-discharge cycles). Moreover, an increase of mass loading to commercial level (9.26 mg cm^{-2}) leads to ultrahigh areal capacitance of 1485.5 mF cm^{-2} in symmetric two-electrode configuration while maintaining excellent gravimetric capacitance (320 F g^{-1}). In addition, a highly dense and compact electrode (2.44 g cm^{-3}) developed from electrolyte protected compressed hydrogel exhibits ultra-high volumetric capacitance of 1522.4 F cm^{-3}. Such an excellent electrochemical performance is largely attributed to the introduction of graphene among the MXene sheets and the intercalated water of hydrogel which synergistically restrict the strong face-to-face restacking tendency of nanosheets and thereby maintain an easy ion transport and high electrolyte accessible surface area. Besides, complete ambient condition processing protects the intrinsic metallic and pseudocapacitive properties of MXene, promoting increased participation of pristine MXene surfaces in electrochemical reaction. Therefore, benefitted with such physical properties coupled with excellent performance matrices, these MXene graphene hydrogels can truly set the bar for future MXene based supercapacitive electrode research and applications.

References

1. A.K. Geim, K.S. Novoselov, The rise of graphene, *Nature Materials.* 6 (2007) 183-191.
2. M. Naguib, M. Kurtoglu, V. Presser, J. Lu, J. Niu, M. Heon, L. Hultman, Y. Gogotsi, M.W. Barsoum, Two-Dimensional Nanocrystals Produced by Exfoliation of Ti3AlC2, *Advanced Materials.* 23 (2011) 4248-4253.
3. M. Acerce, D. Voiry, M. Chhowalla, Metallic 1T phase MoS2 nanosheets as supercapacitor electrode materials, *Nature Nanotechnology.* 10 (2015) 313-318.
4. C. An, Y. Zhang, H. Guo, Y. Wang, Metal oxide-based supercapacitors: progress and prospectives, *Nanoscale Advances.* 1 (2019) 4644-4658.
5. X. Zhan, C. Si, J. Zhou, Z. Sun, MXene and MXene-based composites: synthesis, properties and environment-related applications, *Nanoscale Horizons.* 5 (2020) 235-258.
6. J.L. Hart, K. Hantanasirisakul, A.C. Lang, B. Anasori, D. Pinto, Y. Pivak, J.T. van Omme, S.J. May, Y. Gogotsi, M.L. Taheri, Control of MXenes' electronic properties through termination and intercalation, *Nature Communications.* 10 (2019) 522.
7. C. Zhan, M. Naguib, M. Lukatskaya, P.R.C. Kent, Y. Gogotsi, D.-e. Jiang, Understanding the MXene Pseudocapacitance, *The Journal of Physical Chemistry Letters.* 9 (2018) 1223-1228.
8. Q. Yang, Y. Wang, X. Li, H. Li, Z. Wang, Z. Tang, L. Ma, F. Mo, C. Zhi, Recent Progress of MXene-Based Nanomaterials in Flexible Energy Storage and Electronic Devices, *ENERGY & ENVIRONMENTAL MATERIALS.* 1 (2018) 183-195.
9. B. Anasori, M.R. Lukatskaya, Y. Gogotsi, 2D metal carbides and nitrides (MXenes) for energy storage, *Nature Reviews Materials.* 2 (2017) 16098.
10. A. Kaidarova, M.A. Khan, M. Marengo, L. Swanepoel, A. Przybysz, C. Muller, A. Fahlman, U. Buttner, N.R. Geraldi, R.P. Wilson, C.M. Duarte, J. Kosel, Wearable multifunctional printed graphene sensors, *npj Flexible Electronics.* 3 (2019) 15.
11. S. Hussain, N. Ullah, Y. Zhang, A. Shaheen, M.S. Javed, L. Lin, Zulfiqar, S.B. Shah, G. Liu, G. Qiao, One-step synthesis of unique catalyst Ni9S8@C for excellent MOR performances, *International Journal of Hydrogen Energy.* 44 (2019) 24525-24533.
12. S. Hussain, X. Yang, M.K. Aslam, A. Shaheen, M.S. Javed, N. Aslam, B. Aslam, G. Liu, G. Qiao, Robust TiN nanoparticles polysulfide anchor for Li–S storage and diffusion pathways using first principle calculations, *Chemical Engineering Journal.* 391 (2020) 123595.
13. S. Hussain, M.S. Javed, S. Asim, A. Shaheen, A.J. Khan, Y. Abbas, N. Ullah, A. Iqbal, M. Wang, G. Qiao, S. Yun, Novel gravel-like NiMoO4 nanoparticles on carbon cloth for outstanding supercapacitor applications, *Ceramics International.* 46 (2020) 6406-6412.
14. B. Anasori, Y. Xie, M. Beidaghi, J. Lu, B.C. Hosler, L. Hultman, P.R.C. Kent, Y. Gogotsi, M.W. Barsoum, Two-Dimensional, Ordered, Double Transition Metals Carbides (MXenes), *ACS Nano.* 9 (2015) 9507-9516.
15. M.R. Lukatskaya, O. Mashtalir, C.E. Ren, Y. Dall'Agnese, P. Rozier, P.L. Taberna, M. Naguib, P. Simon, M.W. Barsoum, Y. Gogotsi, Cation Intercalation and High

Volumetric Capacitance of Two-Dimensional Titanium Carbide, *Science.* 341 (2013) 1502.

16. M. Ghidiu, M.R. Lukatskaya, M.-Q. Zhao, Y. Gogotsi, M.W. Barsoum, Conductive two-dimensional titanium carbide 'clay' with high volumetric capacitance, *Nature.* 516 (2014) 78-81.
17. J. Ran, G. Gao, F.-T. Li, T.-Y. Ma, A. Du, S.-Z. Qiao, Ti3C2 MXene co-catalyst on metal sulfide photo-absorbers for enhanced visible-light photocatalytic hydrogen production, *Nature Communications.* 8 (2017) 13907.
18. F. Shahzad, M. Alhabeb, C.B. Hatter, B. Anasori, S. Man Hong, C.M. Koo, Y. Gogotsi, Electromagnetic interference shielding with 2D transition metal carbides (MXenes), *Science.* 353 (2016) 1137.
19. E. Lee, A. VahidMohammadi, Y.S. Yoon, M. Beidaghi, D.-J. Kim, Two-Dimensional Vanadium Carbide MXene for Gas Sensors with Ultrahigh Sensitivity Toward Nonpolar Gases, *ACS Sensors.* 4 (2019) 1603-1611.
20. C. Zhang, S.-H. Park, A. Seral-Ascaso, S. Barwich, N. McEvoy, C.S. Boland, J.N. Coleman, Y. Gogotsi, V. Nicolosi, High capacity silicon anodes enabled by MXene viscous aqueous ink, *Nature Communications.* 10 (2019) 849.
21. Z. Wu, T. Shang, Y. Deng, Y. Tao, Q.-H. Yang, The Assembly of MXenes from 2D to 3D, *Advanced Science*. 7 (2020) 1903077.
22. M.-Q. Zhao, X. Xie, C.E. Ren, T. Makaryan, B. Anasori, G. Wang, Y. Gogotsi, Hollow MXene Spheres and 3D Macroporous MXene Frameworks for Na-Ion Storage, *Advanced Materials*. 29 (2017) 1702410.
23. P. Simon, Two-Dimensional MXene with Controlled Interlayer Spacing for Electrochemical Energy Storage, *ACS Nano.* 11 (2017) 2393-2396.
24. M. Boota, Y. Gogotsi, MXene—Conducting Polymer Asymmetric Pseudocapacitors, *Advanced Energy Materials.* 9 (2019) 1802917.
25. Z. Zhou, W. Panatdasirisuk, T.S. Mathis, B. Anasori, C. Lu, X. Zhang, Z. Liao, Y. Gogotsi, S. Yang, Layer-by-layer assembly of MXene and carbon nanotubes on electrospun polymer films for flexible energy storage, *Nanoscale.* 10 (2018) 6005-6013.
26. Y. Yue, N. Liu, Y. Ma, S. Wang, W. Liu, C. Luo, H. Zhang, F. Cheng, J. Rao, X. Hu, J. Su, Y. Gao, Highly Self-Healable 3D Microsupercapacitor with MXene–Graphene Composite Aerogel, *ACS Nano.* 12 (2018) 4224-4232.
27. M.-Q. Zhao, C.E. Ren, Z. Ling, M.R. Lukatskaya, C. Zhang, K.L. Van Aken, M.W. Barsoum, Y. Gogotsi, Flexible MXene/Carbon Nanotube Composite Paper with High Volumetric Capacitance, *Advanced Materials.* 27 (2015) 339-345.
28. A. VahidMohammadi, J. Moncada, H. Chen, E. Kayali, J. Orangi, C.A. Carrero, M. Beidaghi, Thick and freestanding MXene/PANI pseudocapacitive electrodes with ultrahigh specific capacitance, *Journal of Materials Chemistry A.* 6 (2018) 22123-22133.
29. H. Li, Y. Hou, F. Wang, M.R. Lohe, X. Zhuang, L. Niu, X. Feng, Flexible All-Solid-State Supercapacitors with High Volumetric Capacitances Boosted by Solution Processable MXene and Electrochemically Exfoliated Graphene, *Advanced Energy Materials.* 7 (2017) 1601847.

30. J. Yan, C.E. Ren, K. Maleski, C.B. Hatter, B. Anasori, P. Urbankowski, A. Sarycheva, Y. Gogotsi, Flexible MXene/Graphene Films for Ultrafast Supercapacitors with Outstanding Volumetric Capacitance, *Advanced Functional Materials.* 27 (2017) 1701264.
31. X.-L. Wu, A.-W. Xu, Carbonaceous hydrogels and aerogels for supercapacitors, *Journal of Materials Chemistry A.* 2 (2014) 4852-4864.
32. M. Hu, T. Hu, Z. Li, Y. Yang, R. Cheng, J. Yang, C. Cui, X. Wang, Surface Functional Groups and Interlayer Water Determine the Electrochemical Capacitance of Ti3C2Tx MXene, *ACS Nano.* 12 (2018) 3578-3586.
33. C.J. Zhang, S. Pinilla, N. McEvoy, C.P. Cullen, B. Anasori, E. Long, S.-H. Park, A. Seral-Ascaso, A. Shmeliov, D. Krishnan, C. Morant, X. Liu, G.S. Duesberg, Y. Gogotsi, V. Nicolosi, Oxidation Stability of Colloidal Two-Dimensional Titanium Carbides (MXenes), *Chemistry of Materials.* 29 (2017) 4848-4856.
34. S. Zhao, H.-B. Zhang, J.-Q. Luo, Q.-W. Wang, B. Xu, S. Hong, Z.-Z. Yu, Highly Electrically Conductive Three-Dimensional Ti3C2Tx MXene/Reduced Graphene Oxide Hybrid Aerogels with Excellent Electromagnetic Interference Shielding Performances, *ACS Nano.* 12 (2018) 11193-11202.
35. Kim, H.-J. Koh, C.E. Ren, O. Kwon, K. Maleski, S.-Y. Cho, B. Anasori, C.-K. Kim, Y.-K. Choi, J. Kim, Y. Gogotsi, H.-T. Jung, Metallic Ti3C2Tx MXene Gas Sensors with Ultrahigh Signal-to-Noise Ratio, *ACS Nano.* 12 (2018) 986-993.
36. Z. Wang, Y. Chen, M. Yao, J. Dong, Q. Zhang, L. Zhang, X. Zhao, Facile fabrication of flexible rGO/MXene hybrid fiber-like electrode with high volumetric capacitance, *Journal of Power Sources.* 448 (2020) 227398.
37. T. Shang, Z. Lin, C. Qi, X. Liu, P. Li, Y. Tao, Z. Wu, D. Li, P. Simon, Q.H. Yang, 3D Macroscopic Architectures from Self-Assembled MXene Hydrogels, *Advanced Functional Materials.* 29 (2019).
38. Hummers, R.E. Offeman, Preparation of Graphitic Oxide, *Journal of the American Chemical Society.* 80 (1958) 1339-1339.
39. A. Sikdar, A. Majumdar, P. Dutta, M. Borah, S.O. Kim, U.N. Maiti, Ultra-large area graphene hybrid hydrogel for customized performance supercapacitors: High volumetric, areal energy density and potential wearability, *Electrochimica Acta.* 332 (2020) 135492.
40. J. Halim, K.M. Cook, M. Naguib, P. Eklund, Y. Gogotsi, J. Rosen, M.W. Barsoum, X-ray photoelectron spectroscopy of select multi-layered transition metal carbides (MXenes), *Applied Surface Science.* 362 (2016) 406-417.
41. M. Ghidiu, J. Halim, S. Kota, D. Bish, Y. Gogotsi, M.W. Barsoum, Ion-Exchange and Cation Solvation Reactions in Ti3C2 MXene, *Chemistry of Materials.* 28 (2016) 3507-3514.
42. Q. Jiang, N. Kurra, M. Alhabeb, Y. Gogotsi, H.N. Alshareef, All Pseudocapacitive MXene-RuO2 Asymmetric Supercapacitors, *Advanced Energy Materials.* 8 (2018) 1703043.
43. U.N. Maiti, J. Lim, K.E. Lee, W.J. Lee, S.O. Kim, Three-Dimensional Shape Engineered, Interfacial Gelation of Reduced Graphene Oxide for High Rate, Large Capacity Supercapacitors, *Advanced Materials.* 26 (2014) 615-619.

44. J. Yang, W. Bao, P. Jaumaux, S. Zhang, C. Wang, G. Wang, MXene-Based Composites: Synthesis and Applications in Rechargeable Batteries and Supercapacitors, *Advanced Materials Interfaces.* 6 (2019) 1802004.
45. D. Li, M.B. Müller, S. Gilje, R.B. Kaner, G.G. Wallace, Processable aqueous dispersions of graphene nanosheets, *Nature Nanotechnology.* 3 (2008) 101-105.
46. P. Lian, Y. Dong, Z.-S. Wu, S. Zheng, X. Wang, W. Sen, C. Sun, J. Qin, X. Shi, X. Bao, Alkalized Ti3C2 MXene nanoribbons with expanded interlayer spacing for high-capacity sodium and potassium ion batteries, *Nano Energy.* 40 (2017) 1-8.
47. J. Li, X. Yuan, C. Lin, Y. Yang, L. Xu, X. Du, J. Xie, J. Lin, J. Sun, Achieving High Pseudocapacitance of 2D Titanium Carbide (MXene) by Cation Intercalation and Surface Modification, *Advanced Energy Materials.* 7 (2017) 1602725.
48. A. Lipatov, M. Alhabeb, M.R. Lukatskaya, A. Boson, Y. Gogotsi, A. Sinitskii, Effect of Synthesis on Quality, Electronic Properties and Environmental Stability of Individual Monolayer Ti3C2 MXene Flakes, *Advanced Electronic Materials.* 2 (2016) 1600255.
49. M. Malaki, A. Maleki, R.S. Varma, MXenes and ultrasonication, *Journal of Materials Chemistry A.* 7 (2019) 10843-10857.
50. M. Hu, Z. Li, T. Hu, S. Zhu, C. Zhang, X. Wang, High-Capacitance Mechanism for Ti3C2Tx MXene by in Situ Electrochemical Raman Spectroscopy Investigation, *ACS Nano.* 10 (2016) 11344-11350.
51. M. Fan, Y. Chen, Y. Xie, T. Yang, X. Shen, N. Xu, H. Yu, C. Yan, Half-Cell and Full-Cell Applications of Highly Stable and Binder-Free Sodium Ion Batteries Based on Cu3P Nanowire Anodes, *Advanced Functional Materials.* 26 (2016) 5019-5027.
52. C. Yang, Y. Tang, Y. Tian, Y. Luo, Y. He, X. Yin, W. Que, Achieving of Flexible, Free-Standing, Ultracompact Delaminated Titanium Carbide Films for High Volumetric Performance and Heat-Resistant Symmetric Supercapacitors, *Advanced Functional Materials.* 28 (2018) 1705487.
53. Z. Ling, C.E. Ren, M.-Q. Zhao, J. Yang, J.M. Giammarco, J. Qiu, M.W. Barsoum, Y. Gogotsi, Flexible and conductive MXene films and nanocomposites with high capacitance, *Proceedings of the National Academy of Sciences.* 111 (2014) 16676.
54. F. Wang, M. Cao, Y. Qin, J. Zhu, L. Wang, Y. Tang, ZnO nanoparticle-decorated two-dimensional titanium carbide with enhanced supercapacitive performance, *RSC Advances.* 6 (2016) 88934-88942.
55. M.-Q. Zhao, C.E. Ren, Z. Ling, M.R. Lukatskaya, C. Zhang, K.L. Van Aken, M.W. Barsoum, Y. Gogotsi, Flexible MXene/Carbon Nanotube Composite Paper with High Volumetric Capacitance, *Advanced Materials.* 27 (2015) 339-345.
56. S. Xu, G. Wei, J. Li, W. Han, Y. Gogotsi, Flexible MXene–graphene electrodes with high volumetric capacitance for integrated co-cathode energy conversion/storage devices, *Journal of Materials Chemistry A.* 5 (2017) 17442-17451.
57. M. Ghidiu, M.R. Lukatskaya, M.-Q. Zhao, Y. Gogotsi, M.W. Barsoum, Conductive two-dimensional titanium carbide 'clay' with high volumetric capacitance, *Nature.* 516 (2014) 78-81.
58. M. Boota, B. Anasori, C. Voigt, M.-Q. Zhao, M.W. Barsoum, Y. Gogotsi, Pseudocapacitive Electrodes Produced by Oxidant-Free Polymerization of Pyrrole

between the Layers of 2D Titanium Carbide (MXene), *Advanced Materials.* 28 (2016) 1517-1522.

59. Y. Dall'Agnese, M.R. Lukatskaya, K.M. Cook, P.-L. Taberna, Y. Gogotsi, P. Simon, High capacitance of surface-modified 2D titanium carbide in acidic electrolyte, *Electrochemistry Communications.* 48 (2014) 118-122.
60. M.R. Lukatskaya, S. Kota, Z. Lin, M.-Q. Zhao, N. Shpigel, M.D. Levi, J. Halim, P.-L. Taberna, M.W. Barsoum, P. Simon, Y. Gogotsi, Ultra-high-rate pseudocapacitive energy storage in two-dimensional transition metal carbides, *Nature Energy.* 2 (2017) 17105.
61. Z. Fan, Y. Wang, Z. Xie, D. Wang, Y. Yuan, H. Kang, B. Su, Z. Cheng, Y. Liu, Modified MXene/Holey Graphene Films for Advanced Supercapacitor Electrodes with Superior Energy Storage, *Advanced Science.* 5 (2018) 1800750.
62. J. Yan, C.E. Ren, K. Maleski, C.B. Hatter, B. Anasori, P. Urbankowski, A. Sarycheva, Y. Gogotsi, Flexible MXene/Graphene Films for Ultrafast Supercapacitors with Outstanding Volumetric Capacitance, *Advanced Functional Materials.* 27 (2017) 1701264.
63. M.D. Stoller, R.S. Ruoff, Best practice methods for determining an electrode material's performance for ultracapacitors, *Energy & Environmental Science.* 3 (2010) 1294-1301.
64. S. Xu, G. Wei, J. Li, W. Han, Y. Gogotsi, Flexible MXene–graphene electrodes with high volumetric capacitance for integrated co-cathode energy conversion/storage devices, *Journal of Materials Chemistry A.* 5 (2017) 17442-17451.
65. M. Boota, B. Anasori, C. Voigt, M.-Q. Zhao, M.W. Barsoum, Y. Gogotsi, Pseudocapacitive Electrodes Produced by Oxidant-Free Polymerization of Pyrrole between the Layers of 2D Titanium Carbide (MXene), *Advanced Materials.* 28 (2016) 1517-1522.
66. Z. Ling, C.E. Ren, M.-Q. Zhao, J. Yang, J.M. Giammarco, J. Qiu, M.W. Barsoum, Y. Gogotsi, Flexible and conductive MXene films and nanocomposites with high capacitance, *Proceedings of the National Academy of Sciences.* 111 (2014) 16676.
67. M. Hu, Z. Li, H. Zhang, T. Hu, C. Zhang, Z. Wu, X. Wang, Self-assembled Ti3C2Tx MXene film with high gravimetric capacitance, *Chemical Communications.* 51 (2015) 13531-13533.
68. D. Pech, M. Brunet, H. Durou, P. Huang, V. Mochalin, Y. Gogotsi, P.-L. Taberna, P. Simon, Ultrahigh-power micrometre-sized supercapacitors based on onion-like carbon, *Nature Nanotechnology.* 5 (2010) 651-654.

Chapter 3

Critical Density Controlled Assembly of MXene for Freestanding Pristine Hydrogel Development: Excellent Energy Storage Performance Electrodes with Ultrahigh Capacitive Contribution

Chapter 3

Critical Density Controlled Assembly of MXene for Freestanding Pristine Hydrogel Development: Excellent Energy Storage Performance Electrodes with Ultrahigh Capacitive Contribution

Solvated network of two-dimensional materials in the form of hydrogel offers a unique platform for full utilization of surface dominated properties at the macroscopic scale. However, development of such hydrogels with ceramic sheets of MXene is highly challenging, and thus, are often critically dried to aerogel form to make them self-standing. Here, we report a freestanding thin MXene hydrogel through spontaneous, quasi-ordered assembly over metal plate and concurrent partial surface de-functionalization. We have established that self-standing hydrogel can only be assembled from MXene solution above a critical dispersion concentration (C_{ct}) depending on the size of the sheets. On behalf of ordered porous structure with intrinsic hydrated ion permeable channels, MXene hydrogels display very high surface capacitive contribution (>94%) in their pseudocapacitive energy storage performance. Consequently, as-developed hydrogels display excellent gravimetric capacitance of 391 F g^{-1} and rate performance, and continue to display outstanding performance (>337 F g^{-1}) at high enough mass loading up to ~15 mg cm^{-2}. As a versatility of hydrogel structure, an electrolyte protected mechanical compression method was employed to obtain a compact yet ion channel decorated electrode. As a result, compact MXene hydrogels achieved excellent volumetric capacitance (1120 F cm^{-3}) and rate capability (73% at 1000 mV s^{-1}).

3.1. Introduction

Hydrogels represent unique macroscopic materials that endow hydrophilic porosity and high surface area, and have been used in a plethora of applications.[1,2] As compared to frequently used polymeric counterparts that are built through bottom-up approaches starting with monomers, hydrogels made of nanoscale building blocks are relatively harder to realize.[3] The challenges to realize such hydrogels arise due to poor cross-linking possibility and difficulty while controlling the self-organization of the constituents. In particular, two dimensional nanomaterials have high intrinsic tendency to restack in a face-to-face pattern *via* van der Waals (vdW) interaction, and thus offer critical challenge to their assembly in the form of porous hydrogel.[4,5] In this direction, graphene hydrogels have been developed with great success by

assembling reduced graphene oxide (rGO) nanosheets, in which high deformability of flexible sheets and strong pi-pi interaction among pristine domains of rGO play an instrumental role in the structural stabilization.[6–8] Notably, such hydrogel structures have already been proven to be the key behind the enormous success of graphene in the area of energy storage,[9–11] catalysis,[12–14] biomedical applications,[15,16] and so on. However, unlike graphene, it is not so obvious to form self-standing hydrogels by assembling nanosheets of inorganic 2D materials due to the lack of inter-sheet interactions, their tough surfaces and availability in relatively much lower sheet sizes, typically in sub-micron scale. Nevertheless, inorganic hydrogels obviously can offer great advantages over powder or dried film form, but still rarely reported.

Transition metal carbides and nitrides, popularly known as MXenes, have recently attracted great research attention around the globe due to their unmatched material properties.[17–21] Particularly, titanium carbide based MXene ($Ti_3C_2T_x$, T_x being functional groups such as –O, –OH, –F) possess unique synergy of functionalization independent excellent conductivity, redox active pseudo capacitive surface, and easy solution processability.[22,23] As a consequence, it shows great potential in the fields of energy storage,[24–31] EMI shielding,[32] gas sensing,[33,34] wastewater treatment[35] *etc*. However, unlike other analogous 2D materials like graphene, development of pristine MXene hydrogels face numerous challenges due to smaller sheet size and intrinsic stiffness of MXene sheets.[25,36] Thus research on MXene have predominantly been focused on dried films obtained *via* vacuum filtration and aerogels made through direct freeze-drying of aqueous dispersion, while MXene hydrogel research kept relatively silent.[37–39]

In recent years, polymers,[40] graphene,[41] or metallic ions[42] have been used frequently as gelators to obtain self-standing hydrogel, but significant sacrifice of intrinsic MXene properties is anticipated due to these additives. Development of additive-free pure MXene hydrogel is still at a very premature stage and very recently only few successful attempts have been made toward its development. Li *et al.* used instant freezing induced preassembly followed by thawing in protic acid to induce intercalation in MXene sheets.[43] Although they were able to create MXene monoliths, rapid increase in pore volume due to water to ice crystallization forces 2D sheets to restack around those pores.[44] Thus, such hydrogels are left with large macro channels originating from the ice crystal network. Possible restacking between MXene sheets at the pore walls limits their usage in many applications where high surface area is essential. Two other recent reports employed self-assembly of MXene over metallic templates to form hydrogels. However, due to poor integrity of the material, substrates were needed as

mechanical support for handling and eventually they were used as aerogels.[45,46] Aerogels significantly sacrifice the benefits of corresponding hydrogels due to considerable restacking of sheets during freeze-drying.[44] In the current scenario, it is highly demanding to develop pure, freestanding MXene hydrogel having suitable porosity that can ensure full utilization of MXene surfaces. If such self-standing MXene-hydrogels are developed, the benefits of their hydrated structure can be extended to make solvated MXene frameworks (SMF) *via* solvent exchange, which can open a plethora of new possibilities in the field of battery, polymer hybrids, and so on.[44]

Here we report, self-standing pure MXene ($Ti_3C_2T_x$) hydrogel developed by simple self-assembly over zinc metal surface. We have demonstrated that development of freestanding MXene hydrogels strongly correlates with the MXene dispersion density and sheet size. Freestanding MXene hydrogels can only be achieved above a critical dispersion concentration (C_{ct}) depending on MXene sheet size. Importantly, as opposed to 3D hydrogel monoliths of randomly cross-linked sheets, MXene flakes self-organize in quasi-parallel alignment to make this thin hydrogel framework. Such structural characteristics make it an excellent candidate for energy storage applications. Achieving commercial scale mass loadings (>5 mg cm^{-2}) while simultaneously maintaining excellent energy storage metrics is considered as a major bottleneck for the development of energy storage electrodes.[47,48] We have achieved excellent areal capacitance of 5043 mF cm^{-2} with a high mass loading electrode (14.9 mg cm^{-2}) while maintaining a gravimetric capacitance of 337 F g^{-1} at 2 mV s^{-1}. Such gravimetric capacitance is above 86% of the value obtained with our similar hydrogel electrode of 1.2 mg cm^{-2} areal mass loading. For MXene based supercapacitive electrodes, the charging/discharging current incorporates capacitive and diffusion limited contribution, and large value of the former is desirable as it signifies high surface utilization during charge storage. Capacitive contribution as high as 96% is achieved with thin electrode (3.4 mg cm^{-2}), which only reduces to 93% for electrodes with high mass loading (~15 mg cm^{-2}). This demonstrates that the hydrogel structure offers suitable porosity and hydrophilicity to near full utilization of MXene surface even with very high areal mass loading.

3.2. Experimental section

3.2.1. Preparation of MXene:

MXene was prepared from MAX phase Ti_3AlC_2 using the minimally intensive layer delamination (MILD) method as introduced by Gogotsi group.[49] Typically, for the etchant

solution, 1.6 g LiF was dissolved in 20 mL 9M HCl and kept under continuous stirring until the solution became clear. Later, 1 g Ti_3AlC_2 was slowly mixed with the above solution in an ice bath. After the addition of Ti_3AlC_2 into the etchant solution, the mixture was kept at 35 ºC in oil bath under continuous stirring for 24 hours to let the etchant remove the metallic Al layers from MAX phase. Finally, to wash the acidic solution, it was repeatedly centrifuged at 3500 rpm for 5 min with deionized water until the pH of the solution became ~ 6. Between each centrifugation step, the mixture was allowed to self-delaminate *via* manual handshaking.

To make large sheet MXene (L-MXene), the above dispersion was first centrifuged at 3500 rpm for 30 min and the delaminated MXene was collected as supernatant which consists of both large and small MXene sheets. Subsequently, to separate the large MXene sheets, the supernatant was again centrifuged at 4500 rpm for 40 min to let the larger sheets sediment at the bottom which was then mixed with deionized water to achieve MXene dispersion with large sheets.

For the small sheet MXene (S-MXene) dispersion, the supernatant obtained from washing was first sonicated under continuous argon purging for 1 hr. During the sonication, the temperature of the sonication bath was maintained below 30ºC. The mixture was then centrifuged for 1 hr. at 3500 rpm to separate the delaminated MXene, which was collected as supernatant from the centrifuge tube. To achieve desired concentrations of MXene, the MXene dispersion was centrifuged at 14000 rpm for 40 min and then mixed with carefully measured amounts of water.

3.2.2. Preparation of MXene hydrogels:

To prepare the MXene hydrogels, a polished Zn plate (2 cm×2 cm) was first washed with ethanol and water under sonication. Then the Zn plate was put in MXene dispersion of different concentrations for 20-120 min. During the gelation period, MXene sheets would self-assemble over the Zn plate to form a continuous hydrogel. After gelation, the Zn plate, along with the hydrogel, was transferred to another vial containing deionized water for several hours to allow further reduction of the self-assembled MXene sheets. To separate the MXene hydrogel from the Zn foil, the assembly was immersed in 6M KOH solution. After that, the hydrogel was washed with DI water several times to restore pH neutrality.

For compressing the electrodes, electrolyte assisted compression was used. The as-prepared hydrogels were first immersed in 3M H_2SO_4 for 24 hours to saturate them with the electrolyte. Thereafter they were compressed with a hydraulic press at 10MPa pressure to make thin

hydrogel electrodes. Finally, the compressed electrodes were again dipped in 3M H_2SO_4 before using them as electrodes.

3.2.3. Material characterization:

The morphological properties of MXene hydrogel were analyzed using field emission scanning electron microscope (FESEM, Zeiss, Sigma-300) equipped with energy-dispersive X-ray spectroscopy (EDS). Structural and crystal properties of delaminated MXene layers were studied using transmission electron microscopy (FETEM, JEM 2100F, JEOL) and selected area electron microscopy (SAED) respectively. To observe the birefringence of MXene dispersions, a polarized optical microscope (POM) (Nikon Eclipse LV100POL) was used. A powder diffractometer (Rigaku, Japan) with Cu Kα radiation source was used to acquire the X-ray diffraction (XRD) patterns of MAX phase and MXene hydrogels. For X-ray photoelectron spectroscopy (XPS) analysis of hydrogels, LMH_4.4 was analyzed using ESCALAB Xi+ (Thermo Fisher Scientific Pvt. Ltd.). To analyze the size distribution of MXene sheets, dynamic light scattering (DLS) using Zetasizer nano, Malvern Instruments was used. For each sample, DLS results were analyzed from an average of five measurements.

3.2.4. Electrochemical characterization:

All the electrochemical performances were performed in three-electrode configuration with a Teflon Swagelok type cell with Biologic SP-150 electrochemical workstation. The as-prepared MXene hydrogel and activated carbon were used as working and counter electrodes respectively along with Ag/AgCl in 1M KCl working as reference electrode. The working and the counter electrodes were separated using a Celgard 3400 membrane. The measurements were performed in 3M H_2SO_4 electrolyte in a potential range of -0.7V to 0.3V vs Ag/AgCl. For the electrochemical impedance spectroscopy (EIS) measurements, a frequency range between 10 mHz to 100 kHz was used with an amplitude of 10 mV. These measurements were performed at open circuit potential (OCP) as well as different applied potentials vs the Ag/AgCl electrode after holding each potential for 10 min.

The gravimetric capacitance (C_g) was measured from the cyclic voltammetry (CV) curves using the equation,

$$C_g = \frac{1}{mv\Delta U}\int i\, dU \qquad (1)$$

and for the volumetric capacitance (C_V),

$$C_V = \frac{1}{Vv\Delta U}\int i\, dU \tag{2}$$

where, ΔU is the potential window, v is the scan rate and i corresponds to the current density, m and V are the mass and volume of the electrode respectively. To measure the volumetric capacitance (C_V), cross sectional area of the electrodes was measured carefully using FESEM.

The gravimetric energy (E_g) and power density (P_g) of the electrodes were calculated using the following equations,

$$E_g = \frac{C_g \times (\Delta U)^2}{2 \times 3.6} \tag{3}$$

$$P_g = \frac{E_g \times v \times 3600}{\Delta U} \tag{4}$$

3.3. Results and discussion

Freestanding MXene hydrogels were developed from suitably adjusted MXene aqueous dispersion *via* self-assembly over zinc (Zn) foil. In brief, a polished Zn plate was placed into concentrated MXene dispersion. After certain time of gelation and assembly over Zn foil, the hydrated macrostructure was detached in the form of self-standing hydrogel by etching the metal interface with KOH solution (Fig. 3.1.a,b). These hydrogels, being freestanding in nature, do not require any additional freeze-drying steps, which reduces the benefits of such

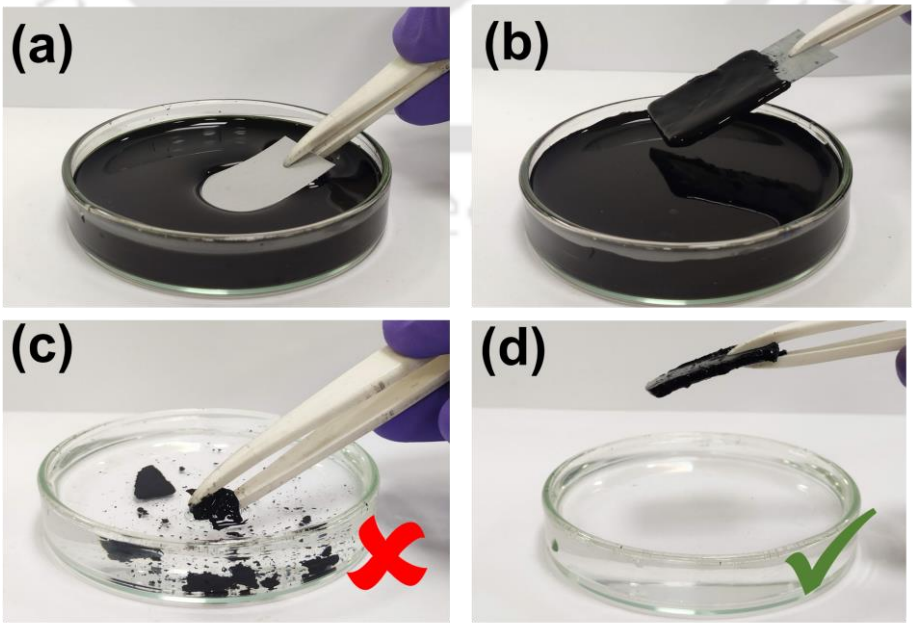

Figure 3.1. Freestanding MXene hydrogel development: (a-b) Processing of hydrogel from aqueous dispersion of MXene via spontaneous assembly over zinc plate; hydrogel developed from MXene dispersion (c) below and (d) above critical concentration (C_{cr}), former one gets disintegrated when picked-up, the gel is free-standing only above C_{cr}.

hydrogel structure significantly. However, the freestanding nature of hydrogel can only be obtained above a certain critical concentration (C_{ct}) whereas previous attempts of such MXene self-assembly ended up in soft macrostructures which required additional freeze-drying processing steps. (Fig. 3.1.c,d).[45,46,50] A sheet size dependent study on freestanding hydrogel development revealed that C_{ct} is much lower for larger MXene sheets (L-MXene) as compared to MXene with sheets of smaller dimension (S-MXene). FESEM images of L-MXene and S-MXene reveal the difference in their lateral dimension with large sheets reaching up to 9.5 µm, whereas DLS measurement indicates an average sheet size of 1.37 µm and 337 nm respectively (Fig. 3.2.a,b). Typical values of C_{ct} for L-MXene and S-MXene dispersion are close to 40 mg mL^{-1} and 60 mg mL^{-1} respectively.

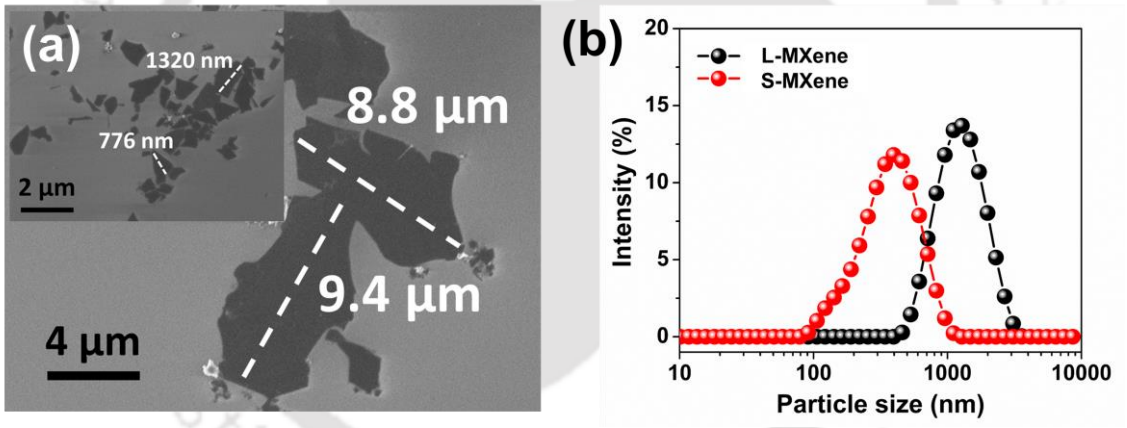

Figure 3.2. (a) FESEM images of MXene sheets showing large size difference between L-MXene and S-MXene (inset); (b) DLS measurement of large and small MXene dispersion indicating the sheet size distribution.

3.3.1. Assembly process and structural analysis:

The assembly of MXene hydrogel results from interfacial layer-by-layer reduction of MXene sheets over zinc foil as shown schematically in Fig. 3.3.a. Partial removal of oxidative functional groups from MXene basal planes, which will be discussed in the subsequent section, increases the vdW interaction among the nanosheets. However, their complete face-to-face restacking is prohibited by water molecules that remain associated with the residual functional

groups, thereby resulting in a hydrogel structure.[7] Such reduction also simultaneously generates Zn^{2+} ions over the zinc plate, which further attract negatively charged MXene sheets towards the interface helping layer-by-layer assembly. Despite the fact that MXene can assemble over zinc foil from low-density dispersion,[45] freestanding hydrogel can only be

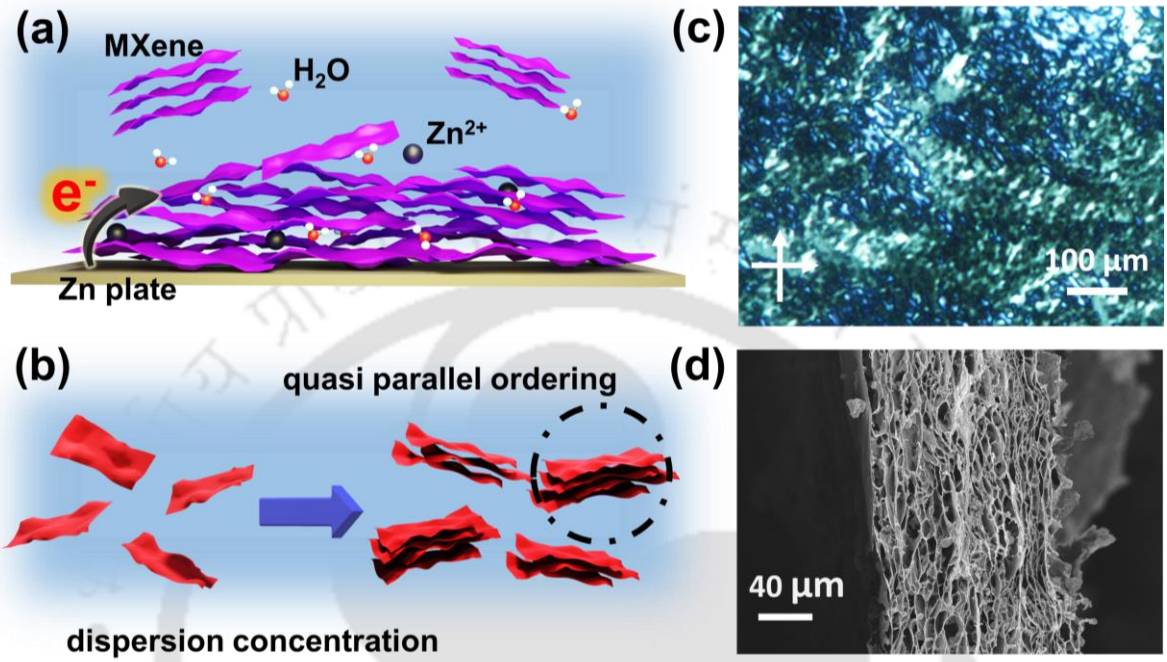

Figure 3.3. Schematic illustrations of (a) MXene self-assembly over zinc plate, (b) increasing orderness of MXene sheets with increasing dispersion concentration; (c) POM image of aqueous L-MXene dispersion (40 mg mL^{-1}) showing the liquid crystalline nematic phase formation; (d) cross sectional FESEM image of freeze-dried hydrogel.

achieved through maximizing the inter-sheet interactions. Increasing the dispersion density of MXene can lead to an assembly having lesser inter-sheet separation (d) and hence larger vdW interaction as this energy varies $\propto {}^{L}/_{d^{9/2}}$ in similar 2D systems of graphene, where L and d correspond to length of graphene sheet and inter-sheet distance respectively.[51] In addition to stronger vdW interaction, structural stability also results from long range ordering of MXene sheets within hydrogel that arises from spontaneous ordering of sheets in the concentrated dispersions (Fig. 3.3.b). MXene, similar to any other 2D nanomaterial, is anisotropic in nature and shows spontaneous liquid crystalline order in its dispersed state above a critical concentration to maximize configurational entropy.[52] Domains of liquid crystalline nematic phase are evident from polarized optical microscopy (POM) image of MXene dispersion (40 mg ml^{-1} of L-MXene), which confirms such ordering of MXene sheets in its dispersed state at

high concentrations (Fig. 3.3.c). The measured higher C_{ct} value for S-MXene dispersion is associated with their lesser vdW interaction, as it is directly proportional to the sheet size. Thus, high compactness can be achieved by increasing the dispersion density to get freestanding hydrogel.

The structural information of the hydrogel was probed by freeze drying the sample and making the corresponding aerogel structure. FESEM image of the aerogel shows its highly porous structure having quasi-oriented alignment of the sheets (Fig. 3.3.d). Such structure is markedly different from previously reported 2D and 3D hydrogels which generally show random cross linking of sheets.[42,46] The freeze-dried hydrogel comprises of pores of different dimensions ranging from submicron to few tens of microns. These porous networks are expected to be highly beneficial for electrochemical energy storage applications as it can allow efficient diffusion of electrolyte ions through the bulk of the hydrogels for easy access of MXene basal planes. Elemental mapping across the hydrogel cross-section with EDS shows uniform distribution of MXene constituent elements like carbon, titanium and oxygen, thus confirming regular distribution of MXene throughout the hydrogel structure (Fig. 3.4.a). In addition, negligible EDS count of Zn verifies the successful washing of the same and its absence in the hydrogel network.

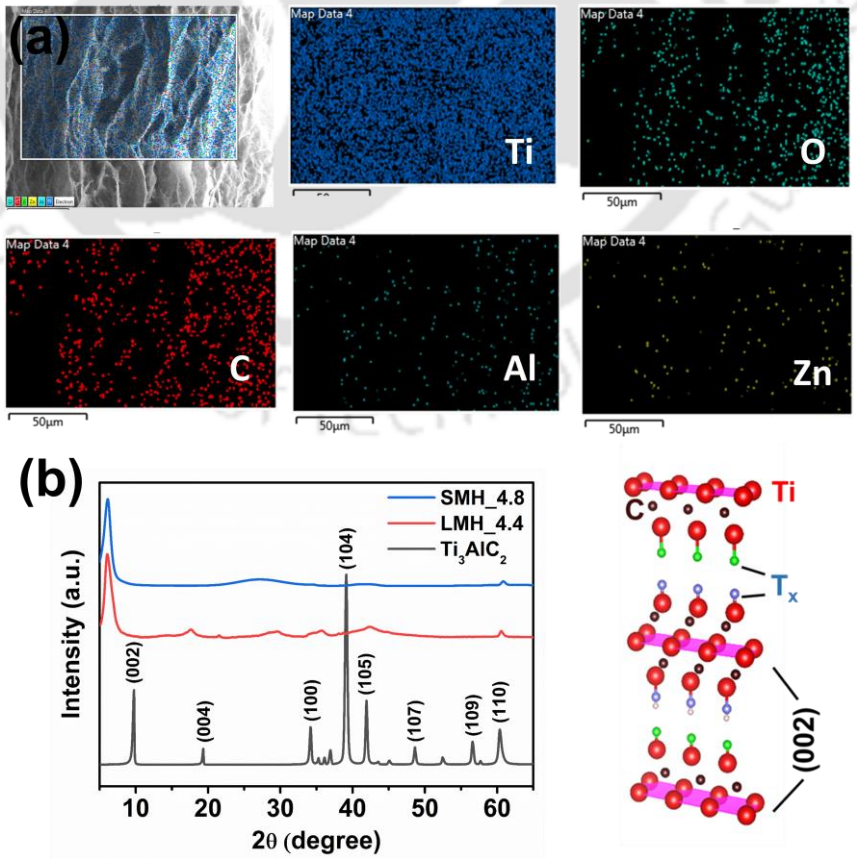

Figure 3.4. (a) Cross sectional FESEM EDS spectra of freeze-dried MXene hydrogel with mapping of different elements over the hydrogel cross section and the corresponding mapping of individual elements over the structure; (b) XRD pattern of aerogels corresponding to MXene hydrogels developed with dispersion of large and small sheet sizes and its comparison with parent MAX phase Ti_3AlC_2. Side panel showing the increased interlayer spacing due to functionalization.

Crystalline structure of the hydrogels was analyzed with X-ray diffraction studies on corresponding aerogel samples. As shown in Fig. 3.4.b, the (002) diffraction peak occurs around similar position for large MXene sheet hydrogel with areal mass loading of 4.4 mg cm^{-2} (LMH_4.4, at 6.1º) and small MXene hydrogel with areal loading 4.8 mg cm^{-2} (SMH_4.8, at 6.2º). This corresponds to an interlayer distance of 1.45 nm and 1.42 nm for LMH_4.4 and SMH_4.8 respectively. However, for MAX phase Ti_3AlC_2, it occurs around 9.76 º, indicating a smaller interlayer separation of 0.91 nm. The large shift in 2θ value of (002) peaks in the aerogel samples is associated with increased interlayer spacing after etching of Al from MAX phase and subsequent functionalization in the basal planes of MXene sheet. Such functionalization increases the interlayer spacing between subsequent MXene flakes as shown in the side panel of Fig. 3.4.b. Furthermore, the characteristic peaks for Ti_3AlC_2 around 40º vanishes in the aerogel sample, which indicates removal of Al from parent MAX phase in the acid etching process. During self-assembly, functional groups over MXene basal planes are partially reduced while interlayer water molecules in hydrogel prohibit the complete restacking of MXene sheets and thereby maintain the increased interlayer spacing and a porous structure as observed in FESEM image.

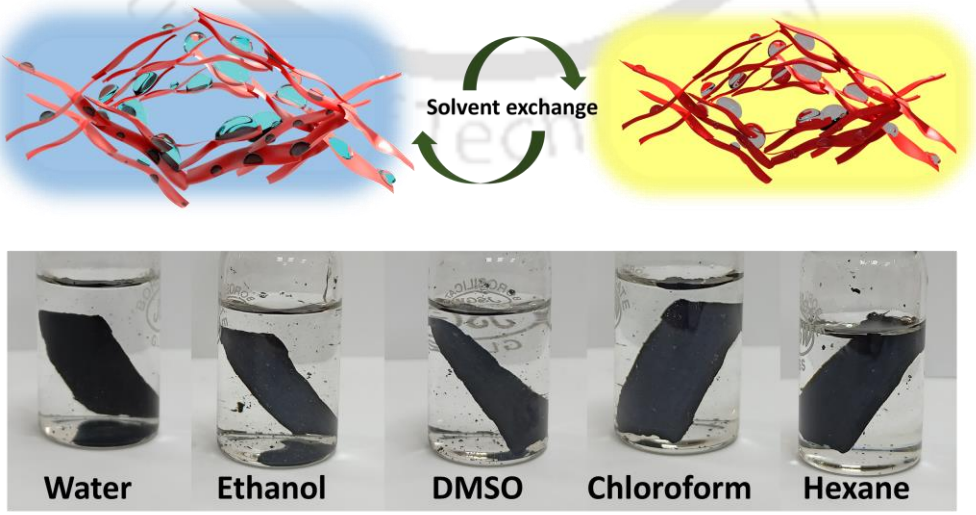

Figure 3.5. Facile solvent exchange in MXene hydrogels for the development of possible solvated MXene framework (SMF).

Freestanding MXene hydrogels can easily leap into an even broader spectrum of materials by facile solvent exchange technique to replace water with miscible organic liquids like ethanol, dimethyl formamide (DMF), dimethyl sulfoxide (DMSO) *etc*. to get a solvated MXene framework (SMF) (Fig. 3.5). Even water immiscible organic solvents like hexane and chloroform can also be introduced by taking a two-step solvent exchange route with ethanol. Such complete infiltration of solvents allows simple development of SMFs from MXene hydrogels which make them readily available to be used in lithium ion batteries, biosensors, wastewater treatment *etc*. Therefore, solvated MXene frameworks can emerge as a versatile one-stop solution for various research problems extending the importance of freestanding MXene hydrogels beyond its application domain.

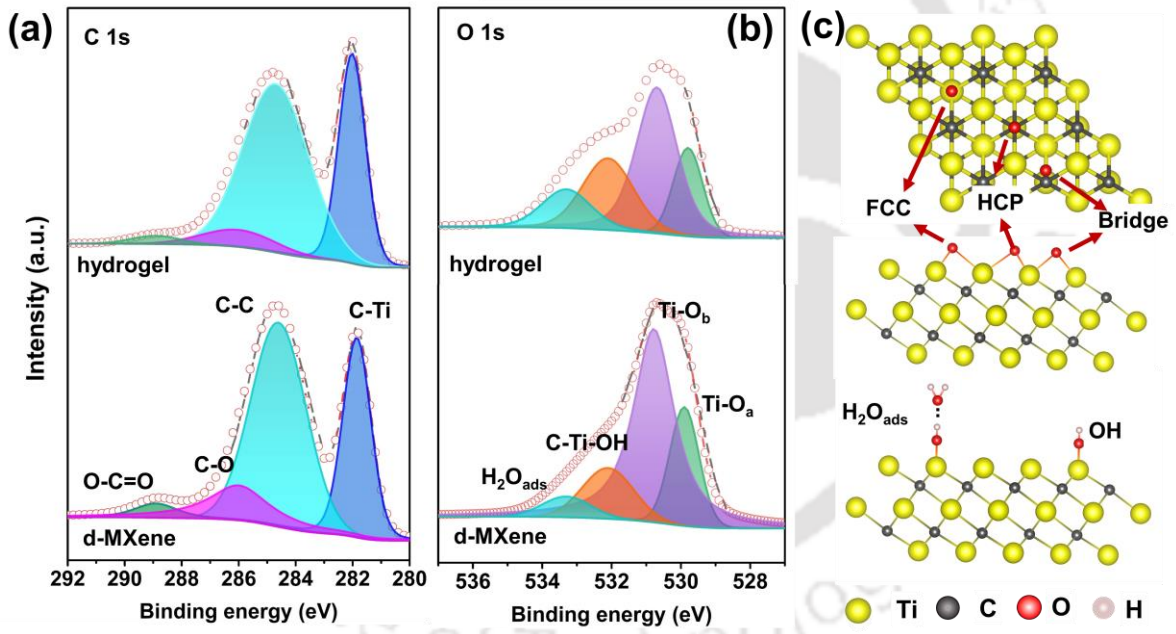

Figure 3.6. Chemical compositional analysis of MXene hydrogels with XPS: high resolution XPS spectrum of (a) C1s and (b) O1s for freestanding MXene hydrogel and d-MXene; (c) top view and side view of different $Ti_3C_2T_x$ terminations used in corresponding XPS analysis.

3.3.3. XPS analysis of MXene hydrogels:

To investigate the effect of gelation in chemical modification of MXene, XPS study was performed with freeze-dried MXene hydrogel and similarly dried delaminated MXene dispersion (d-MXene). In comparison to d-MXene, the increased atomic ratio of C/O (from

1.54 to 1.74) and Ti/O (from 0.95 to 1.10) for hydrogels indicate the considerable removal of oxygen containing functional groups during gelation. To further investigate the nature of these functional groups and change in their relative content on gelation, the high resolution C1s and O1s spectra were analyzed. Both the C1s spectra of MXene before and after gelation can be fitted with four components. The peak at 281.85 eV is related to C–Ti, whereas peaks related to C–C, C-O and O–C=O appear at 284.8 eV, 286 eV and 288.9 eV respectively.[53,54] A significant reduction in C-O and O–C=O related peak intensities were observed in MXene hydrogels as compared to d-MXene which point towards the removal of oxygen containing functional groups on gelation (Fig. 3.6.a). The weakening of C–C related peak also resulted from the removal of C–OH from the 2D sheets of MXene.[54] This de-functionalization is also evident from the high resolution O1s spectra as shown in Fig. 3.6.b. The deconvoluted O1s peak consists of four components.[46] The Ti–O_a (529.9 eV) and Ti–O_b (530.8 eV) represent oxygen terminations positioned at a bridge site and FCC or HCP site respectively as shown in Fig. 3.6.c.[55] For hydrogels, both the peaks due to oxygen groups at bridge and FCC/HCP site decrease and successively convert into C–Ti–OH terminations, which is reflected through the relative increase of the corresponding peak in hydrogel O1s spectrum. Thus, both the C1s and O1s spectra confirm the reduction of MXene to remove oxygen containing functional groups during self-assembly and gelation of MXene hydrogels. The decrease of functional groups over the MXene surface due to gelation results from the reducing ability of Zn, which partially removes the functional groups *via* electron transfer to MXene. This partial reduction of functional groups can help MXene to come closer in its assembled structure and hence vdW interaction increases which result in a stable hydrogel structure as discussed in earlier section.

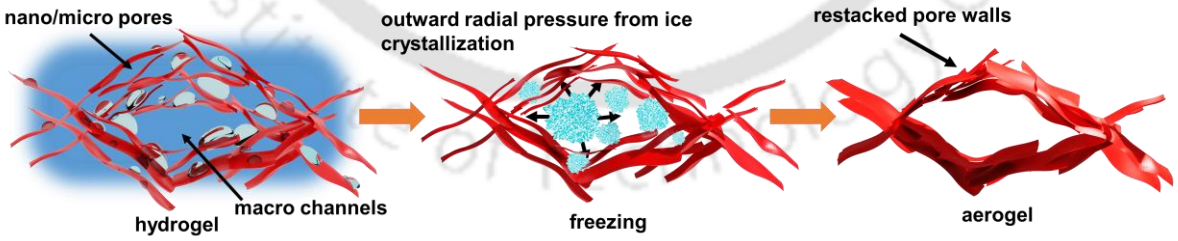

Figure 3.7. Schematic illustration of structural differences in hydrogel and freeze-dried aerogels.

3.3.4. Electrochemical analysis:

From the structural analysis, it is evident that the self-assembled MXene hydrogels possess many of the essential characteristics required for an ideal supercapacitive electrode material.

For example, the improved electrolyte accessibility due to the interconnected porous hydrated network along with excellent intrinsic conductivity and pseudocapacitive properties of MXene should synergistically lead to excellent energy storage performance. In particular, hydration of gel structures is highly important to avoid restacking of 2D sheets and hence to preserve sufficient electrolyte accessible ion channels as presented schematically in Fig. 3.7. Freeze-drying of hydrogel into aerogel structure generally leads to restacking of sheets around the pore walls and hence considerable blocking of ion channel arises. This restacking results

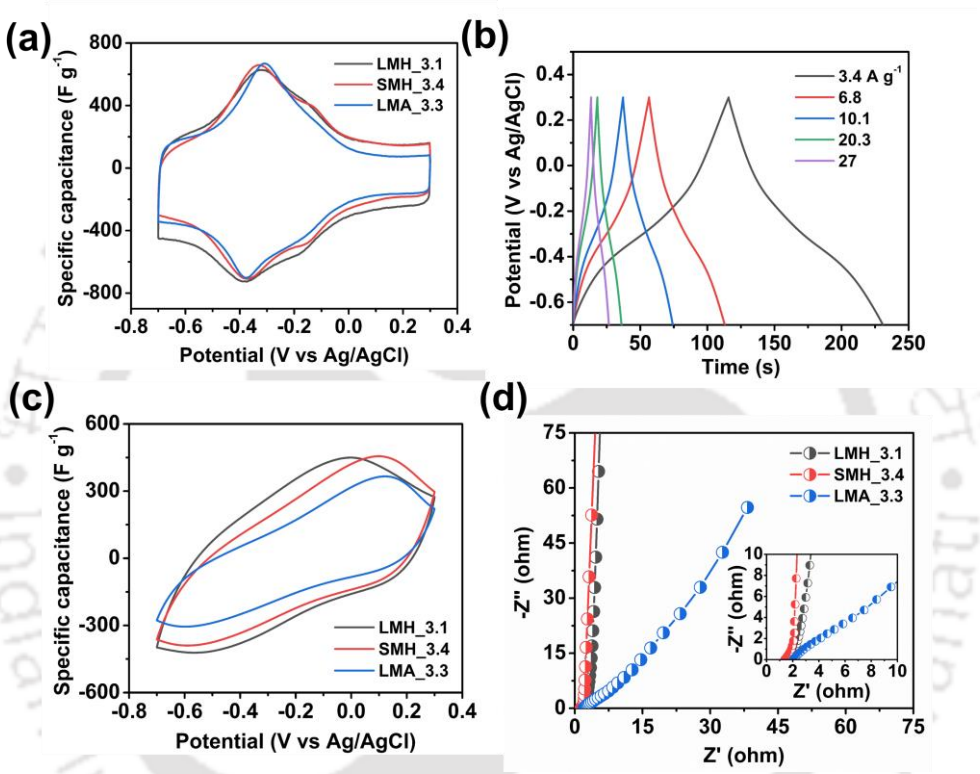

Figure 3.8. Electrochemical energy storage performance of MXene hydrogels: (a) comparison of CV curves at 10 mV s^{-1} between the MXene hydrogel and aerogel samples; (b) GCD curves of LMH_3.1 showing the slightly deviated triangular nature; (c) CV curves at 1000 mV s^{-1}; (d) comparative EIS spectra with inset showing the corresponding high frequency region.

from the outward radial pressure on sheets during rapid ice crystallization within hydrogel pores (Fig. 3.7). Freestanding MXene hydrogels were directly used as supercapacitor electrode and its performance was compared with the corresponding aerogel form to emphasize the importance of the former. Cyclic voltammograms (CV) corresponding to representative hydrogels of L-MXene (LMH_3.1) and S-MXene (SMH_3.4), electrodes that differ in sheet size but have similar areal mass loading (mg cm^{-2}), are presented in Fig. 3.8.a. Further, CV profile of the aerogel (LMA_3.3) derived from LMH is also presented in the same panel to

highlight the importance of hydrogel framework over aerogel. The characteristic pseudocapacitive redox peaks at about -0.32 V and -0.38 V (vs Ag/AgCl) are obvious in all the respective CV profiles. It is noteworthy that the area under the CV curve, and hence the specific capacitance is higher for LMH_3.1 (391 F g^{-1} at 2 mV s^{-1}) as compared to LMA_3.3 (321 F g^{-1}), which clearly demonstrates the superiority of hydrogel over aerogel form. On the other hand, sheet size of MXene also has a significant impact on capacitance, which is evident from larger specific values in LMH_3.1 (391 F g^{-1}) over SMH_3.4 (345 F g^{-1}) (Table 3.1).

Table 3.1: List of MXene hydrogel samples and their energy storage matrices calculated from CV curves at 2 mV s^{-1}.

Sample name	Mass loading (mg cm^{-2})	Gravimetric capacitance (F g^{-1})	Areal capacitance (mF cm^{-2})
LMH_3.1	3.1	391.01	1212.1
LMH_4.4	4.4	386.33	1699.85
LMH_6.9	6.9	363.05	2505.07
SMH_1.2	1.2	342.57	411.09
SMH_3.4	3.4	344.76	1168.73
SMH_4.8	4.8	340.65	1635.12
SMH_14.96	14.96	337.08	5042.81

To probe into the charge storage mechanism and rate performance, galvanostatic charge discharge (GCD) measurement for LMH_3.1 was performed at different current densities, and presented in Fig. 3.8.b. Symmetric GCD curves are slightly deviated from the usual triangular nature, which

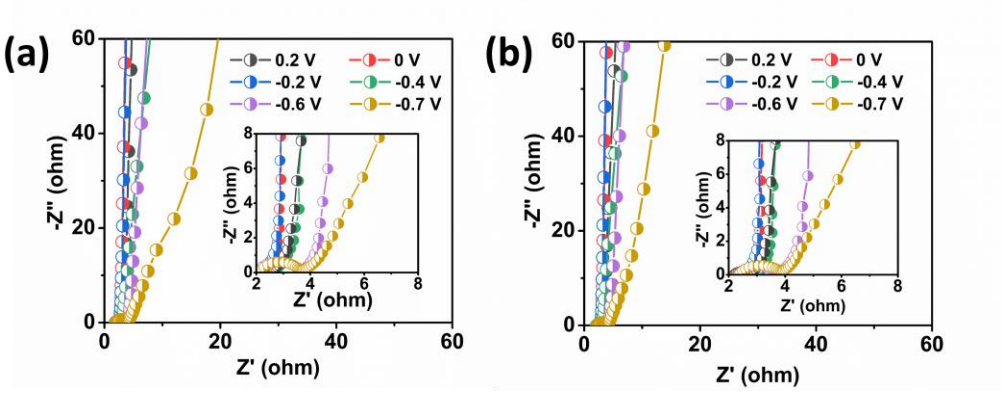

Figure 3.9. EIS spectra of hydrogels at different applied potentials for (a) LMH_3.1, (b) SMH_3.4.

confirms the pseudocapacitive charge storage mechanism of the hydrogels at all the current densities. As discussed above, lower specific capacitance of LMA_3.3 as compared to LMH_3.1 can be associated with increased restacking, and considerable blocking of ion channels during aerogel preparation by freeze-drying of corresponding hydrogel. This is especially more obvious from the CV curves of the corresponding samples at high scan rate of 1000 mV s^{-1}, where a significant reduction in area under CV curve for the aerogel electrode is apparent (Fig. 3.8.c). To validate this inference, diffusion resistance of electrolyte ions within electrode structure was estimated from low frequency knee region (Warburg region) of EIS. Near vertical rise of the EIS spectra corresponding to both LMH_3.1 and SMH_3.4 is observed compared to LMA_3.3, which has a near 45º alignment indicating easy diffusion of electrolyte ions in hydrogel electrodes compared to aerogel ones (Fig. 3.8.d). It is important to highlight that SMH_3.4 possesses better ion diffusion capabilities as compared to LMH_3.1 despite its lesser specific capacitance. This confirms that, the origin of lesser specific capacitance of the hydrogel constructed with S-MXene (SMH) is not linked with diffusion limitation, but attributable to the intrinsic size dependent characteristic of the MXene sheets. As the MXene sheets are sonicated to fragment them into smaller sizes, more and more edge sites and surface defects are introduced in MXene basal planes. This reduces the number of redox active sites participating in redox reactions, and hence the reduction in specific capacitance with decrease in MXene sheet size is observed.[56] To further understand the response of MXene hydrogels in the applied potential range of CV, we investigated the EIS spectra at different intercalation potentials. As shown in Fig. 3.9, Nyquist plots around lower intercalation potentials (0.2 V to -0.2 V) show a steep rise in imaginary capacitance, which correspond to surface capacitive or non-diffusion limited charge storage. However, as the potential is increased to more negative values, the steepness of the curve reduces and a significant increase in the 45º component is evident for EIS spectra recorded at -0.6 V and -0.7 V. Such behavior arises from the greater intercalation of protons from liquid electrolyte into the bulk of hydrogel, which contribute to the increased ion diffusion resistance as seen in both the LMH_3.1 and SMH_3.4 electrodes.[57]

Areal capacitance, which determines the energy storage capability per unit device footprint, is considered as a very important metric for practical applications. It is also recognized as a major bottleneck in the energy storage research to achieve high areal metrics without significantly compromising mass specific values and rate performance.[48] Most of the

MXene based supercapacitive electrodes use very thin material with low areal mass loading, typically below 2 mg cm^{-2}, which are far from the commercial requirement (>5 mg cm^{-2}) (Table 3.2). Just by extending the gelation period, hydrogels of different mass loadings were developed and progressively higher areal capacitances were achieved, but surprisingly with only slight decrease in mass specific performances (Table 3.1). For instance, increase of areal mass loading of LMH from 3.1 mg cm^{-2} (20 min gelation) to 6.9 mg cm^{-2} (120 min gelation) leads to the increase in areal capacitance from 1212 mF cm^{-2} to 2505 mF cm^{-2} (at 2 mV s^{-1}), but gravimetric value only decreases by 9% from 391 F g^{-1} to 363.1 F g^{-1}. Importantly, for SMH the gravimetric values, calculated from CV curves at 2 mV s^{-1}, remain nearly independent

Table 3.2. Electrochemical performance comparison of freestanding MXene hydrogels with previously reported MXene based electrodes.

Sample type	Gravimetric capacitance (F/g)	Mass loading	Rate performance	Electrolyte	Reference
$Ti_3C_2T_x$ clay	245 Fg^{-1} at 2 mV s^{-1}	-	80% @ 100 mV s^{-1}	1 M H_2SO_4	[58]
$Ti_3C_2T_x$ film	195 Fg^{-1} at 2 mV s^{-1}	0.75mg cm^{-2}	61% @ 1 V s^{-1}	LiTFSI–PC	[59]
d-Ti_3C_2 film	325 Fg^{-1} at 2 mV s^{-1}	1.3 mg cm^{-2}	42.3% @ 100 mV s^{-1}	1M H_2SO_4	[60]
Rolled MXene aerogel	315 Fg^{-1} at 10 mV s^{-1}	0.6 mg cm^{-2}	39% at 200 mV s^{-1}	3M H_2SO_4	[61]
Alkali treated $Ti_3C_2T_x$	314 Fg^{-1} at 2 mV s^{-1}	8.5 mg cm^{-2}	-	1M H_2SO_4	[62]
Cation intercalated $Ti_3C_2T_x$	130 Fg^{-1} at 2 mV s^{-1}	-	61.5% at 100	1M KOH	[63]
$Ti_3C_2T_x$-rGO film	391 Fg^{-1} at 2 mV s^{-1}	-	49 % at 1 V s^{-1}	3M H_2SO_4	[64]
rGO/$Ti_3C_2T_x$ film	335.4 Fg^{-1} at 2 mV s^{-1}	-	61% @ 1 V s^{-1}	3M H_2SO_4	[65]
$Ti_3C_2T_x$-SWCNT	134 Fg^{-1} at 2 mV s^{-1}	0.73	71.8 at 200	1M $MgSO_4$	[66]
d-Mo_2CT_x film	196 Fg^{-1} @ 2 mV s^{-1}	0.6mg cm^{-2}	61.2 at 100	1M H_2SO_4	[67]
$Ti_3C_2T_x$-PVA	167 Fg^{-1} at 2 mV s^{-1}	-	56.8 at 100	1M KOH	[37]
LMH_3.1	391 Fg^{-1} at 2 mV s^{-1}	3.1	60% at 1 V s^{-1}	3M H_2SO_4	This work
SMH_1.2	342.6 Fg^{-1} at 2 mV s^{-1}	1.2	76% at 1 V s^{-1}	3M H_2SO_4	This work
SMH_14.96	337.08 Fg^{-1} at 2 mV s^{-1}	14.96	82% at 100 mV s^{-1}	3M H_2SO_4	This work

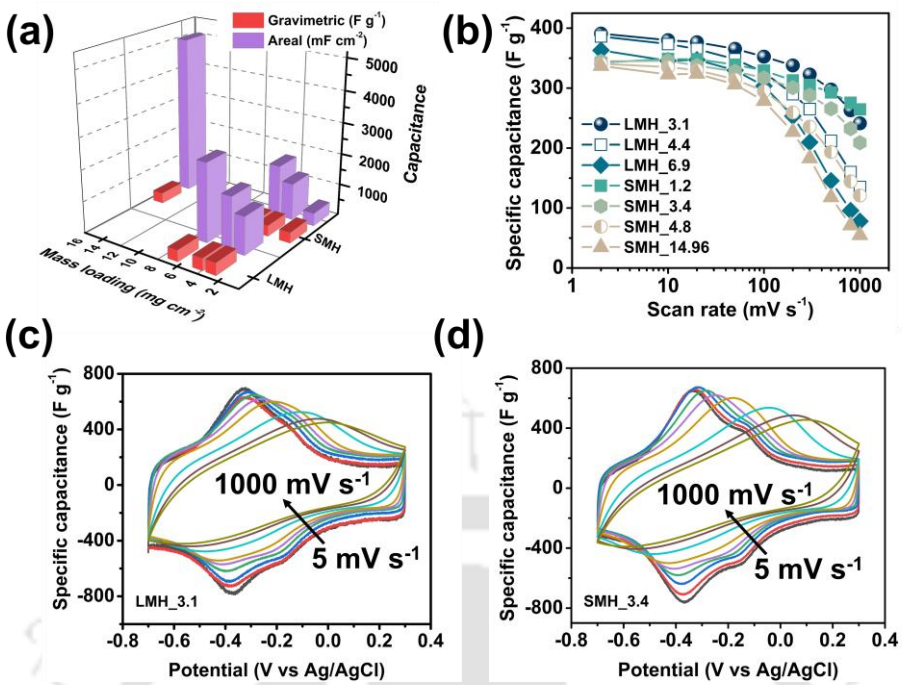

Figure 3.10. (a) gravimetric and areal capacitance of MXene hydrogels with different mass loadings; (b) specific capacitance of LMH, SMH electrodes at different scan rates; (c) CV curves of (c) LMH_3.1 and (d) SMH_3.4 electrodes at scan rates from 5 mV s^{-1} to 1000 mV s^{-1}.

of mass loading even up to very large areal loading of 14.9 mg cm^{-2} (120 min gelation time). By simply increasing the gelation time, we were able to achieve outstanding areal capacitance of 5043 mF cm^{-2} (SMH_14.96) as shown in chart (Fig. 3.10.a). Such flexibility over mass loading with simultaneous excellence in gravimetric and areal performance allows facile development of application specific electrodes suitable for modern applications.

Performance of the as-developed hydrogels was also measured at different scan rates starting from 2 mV s^{-1} to 1000 mV s^{-1} to inspect the effect of mass loading and sheet size on rate capability (Fig. 3.10.b). All the hydrogels exhibit good rate performance, which was determined by calculating the retention of specific capacitance at higher scan rates as compared to the values at 2 mV s^{-1}. It is noteworthy that SMH can show high capacity retention of 82% at 100 mV s^{-1} even with very high areal mass loading of 14.96 mg cm^{-2}. Such high retention with this much areal loading is rarely reported in MXene based supercapacitor research (Table 3.2). The excellent rate capability of all the hydrogels is obvious from the CV profiles of SMH and LMH, which retain the overall shape and characteristic redox peak profiles even at large scan rates (Fig. 3.10.c-d). Out of them, SMH_3.4 and SMH_1.2 show an excellent capacitive

retention of 61% and 76% at 1000 mV s^{-1} respectively. The better rate performance of SMH can be ascribed to the ample ion transport channels present in smaller sheet hydrogels compared to the larger sheet counterpart (LMH). Such promising rate performance of the

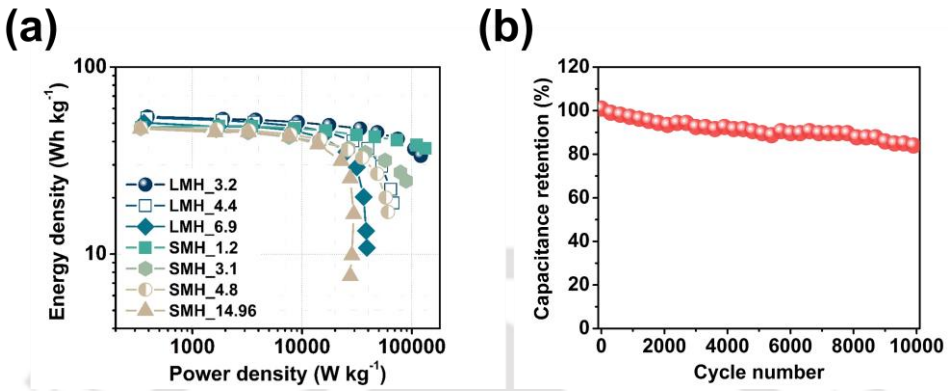

Figure 3.11. (a) Regone plot showing gravimetric energy and power densities of freestanding hydrogel electrodes; (b) stability test of LMH_3.1 over 10000 charge-discharge cycles at 5 A g^{-1}.

hydrogel electrodes allow outstanding gravimetric energy and power densities as shown in Regone plot of the hydrogel electrodes (Fig. 3.11.a). L-MXene hydrogel (LMH_3.1) can deliver 54.3 Wh kg^{-1} energy density at a power density of 391 W kg^{-1}, whereas hydrogel with S-MXene (SMH_1.2) continues to deliver 36.7 Wh kg^{-1} at an ultrahigh power density of 132.2 kW kg^{-1}, which is at par or much higher than other MXene based electrodes reported thus far.[68] To investigate the long-term operational stability, the hydrogel electrode (LMH_3.1) was repeatedly charged and discharged over 10,000 cycles at 5 A g^{-1}. The MXene hydrogel electrode showed excellent cyclic stability retaining 87% of initial performance making it a promising candidate for its commercial use (Fig. 3.11.b).

To inspect the origin of excellent charge storage properties of the hydrogels and their dependence on sheet size, detailed analysis of EIS spectra along with the current response of hydrogels as a function of scan rates were mapped with power law and Dunn model. The Nyquist plots show a nearly vertical rise of EIS spectra parallel to the imaginary axis, which indicates easy diffusion of electrolyte ions through the electrodes (Fig. 3.12.a). The real part of impedance (Z') as a function of frequency (ω) follows the equation $Z' = R_e + R_{ct} + \sigma\omega^{-\frac{1}{2}}$, where σ is the Warburg factor, and the R_e and R_{ct} are the equivalent series resistance and charge transfer resistance respectively.[69] Value of σ, estimated from the slope in plot between

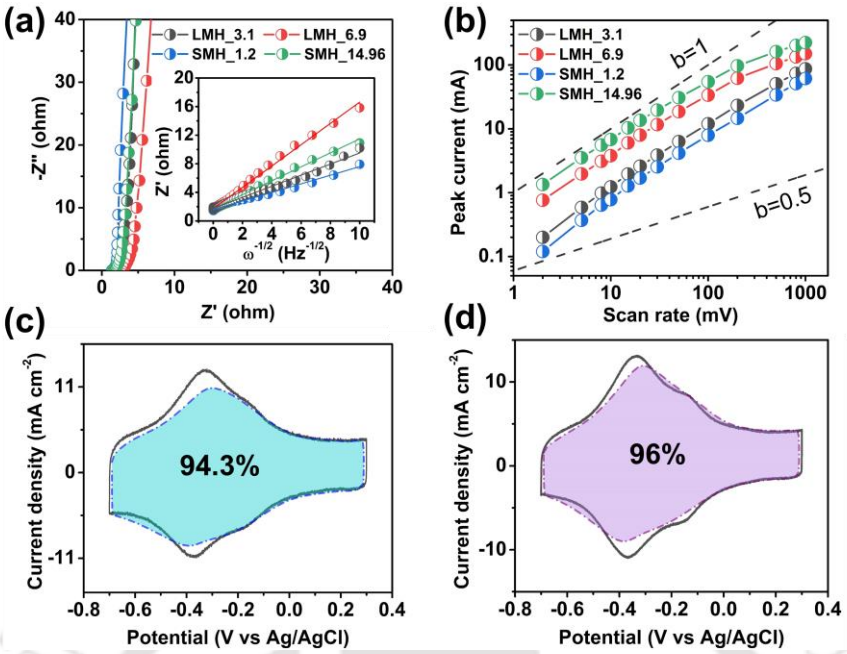

Figure 3.12. Energy storage mechanism analysis of MXene hydrogels: (a) Comparative EIS spectra between different LMH and SMH electrodes with inset showing the variation of Z´ with $\omega^{-1/2}$; (b) logarithmic plot of peak current and scan rates for LMH and SMH electrodes indicating the charge storage behavior of the corresponding electrodes; quantification of surface and diffusion limited contribution in charge storage for (c) LMH_3.1 and (d) SMH_3.4 at 5 mV s^{-1}.

Z' and $\omega^{-\frac{1}{2}}$, gives valuable information about the diffusion process, and larger the value of σ higher is the resistance offered by capacitive electrodes to ionic diffusion. From the inset of Fig. 3.12.a, it is evident that the slopes are low for all the hydrogels, especially for the electrodes with S-MXene. These plots excellently support that hydrogels offer very less resistance to diffusion of electrolyte ions, and diffusion is more favourable in S-MXene hydrogels (SMH) over L-MXene counterparts (LMH), which again reflects their overall better rate capability.

Further, to understand the kinetics of charge storage in MXene hydrogel electrodes, peak current of the CV cycles as a function of scan rate was fitted with well-known power law,

$$i = av^b \tag{5}$$

with a and b being variables. While, $b = 1$ corresponds to a fast surface controlled current, for diffusion limited processes, the current usually depends on the square root of scan rate, i.e. $b = 0.5$. The value of b was determined from the $\log(i)$ vs. $\log(v)$ plot, and all the values are close

to 1, which indicates that hydrogels store charge dominantly *via* surface controlled process. [70] Typically, the samples with lower mass loading exhibits value that are close to 1 for SMH_1.2 ($b = 1$) and LMH_3.1 ($b = 0.98$) (Fig. 3.12.b), due to easy ionic diffusion in thin electrodes and high accessibility of MXene surface by electrolyte ions. Importantly, the samples with higher mass loadings still maintain surface controlled behavior following , $b = 1$ upto 100 mV s^{-1}, which highlights the importance of the hydrogel structure that allows excellent surface accessibility even with thick electrodes. For detailed quantification of surface capacitive and diffusion limited fractional contributions, currents as a function of scan rates at each potential value is fitted with modified power law

$$i(V) = k_1 v + k_2 v^{\frac{1}{2}} \quad (6)$$

Where, $k_1 v$ and $k_2 v^{1/2}$ correspond to the capacitive and diffusion limited contributions respectively.[71] Through determination of k_1 and k_2 following Dunn model, the two different contributions were estimated for the MXene hydrogel electrodes. LMH_3.1 and SMH_3.4, having comparable mass loading, but of different sheet sizes were chosen as the representative samples for the analysis through the Dunn model. As shown in Fig. 3.12.c, the capacitive contribution was calculated to be 94.3% for LMH_3.1 hydrogel at 5 mV s^{-1} whereas for smaller SMH_3.4 it reached up to 96% (Fig. 3.12.d). Such a large capacitive contribution is much higher than the previous reports of MXene based supercapacitors (Table 3.3). Such excellent storage kinetics explains the sustained rate capabilities of MXene hydrogels benefitting from the hydrated ion accessible MXene basal planes in the hydrogel network.

Table 3.3: Comparison of surface capacitive contribution in MXene based electrodes:

Sample	Surface capacitive contribution	Reference
$Ti_3C_2T_x$ aerogel	60.1% at 2 mV s^{-1}	[72]
Pristine $Ti_3C_2T_x$	87.2% at 10 mV s^{-1}	[73]
N doped $Ti_3C_2T_x$ film	65.5% at 10 mV s^{-1}	[73]
MXene/PANI film electrodes	82% at 2 mV s^{-1}	[74]
Large sheet $Ti_3C_2T_x$ films	66.5% at 5 mV s^{-1}	[68]
Small sheet etched $Ti_3C_2T_x$ films	90.5% at 5 mV s^{-1}	[68]

LMH_3.3	94.3% at 5 mV s^{-1}	This work
SMH_3.1	96% at 5 mV s^{-1}	This work

Besides the excellent gravimetric and areal performance, high volumetric energy storage is often considered as an important performance metric, particularly for compact portable devices. Compacting electrodes to get high volumetric values generally lead to severe blockage of ion transport channels resulting in poor rate capabilities, and the situation becomes more challenging with increase of areal mass loading due to the problem of ion diffusion within thick and compact electrodes. Here, to demonstrate the possibility of constructing high performance volumetric electrodes from MXene hydrogels, electrolyte protected compression method was employed.[75] This process can give rise to compact hydrated electrodes, which are expected to offer excellent volumetric capacitance retaining good rate capability. To validate this proposal, MXene hydrogel electrode was infiltrated with H_2SO_4 electrolyte (see experimental section) and was subsequently mechanically compressed with 10 MPa pressure to obtain highly compact MXene hydrogel electrode (SCMH) with high density (3.6 g cm^{-3}) as shown in Fig. 3.13.a. The volumetric capacitance of the SCMH_3.6 is 1101.6 F cm^{-3} at 2 mV s^{-1} as calculated from the CV curves (Fig. 3.13.b). With the increase of scan rates, SCMH electrode display outstanding capacity retention capability as high as 73% at 1000 mV s^{-1}, which is clearly evident from the excellent shape retention of CV curves at high scan rates. In electrolyte assisted compression, as originally proposed by Dan Li *et al.* for graphene, the large electrolyte ions get trapped in the intermediate MXene sheets which effectively maintain the ion transporting channels even after compacting.[75] Thus, the benefit of hydrogel structure like high surface accessibility can still be accessed in the compact electrode due to these ion channels, which gives rise to high volumetric value with excellent rate performance. EIS spectra of the compressed electrode also indicate low ion diffusion and ESR values for SCMH_3.6 electrode due to the reasons discussed above (Fig. 3.13.c). This is also supported by the low slope in the Warburg impedance analysis between Z' and $\omega^{-\frac{1}{2}}$ confirming better ion diffusion in electrolyte protected compressed structure (Fig. 3.13.c inset). The large volumetric value with such a high capacity retention is better than most of the reports on MXene electrodes having similar mass loading, and comparable to best values reported till date (Fig. 3.13.d).[66,76–79] Thus, the outstanding performance of these MXene hydrogels in all the three aspects of

energy storage highlights its ability for each application specific development. Paired with excellent

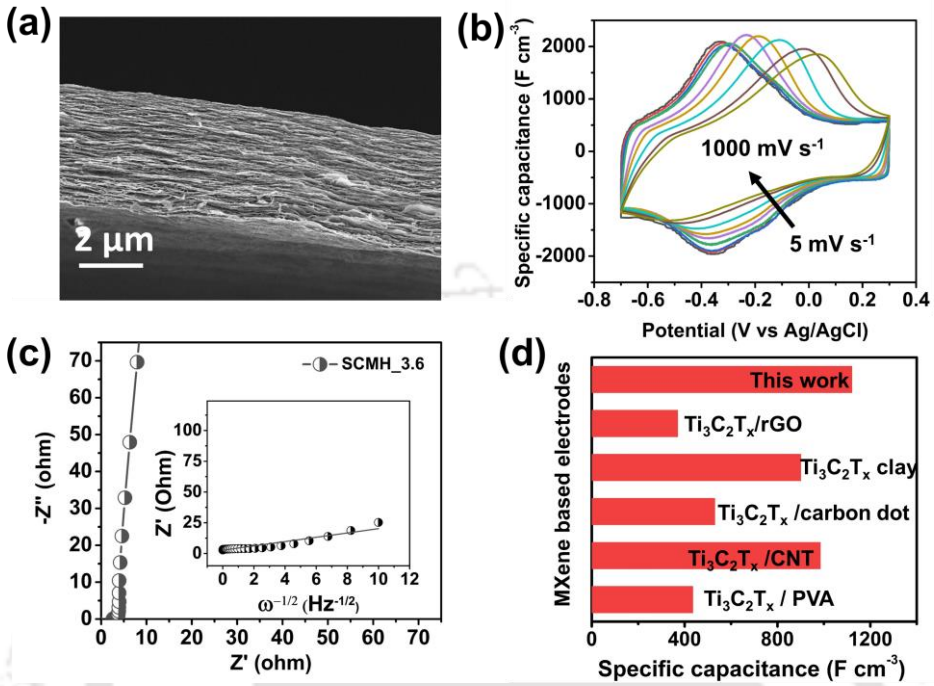

Figure 3.13. Volumetric performance of compact MXene hydrogel electrodes developed via electrolyte assisted compression: (a) cross-sectional FESEM image of compressed SCMH_3.6 electrode; (b) CV curves at different scan rates between 5 mV s^{-1} to 1000 mV s^{-1}; (c) corresponding EIS spectra with inset showing the variation of Z´ with $\omega^{-1/2}$; (d) Comparison of volumetric capacitance of SCMH_3.6 electrode with other MXene based electrodes at 2 mV s^{-1}.

rate performance, and energy and power densities, these MXene hydrogels are the potential candidates for future energy storage solutions.

3.4. Conclusions

In summary, self-standing hydrogels of pristine MXene have been developed over Zn metal plate *via* auto-assembly of nanosheets without using any additional gelator or binder. Transition from a dispersed state to freestanding hydrogel structure happened only above a critical dispersion concentration of the MXene nanosheets used for the assembly, and it was shown to be 40 mg mL^{-1} and 60 mg mL^{-1} for an average sheet size of 1.37 µm and 337 nm respectively. Owing to its intrinsic hydrated structure having porous network of sheets, MXene hydrogels display excellent gravimetric charge storage metrics, which are much better than the commonly

developed dried aerogel form, signifying the potential of the former. Gravimetric capacitance as high as 391 F g^{-1} and 343 F g^{-1} (at 2 mV s^{-1}) were achieved with hydrogels of L-MXene and S-MXene respectively, and the later show superior rate performance retaining 76% capacitance even at 1000 mV s^{-1}. By developing hydrogels of commercially demanding mass loadings (up to 14.9 mg cm^{-2}), very high areal capacitance of 5043 mF cm^{-2} was realized without sacrificing the gravimetric performance. Further, electrolyte intercalated compact hydrogel structure allowed to attain a high volumetric capacitance of 1120 F cm^{-3} at a scan rate of 2 mV s^{-1} with excellent rate performance of 73% at 1000 mV s^{-1}. With detailed analysis of the pseudo-capacitive energy storage, it was found that the current contribution is highly dominated by the surface capacitive effect (>92%) rather than intercalation type diffusion limited process, which signifies the highly efficient surface accessibility by electrolyte ions within hydrogel structures. Learning a lesson from analogous graphene hydrogel, this research can open up enormous applications ranging from energy storage, catalysis, capacitive deionization, cell growth scaffold and electro-tunable ion sieving membrane and so on.

References

1. Ahmed, E. M. Hydrogel: Preparation, characterization, and applications: A review. *J. Adv. Res.* **6**, 105–121 (2015).
2. Mahinroosta, M., Jomeh Farsangi, Z., Allahverdi, A. & Shakoori, Z. Hydrogels as intelligent materials: A brief review of synthesis, properties and applications. *Mater. Today Chem.* **8**, 42–55 (2018).
3. Yi, J., Choe, G., Park, J. & Lee, J. Y. Graphene oxide-incorporated hydrogels for biomedical applications. *Polym. J. 2020 528* **52**, 823–837 (2020).
4. Ajayan, P., Kim, P. & Banerjee, K. Two-dimensional van der Waals materials. *Phys. Today* **69**, 38 (2016).
5. Li, B. *et al.* Probing van der Waals interactions at two-dimensional heterointerfaces. *Nat. Nanotechnol. 2019 146* **14**, 567–572 (2019).
6. Xu, Y., Sheng, K., Li, C. & Shi, G. Self-Assembled Graphene Hydrogel via a One-Step Hydrothermal Process. *ACS Nano* **4**, 4324–4330 (2010).
7. Maiti, U. N., Lim, J., Lee, K. E., Lee, W. J. & Kim, S. O. Three-dimensional shape engineered, interfacial gelation of reduced graphene oxide for high rate, large capacity supercapacitors. *Adv. Mater.* **26**, 615–619 (2014).
8. Qiaomei Luo, Yangyang Shan, Xia Zuo & Jiaqi Liu. Anisotropic tough poly(vinyl alcohol)/graphene oxide nanocomposite hydrogels for potential biomedical applications. *RSC Adv.* **8**, 13284–13291 (2018).
9. Xu, D. *et al.* High-rate aqueous zinc-ion batteries enabled by a polymer/graphene composite cathode involving reversible electrolyte anion doping/dedoping. *J. Mater. Chem. A* **9**, 10666–10671 (2021).
10. Zhang, J. *et al.* 3D free-standing nitrogen-doped reduced graphene oxide aerogel as anode material for sodium ion batteries with enhanced sodium storage. *Sci. Reports 2017 71* **7**, 1–7 (2017).
11. Sikdar, A. *et al.* Ultra-large area graphene hybrid hydrogel for customized performance supercapacitors: High volumetric, areal energy density and potential wearability. *Electrochim. Acta* **332**, 135492 (2020).
12. Chen, S., Duan, J., Jaroniec, M. & Qiao, S. Z. Three-Dimensional N-Doped Graphene Hydrogel/NiCo Double Hydroxide Electrocatalysts for Highly Efficient Oxygen Evolution. *Angew. Chemie Int. Ed.* **52**, 13567–13570 (2013).
13. Chen, S., Duan, J., Tang, Y., Jin, B. & Zhang Qiao, S. Molybdenum sulfide clusters-nitrogen-doped graphene hybrid hydrogel film as an efficient three-dimensional hydrogen evolution electrocatalyst. *Nano Energy* **11**, 11–18 (2015).
14. Sikdar, A. *et al.* Diffusion driven nanostructuring of metal–organic frameworks (MOFs) for graphene hydrogel based tunable heterostructures: highly active electrocatalysts for efficient water oxidation. *J. Mater. Chem. A* **9**, 7640–7649 (2021).
15. Song, H. S., Kwon, O. S., Kim, J. H., Conde, J. & Artzi, N. 3D hydrogel scaffold doped with 2D graphene materials for biosensors and bioelectronics. *Biosens. Bioelectron.* **89**, 187–200 (2017).

16. L. Burrs, S. *et al.* A comparative study of graphene–hydrogel hybrid bionanocomposites for biosensing. *Analyst* **140**, 1466–1476 (2015).

17. Naguib, M. *et al.* Two-dimensional nanocrystals produced by exfoliation of Ti 3AlC 2. *Adv. Mater.* **23**, 4248–4253 (2011).

18. Mashtalir, O. *et al.* Intercalation and delamination of layered carbides and carbonitrides. *Nat. Commun.* **4**, 1716 (2013).

19. Naguib, M. *et al.* Two-Dimensional Transition Metal Carbides. *ACS Nano* **6**, 1322–1331 (2012).

20. Naguib, M. *et al.* New Two-Dimensional Niobium and Vanadium Carbides as Promising Materials for Li-Ion Batteries. *J. Am. Chem. Soc.* **135**, 15966–15969 (2013).

21. Hart, J. L. *et al.* Control of MXenes' electronic properties through termination and intercalation. *Nat. Commun.* **10**, 522 (2019).

22. Hantanasirisakul, K. & Gogotsi, Y. Electronic and Optical Properties of 2D Transition Metal Carbides and Nitrides (MXenes). *Adv. Mater.* **30**, 1804779 (2018).

23. Li, L. Lattice dynamics and electronic structures of Ti3C2O2 and Mo2TiC2O2 (MXenes): The effect of Mo substitution. *Comput. Mater. Sci.* **124**, 8–14 (2016).

24. Anasori, B., Lukatskaya, M. R. & Gogotsi, Y. 2D metal carbides and nitrides (MXenes) for energy storage. *Nature Reviews Materials* vol. 2 16098 (2017).

25. Dutta, P. *et al.* Graphene aided gelation of MXene with oxidation protected surface for supercapacitor electrodes with excellent gravimetric performance. *Carbon N. Y.* **169**, 225–234 (2020).

26. Yang, Q. *et al.* Recent Progress of MXene-Based Nanomaterials in Flexible Energy Storage and Electronic Devices. *Energy Environ. Mater.* **1**, 183–195 (2018).

27. Luo, J., Matios, E., Wang, H., Tao, X. & Li, W. Interfacial structure design of MXene-based nanomaterials for electrochemical energy storage and conversion. *InfoMat* **2**, 1057–1076 (2020).

28. Luo, J. *et al.* Tunable MXene-Derived 1D/2D Hybrid Nanoarchitectures as a Stable Matrix for Dendrite-Free and Ultrahigh Capacity Sodium Metal Anode. *Nano Lett.* **20**, 7700–7708 (2020).

29. Luo, J. *et al.* Atomic Sulfur Covalently Engineered Interlayers of Ti_3C_2 MXene for Ultra-Fast Sodium-Ion Storage by Enhanced Pseudocapacitance. *Adv. Funct. Mater.* **29**, 1808107 (2019).

30. Luo, J. *et al.* Pillared MXene with Ultralarge Interlayer Spacing as a Stable Matrix for High Performance Sodium Metal Anodes. *Adv. Funct. Mater.* **29**, 1805946 (2019).

31. Jianmin Luo *et al.* Tunable pseudocapacitance storage of MXene by cation pillaring for high performance sodium-ion capacitors. *J. Mater. Chem. A* **6**, 7794–7806 (2018).

32. Shahzad, F. *et al.* Electromagnetic interference shielding with 2D transition metal carbides (MXenes). *Science (80-.).* **353**, 1137–1140 (2016).

33. Kim, S. J. *et al.* Metallic Ti3C2Tx MXene Gas Sensors with Ultrahigh Signal-to-Noise Ratio. *ACS Nano* **12**, 986–993 (2018).

34. Zhang, Y.-Z. *et al.* MXenes stretch hydrogel sensor performance to new limits. *Sci. Adv.* **4**, eaat0098 (2018).

35. Guo, L. *et al.* Ar plasma modification of 2D MXene Ti3C2Tx nanosheets for efficient capacitive desalination. *FlatChem* **8**, 17–24 (2018).

36. Lipatov, A. *et al.* Elastic properties of 2D Ti3C2Tx MXene monolayers and bilayers. *Sci. Adv.* **4**, eaat0491 (2018).

37. Ling, Z. *et al.* Flexible and conductive MXene films and nanocomposites with high capacitance. *Proc. Natl. Acad. Sci.* **111**, 16676–16681 (2014).

38. Orangi, J. *et al.* Conductive and highly compressible MXene aerogels with ordered microstructures as high-capacity electrodes for Li-ion capacitors. *Mater. Today Adv.* **9**, 100135 (2021).

39. Bian, R. *et al.* Ultralight MXene-based aerogels with high electromagnetic interference shielding performance. *J. Mater. Chem. C* **7**, 474–478 (2019).

40. Boota, M. & Gogotsi, Y. MXene—Conducting Polymer Asymmetric Pseudocapacitors. *Adv. Energy Mater.* **9**, 1802917 (2019).

41. Sikdar, A. *et al.* Spontaneous three-dimensional self-assembly of MXene and graphene for impressive energy and rate performance pseudocapacitors. *Electrochim. Acta* **391**, 138959 (2021).

42. Deng, Y. *et al.* Fast Gelation of Ti3C2Tx MXene Initiated by Metal Ions. *Adv. Mater.* **31**, 1902432 (2019).

43. Chen, H. *et al.* Pristine Titanium Carbide MXene Hydrogel Matrix. *ACS Nano* **14**, 10471–10479 (2020).

44. Xu, Y. *et al.* Solvated graphene frameworks as high-performance anodes for lithium-ion batteries. *Angew. Chemie - Int. Ed.* **54**, 5345–5350 (2015).

45. Zhao, Z., Wang, S., Wan, F., Tie, Z. & Niu, Z. Scalable 3D Self-Assembly of MXene Films for Flexible Sandwich and Microsized Supercapacitors. *Adv. Funct. Mater.* **31**, 2101302 (2021).

46. Yun, T. *et al.* Multidimensional Ti 3 C 2 T x MXene Architectures via Interfacial Electrochemical Self-Assembly. *ACS Nano* **15**, 10058–10066 (2021).

47. Stoller, M. D. & Ruoff, R. S. Best practice methods for determining an electrode material's performance for ultracapacitors. *Energy and Environmental Science* vol. 3 1294–1301 (2010).

48. Gogotsi, Y. & Simon, P. True Performance Metrics in Electrochemical Energy Storage. *Science (80-.).* **334**, 917–918 (2011).

49. Alhabeb, M. *et al.* Guidelines for Synthesis and Processing of Two-Dimensional Titanium Carbide (Ti3C2Tx MXene). *Chem. Mater.* **29**, 7633–7644 (2017).

50. Lin, Z. *et al.* Highly Stable 3D Ti3C2Tx MXene-Based Foam Architectures toward High-Performance Terahertz Radiation Shielding. *ACS Nano* **14**, 2109–2117 (2020).

51. Kumar, S., Rama, P. & Panwar, A. S. Scaling relations for the interactions between curved graphene sheets in water. *Phys. Chem. Chem. Phys.* **19**, 30217–30226 (2017).

52. Zhang, J. *et al.* Additive-Free MXene Liquid Crystals and Fibers. *ACS Cent. Sci.* **6**, 254–265 (2020).

53. Liu, J. *et al.* Hydrophobic, Flexible, and Lightweight MXene Foams for High-Performance Electromagnetic-Interference Shielding. *Adv. Mater.* **29**, 1702367 (2017).

54. Zhang, N. *et al.* Direct Self-Assembly of MXene on Zn Anodes for Dendrite-Free Aqueous Zinc-Ion Batteries. *Angew. Chemie Int. Ed.* **60**, 2861–2865 (2021).

55. Schultz, T. *et al.* Surface Termination Dependent Work Function and Electronic Properties of Ti3C2Tx MXene. *Chem. Mater.* **31**, 6590–6597 (2019).

56. Kayali, E., VahidMohammadi, A., Orangi, J. & Beidaghi, M. Controlling the Dimensions of 2D MXenes for Ultrahigh-Rate Pseudocapacitive Energy Storage. *ACS Appl. Mater. Interfaces* **10**, 25949–25954 (2018).

57. Lukatskaya, M. R. *et al.* Ultra-high-rate pseudocapacitive energy storage in two-dimensional transition metal carbides. *Nat. Energy* **2**, 17105 (2017).

58. Ghidiu, M., Lukatskaya, M. R., Zhao, M.-Q., Gogotsi, Y. & Barsoum, M. W. Conductive two-dimensional titanium carbide 'clay' with high volumetric capacitance. *Nature* **516**, (2014).

59. Wang, X. *et al.* Influences from solvents on charge storage in titanium carbide MXenes. *Nat. Energy* doi:10.1038/s41560-019-0339-9.

60. Dall'Agnese, Y. *et al.* High capacitance of surface-modified 2D titanium carbide in acidic electrolyte. *Electrochem. commun.* **48**, 118–122 (2014).

61. Bayram, V. *et al.* MXene Tunable Lamellae Architectures for Supercapacitor Electrodes. *ACS Appl. Energy Mater.* **3**, 411–422 (2019).

62. Li, T. *et al.* Two-Dimensional Materials Fluorine-Free Synthesis of High-Purity Ti 3 C 2 T x (T = OH, O) via Alkali Treatment. doi:10.1002/ange.201800887.

63. Lukatskaya, M. R. *et al.* Cation Intercalation and High Volumetric Capacitance of Two-Dimensional Titanium Carbide. *Science (80-.).* **341**, 1502–1505 (2013).

64. Wu, G. *et al.* Molecular Ligand-Mediated Assembly of Multicomponent Nanosheet Superlattices for Compact CapacitiveEnergy Storage. doi:10.1002/anie.202009086.

65. Yan, J. *et al.* Flexible MXene/Graphene Films for Ultrafast Supercapacitors with Outstanding Volumetric Capacitance. *Adv. Funct. Mater.* **27**, 1701264 (2017).

66. Zhao, M.-Q. *et al.* Flexible MXene/Carbon Nanotube Composite Paper with High Volumetric Capacitance. *Adv. Mater.* **27**, 339–345 (2015).

67. Halim, J. *et al.* Synthesis and Characterization of 2D Molybdenum Carbide (MXene). (2016) doi:10.1002/adfm.201505328.

68. Tang, J. *et al.* Optimizing Ion Pathway in Titanium Carbide MXene for Practical High-Rate Supercapacitor. *Adv. Energy Mater.* 2003025 (2020) doi:10.1002/aenm.202003025.

69. Liu, W., Yi, H., Zheng, Q., Li, X. & Zhang, H. Y-Doped Na3V2(PO4)2F3 compounds for sodium ion battery cathodes: electrochemical performance and analysis of kinetic properties. *J. Mater. Chem. A* **5**, 10928–10935 (2017).

70. Augustyn, V. *et al.* High-rate electrochemical energy storage through Li + intercalation pseudocapacitance. *Nat. Mater.* **12**, 518–522 (2013).

71. Wang, J., Polleux, J., Lim, J. & Dunn, B. Pseudocapacitive contributions to electrochemical energy storage in TiO 2 (anatase) nanoparticles. *J. Phys. Chem. C* **111**, 14925–14931 (2007).

72. Bayram, V. *et al.* MXene Tunable Lamellae Architectures for Supercapacitor Electrodes. **10**, 16 (2021).

73. Tian, Y. *et al.* Surface nitrogen-modified 2D titanium carbide (MXene) with high energy density for aqueous supercapacitor applications †. (2019) doi:10.1039/c9ta00076c.

74. Vahidmohammadi, A. *et al.* Thick and freestanding MXene/PANI pseudocapacitive electrodes with ultrahigh specific capacitance. *J. Mater. Chem. A* **6**, 22123–22133 (2018).

75. Yang, X., Cheng, C., Wang, Y., Qiu, L. & Li, D. Liquid-mediated dense integration of graphene materials for compact capacitive energy storage. *Science (80-.).* **341**, 534–537 (2013).

76. Xu, S., Wei, G., Li, J., Han, W. & Gogotsi, Y. Flexible MXene–graphene electrodes with high volumetric capacitance for integrated co-cathode energy conversion/storage devices. *J. Mater. Chem. A* **5**, 17442–17451 (2017).

77. Ghidiu, M., Lukatskaya, M. R., Zhao, M.-Q., Gogotsi, Y. & Barsoum, M. W. Conductive two-dimensional titanium carbide 'clay' with high volumetric capacitance. *Nat. 2014 5167529* **516**, 78–81 (2014).

78. Li, L. *et al.* Carbon Dot-Regulated 2D MXene Films with High Volumetric Capacitance. *Ind. Eng. Chem. Res.* **59**, 13969–13978 (2020).

79. Ling, Z. *et al.* Flexible and conductive MXene films and nanocomposites with high capacitance. *Proc. Natl. Acad. Sci.* **111**, 16676–16681 (2014).

Chapter 4

Electric Field Assisted Fast and Controlled Assembly of MXene into Highly Scalable Pristine Hydrogels for Supercapacitive Energy Storage Applications

Chapter 4

Electric Field Assisted Fast and Controlled Assembly of MXene into Highly Scalable Pristine Hydrogels for Supercapacitive Energy Storage Applications

Assembly of MXene nanosheets into hydrogel framework is a road to their grand success in practical applications. However, scalable realization of such stable structure is challenging and requires critically high dispersion concentration for gelation. Herein, a simple yet highly controllable approach for the development of 2D and 3D-monolithic hydrogels of MXene via electro-tunable ordered assembly is reported. Directional electrophoretic drag of MXene and their gelation by voltage-controlled in-situ released ions at the electrode interface gives rise to stable hydrogels with tunable sheet orientations. Nanosheets can be arranged in-plane or out-of-plane depending on parallel or radial field created by customized electrode assembly. Further, the gelation rate can be easily regulated by applied potential to achieve self-standing hydrogel films in a few tens of seconds. The 2D hydrogels display excellent supercapacitive performance of 395 F g^{-1} at 2 mV s^{-1} with high retention of 42% at 5000 mV s^{-1}. This simple, fast, scalable and sheet orientation-controlled assembly can pave the way for future development of MXene hydrogels and beyond.

4.1. Introduction

The presence of robust, low-cost, facile assembly techniques for the development of macrostructures from nanoscale building blocks that incorporates intrinsic application-specific adaptability with practical scalability is the ultimate decisive element for their widespread application.[1] However, realization of such ideal assembly methods become difficult for a number of macrostructures, specially hydrogels, which offer multi-dimensional benefits with their hydrophilic porous structure and restacking controlled high surface characteristics.[2–4] Due to the relatively nascent stage of MXene hydrogel research, the search for an ideal assembling strategy that is versatile enough to meet the modern-day application requirements while being equally sustainable is still on.

Since its discovery, MXene,[5,6] a layered two-dimensional material derived from parent MAX phase counterparts (M represents transition metals, A being group III A or IV A elements, and X can be C and or N) has shown tremendous potential in several applications like energy storage,[7–9] catalysis,[10] electromagnetic interface shielding,[11] bio-medical applications,[12] *etc*.

However, the development of MXene hydrogel is often confronted with several difficulties due to the intrinsic stiffness of MXene sheets,[13] severe restacking during assembly,[14] and weak cross-linking of constituent nanosheets. To bypass the practical challenges of getting purely MXene based hydrogel, a number of reports introduced secondary gelators like graphene,[8,15] polymers [16] and carbon nanotubes [17] to develop hybrid hydrogels. However, the addition of foreign materials often mitigates the performance of pristine MXene in practical applications.[18] The addition of metal ions has also been a popular strategy to weaken the electrostatic repulsion in negatively charged MXene sheets in dispersion.[19] However, lack of control over the ion-induced assembly in bulk solution promotes random aggregation of sheets which results in soft hydrogels of MXene having weak cross-linking among the building blocks. To overcome these limitations, the self-assembly of MXene over metal plates through interfacial assembly and simultaneous reduction was introduced.[20,21] However, the self-limiting nature of this assembly process along with the requirement of very high critical concentration of MXene dispersion, are the major concerns for their practical adoptability. More importantly, this self-gelation cannot give any customized control over hydrogel thickness and it's impossible to extend beyond thin 2D hydrogel to 3D monolithic structure.[20] Nevertheless, principal concern with this technique is that the usable free-standing hydrogel can only be obtained from MXene dispersion of very high critical concentration which is highly dependent on sheet sizes. Thus, the requirement of such high critical concentration and sheet size dependency increases the overall complexity of MXene hydrogel development with reduced scalability.

The other important aspect of hydrogel research lies in its facile controllability over nanosheets assembly. The vertical arrangement of 2D sheets with quasi-parallel alignment has always been a center of attraction due to its optimized transport channels with long-range ordering.[22–25] Such unique structural characteristics are highly beneficial for applications requiring easy solvent or ion transport through the bulk of the macrostructure.[26] Further, the previously mentioned self-assembly or metal-ion gelation does not allow such controlled vertical assembly. The only known successful method for vertical MXene hydrogel include direction freezing of MXene dispersions followed by thawing in protic acids.[27,28] However, rapid water crystallization during freezing develops micron-sized channels with restacking of MXene in the thick pore walls and thus reduces the overall surface area, which is a major concern for applications that require limited restacking with high surface accessibility.

Here in this report, we introduce an electric field-assisted forced-assembly technique to develop free-standing, pristine $Ti_3C_2T_x$ MXene hydrogels. Electrophoretic drag of negatively charged

MXene towards anode and the field-stimulated controlled interfacial release of ions; paired with simultaneous reduction drastically improves the gelation and overcomes most of the current limitations in pristine MXene hydrogel development. The field-assisted gelation not only conquers the demand of critical high-density requirements to develop large-scale freestanding 2D hydrogels of MXene but also allows fast-customized oriented sheets assembly within the structure depending on field orientations. Modification of field direction via simple electrode arrangement can lead to hydrogels of different dimensions and sheet orientations. Parallel field between electrodes leads to sheet-like MXene hydrogels whereas radial field gives rise to columnar hydrogel monoliths with horizontally and vertically oriented assembly of sheets respectively. Importantly, this field-assisted process is ultrafast as free-standing MXene hydrogels can be produced within a few seconds only. We have established that this gelation process is not a simple electrophoretic deposition and is highly dependent on the redox potential of the metal substrate and its efficiency of interfacial ion release, which is also supported by density functional theory (DFT) calculations. As a potential application, the MXene hydrogels were used to develop high rate performance supercapacitors and highly efficient thermal water evaporators. The free-standing, 2D MXene hydrogel developed in only 30 seconds, shows an excellent supercapacitive energy storage performance of up to 395 F g^{-1} (at 2 mV s^{-1}) with superb rate performance having retention of 42% at high scan rates of 5000 mV s^{-1}.

4.2. Experimental section

4.2.1. Preparation of MXene:

'Minimally intensive layer delamination' (MILD) method was used for the preparation of $Ti_3C_2T_x$ MXene from the Ti_3AlC_2 MAX phase as reported earlier.[29] In brief, to remove the aluminum layer from the MAX phase, an etchant solution was prepared by slowly mixing LiF (3.2g) with 40 mL of 9M HCl acid. After complete dissolution of LiF into the acid solution, 2 g of Ti_3AlC_2 was slowly mixed with the above solution in presence of an ice bath. Later, the solution was kept at 35ºC for 24 hours for complete etching of Al from the MAX phase. The product after Al etching was washed with de-ionized (DI) water through centrifugation at 3500 rpm for 5 min until the pH of the solution became ~ 6. The resultant clay-like product was delaminated into individual MXene nanosheets via bath-sonication for 1 h under argon purging while maintaining the temperature of the bath under 30ºC. Finally, the mixture was centrifuged for 1 h at 3500 rpm to collect the delaminated MXene as supernatant.

4.2.2. Development of field-assisted MXene hydrogels:

2D hydrogel: For the development of MXene 2D hydrogels, Zn plates were mechanically polished and successively washed with ethanol and DI water under sonication. Two such Zn plates were arranged within a custom-built chamber in parallel plate assembly with an inter-plate separation of 1 cm while keeping the rear surfaces covered with Kapton tape to avoid any gelation on those surfaces. These two zinc plates serve as positive and negative electrodes respectively. Electric field-induced gelation was performed from MXene dispersion of 10-25 mg mL^{-1} concentrations by applying a potential difference of 1V between the plates. MXene hydrogel immediately started to develop over the positive plate and gelation duration was varied from a few seconds to several minutes depending on the desired thickness of the hydrogel. Finally, the hydrogel was separated from the Zn plate with 5 wt% HCl solution and washed several times with DI water to bring the pH of the hydrogels to neutral. To inspect the dependency of this electric field-induced gelation, other metallic (copper) and non-metallic (graphite) conducting sheets were also employed keeping all other assembly conditions the same.

4.2.3. Monolithic MXene hydrogel with vertical sheet assembly:

For the preparation of monolithic MXene hydrogel composed of vertically oriented sheets, a cylindrical electrode assembly was used with a Zn wire of diameter (Φ) 1 mm as the central positive electrode. A thin hollow cylindrical zinc (Φ = 25 mm) was used as the negative electrode to produce a radial electric field. Field-assisted gelation was performed over the central zinc wire with an applied potential difference of 1 V, the radius of the monolithic cylindrical hydrogel was controlled by extending the gelation time from a few hours to several hours. The monolithic hydrogel was detached from the zinc wire by interlayer etching with 5 wt.% HCl solution. Monoliths were then washed with DI water before using them for water evaporation tests.

4.2.4. Preparation of MXene films from hydrogel:

2D MXene hydrogel was first developed by electric field-induced gelation for 60s which resulted in a self-standing hydrogel. This hydrogel was then dried in ambient conditions over Nylon membranes overnight. After complete drying, it was peeled off from the membranes to achieve the flexible MXene film.

4.2.5. Preparation of vacuum filtered films:

MXene films were also prepared via conventional vacuum filtration technique to show the superiority of hydrogel and hydrogel-derived films. To prepare the vacuum filtered MXene films, MXene water dispersions were vacuum filtered through nylon membrane (0.8 µm). After filtration, they were dried at room temperature and then peeled off from the membranes. These films were then used as electrodes without further modification.

4.2.6. Computational details:

First principle density functional theory (DFT), as implemented in Quantum Espresso [30] package, was used to determine the work functions of Zn and MXene surfaces. Perdew–Burke–Ernzerhof (PBE) exchange co-relation functionals with Projected augmented and ultrasoft pseudopotentials were used as distributed from Standard Solid State Pseudopotentials (SSSP) precision library.[31,32] For MXene, $Ti_3C_2O_2$ was used with O atoms being in the FCC position. Zn and MXene surface was modelled using (4x4x2) and (4x4x1) supercell respectively with 20 Å vaccum to separate the interaction due to periodic images. All the atoms in the supercell were relaxed until forces on the atoms were less than 2 meV $Å^{-1}$. Plane wave kinetic energy cut-off energy of 680 eV for MXene and 544 eV for Zn was used to attain a total energy convergence less than 0.15 meV/atom. Monkhorst-Pack grid with k point density of 0.2 eV $Å^{-1}$ was used for brillouin zone sampling.[33]

4.2.7. Electrochemical characterization:

Electrochemical characterizations of field-assisted MXene hydrogels were performed in three-electrode configuration with Biologic SP-150 electrochemical workstation. The three-electrode was configured with MXene electrodes, activated carbon and Ag/AgCl in 1M KCl as working, counter, and reference electrode respectively. All the characterizations were performed in a Teflon Swagelok type cell with Celgard 3400 membrane acting as separator. 3M H_2SO_4 was used as electrolyte for the electrochemical measurements. Cyclic voltammetry (CV) and charge-discharge (CD) methods were performed in a potential range of -0.7 to 0.3 V vs Ag/AgCl. For symmetric cell measurements, field-assisted MXene hydrogel electrodes were used as both the working and counter electrodes. Electrochemical impedance spectroscopy (EIS) was performed in a frequency range between 10 mHz to 100 kHz with 10 mV amplitude applied at open circuit potential (OCP).

Gravimetric performance (C_g) of the hydrogels were measured using the following equation,

$$C_g = \frac{1}{mv\Delta U}\int i\, dU \tag{1}$$

also for volumetric capacitance (C_V),

$$C_V = \frac{1}{Vv\Delta U}\int i\, dU \tag{2}$$

where ΔU and v is the potential difference and the scan rate respectively. m and V represent the mass and volume of the working electrode in the three-electrode cell. For symmetric device measurements, the device capacitance was measured with m being the mass of both the active materials.

The energy (E_g) and power (P_g) densities were calculated using,

$$E_g = \frac{C_g \times (\Delta U)^2}{2 \times 3.6} \tag{3}$$

$$P_g = \frac{E_g \times v \times 3600}{\Delta U} \tag{4}$$

4.2.8. Active surface area measurement in field-assisted dried hydrogel (d-MF) and vacuum filtered (VF) film:

To determine the difference between active surface area of d-MF and VF films, comparison between their electrochemically active surface area (EASA) was made. The EASA was determined from double layer capacitance (C_{dl}) measured from cyclic voltammetry (CV). All the CV scans were performed in a non-faradaic region with various scan rates of 5, 8, 10, 15, 20, 30, 40 mV s^{-1}. Thereafter, the C_{dl} was determined from the slope in the plot between current density difference at -0.65 V vs Ag/AgCl and scan rates. From C_{dl}, the EASA can be measured as EASA = C_{dl}/C_s, where C_s denotes the specific capacitance of flat surface with unit surface area. Thus for both material consisting MXene, the comparison between their active surface area can be estimated from the ratio of C_{dl} as,

$$\frac{EASA_{d_{MF}}}{EASA_{VF}} = \frac{C_{dl}^{d_{MF}}}{C_{dl}^{VF}} \quad (5)$$

4.3. Results and discussion

Free-standing hydrogels were developed via layer-by-layer assembly of MXene nanosheets over appropriately chosen metal electrodes (zinc) under an applied electric field (Experimental section). In brief, zinc-based electrode assembly was placed within aqueous MXene dispersion of desired concentration (10-25 mg mL^{-1}), and an electric field was applied by connecting them

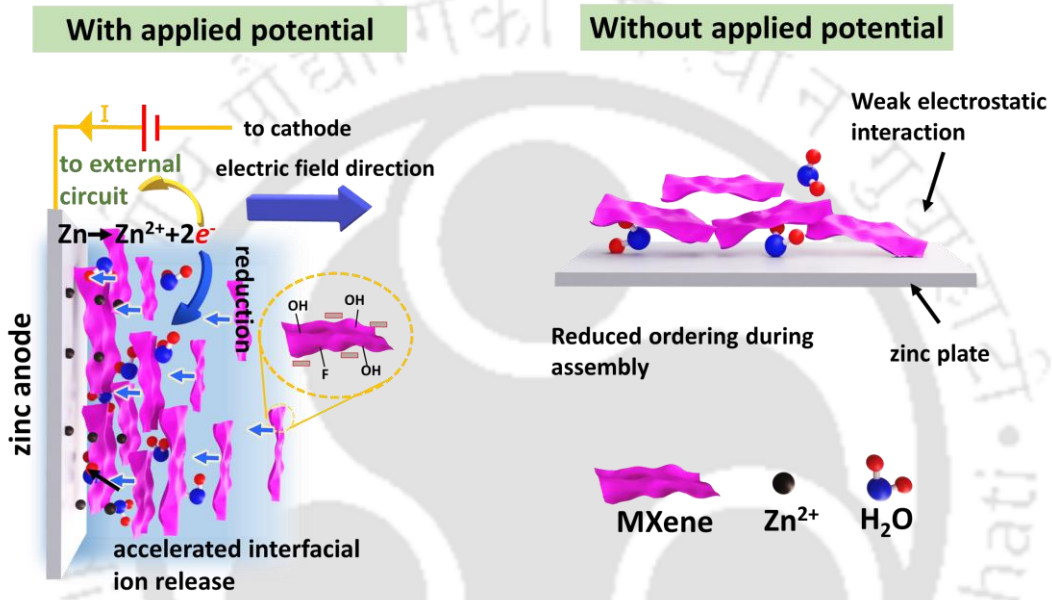

Figure 4.1. Electric field-induced gelation of MXene hydrogels: schematic illustration of MXene gelation with and without applied potential.

with DC voltage of 0-1 V which results in the development of MXene over the positive electrode as shown schematically in Fig. 4.1. The as developed hydrogel was detached by interfacial etching with dilute acid, and finally, acid washing was done to remove zinc (Zn) impurities. This gelation process can be understood by considering the electrophoretic drag of negatively charged MXene sheets towards the positive Zn electrode, the voltage-assisted interfacial release of Zn^{2+} ions, and its electron transfer from Zn to MXene, all of which happen simultaneously. The basal plane of MXene is decorated with functional groups like –F, -O, and -OH which makes them negatively charged in their aqueous dispersion (Fig. 4.2). During the gelation process, negatively charged MXene nanosheets move towards the positive anode due to the applied field and assemble over the Zn plate in a layer-by-layer manner. Zn having high reduction potential is easily oxidized at the anode by applied voltage and releases Zn^{2+} locally

at its surface. These in-situ generated Zn^{2+} ions help in mitigating the electrostatic repulsion between negatively charged MXene nanosheets to induce faster gelation over the anode surface. Local in-situ release of Zn^{2+} ion is key for this electro-induced process as it accelerates the interfacial assembly while the applied electric field ensures oriented layer-by-layer assembly and long-range ordering of the sheets in the hydrogel structure. Thus, with reduced electrostatic repulsion and ordered assembly, a compact macrostructure is obtained which gives rise to increased strong van der Waals interaction among the nanosheets, enabling self-supporting hydrogels at lower concentrations. Without any applied bias, the self-assembly of MXene over Zn suffers from weak electrostatic attraction of MXene towards Zn (Fig. 4.1).

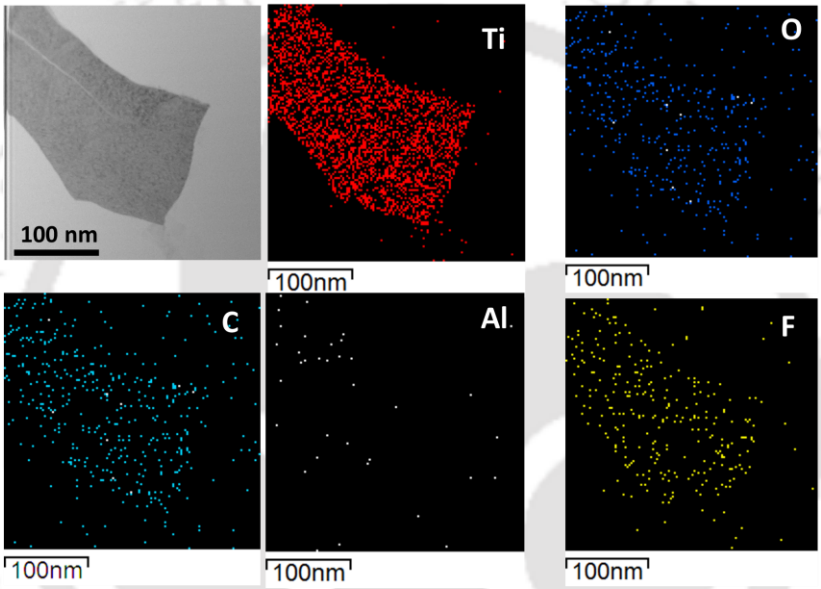

Figure 4.2. Transmission electron microscopy image of $Ti_3C_2T_x$ with corresponding EDS spectra indicating removal of Al from MAX phase Ti_3AlC_2 and decoration of O and F functional groups on the basal planes of MXene.

Thus in order to achieve sufficient ordering and compactness, the process heavily relies on relative alignment of MXene sheets in dispersion which requires certain liquid crystalline phases, obtained only above high concentrations depending on sheet size.[20] The proposed voltage controlled release of Zn ions was confirmed from energy-dispersive X-ray spectroscopy (EDS) analysis of the MXene hydrogel samples; developed at different potentials but before acid washing. As confirmed from EDS, the presence of Zn in hydrogels increase by five folds when under 1 V bias (7.51 *at*%) compared to that of normal gelation (1.36 *at*%) without any potential (0 V); and double the amount present in samples developed from 0.5 V applied bias (3.59 *at*%). Further, the hydrogel matrix of MXene contains plenty of water stably

bound within its porous framework, which prohibits restacking of the nanosheets in the hydrogel structure. The water content of the hydrogel was measured to be ~96% of its own weight which was determined from the mass of hydrogel structure before and after drying.

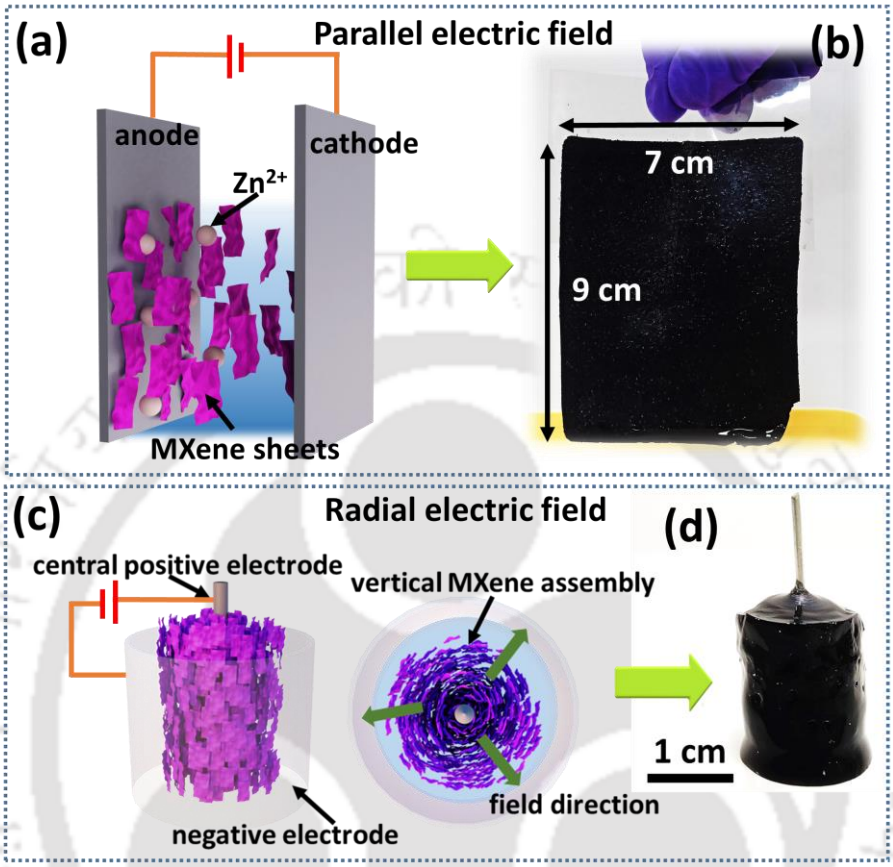

Figure 4.3. (a) Schematic illustration of electrode arrangement for parallel field guided layer-by-layer gelation; (b) large scale freestanding MXene 2D hydrogel developed from field-induced gelation technique with parallel electrode arrangement; (c) schematic of concentric electrodes for vertically aligned cylindrical MXene assembly for the development of (d) monolithic MXene hydrogel.

4.3.1. Facile controllability over MXene sheet orientation in hydrogels:

Since the gelation is administered by the applied electric field, the strategic arrangement of the metal electrodes allows easy controllability over field distribution, which in turn permits the facile development of MXene hydrogels with guided sheet assembly. For example, the parallel arrangement of Zn plates enables the development of MXene 2D hydrogels having an in-plane sheet arrangement, and importantly a free-standing hydrogel can be realized within seconds (Fig. 4.3.a,b). On the other hand, a radial electric field in a cylindrical configuration with a hollow Zn tube and a central positive Zn wire allows facile development of a cylindrical

MXene monolithic structure having vertical sheet assembly (Fig. 4.3.c,d). Moreover, this fast, one-step simple approach is easily scalable to develop large-area hydrogels of MXene as shown in Fig. 4.3.b.

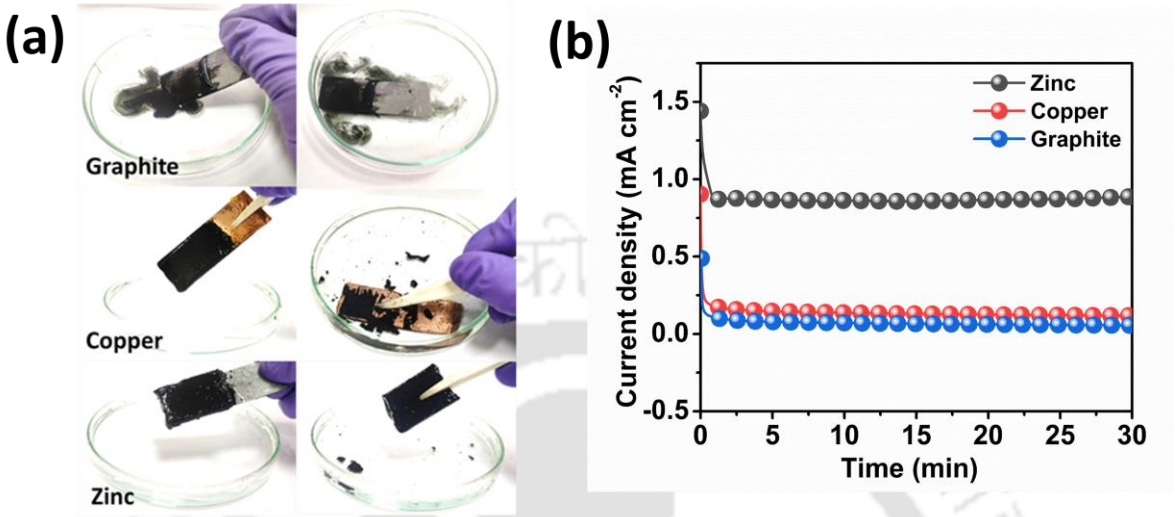

Figure 4.4. (a) Metal plate dependency over MXene gelation in field-assisted gelation, (b) current density during gelation with different electrodes showing the effect of electrodes in field-induced assembly method.

4.3.2. Dependence of electric field assisted gelation over different anodes:

To confirm the role of in-situ generated ions over the electrode surface and check the dependency of the metal in this electric field-controlled gelation process, metals of different redox potential as well as non-metallic graphitic were considered as electrodes. First, in order to inspect the effect of in-situ metal ion release, graphite sheets were used as positive and negative electrodes. In this case, no hydrogel was developed, however, only a thin layer of MXene deposit was observed which resulted from conventional electrophoretic deposition of negatively charged MXene over the positive electrode. Furthermore, the deposited film was so loosely bound that it readily dispersed in water under little external disturbance (Fig. 4.4.a). This observation confirms that the voltage-controlled interfacial release of ions play a key role in the gelation process. The efficiency of ion release depends on the redox potential of the metal used as anode. Zn, having high redox potential, is a favorable candidate in this regard as it can easily be oxidized to generate ions, which helps in getting a stable hydrogel structure. When Zn anode was replaced with copper (Cu) having lower reduction potential, a thin and unstable hydrogel resulted. This metal dependency is caused by the fact that under the same applied potential release of Zn^{2+} from Zn anodes will be much higher than the Cu electrodes due to its

lower redox potential (-0.76 V Zn^{2+}/Zn compared to 0.34 V for Cu^{2+}/Cu). This can be also confirmed from the overall current density in the circuit during gelation where graphite showed the lowest value among the electrodes under comparison (Fig. 4.4.b). Increased release of metal ions increases the number of electrons flowing through the circuit which contributes to the higher overall current density in Zn as compared to Cu.

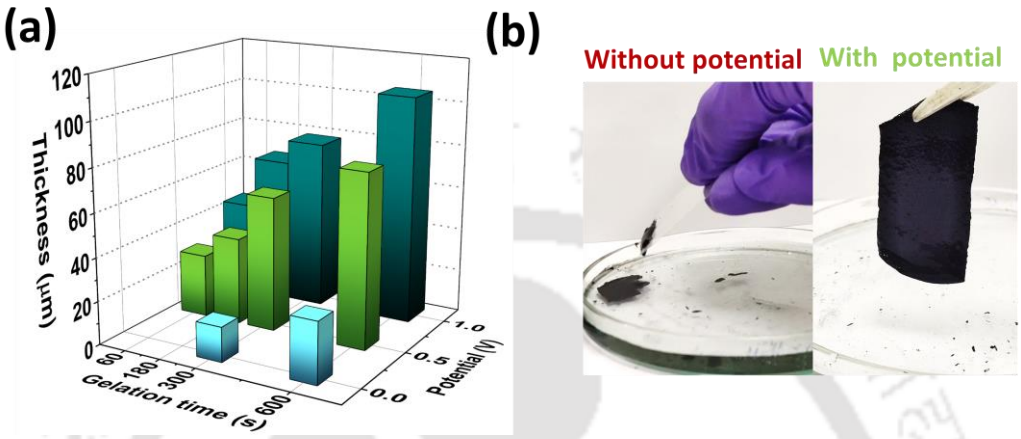

Figure 4.5. (a) Strong effect of applied potential over controlled assembly and variation in hydrogel thickness with time; (b) digital image of 2D-hydrogels developed with and without electric field indicating the difference in their self-supporting nature.

4.3.3. Effect of applied potential and gelation time:

The applied potential is the key parameter for this controlled gelation in field-assisted method, and its variation can help to control the gelation rate. Fig. 4.5.a displays the difference in gel thickness with time at different applied potentials which again confirms the major role of potential in controlling the gelation. Most importantly, application of potential enables the development of self-standing hydrogel from MXene dispersions of <10 mg mL^{-1} overcoming the high sheet size dependent critical concentration (C_{ct} > 40-60 mg mL^{-1}) requirement when no voltage was applied.[20] Fig. 4.5.b demonstrate the comparison between hydrogels developed with 10 mg mL^{-1} MXene dispersion with and without applied potential where a clear difference between their stability can be observed. Importantly, the stability of the field-induced hydrogel developed in 30s compared to the 20 min conventional 0 V hydrogel indicates the strong difference in the two gelation methods. Along with the increased flux of metal ions, stability of field-assisted hydrogels at concentrations lower than the critical value can be attributed to the increased electrostatic interaction of MXene sheets with the positive anode which enhances the local concentration around the electrode, thus leading to stable gelation of MXene. Further,

the added controllability over Zn ion release increases the interaction of MXene sheets with the anode while avoiding uncontrolled bulk gelation in the solution which generally happens in the case of conventional ion-induced bulk gelation.[19] This results in defined self-supporting structures of MXene hydrogel compared to soft formless assembly in ion-induced gelation. More importantly, the self-assembly or the ion-assisted technique fails to provide any control over desired nanosheet orientation in the hydrogel structure which can be easily achieved with facile electrode arrangement in field-assisted gelation strategy. Thus, critical-concentration independent large-scale assembly with facile controllability for in-plane or vertical sheet arrangement provides multifold advantage over previous gelation methods.

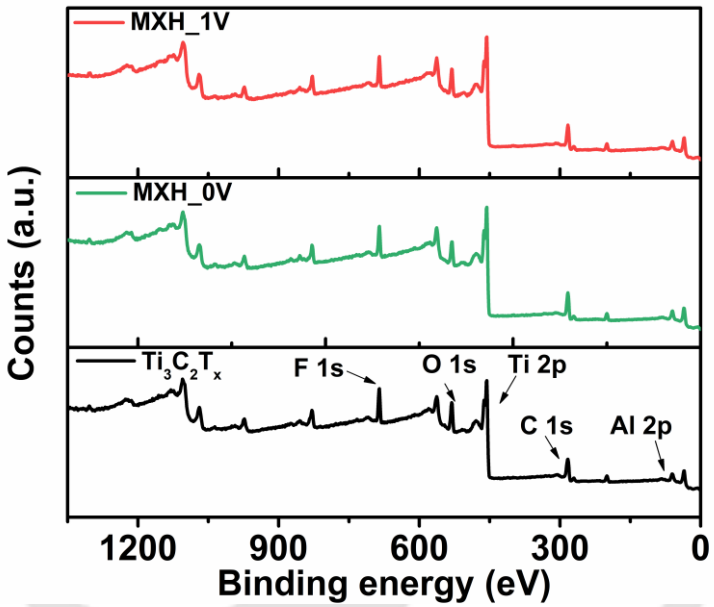

Figure 4.6. XPS survey spectra of $Ti_3C_2T_x$, MXene hydrogel without (MXH_0V) and with potential (MXH_1V).

4.3.4. Structural and physiochemical analyses of hydrogels:

Together with anodic gelation, this process also makes significant changes in the surface functional characteristic of MXene as was confirmed from a detailed X-ray photoelectron spectroscopy (XPS) analysis. XPS survey scan revealed an increase in C/O in the hydrogel (MXH_1V) as compared to exfoliated MXene precursor (pristine $Ti_3C_2T_x$) nanosheets, which signifies considerable removal of oxidative surface functional groups during the gelation process (Fig. 4.6). Complete removal of Zn ions from the hydrogel after acid washing was also confirmed from the survey spectra which shows negligible presence (0.5 *at*%) of the metal ions in the hydrogel structure. De-functionalization of the MXene surface was further confirmed

from high-resolution C1s and Ti2p XPS spectra (Fig. 4.7.a,b). In C1s, peaks due to C–Ti–T_x (282.7 eV), C–C (248.6 eV), C–O (286.3 eV) and C=O (289.1 eV) are obvious and the significantly reduced C=O peak of hydrogel signifies the removal of functional groups (Fig. 4.7.a).[34,35] The de-functionalization happens as a result of the reduction of MXene by Zn metal.

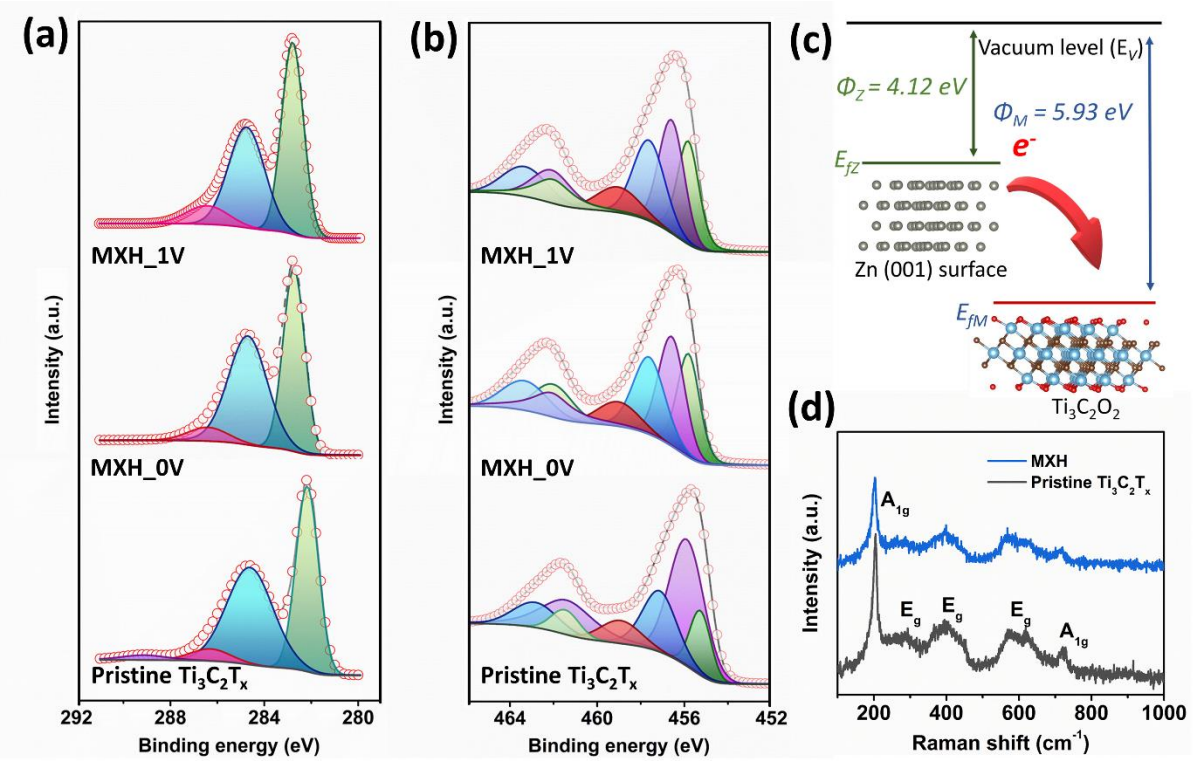

Figure 4.7. Analysis of chemical composition and synthesis induced modification in MXene hydrogels developed from field-induced gelation: high resolution XPS spectra of (a) C1s (from right to left the peaks denote C–Ti–T_x, C–C, C–O and C=O respectively) and (b) Ti 2p (green, purple, blue and red peaks correspond to doublets of Ti, Ti^{2+}, Ti^{3+} and TiO_2 respectively with $2p_{3/2}$ being in the higher binding energies); (c) DFT analysis of MXene and Zn surface for possible reduction analysis; (e) corresponding Raman spectra of MXene hydrogels.

However, this statement is counterintuitive as gelation happens over the anode where generally oxidation occurs. To shed light on this issue, we first checked the C/O ratio of the hydrogel developed without applied voltages (MXH_0V) and found that this ratio is higher in this sample (C/O =2.52) as compared to exfoliated MXene (C/O =2.02) which establishes that Zn metal can do reductive de-functionalization. Interestingly, the XPS survey spectra further reveals that similar to the MXH_0V, the C/O ratio is also higher in MXH_1V (2.46) as compared to pristine $Ti_3C_2T_x$, which indicates similar reduction in field-induced gelation method. The corresponding Ti/O ratio from XPS survey also increases from 1.58 for pristine

$Ti_3C_2T_x$ to 2.12 for MXH_1V, which further corroborates decrease of oxygen containing functional groups in the assembly process. These observations clarify that reduction of MXene indeed happens via surface de-functionalization in the field-induced gelation, however, the level of reduction may get lowered depending on the applied potential.

To better understand the XPS results and MXene reduction under an anodic environment, we performed DFT calculations on MXene and Zn (001) surface to calculate their work function. DFT suggests a corresponding work function of 5.93 eV for MXene and 4.12 eV for Zn (001) surface respectively (Fig. 4.7.c).[36,37] Since the Fermi level of Zn lies above MXene, spontaneous transfer of electrons can happen from Zn to MXene, thus reducing the latter. It is important to note that the energy separation in the Fermi levels (or work function) between Zn and MXene is the driving force for electron transfer and hence MXene reduction. With the application of a positive potential to the Zn anode, the energy of its electrons will decrease, and hence its Fermi level will go deeper which decreases the separation between the same. However, the large difference in work functions (1.81 eV) provides a potential window up to which the electron transfer will still be possible from Zn to MXene. According to the energy diagram, the application of 1V potential across the two electrodes would still maintain the Fermi level of Zn higher than that of MXene, indicating a reduction of MXene as also evident from XPS analysis (Fig. 4.7.c). Oxidation of the titanium sites of MXene into insulating titanium dioxide (TiO_2) is a major problem for any high-temperature gelation process which can degrade its intrinsic high conductivity.[38,39] Any change in content of the TiO_2 phase within hydrogels (MXH_1V and MXH_0V) was investigated by analyzing the deconvoluted XPS Ti2p peaks and a comparison was made with exfoliated pristine $Ti_3C_2T_x$ (Fig. 4.7.b). The Ti 2p spectra is fitted with four doublets (Ti $2p_{3/2}$ and Ti $2p_{1/2}$) which correspond to the Ti, Ti^{2+}, Ti^{3+} and TiO_2 peaks of MXene.[34,35] Significant increase in the contribution of metallic Ti is observed in MXH_0V and MXH_1V samples which indicate towards defunctionalization induced reduction in the corresponding process. Importantly, the contribution from TiO_2 (458.9 eV) as estimated from the deconvoluted spectra was found to remain almost similar to exfoliated MXene, which indicates that the gelation does not lead to oxidation of titanium sites to the insulating phase (Table 4.1). From XPS observation it can be concluded that the gelation does lead to neither oxidation of titanium site nor incorporates oxidative functional groups, instead it does the de-functionalization by reduction through spontaneous electron transfer from Zn to MXene. An increase of anodic current with an increase of voltage appears due to oxidation of the Zn anode itself but not the deposited MXene over it.

Table 4.1: Atomic % of constituent peaks fitted from Ti 2p high resolution spectra for pristine $Ti_3C_2T_x$, MXene hydrogel with (MXH_1V) and without (MXH_0V) potential.

	Pristine $Ti_3C_2T_x$	**MXH_0V**	**MXH_1V**
Ti	15	28	27
Ti^{2+}	49	32	32
Ti^{3+}	26	29	29
TiO_2	10	11	12

To further rule out any possibility of oxidation, Raman spectra were studied. The Raman spectra of MXene, which consist of symmetric out-of-plane vibrations A_{1g} (204 cm^{-1}, 729 cm^{-1}) and in plane vibration E_g (292 cm^{-1}, 397 cm^{-1}, 618 cm^{-1}) of Ti, C and functional groups is consistent in both pristine $Ti_3C_2T_x$ MXene and field-assisted hydrogels (Fig. 4.7.d).[8] The Raman spectra after gelation also do not suggest any peak regarding TiO_2 which further solidifies the prevention of oxidation of MXene in the field-assisted assembly technique.

The porous structure of the hydrogel was confirmed from the cross-sectional image of the corresponding aerogel sample, which discloses a highly porous interconnected structure having an in-plane quasi-parallel arrangement of the sheets (Fig. 4.8.a). Interestingly, the face-to-face quasi-parallel assembly, which arranges the nanosheets horizontally in a plane for 2D hydrogels, can be also used to develop field-induced vertically aligned MXene hydrogels (F-VMH). With the Zn wire/Zn tube co-axial cylindrical electrode assembly, field-assisted gelation allows a facile development procedure for VMH where continuous radial face-to-face

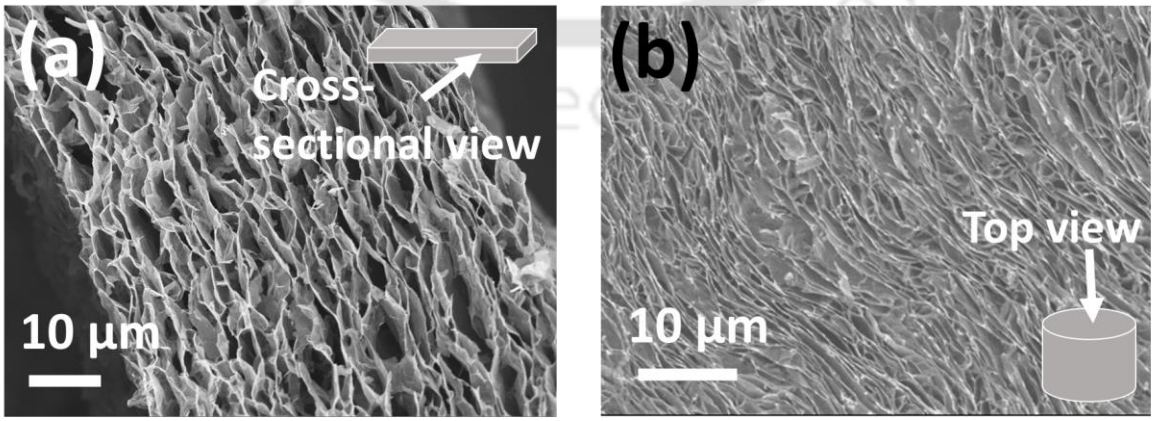

Figure 4.8. Structural analysis of MXene hydrogels and 2D hydrogel derived MXene films: (a) cross-sectional FESEM image of MXene 2D hydrogel showing its porous assembly; (b) FESEM top view of MXene monolith indicating long range vertically aligned structure.

assembly and extended gelation time (5-7 hours) resulted in cylindrical monolith of hydrogel. Field emission scanning electron microscope (FESEM) image of the top surface of cylindrical hydrogel monolith shows vertically aligned nanosheets and long-range ordered arrangement along with uniformly distributed pores (Fig. 4.8.b). Difference in the special arrangement of sheets within F-VMH can also be determined macroscopically by measuring electrical properties in the axial and transverse direction of these cylindrical monoliths as shown schematically in Fig. 4.9.a. In a vertical assembly, the interconnected vertical sheets of MXene assembled in a quasi-parallel structure should provide greater conductivity along the vertical direction. On the other hand, the longitudinal path should consist of alternating MXene pore walls with the intermediatory space being filled with water, resulting in higher resistance to current flow. To validate this conjecture, the hydrogel was placed in between two platinum plates in both longitudinal and vertical directions while a small bias was applied. As evident from Fig. 4.9.b, the linear sweep curves clearly show the greater current response in the hydrogels while placed in the vertical orientation compared to being in the longitudinal state. This clearly demonstrates the difference in spatial properties of the macrostructure which originates from its vertical assembly in the hydrogel.

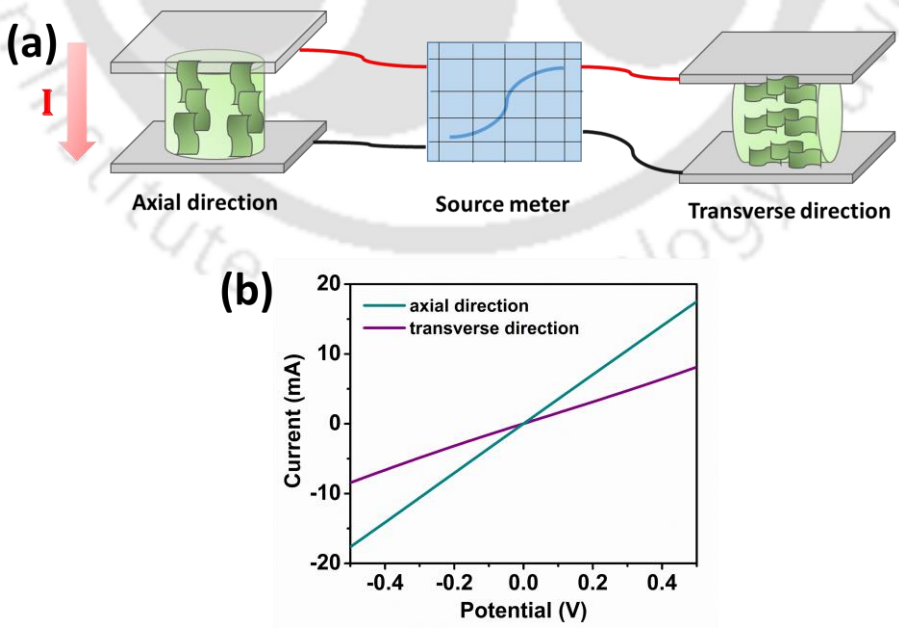

Figure 4.9. (a) Schematic illustration of conductivity measurement for F-VMH hydrogel to determine orientation anisotropy; (b) linear sweep curves in axial and transverse direction of a 1x1x1 cm^3 F-VHM monolith indicating special anisotropy

4.3.5. Flexible film electrodes development and structural analyses:

It is worthwhile to mention that vertical alignment of the two-dimensional nanosheets are extremely challenging and only a few complex strategies were adopted previously including sudden freezing of surfactant guided liquid crystal assembly and directional freezing. As per our knowledge, this is the first report of monolithic hydrogel with in-situ control of vertical nanosheets arrangement.

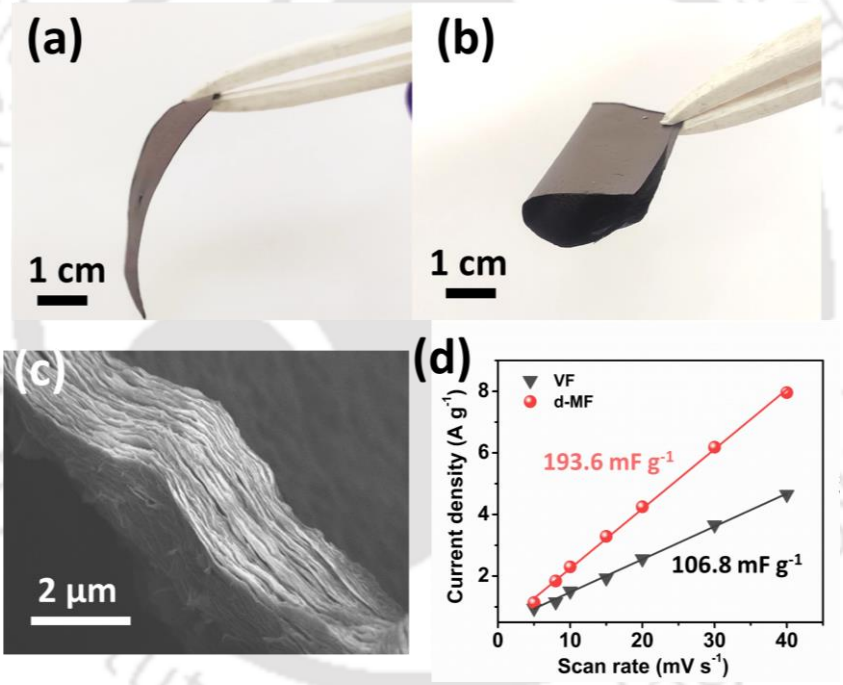

Figure 4.10. Digital image of MXene 2D hydrogel derived film (d-MF) in (a) normal and (b) bending state with its corresponding (c) cross-sectional FESEM image; (d) linear regression between current density difference and scan rate for d-MF and VF MXene films for ECSA determination.

Compact strong MXene films are often required for electronic, bio membrane and filtration applications, for which time and energy consuming vacuum filtration technique is mainly used.[40,41] Interestingly, the 2D hydrogel developed in seconds can be made into strong and flexible films via simple air-drying (Fig. 4.10.a,b). The film size is arbitrarily scalable as it

depends on the size of Zn electrode only, which demonstrates the versatility of our electric field-assisted fast assembly technique. The cross-sectional image of the d-MF shows highly compact nanosheets similar to the film developed by the vacuum filtration technique (Fig. 4.10.c). However, on inspection in higher magnification, it reveals that d-MF preserves nano-channels of 10-100 nm among the compacted nanosheets. The presence of such nano-channels in d-MF can play a vital role in energy storage applications as electrolytic ions pass through the pores to access the nanosheet surfaces. To further investigate the difference in their porous morphology, electrochemically active surface area (EASA) was compared via cyclic voltammetry (CV) in their non-faradaic region as described in experimental section (Fig. 4.10.d). The calculation indicates a 1.8-fold higher surface area in d-MF compared to VF which confirms the role of water intercalated porous structure in hydrogel that prohibits complete restacking of nanosheets during drying. Furthermore, the mechanical strength of MXene film is a key parameter for their scalable use in flexible electronics, electromagnetic interface shielding *etc*. The mechanical property of the hydrogel-derived MXene films (d-MF) was estimated through a tensile stress-strain test and compared with the strength of film developed with the conventional vacuum filtration technique (VF). From the stress-strain curve, it can be seen that compared to VF films which have a tensile strength of 16.4 MPa, the d-MF shows significant improvement with maximum tensile strength reaching 27 MPa for a 6 µm thick film (Fig. 4.11).[42] The corresponding fracture strain was 0.6 % and 0.88% for VF and d-MF respectively.

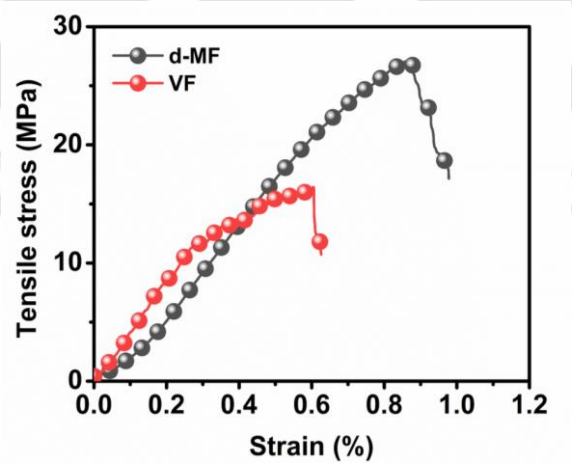

Figure 4.11. Comparison of mechanical strength between conventional vacuum dried and d-MF films.

4.3.6. Electrochemical analysis:

MXene hydrogels are highly attractive candidate for supercapacitive energy storage owing to several beneficial characteristics like the high metallic conductivity of MXene, its intrinsic pseudo-capacitance, restacking controlled highly porous structure, and abundance of hydrated ion transport channels.[20,42] 2D hydrogels are highly suitable in this regard due to their ready-to-use structure for a large area electrode assembly and easy controllability of areal mass loading by tuning the time of gelation. The supercapacitive performance of field-assisted MXene 2D hydrogels (FMH) of different areal mass loading (gelation time 30, 60, 180 and 300 seconds) was investigated in a three-electrode Swagelok type cell in presence of 3M H_2SO_4 electrolyte. The performance of the hydrogels was also compared with vacuum filtered (VF_2.2) one to highlight the importance of the hydrogel structures. Cyclic voltammetry (CV) curves of FMH samples are presented in Fig. 4.12.a where all the electrodes display characteristic MXene redox peaks at -0.26 V and -0.38 V (vs Ag/AgCl). Such pseudocapacitive behavior is also evident in the galvanostatic charge-discharge (GCD) curves which show a little deviation from their usual triangular nature (Fig. 4.12.b). The CV curves indicate that all the FMH electrodes have a greater area enclosed by the polarization curves compared to the VF_2.2, which is indicative of their higher specific capacitance. The gravimetric capacitance of FHM_0.5, FHM_0.8, FMH_2.1 and FMH_3.4 (numbers after FMH denotes the corresponding mass loading of the electrodes) are calculated to be 395.2 F g^{-1}, 381.6 F g^{-1}, 366.5 F g^{-1} and 361.1 F g^{-1} respectively at 2 mV s^{-1}.

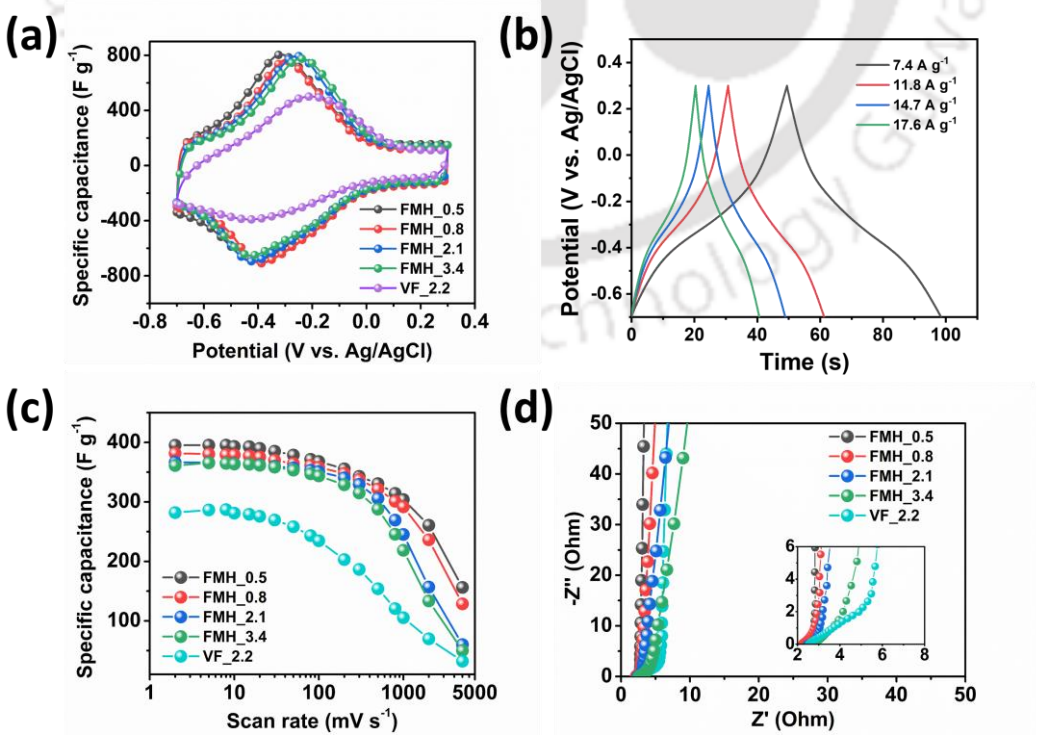

Figure 4.12. Electrochemical energy storage performance of field-induced MXene 2D-hydrogels of different areal mass loading and hydrogel derived dried films: (a) CV curves at 100 mV s^{-1}; (b) galvanostatic charge-discharge curves of FMH_3.4 electrodes showing pseudocapacitive response; (c) capacitive performance of FMH electrodes as a function of scan rates; (d) Nyquist plot showing frequency response with inset showing the high frequency region;

The importance of hydrogel structure can easily be determined by comparing this performance with that of VF_2.2 electrode. The gravimetric capacitance of VF_2.2 was measured to be 281.9 F g^{-1} (at 2 mV s^{-1}) which is much less compared to the hydrogel (FMH_2.1, 366.1 F g^{-1}) with similar mass loading. Restacking controlled porous structure of hydrogels not only provide a higher surface area for electrolytic double-layer capacitance (EDLC) but also allows the redox-active sites in the basal planes of MXene sheets to contribute to the capacitance. The much lower strength of the redox peak in VF also reflects that the redox activity of its MXene surfaces is poor due to a face-to-face restacked structure having less surface accessibility (Fig. 4.12.a). High rate performance of electrodes is of prime importance for supercapacitive energy storage devices as they are mainly used for high power applications. The presence of numerous porous channels greatly reduces the ion diffusion path to the active sites in hydrogels, which can benefit the storage kinetics by providing better rate performance of the material. Such morphological characteristics result in excellent rate performances in all of the hydrogels as shown in Fig. 4.12.c. Particularly, the FMH_0.5 hydrogel electrode exhibits the highest specific capacitance of 395 F g^{-1} at 2 mV s^{-1} with an impressive rate performance of 42% capacity retention at 5000 mV s^{-1} (Fig. 4.12.c). In comparison, VF_2.2 retains only 37% of initial capacitance at 1000 mV s^{-1} which implies the importance of hydrogel structure for high rate supercapacitive energy storage.

Electrochemical impedance spectroscopy (EIS) can provide insightful information on the ion diffusion characteristics of the electrodes. The near-vertical rise in Nyquist plots indicate low diffusion resistance of the MXene electrodes (Fig. 4.12.d). Quite naturally, as the mass loading increases, slight inclination at the low-frequency region is seen which corresponds to the increased resistance to the ions diffusing through the bulk of the electrodes. Notably, in the high-frequency Warburg region, near 45º alignment in the EIS spectra of VF_2.2 is observed which indicates its higher ion-diffusion resistance compared to the hydrogel electrodes (Fig. 4.12.d, inset). Lower ion diffusion resistance of the hydrogels leads to their observed high rate performance, and it is associated with the unique porous hydrated structure that allows

unimpeded ionic motion to the depth of the electrode. Furthermore, to determine the charge storage kinetics and their difference in corresponding FMH and VF electrodes, a logarithmic plot of current density (i) and scan rate (v) is presented following the current law,

$$i = av^b \tag{6}$$

where a and b are variables with b= 1 and 0.5 representing surface-controlled and diffusion-limited processes respectively. The representative FMH_0.5 and FMH_3.4 hydrogel electrodes

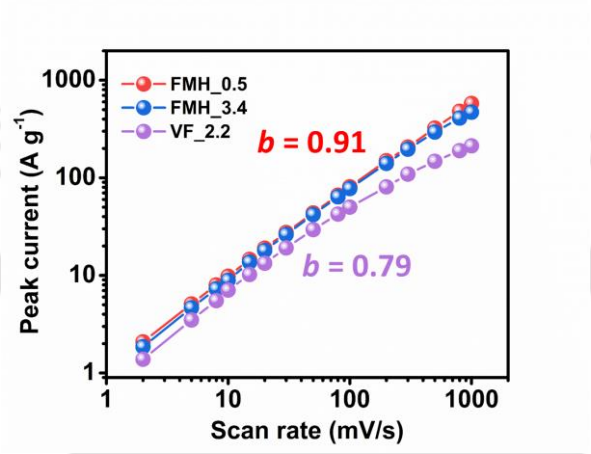

Figure 4.13. Logarithmic plot between peak current and scan rate indicating difference in charge storage between FMH and VF electrodes

maintain a b value upto 0.91 and 0.89 at upto 1000 mV s^{-1} respectively which indicate their fast surface-controlled storage behavior and easy surface accessibility (Fig. 4.13). The corresponding b value for VF_2.2 nears 0.79 indicating its slight diffusion limited behavior that explains the higher diffusion resistance and low rate performance of the material.

The electrochemical performance of the field-controlled hydrogels was also investigated in device configuration where the electrodes were measured in symmetric two-electrode setup with MXene hydrogels implemented as both the working and counter electrode. Presence of redox humps in the CV curves of all the hydrogel electrodes, which is the typical nature of MXene in symmetric cell measurements, indicates the redox activity of MXene in the acidic electrolyte as also discussed for corresponding three-electrode measurements (Fig. 4.14.a).[43] This is further reflected in the GCD curves of FMH_0.5 where near triangular profiles can be observed (Fig. 4.14.b). The full device capacitance (calculated taking both electrode mass into account) of FMH_0.5, estimated from two-electrode measurements is found to be 92.2 F g^{-1} followed by 87.6 F g^{-1}, 80.9 F g^{-1} and 74.8 F g^{-1} for FMH_0.8, FMH_2.1 and FMH_3.4

respectively. Such device capacitance for pristine MXene symmetric supercapacitors are far better than previous reported MXene based materials (Table 4.2). The near vertical rise of

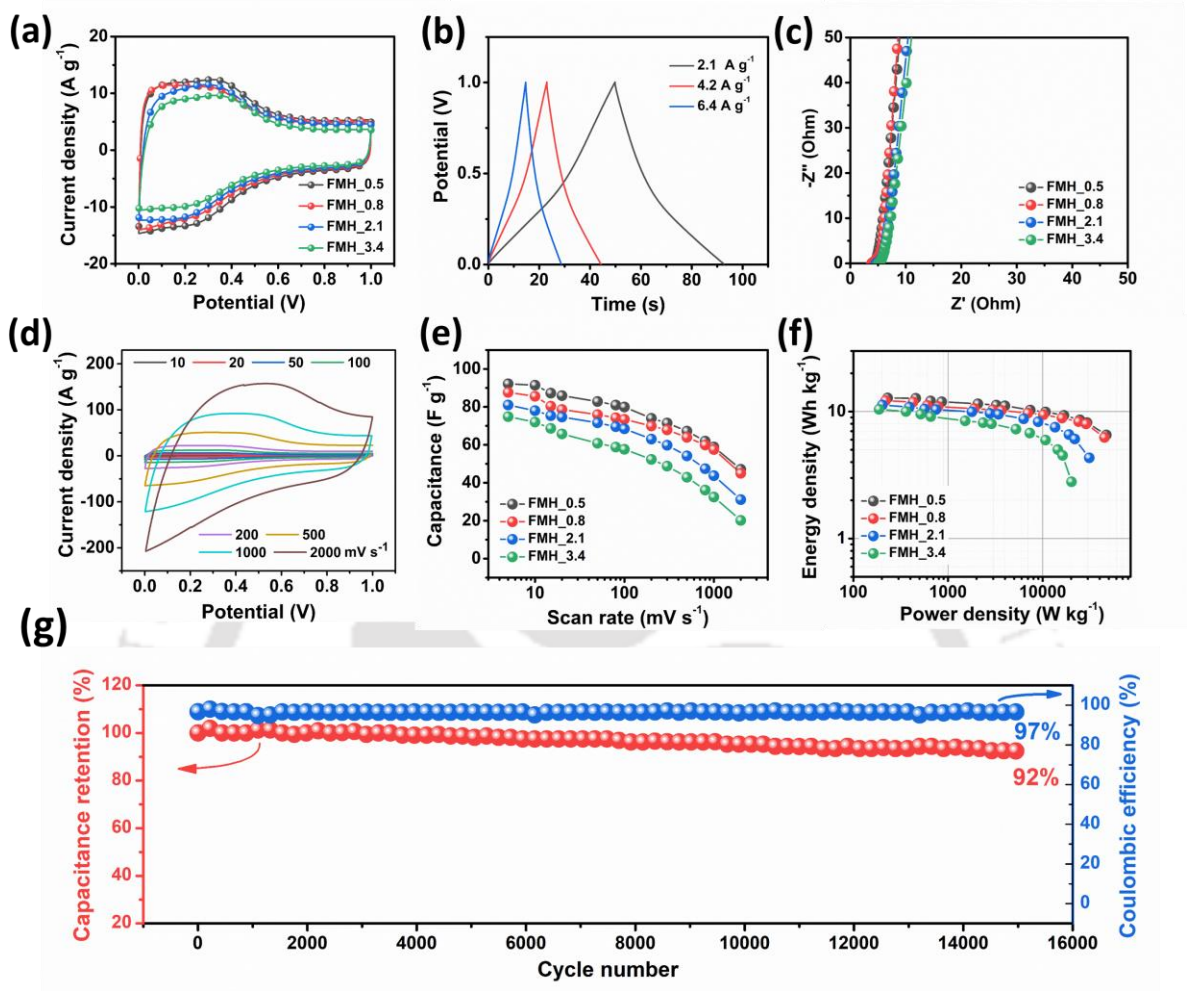

Figure 4.14. Electrochemical analysis of field-assisted MXene electrodes in symmetric two-electrode setup: (a) CV curves of FMH electrode devices at 100 mV s^{-1}; (b) GCD curves of FMH_0.5; (c) Nyquist plots of field-assisted electrodes showing the near vertical rise; (d) CV curves of FMH_0.5 electrode device at different scan rates; (e) rate performance and (f) Regone plot of FMH electrodes showing energy and power densities of the devices. (g) Cycling stability test of FMH_0.5 at 10 A g^{-1} for 15000 charge-discharge cycles showing its excellent stability and high Coulombic efficiency.

imaginary impedance in Nyquist plot shows the decreased ion diffusion resistance in the hydrogel electrodes (Fig. 4.14.c). This is more evident in the corresponding CV curves of FMH_0.5 measured at different scan rates. Interestingly, the CV curves maintain very similar shape even at very high scan rates of 2000 mV s^{-1} (Fig. 4.14.d). Such excellent rate performance is evident in all the hydrogel electrodes as shown in Fig. 4.14.e. The outstanding rate capability

of the MXene hydrogel devices is a result of the numerous ion transport porous hydrated network uniformly distributed in the hydrogel matrix. As a direct consequence of such superior rate performance and high capacitance, excellent power and energy density can be achieved from all the devices as evident from the Regone plot (Fig. 4.14.f). As an example, the FMH_0.5 symmetric device can deliver 12.8 Wh kg^{-1} at a power density of 230.4 W kg^{-1} and continues to deliver an ultrahigh power density of 29.4 kW kg^{-1} at 8.2 Wh kg^{-1} which further consolidates its applicability as potential candidate for supercapacitive energy storage solutions. To inspect the long-term operational stability of our symmetric device, we performed cycling stability test at 10 A g^{-1} for 15000 charge-discharge cycles for the representative best performing sample (FMH_0.5). The device demonstrates excellent long-term stability with 92% retention of initial capacitance as shown in Fig. 4.14.g. Furthermore, the device excellently maintains its high Coulombic efficiency (97%) for the entire operation indicating the outstanding reversibility of the electrochemical processes in the electrodes. The excellent stability and the high Coulombic efficiency can be attributed to the stable structure with numerous porous channels of the hydrogel electrodes, which reduces the energy loss in the charge-discharge process and maintains the stability of the devices in the long run.

Table 4.2. Energy storage performance of MXene based symmetric devices compared with field-assisted MXene hydrogels.

Sample	**Device capacitance ($F\ g^{-1}$)**	**Electrolyte**	**Reference**
d-Ti_3C_2/NF	51.1	6M KOH	[44]
$Ti_3C_2T_x$	85.5	3M H_2SO_4	[45]
Flexible MXene-rGO	80.3	3M H_2SO_4	[45]
$Ti_3C_2T_x$ Annealed in N_2/H_2	51	30 wt% KOH	[46]
V_2CT_x-$Ti_3C_2T_x$	78.7	1M H2SO4	[47]
$Ti_3C_2T_x$	35.4	1M H2SO4	[47]
$Ti_3C_2T_x$-rGO*	54	1M H2SO4	[48]
N-doped $Ti_3C_2T_x$*	81.8	6M KOH	[49]
Pristine $Ti_3C_2T_x$	58.4	6M KOH	[49]

Hydrothermal graphene-$Ti_3C_2T_x$*	66.9	6M KOH	[50]
Holey graphene/ $Ti_3C_2T_x$*	82.8	3 M H2SO4	[51]
N, O co-doped C@Ti_3C_2	53.8	6M KOH	[52]
MnO_2-$Ti_3C_2T_x$	60	1M Na_2SO_4	[53]
Field-assisted FMH_0.5	92.2	3M H_2SO_4	This work

In the current age of miniaturization, the charge stored per unit volume of electrode *i.e.* volumetric capacitance is considered as a highly important metric. However, any effort to increase volumetric capacitance by compacting the electrode generally lead to severe blockage of ion channels which result in a large sacrifice in gravimetric and rate performance. It is highly challenging yet extremely desirable to simultaneously achieve high volumetric and gravimetric values while retaining excellent charge-discharge rate performance. Interestingly, the hydrogels can be made into compact films by simply air-drying the electrodes in ambient conditions, and the films can still retain nano-channels with excellent surface availability as discussed earlier. These flexible dried films show a 50-fold reduction in thickness of electrode after the air-drying process, which drastically improves their volumetric density (Fig. 4.15).

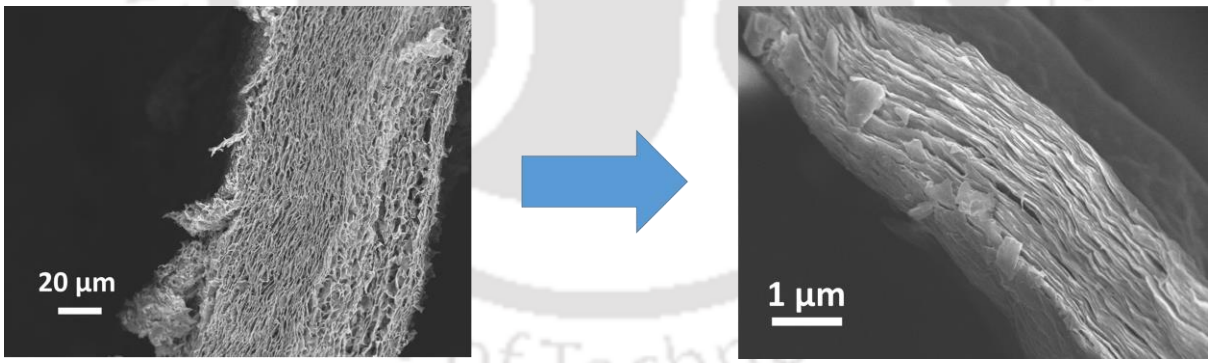

Figure 4.15. Thickness of field-assisted MXene electrodes before and after ambient drying.

The cyclic voltammetry curves of d-MF at different scan rates is shown in Fig. 4.16.a. Despite the compactness, the d-MF (3.4 g cm^{-3}) electrode shows excellent retention of the shape of CV curve which itself shows its outstanding rate capability. The d-MF electrode can provide an excellent volumetric capacitance of 1251 F cm^{-3} while maintaining an equally good gravimetric capacitance of 357 F g^{-1}. Excellent retention of gravimetric capacitance from hydrogel to dried film indicates that the presence of characteristic porous structure can potentially avoid

complete restacking of nano-sheets while drying and thus can maintain the high surface accessibility in even dried electrodes as also discussed earlier. This is also evident from the rate

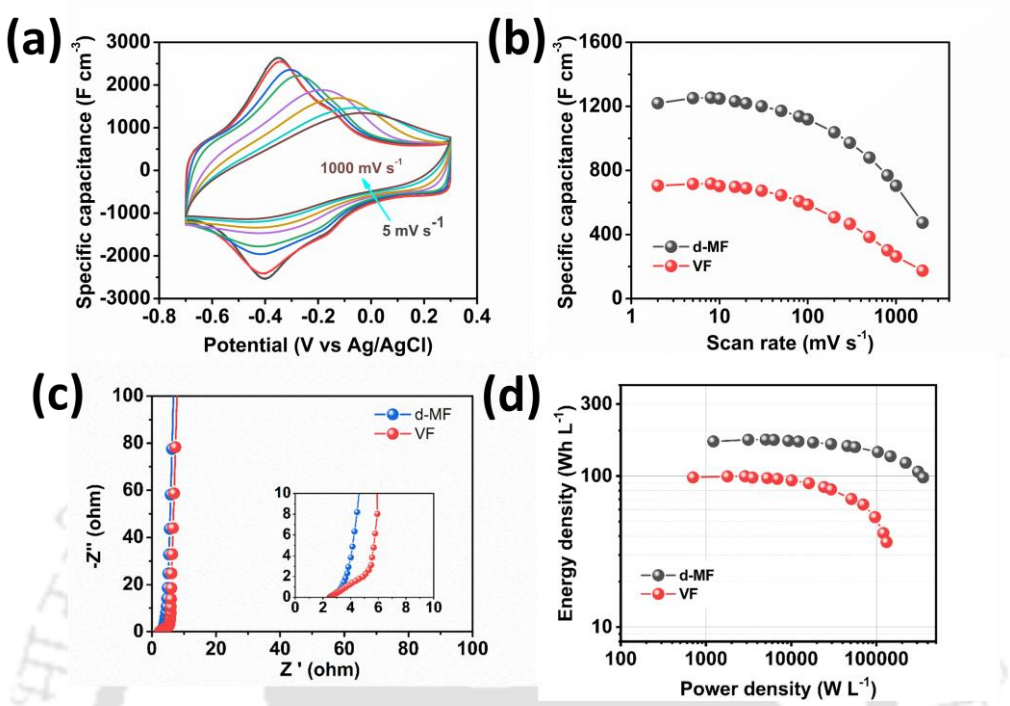

Figure 4.16. Electrochemical performance of d-MF electrodes measured in three-electrode configuration: (a) CV curves at different scan rates for d-MF electrode; (b) Change of specific capacitance with scan rate for Vacuum filtered (VF) and dried MXene hydrogel films (d-MF); (c) Nyquist plot of d-MF and VF electrodes with low frequency Warburg region indicating higher diffusion resistance for VF electrodes; (d) Regone plot of d-MF and VF electrodes exhibiting the superior energy and power density metrics of d-MF.

performance of the d-MF which retains almost 58% capacitance at 1000 mV s^{-1} (Fig. 4.16.b). In comparison, the VF electrode (3.5 g cm^{-3}) provides 704 F cm^{-3} at 2 mV s^{-1} and retains 37% of the initial capacitance at similar scan rates. The corresponding EIS spectra of the two electrodes also indicates lower diffusion resistance in d-MF as the Nyquist plot shows a steeper rise of imaginary capacitance compared to the vacuum filtered electrode (Fig. 4.16.c). Such excellent rate capability along with high volumetric capacitance enables high energy and power densities in d-MF electrodes. The d-MF electrode delivers a maximum energy density of 169.4 Wh L^{-1} with a maximum power density of 332.1 kW L^{-1} which is much better than that of VF (131.5 kW L^{-1}) electrodes (Fig. 4.16.d). This volumetric value is among one of the best value reported with pure MXene based systems.[27,54,55] The stability of the d-MF was investigated for 15000 charge-discharge cycles where the electrodes show an outstanding capacity retention of

95% which validates its long-term stability and usability (Fig. 4.17). Thus the excellent performance of electric field assisted MXene electrodes in energy storage, paired with the simplified, highly scalable gelation strategy can truly set the tune for widespread MXene application and adoptation.

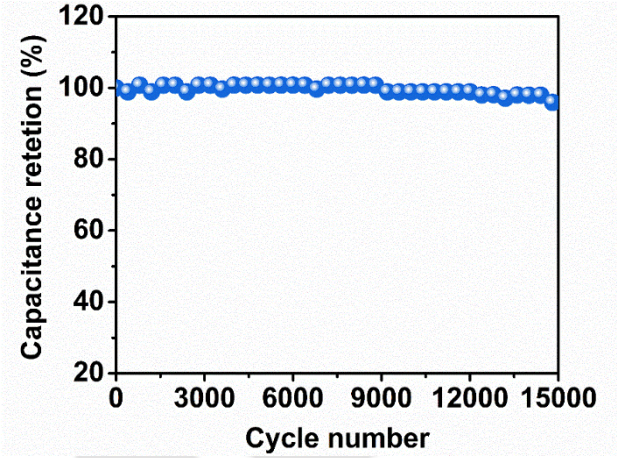

Figure 4.17. Stability test of d-MF electrode for 15000 charge-discharge cycles at 5 A g^{-1}.

4.4. Conclusions

In summary, an electric field-controlled and highly scalable scheme has been introduced for the ordered assembly of MXene nanosheets into customized self-standing hydrogels. Such an oriented gelation is highly dependent on the type of metal electrodes and their redox potentials. Voltage tunable regulation of redox potentials and hence, control in in-situ local release of positive ions from metal electrode in combination with the field-guided ordered assembly of MXene nanosheets can bypass the requirement of high critical dispersion concentrations to obtain stable, self-standing hydrogels. Through alteration of electric field distribution with proper electrode assembly, MXene hydrogels having in-plane or out-of-plane sheet arrangement can be achieved. The porous hydrated network of MXene 2D hydrogels provides numerous ion transport channels while water intercalated hydrogel matrix restricts face-to-face restacking of nanosheets. As a result, the MXene hydrogels exhibit excellent energy storage with superb charge-discharge rate performance, and capacitance as high as 395 F g^{-1} was achieved with 42% retention at 5000 mV s^{-1}. In a nutshell, these multi-dimensional, highly scalable MXene hydrogels developed through the field-induced gelation method can truly lead the future of MXene hydrogel research to reach its full potential.

References

1. Yin, J. *et al.* Large scale assembly of nanomaterials: mechanisms and applications. *Nanoscale* **12**, 17571–17589 (2020).
2. Guo, Y. *et al.* Hydrogels and Hydrogel-Derived Materials for Energy and Water Sustainability. *Chem. Rev.* **120**, 7642–7707 (2020).
3. Thoniyot, P. *et al.* Nanoparticle–Hydrogel Composites: Concept, Design, and Applications of These Promising, Multi-Functional Materials. *Adv. Sci.* **2**, 1400010 (2015).
4. Zhang, Z. *et al.* Recent Developments of Nanomaterials in Hydrogels: Characteristics, Influences, and Applications. *ChemistrySelect* **6**, 12358–12382 (2021).
5. Naguib, M. *et al.* Two-dimensional nanocrystals produced by exfoliation of Ti 3AlC 2. *Adv. Mater.* **23**, 4248–4253 (2011).
6. Naguib, M. *et al.* Two-Dimensional Transition Metal Carbides. *ACS Nano* **6**, 1322–1331 (2012).
7. Xu, D. *et al.* High-rate aqueous zinc-ion batteries enabled by a polymer/graphene composite cathode involving reversible electrolyte anion doping/dedoping. *J. Mater. Chem. A* **9**, 10666–10671 (2021).
8. Dutta, P. *et al.* Graphene aided gelation of MXene with oxidation protected surface for supercapacitor electrodes with excellent gravimetric performance. *Carbon N. Y.* **169**, 225–234 (2020).
9. Sikdar, A. *et al.* Spontaneous three-dimensional self-assembly of MXene and graphene for impressive energy and rate performance pseudocapacitors. *Electrochim. Acta* **391**, 138959 (2021).
10. Morales-Garciá, Á., Calle-Vallejo, F. & Illas, F. MXenes: New Horizons in Catalysis. *ACS Catal.* **10**, 13487–13503 (2020).
11. Shahzad, F. *et al.* Electromagnetic interference shielding with 2D transition metal carbides (MXenes). *Science (80-.).* **353**, 1137–1140 (2016).
12. Huang, J., Li, Z., Mao, Y. & Li, Z. Progress and biomedical applications of MXenes. *Nano Sel.* **2**, 1480–1508 (2021).
13. Hu, T., Yang, J., Li, W., Wang, X. & Li, C. M. Quantifying the rigidity of 2D carbides (MXenes). *Phys. Chem. Chem. Phys.* **22**, 2115–2121 (2020).
14. Wu, Z. *et al.* The Assembly of MXenes from 2D to 3D. *Adv. Sci.* **7**, 1903077 (2020).
15. Yan, J. *et al.* Flexible MXene/Graphene Films for Ultrafast Supercapacitors with Outstanding Volumetric Capacitance. *Adv. Funct. Mater.* **27**, (2017).
16. Yuan, W. *et al.* MXene-composited highly stretchable, sensitive and durable hydrogel for flexible strain sensors. *Chinese Chem. Lett.* **32**, 2021–2026 (2021).

17. Xu, C. *et al.* MXene (Ti3C2Tx) and Carbon Nanotube Hybrid-Supported Platinum Catalysts for the High-Performance Oxygen Reduction Reaction in PEMFC. *ACS Appl. Mater. Interfaces* **12**, 19539–19546 (2020).

18. Chen, H. *et al.* Pristine Titanium Carbide MXene Hydrogel Matrix. *ACS Nano* **14**, 10471–10479 (2020).

19. Deng, Y. *et al.* Fast Gelation of Ti3C2Tx MXene Initiated by Metal Ions. *Adv. Mater.* **31**, 1902432 (2019).

20. Dutta, P. *et al.* Freestanding MXene-hydrogels prepared via critical density-controlled self-assembly: high-performance energy storage with ultrahigh capacitive vs. diffusion-limited contribution. *J. Mater. Chem. A* **9**, 25013–25023 (2021).

21. Yun, T. *et al.* Multidimensional Ti 3 C 2 T x MXene Architectures via Interfacial Electrochemical Self-Assembly. *ACS Nano* **15**, 10058–10066 (2021).

22. Liu, Y. *et al.* Controllable growth of vertically aligned graphene on C-face SiC. *Sci. Reports 2016 61* **6**, 1–10 (2016).

23. Aradilla, D., Delaunay, M., Sadki, S., Gérard, J. M. & Bidan, G. Vertically aligned graphene nanosheets on silicon using an ionic liquid electrolyte: towards high performance on-chip micro-supercapacitors. *J. Mater. Chem. A* **3**, 19254–19262 (2015).

24. Wang, H. *et al.* Facile growth of vertically-aligned graphene nanosheets via thermal CVD: The experimental and theoretical investigations. *Carbon N. Y.* **121**, 1–9 (2017).

25. Liao, Q. Y., Li, S. Y., Cui, H. & Wang, C. Vertically-aligned graphene@Mn3O4 nanosheets for a high-performance flexible all-solid-state symmetric supercapacitor. *J. Mater. Chem. A* **4**, 8830–8836 (2016).

26. Zhang, P., Li, J., Lv, L., Zhao, Y. & Qu, L. Vertically Aligned Graphene Sheets Membrane for Highly Efficient Solar Thermal Generation of Clean Water. *ACS Nano* **11**, 5087–5093 (2017).

27. Bayram, V. *et al.* MXene Tunable Lamellae Architectures for Supercapacitor Electrodes. *ACS Appl. Energy Mater.* **3**, 411–422 (2019).

28. Chen, H. *et al.* Pristine Titanium Carbide MXene Hydrogel Matrix. *ACS Nano* **14**, 10471–10479 (2020).

29. Alhabeb, M. *et al.* Guidelines for Synthesis and Processing of Two-Dimensional Titanium Carbide (Ti3C2Tx MXene). *Chem. Mater.* **29**, 7633–7644 (2017).

30. Giannozzi, P. *et al.* QUANTUM ESPRESSO: A modular and open-source software project for quantum simulations of materials. *J. Phys. Condens. Matter* **21**, 395502 (2009).

31. Perdew, J. P., Burke, K. & Ernzerhof, M. Generalized gradient approximation made simple. *Phys. Rev. Lett.* **77**, 3865–3868 (1996).

32. Prandini, G., Marrazzo, A., Castelli, I. E., Mounet, N. & Marzari, N. Precision and efficiency in solid-state pseudopotential calculations. *npj Comput. Mater. 2018 41* **4**, 1–13 (2018).

33. Monkhorst, H. J. & Pack, J. D. Special points for Brillouin-zone integrations. *Phys. Rev. B* **13**, 5188–5192 (1976).

34. Halim, J. *et al.* X-ray photoelectron spectroscopy of select multi-layered transition metal carbides (MXenes). *Appl. Surf. Sci.* **362**, 406–417 (2016).

35. Ghidiu, M. *et al.* Ion-Exchange and Cation Solvation Reactions in Ti3C2 MXene. *Chem. Mater.* **28**, 3507–3514 (2016).

36. Mariano, M. *et al.* Solution-processed titanium carbide MXene films examined as highly transparent conductors. *Nanoscale* **8**, 16371–16378 (2016).

37. Caffrey, N. M. Effect of mixed surface terminations on the structural and electrochemical properties of two-dimensional Ti3C2T2 and V2CT2 MXenes multilayers. *Nanoscale* **10**, 13520–13530 (2018).

38. Shang, T. *et al.* 3D Macroscopic Architectures from Self-Assembled MXene Hydrogels. *Adv. Funct. Mater.* **29**, (2019).

39. Zhao, S. *et al.* Highly Electrically Conductive Three-Dimensional Ti3C2Tx MXene/Reduced Graphene Oxide Hybrid Aerogels with Excellent Electromagnetic Interference Shielding Performances. *ACS Nano* **12**, 11193–11202 (2018).

40. Ling, Z. *et al.* Flexible and conductive MXene films and nanocomposites with high capacitance. *Proc. Natl. Acad. Sci. U. S. A.* **111**, 16676–16681 (2014).

41. Huang, Y. L. & Bian, S. W. Vacuum-filtration assisted layer-by-layer strategy to design MXene/carbon nanotube@MnO2 all-in-one supercapacitors. *J. Mater. Chem. A* **9**, 21347–21356 (2021).

42. Cui, Z. *et al.* Lightweight MXene/Cellulose Nanofiber Composite Film for Electromagnetic Interference Shielding. *J. Electron. Mater.* **50**, 2101–2110 (2021).

43. Tian, Y. *et al.* Understanding MXene-Based 'symmetric' Supercapacitors and Redox Electrolyte Energy Storage. *ACS Appl. Energy Mater.* **3**, 5006–5014 (2020).

44. Guo, J., Zhao, Y., liu, A. & Ma, T. Electrostatic self-assembly of 2D delaminated MXene (Ti3C2) onto Ni foam with superior electrochemical performance for supercapacitor. *Electrochim. Acta* **305**, 164–174 (2019).

45. Yan, J. *et al.* Flexible MXene/Graphene Films for Ultrafast Supercapacitors with Outstanding Volumetric Capacitance. *Adv. Funct. Mater.* **27**, 1701264 (2017).

46. Rakhi, R. B., Ahmed, B., Hedhili, M. N., Anjum, D. H. & Alshareef, H. N. Effect of Postetch Annealing Gas Composition on the Structural and Electrochemical Properties of Ti2CTx MXene Electrodes for Supercapacitor Applications. *Chem. Mater.* **27**, 5314–5323 (2015).

47. Chen, K. *et al.* Vertically pillared V2CTx/Ti3C2Tx flexible films for high-performance supercapacitors. *J. Alloys Compd.* **906**, 164302 (2022).

48. Guo, B. *et al.* A binder-free electrode based on Ti3C2Tx-rGO aerogel for supercapacitors. *Colloids Surfaces A Physicochem. Eng. Asp.* **595**, 124683 (2020).

49. Yoon, Y. *et al.* A Strategy for Synthesis of Carbon Nitride Induced Chemically Doped 2D MXene for High-Performance Supercapacitor Electrodes. *Adv. Energy Mater.* **8**, 1703173 (2018).

50. Zhang, L. & Or, S. W. Self-assembled three-dimensional macroscopic graphene/MXene-based hydrogel as electrode for supercapacitor. *APL Mater.* **8**, 091101 (2020).

51. Fan, Z. *et al.* Modified MXene/Holey Graphene Films for Advanced Supercapacitor Electrodes with Superior Energy Storage. *Adv. Sci.* **5**, 1800750 (2018).

52. Pan, Z. & Ji, X. Facile synthesis of nitrogen and oxygen co-doped C@Ti3C2 MXene for high performance symmetric supercapacitors. *J. Power Sources* **439**, 227068 (2019).

53. Liu, W. *et al.* Molecularly Stacking Manganese Dioxide/Titanium Carbide Sheets to Produce Highly Flexible and Conductive Film Electrodes with Improved Pseudocapacitive Performances. *Adv. Energy Mater.* **7**, 1602834 (2017).

54. Dall'Agnese, Y. *et al.* High capacitance of surface-modified 2D titanium carbide in acidic electrolyte. *Electrochem. commun.* **48**, 118–122 (2014).

55. Ghidiu, M., Lukatskaya, M. R., Zhao, M.-Q., Gogotsi, Y. & Barsoum, M. W. Conductive two-dimensional titanium carbide 'clay' with high volumetric capacitance. *Nat. 2014 5167529* **516**, 78–81 (2014).

Chapter 5

Guided Co-Assembly of MXene and Cellulose Nanofibers: Simultaneous Achievement of All Three Energy Metrics with Ultrahigh Loading Electrodes

Chapter 5

Guided Co-Assembly of MXene and Cellulose Nanofibers: Simultaneous Achievement of All Three Energy Metrics with Ultrahigh Loading Electrodes

Development of supercapacitive electrodes with simultaneous achievement of all three pillars of energy storage metrics, i.e. gravimetric, volumetric and areal capacitance, while reaching the commercial scale requirements is nothing less than a story of wonderland. The strong van der Waals interaction induced face-to-face restacking in nanosheets still remains the fundamental challenge to be addressed in supercapacitive electrode design. While a compact thin electrode is essential for volumetric performance, it reduces the gravimetric and areal capacitance in the electrode. On the other hand, a porous structure with ample pores may increase the gravimetric performance but severely affects the volumetric one. Such conflicting characteristics imposes a huge challenge to be addressed in supercapacitive electrode development. In this chapter, we introduce an electric field assisted co-assembly of MXene and bio derived cellulose nanofibers to develop highly scalable and flexible composite films for supercapacitive energy storage research. The cellulose nanofibers act as spacers that gives rise to ion transport veins in the compact MXene films which allows development of supercapacitive electrode with mass loadings as high as 73.4 mg cm^{-2} with an areal and volumetric capacitance of 16 F cm^{-2} and 1356 F cm^{-3}. The assembly method can be further used to develop MXene composite over other ion-permeable substrates. As an example MXene cellulose composite is developed over carbon cloths to fabricate wearable energy storage devices. Such versatile, scalable strategy can truly lead MXene research to break free from the existing bottlenecks in supercapacitive research.

5.1. Introduction

The outstanding energy storage properties of supercapacitors are yet to see the daylight when it comes to widespread commercialization. Despite numerous research with intensive studies in several two-dimensional (2D) materials, the situation always trickles down to three fundamental major challenges. These can be summarized as, 1) realization of a commercially viable and scalable synthesis strategy, 2) stability of materials and lastly 3) the ability to scale up electrode mass loading to commercial levels without compromising performance.[1–3] Among these issues the last is rarely discussed as increase in mass loadings, i.e. mass of electrode per

unit area, inevitably increases the face-to-face restacking in 2D materials which gives rise to plethora of challenges to be addressed.[4–6] Decrease in surface active site availability, increase in electrolyte ion transfer resistance, ohmic losses leading to decreased coulombic efficiency, compromise in power density metrics are some of such indispensable difficulties associated with mass loading upscaling.

Transition metal carbides and or nitrides or popularly known as MXene, has been the epicenter of supercapacitive research for the last few years.[7] Among 150+ predicted MXene structures, titanium based $Ti_3C_2T_x$ (T_x represents surface functional groups like O, OH, F) MXene has been leading the MXene family towards multidisciplinary research in areas such as energy storage,[8,9] electromagnetic interference shielding,[10,11] sensors,[12,13] solar water evaporation,[14] catalysis[15] etc. However, similar to graphene, the 2D sheet like structures of MXene also suffer from strong van der Waals interaction induced restacking while developing macrostructures.[16] This along with the increased ion-diffusion resistance reduces the accessible electroactive pseudocapacitive sites in MXene materials and thus limits the gravimetric capacitance of the material. To address this, several strategies have been proposed in recent times. Nanomaterials like graphene,[17] carbon nanotubes (CNT),[18] transition metal oxides[19,20] have been extensively used to act as spacers in the MXene based macrostructures. For example, Zhao et al. introduced multi walled CNT in MXene films via alternating vacuum filtration of MXene and CNT dispersion. Presence of CNT as spacer improved the capacitance and rate performance of the material and reached 390 F cm^{-3} and 150 F g^{-1} volumetric and gravimetric capacitance respectively.[21] Further, holey graphene was also introduced in MXene via vacuum filtration method to develop MXene/holey graphene films.[17] Although such hybrid structures vastly improved the volumetric capacitance reaching upto 1445 F cm^{-3}, the capacitance quickly decreased to 988 F cm^{-3} (12.6 mg cm^{-2}) as the mass loading of the electrodes were increased to match the commercial levels. It is important to note that development of thin films of MXene has been the popular strategy due to its easy processability, flexible nature and ease of handling.[22] In this regard, most of the reported MXene and MXene based films are developed through vacuum filtration method where the severe pressure gradient during synthesis effects the restacking and thus the electrochemical performance of the electrodes which is often not completely compensated by introducing the above mentioned spacers.

Here in this report, we introduce co-assembly of MXene and bioinspired cellulose nanofibers in an electric field assisted guided layer-by-layer interfacial assembly method. The garlic husk derived ultrathin cellulose nanofibers act as spacers in MXene thin film framework and

introduces several ion-transport channels via introducing wrinkled valleys of MXene around the fibers. Such restacking controlled MXene composite films achieved an excellent gravimetric performance of 358 F g^{-1}. More importantly electrode with extremely high mass loading (73.4 mg cm^{-2}) were successfully developed which shows an excellent combination of high storage metrics such as 16 F cm^{-2}, 1356 F cm^{-3} and 221 F g^{-1} of areal, volumetric and gravimetric capacitance respectively. Such a combination of metrics is rarely reported for MXene or other nanomaterial based energy storage research. Furthermore, a full asymmetric device was also developed in conjunction of reduced graphene/CNT/polyaniline positive electrode and MXCF negative anode which delivers 27.8 Wh kg^{-1} energy density at 501 W kg^{-1} power density with a maximum power density output of 123 kW kg^{-1}. Apart from the high performance device and high mass loading electrode development, the versatility of electric field guided co-assembly lies in the fact that such composite films of MXene can be developed over any ion-permeable conducting and non-conducting surfaces. As a proof of concept we developed MXCF films over carbon cloth to develop wearable solid state devices that can uninterruptedly deliver power irrespective to the bending condition. Amalgamation of such characteristics over a single electrode development strategy can not only take MXene energy storage to new heights but also takes the material to a step closer to commercial adaptation.

5.2. Experimental

5.2.1. Preparation of MXene:

MXene was produced from MAX phase Ti_3AlC_2 using insitu HF etching method.[23] Typically, 20 mL (9M) HCl was used to dissolve 1.6 g LiF. The solution was kept under stirring until all the fluoride salt completely dissolved. 1 g Ti_3AlC_2 was then slowly added into the solution which was kept in ice bath. The mixture was kept at 35ºC for 24 hours under continuous stirring to allow the etchant solution to etch out the Al from the MAX phase. After the etching, the acidic mixture was washed with deionized water via centrifugation until the pH became ~ 6. After the centrifugation, the solution was then sonicated under continuous Argon purging for one hour during which the temperature was maintained under 30 ºC. Thereafter, the delaminated solution was again centrifuged at 3500 rpm for one hour and only the supernatant was collected to discard any delaminated parts.

5.2.2. Preparation of CNF from garlic husk:

5 grams of garlic husk was first thoroughly washed and dried before adding it to 200 g of NaOH solution for 5 h at 140 ºC. After washing with deionized water to pH ~7 the treated cellulose

was further put into a mixture of 100 g of H_2SO_4 solution and 150 g of sodium chlorite for 6h stirring at 80 ºC. This removes the lignin in the material and finally the mixture was probe sonicated at 300 W for 3h followed by stirring to collect the colloidal solution.

5.2.3. Preparation of MXene/CNF films:

MXene/CNF hybrid films were prepared using field assisted gelation technique discussed previously.[14] Briefly, dispersions of MXene and CNF were mixed in different weight ratios and the dispersion was then stirred for 3 hours to prepare a homogenous dispersion. The weight of CNF in dispersion was varied with 10% ,20% and 50% while the overall concentration of the solution was fixed at 10 mg mL^{-1}. Two polished Zn plates were dipped into the dispersion at 1 cm apart in parallel and a potential of 1.1 V was applied for varying times. The negatively charged MXene and CNF were co-assembled over the Zn plate to develop a hydrogel structure which was then separated from the Zn plate using 1 M HCl solution. The resulting freestanding hydrogel was washed with de-ionized water several times before drying in ambient condition overnight to develop flexible MXene/CNF film electrodes. The resulting films were denoted as MXCF_X where X denotes the amount of CNF in the MXene-CNF dispersion used to develop the electrode.

The wearable MXene/CNF electrodes were also developed using the previous description. Here, before gelation, the positive Zn plate was covered with a carbon cloth (CC) to allow the gelation to proceed above the material. The resulting hydrogel was separated with above mentioned HCl solution along with the CC which strongly attached with the MXene-CNF framework. The rest of the procedure to develop MXene/CNF over CC is same as above.

5.2.4. Preparation of solution processable rGO/CNT/PANI positive electrode:

Graphene oxide was developed through a modified Hummers method reported earlier.[24,25] Solution processable reduced graphene oxide (rGO) was synthesized using the method proposed by Li *et al.*[26] In brief, in a 30 mL homogenous dispersion of graphene oxide (0.2 mg mL^{-1}) , 5.8 µL hydrazine (35 *wt%*) and 24 µL ammonia solution () was mixed and stirred for few minutes in a glass vial. The mixture was then kept at 90 ºC for one hour in a hot air oven to get uniformly dispersed rGO solution.

Multi-walled carbon nanotubes (MWCNT) were acid treated to develop surface functionalized CNTs. In brief, 60 mg of CNT was put in 200 mL mixture of HNO_3 and H_2SO_4 (1:3 volume ratio). The solution was then heated at 70 ºC for 1 hr. under acid reflux. After cooling the

mixture was then washed with DI water and ethanol until the pH of the solution reached ~7. The resulted solution was then sonicated for 10 min to properly disperse the functionalized CNTs into the mixture.

Polyaniline (PANI) was prepared with an oil-water interfacial polymerization of aniline monomer using a method reported in our earlier work.[24] In brief, the aqueous solution consist of 0.8mmol ammonium persulfate (APS) was dissolved in 50 mL 1M HCl. On the other hand, the organic solution contained 3.2 mmol aniline monomer in 50 mL chloroform. The aqueous mixture was slowly put above the organic chloroform solution in a glass vial where the reaction can be seen to start at the interface instantly. The reaction was allowed overnight after which the PANI nanowires were collected and washed with ethanol and water thoroughly several times.

To develop the rGO/PANI/CNT hybrid film, the as prepared solution processable rGO was mixed with 0.75 *wt%* PANI and stirred thoroughly. Thereafter, 10 *wt%* CNT was mixed with the above solution and bath sonicated for 5 min to prepare a homogenous mixture. The mixture was then vacuum filtered and successively dried in ambient condition to prepare the rGO/PANI/CNT positive electrode.

5.2.5. Material characterization:

The morphological analysis of the samples was performed with field assisted scanning electron microscope (FESEM, Zeiss, Sigma-300) and JEOL-2100F field emission transmission electron microscope (FETEM). Crystal structure of the samples were analyzed with Rigaku made X-ray diffractometer in powder XRD mode with Cu-Kα source. The thermo-gravimetric analysis of the samples was performed with TA instruments Q SDT 600 with 10 ºC heating rate under the flow of nitrogen gas. X-ray photoelectron spectroscopy (XPS) was performed with ESCALAB Xi+ (Thermo Fisher Scientific Pvt.Ltd.).

5.2.6. Electrochemical characterization:

To analyze the electrochemical supercapacitive performance of the electrodes, the MXCF electrodes were analyzed with both three-electrode and two-electrode methods using PERSTAT 3000A-DX (Princeton Applied Research). For three-electrode measurements, MXCF or rGO/CNT/PANI, activated carbon and Ag/AgCl in 1M KCl were used as working, counter and reference electrode respectively. 3M H_2SO_4 was used as electrolyte for the three and two electrode measurements. Electrochemical impedance spectroscopy was performed in

a frequency range of 10 mHz to 100 kHz with an amplitude of 10 mV. To prepare the solid state electrolyte for wearable devices 10 mL 1M H_2SO_4 was mixed with 1g PVA and the mixture was stirred at 85 ºC until the mixture became white. MXCF electrodes prepared over CC were used as both the working and counter electrode with PVA/H_2SO_4 solid state electrolyte to develop the wearable devices.

The gravimetric capacitance of the samples was calculated from the cyclic voltammetry (CV) curves using the equation,

$$C_g = \frac{1}{mv\Delta U}\int i\, dU \tag{1}$$

where, ΔU is the potential window, v is the scan rate and i corresponds to the current density, m is the mass of the single working electrode and mass of both the working electrodes respectively for three-electrode and two-electrode systems respectively. .

For the asymmetric device, the masses of the positive (m_+) and negative (m_-) electrode were carefully balanced using the equation,

$$\frac{m_+}{m_-} = \frac{C_- \times \Delta E_-}{C_+ \times \Delta E_+} \tag{2}$$

where ΔE_+ and ΔE_- are the allowed potential windows for the positive and the negative electrode respectively. C_+ and C_- are the capacitance of the positive and negative electrode respectively.

The energy (E_g) and power (P_g) densities of the two-electrode devices were calculated from the equation,

$$E_g = \frac{C_g \times (\Delta U)^2}{2 \times 3.6} \tag{3}$$

$$P_g = \frac{E_g \times v \times 3600}{\Delta U} \tag{4}$$

5.3. Results and discussions

The integration of MXene and cellulose nanofibers into a freestanding thin film was performed using the electric field guided layer-by-layer assembly approach as described in the previous chapter. CNFs used in this work are prepared from garlic husk waste after lignin removal treatment with H_2SO_4 and sodium chlorite. Successful separation of individual cellulose fibers

can be confirmed from the TEM image as shown in Fig. 5.1, where the micron length CNF strands with a diameter of 10-60 nm can be clearly identified. For electric field guided co-assembly of MXene and CNF, a colloidal dispersion of the two was put between two Zn plates acting as cathode and anode. Chemical etching of MAX phase Ti_3AlC_2 introduces several functional groups like F, O and OH over the basal plane of MXene. Presence of these functional groups along with those over the surface modified CNFs promotes interaction between these nanomaterials through hydrogen bonds. As a bias is applied across the two metal plates, the negatively charged MXene nanosheets gets attracted towards the positive anode. Subsequently the stimulated forced release of Zn^{2+} ions at the interface further interacts with these negatively charged MXenes to mitigate the electrostatic repulsion among the nanosheets. As the reduction potential of Zn is lower than that of MXene, the MXene sheets gets partially reduced though removal of oxygen containing functional groups which increases the van der Waals interaction among these nanosheets. Further, as there exist a mutual interaction between the CNFs and MXene, the CNFs are dragged along with MXene sheets and gets decorated uniformly within the hydrogel framework that builds over the metal surface as shown schematically in Fig. 5.2.

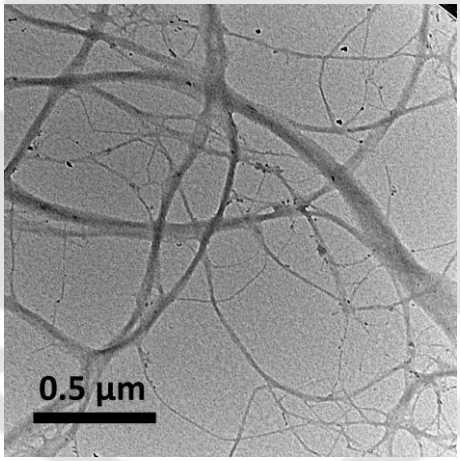

Figure 5.1. TEM image of CNF nanofibers indicating the micron sized fibers after lignin removal treatment.

After separation of the hydrogel from the Zn plate, the resulting macrostructure is then washed and then dried in ambient conditions to develop the MXCF electrodes. It is important to note that during assembly, the complete face-to-face restacking of these nanosheets are reduced due to the intercalated water that remains in the pores of the hydrogel paired with the ultrathin CNF microfibers that wraps the MXene nanosheets around itself to provide ample ion channels even in the dried films.

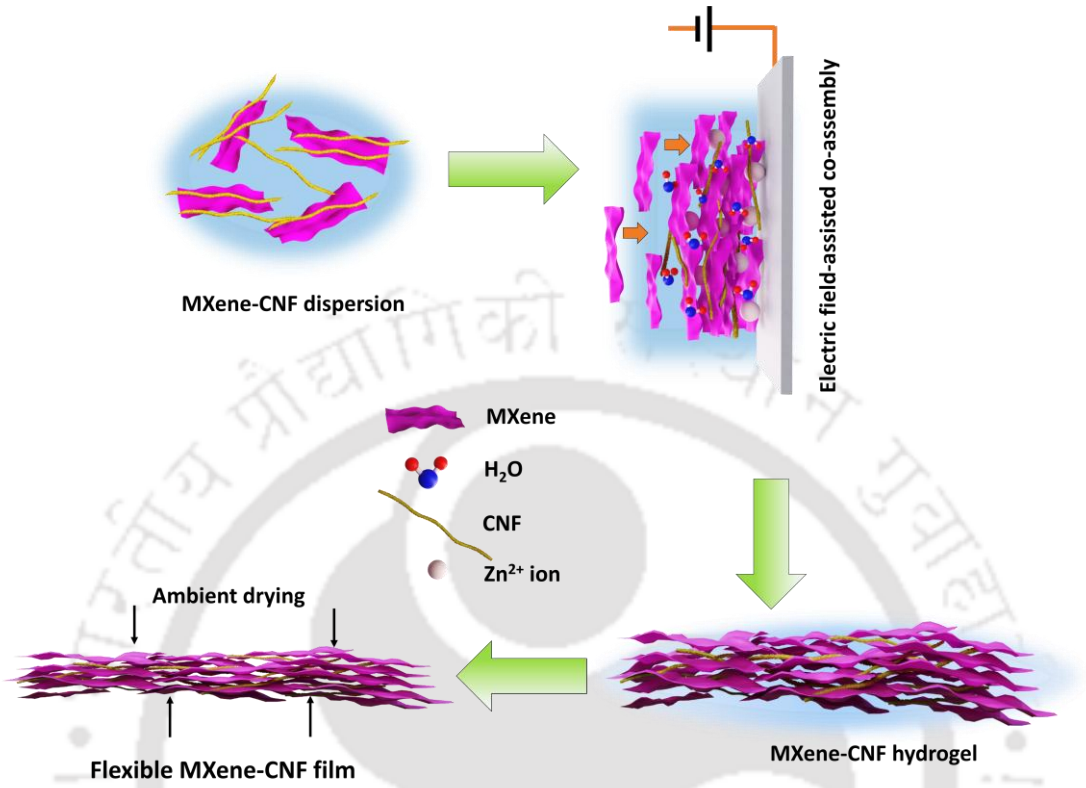

Figure 5.2. Schematic illustration of MXCF preparation with electric field guided forced assembly.

5.3.1. Morphological and structural analyses of MXCF films:

To confirm the presence of CNF over the entire film, we performed a cross-sectional FESEM analysis of the MXCF electrodes. As evident from Fig. 5.3.a, a lot of nanofibers can be identified to be distributed over the entire cross-section of the dried film. On the other hand, the top surface of the composite film shows wrinkled structure due to the interconnected

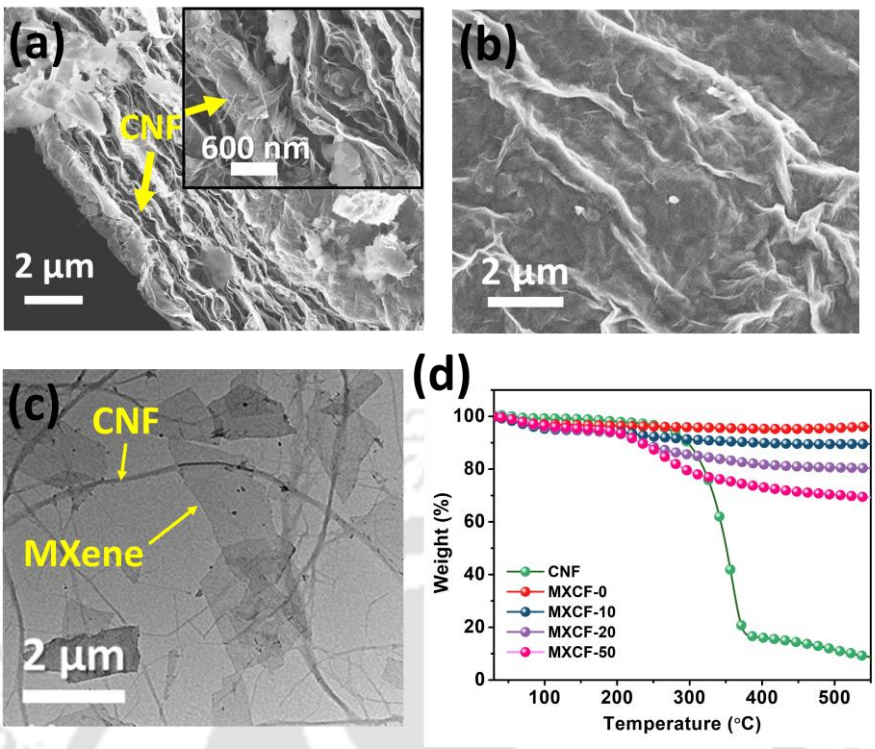

Figure 5.3. Morphological and quantitative analysis of MXCF composites: (a) cross-sectional view and (b) top view of MXCF films; (c) TEM analysis of MXCF films showing co-assembly of MXene and CNFs, (d) TGA analysis to investigate the content of CNF in different samples.

MXene 2D sheets without much of visible CNFs (Fig. 5.3.b). The co-assembly of MXene and CNF in electric field guided assembly can be further confirmed from the TEM analysis of the composite where delaminated thin MXene sheets are accompanied by CNFs (Fig. 5.3.c). Further, to positively estimate the actual content of CNF in the composite structure after gelation, TGA analysis was performed on different MXCF electrodes. For this MXCF films were prepared with different *wt%* of CNF in the parent colloidal dispersion. It can be seen that whereas the CNF loose almost all its weight within the temperature range of 250-400 ºC, the pure MXene sample, *i.e.* MXCF-0 almost retained all its mass over the experiment. This indicates the stability of the MXene in these temperatures unlike the CNFs which annealed entirely in the process. Interestingly, when CNF was added with MXene dispersion in *wt.%* of 10%,20% and 50%, these proportions very well reflect in the composite films also as after TGA analysis the weight loss for MXCF-10 and MXCF-20 and MXCF-50 is 89.4%, 80.5% and 68.6% respectively (Fig. 5.3.d). This indicates that when the content of MXene is higher than the CNF, nanofibers are uniformly adsorbed with MXene nanosheets and as a result the distribution of MXene:CNF remains same as the parent solution. However, when the amount

of CNF increases to about equal or greater than MXene, the adsorption becomes irregular and saturated which results in such reduced contribution of CNFs in MXCF-50 composite film.

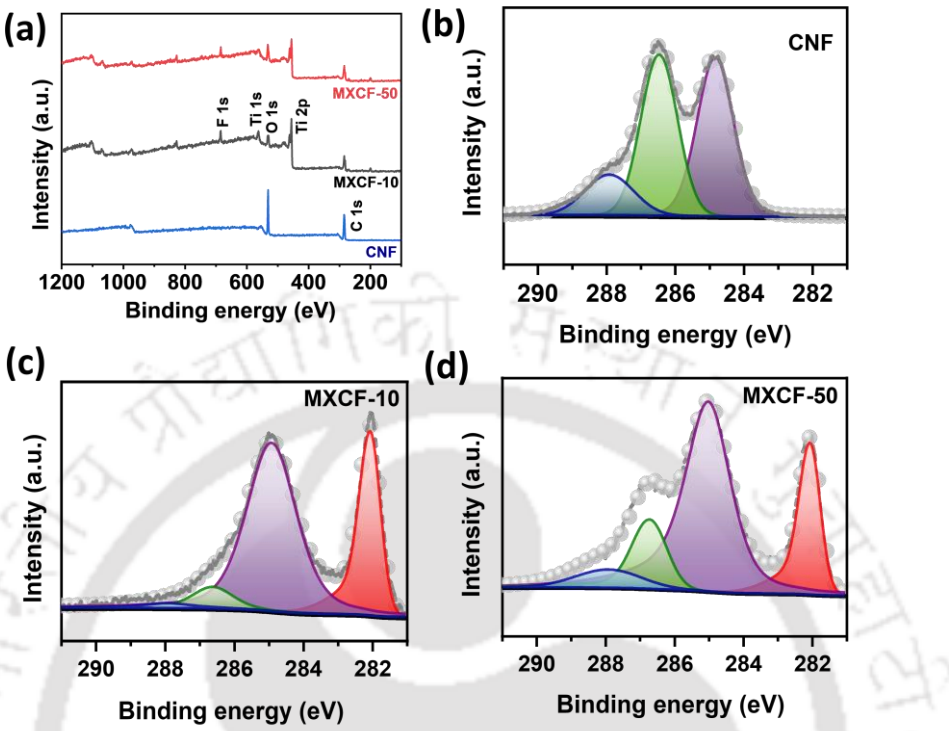

Figure 5.4. XPS study of MXCF and CNF for compositional and chemical property analysis: (a) survey spectra of CNF, MXCF-10 and MXCF-50; high resolution C 1s spectra of (b) CNF, (c) MXCF-10 and (d) MXCF-50. The red, purple, green and blue peaks represents C-Ti (282 eV), C-C (284.8 eV), C-OH (286.6 eV), C=O (287.9 eV) respectively.

5.3.2. Chemical structure analyses:

To further study the chemical structure and any CNF integration induced chemical modification, we performed the XPS analysis of MXCF and CNF samples. Firstly, the MXene containing samples *i.e.* MXCF-10 and MXCF-50 does not show any peaks due to Al which confirms the complete etching of the material from the parent MAX Ti_3AlC_2 (Fig. 5.4.a). The survey spectra of CNF show presence of C and O whereas MXCF includes Ti with O and F representing the functional groups. To further analyse the samples, we performed high-resolution XPS analysis of C 1s spectra. The high resolution C1s spectra can be deconvoluted into three peaks representing C-C (284.8 eV), C-OH (286.6 eV) and C=O (287.9 eV) for CNF (Fig. 5.4.b).[22] On the other hand, the MXCF films contains one more peak contributing from the characteristic C-Ti at 282 eV (Fig. 5.4.c,d).[27] As clearly evident from the XPS spectra, there is a significant increase in the relative peak intensity in C-OH and C=O in MXCF-50 compared

to MXCF-10 which is mainly due to the increased contribution of O containing groups from the nanofibers. Further, compared to MXCF-10, the C-C peak also has an increased intensity which also indicates towards the same.

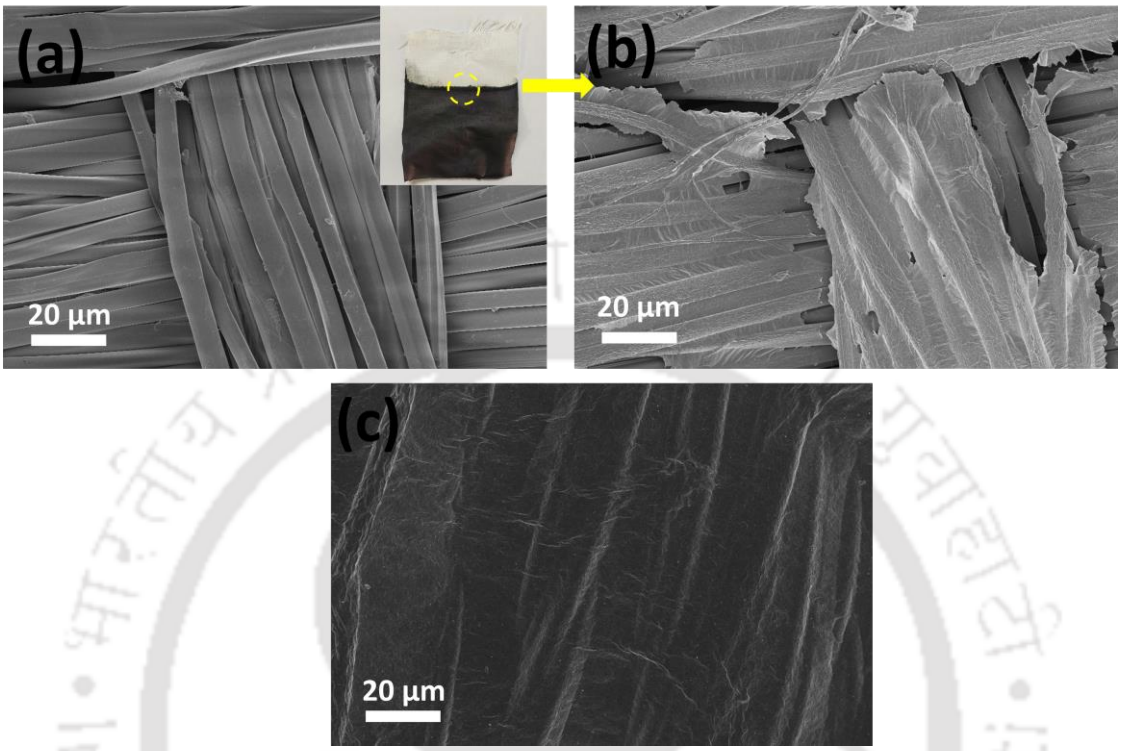

Figure 5.5. Transferability of MXCF composites over different ion-permeable substrate: (a) FESEM image of commercial cloth with the digital image of the composite film developed over the cloth in inset; (b) FESEM image of the cloth and MXCF junction showing covering of the cotton strands with MXene; (c) MXCF film developed over CC where the entire CC substrate is covered with a continuous uniform layer of MXCF.

5.3.3. Development of MXCF hybrids over ion-permeable substrates:

The benefits of electric-field assisted guided co-assembly is manifold. Not only this ultrafast gelation strategy is highly scalable, but due to the Zn^{2+} ion induced gelation, the assembly can take place over any ion-permeable conducting or non-conducting surface. We utilized this to develop MXene/CNF hydrogel structures over commercial non-conducting fabric as well as carbon cloth (CC). Fig. 5.5.a. shows the FESEM image of commercially available cotton fabric over which the MXCF composite film is successfully developed with field-assisted guided assembly (Fig. 5.5.a inset). The fabric and MXCF film junction is highlighted in Fig. 5.5.b where the gradual covering of the cotton fibers can be clearly seen. We also demonstrated the MXCF integration over a conducting CC where a uniform layer of MXCF can be seen to cover

the CC substrate (Fig. 5.5.c). The possibility of integrating MXCF composite over such flexible substrate in a highly scalable process gives rise to greater possibility of wearable energy storage which is presented later in this chapter.

5.3.4. Electrochemical characterization of MXCF electrodes

MXene materials exhibit excellent supercapacitive energy storage properties due to their metallic conductivity and high pseudocapacitive response. Dried films of MXene has always been the native choice for MXene based electrode development. However, the severe restacking in dried structure greatly restricts the fast electrochemical response and thus restricts the development of MXene based electrodes majorly below 5 mg cm^{-2}. In this scenario, the electric field assisted uniform decoration of CNFs over the cross-section can potentially restrict the complete face-to-face restacking and provide ample ion-transport channels. To investigate the electrochemical performance of these MXCF electrodes, the composites are analyzed in three-electrode configuration in 3M H_2SO_4 electrolyte. As seen from Fig. 5.6.a, all the samples exhibit two distinguished pseudocapacitive peaks around -0.4 V and -0.25 V vs Ag/AgCl which corresponds to the redox reaction of Ti site with electrolyte protons during the charge discharge cycles. Further, it is evident that the area under the curve is higher for MXCF_10 followed by MXCF_20 and MXCF_50 which is representative of the capacitance of these electrodes. As a result, the MXCF_10, MXCF_20 and MXCF_50 are able to deliver a capacitance of 358 F g^{-1}, 326 F g^{-1} and 157 F g^{-1} at 2 mV s^{-1} respectively. The significantly reduced capacity of MXCF_50 can be attributed to the significantly high content of CNFs in the structure which other than acting as spacer, behaves as dead weight in supercapacitive applications. To further highlight the importance of electric-field assisted gelation, we developed a MXene CNF composite film with commonly used vacuum filtration method. It is important to note that we kept the CNF content 10 *wt%* and the mass loading of the vacuum filtered film (VMCF_10, 0.45 mg cm^{-2}) similar to that of MXCF_10 (0.48 mg cm^{-2}) to properly compare their supercapacitive performance. As evident from the CV curves in Fig. 5.6.a, the area under the MXCF_10 is much greater than VMCF_10 resulting in a gravimetric capacitance of 276.4 F g^{-1} at 2 mV s^{-1} for VMCF_10, which is only 77% of the total capacitance of electric-field assisted MXCF_10 electrodes. Considering the similarities in their composition and macrostructural properties, such significant increase in capacitive performance can be attributed to the severe restacking in vacuum filtration techniques due to the high pressure gradient induced assembly. On the other hand, in field-assisted gelation, the layer-by-layer assembly of MXene and CNFs are greatly restacking controlled due to the intercalated water which retains the porous

channels. As the MXCF films are developed from these porous stable structures of hydrogels, these porous channels develop wrinkles in the entire structure that benefits overall surface

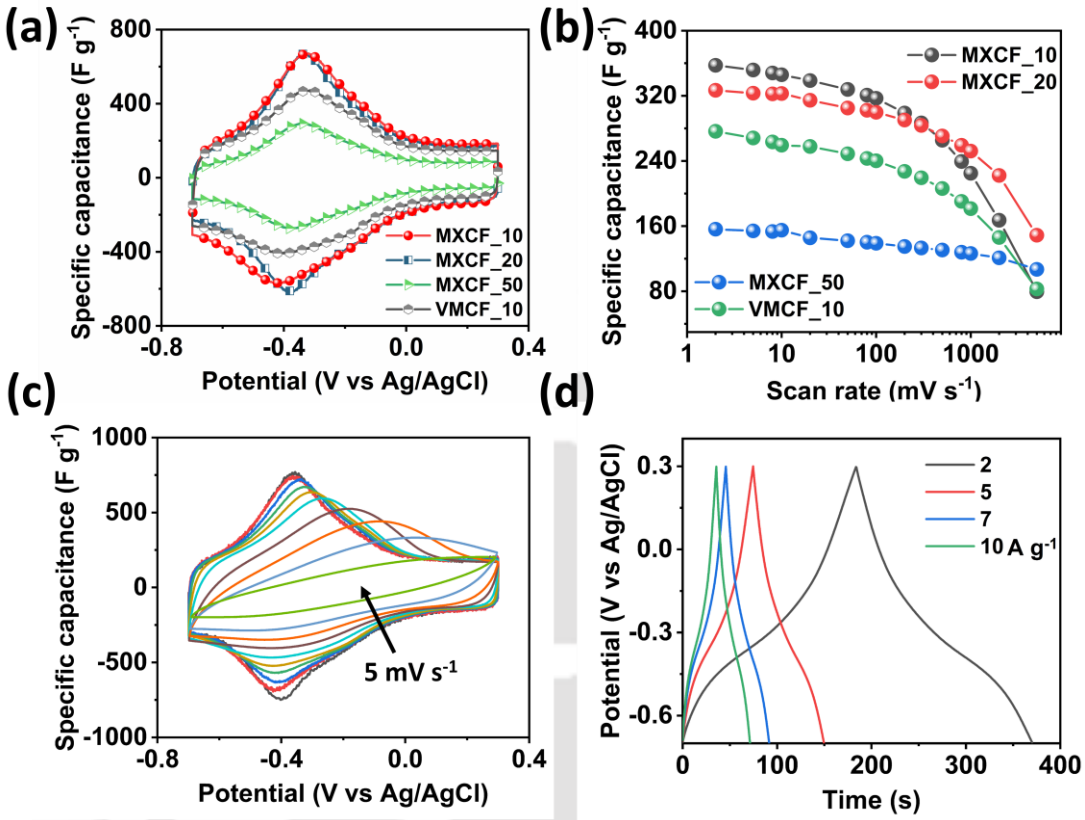

Figure 5.6. Electrochemical performance of MXCF electrodes in three-electrode configuration: (a) CV curves of different MXCF electrodes in comparison with VMCF electrode at 50 mV s^{-1}; (b) rate performance of the MXCF and VMCF electrode. (c) CV curves at different scan rates for MXCF_10 with scan rates 5, 10, 20, 50, 100, 200, 500, 1000, 2000 and 5000 mV s^{-1}, (d) GCD curves of MXCF_10 at different current densities showing the slightly deviated triangular nature.

accessibility and ions transport in the structure. This is further reflected in the rate performance, *i.e.* change of capacitance with increasing scan rate curve as shown in Fig. 5.6.b. As compared to VMCF_10 with 50% retention at 1000 mV s^{-1}, the MXCF_10 retains almost 63% of the capacitance. The excellent rate performance of the electrode also reflects in its CV curves recorded at different scan rates as shown in Fig. 5.6.c, where the polarization curves can be seen to retain excellent shape even at a scan rate of 5000 mV s^{-1}. Further, the GCD curves of MXCF_10 shows slight deviation from the usual triangular nature which is characteristic to MXene pseudocapacitive behavior (Fig. 5.6.d). Notably, the rate performance of the MXCF electrodes indicate a significant improvement with increasing CNF content. For example, the

MXCF_20 retains 77% of initial capacitance at 1000 mV s^{-1} and continues to have 46% of this capacity even at 5000 mV s^{-1}. This further improves in MXCF_50 with excellent 68% retention at 5000 mV s^{-1} (Fig. 5.6.b). This indicates that although MXCF_50 has lower overall capacitance, but the capacity is uniformly maintained even in extremely high scan rates, making it an excellent candidate for high rate applications.

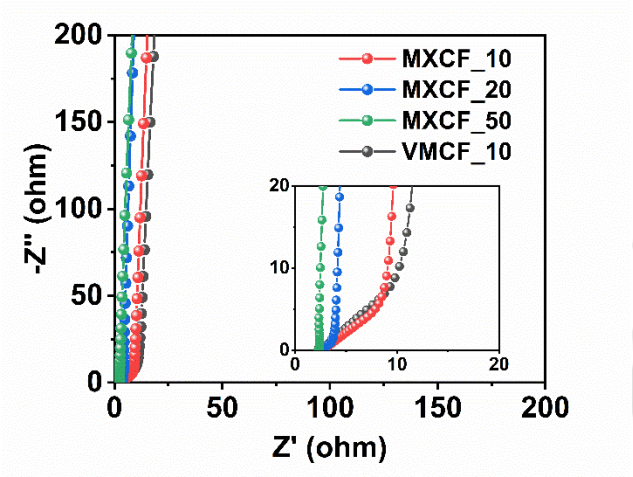

Figure 5.7. Electrochemical impedance spectroscopy of different electrodes. Inset shows the high frequency region of the Nyquist plot.

The EIS spectroscopy of electrodes provides insightful information about material conductivity, diffusion resistance of ions into the bulk of the electrode among others. The 45° line in the mid-frequency range of Nyquist plot indicates the Warburg resistance i.e. the semi-infinite diffusion resistance of ions into the electrode. As evident from the Fig. 5.7, the MXCF electrodes with 20% and 50% CNF content shows a much vertical increase of imaginary impedance than MXCF_10 which is indicative towards its better ion-diffusion capability as also found from CV tests. Notably, the VMCF_10 shows higher resistance to ion-diffusion compared to field-assisted MXCF_10 electrodes which further establishes its superiority over the vacuum filtration technique.

5.3.4.1. Energy storage performance of ultrahigh mass loading MXCF electrodes:

One of the biggest hurdles in supercapacitor development lies in simultaneous achievement of the three metrics of energy storage, *i.e.* a. gravimetric capacitance, b. areal capacitance and c. volumetric capacitance. Optimization of one of these metrics often lead to degradation of the other due to the very nature of how these parameters are defined. For example, increasing areal capacitance, *i.e.* the capacitance per unit area of electrode requires increasing the mass loading of the material. However, it increases the thickness and further due to the increased loading,

the restacking increases and the bulk of the material gets more restricted to electrolyte ions, which results in compromised gravimetric performance. Thus mass loading upscaling leads to a highly important challenge to be addressed due to which most of the reported electrodes are

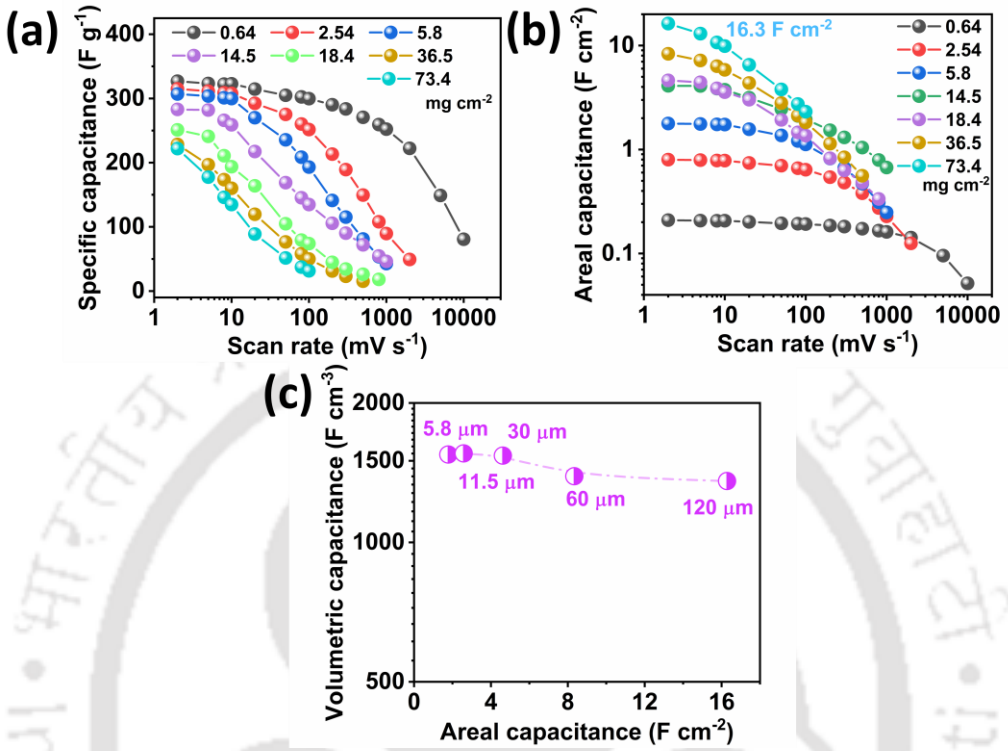

Figure 5.8. Specific capacitance of high mass loading MXCF electrodes showing the variation of (a) gravimetric capacitance and (b) areal capacitance at different scan rates; (c) volumetric capacitance of different MXCF electrodes with varying thickness.

often optimized for only one or two of the above metrics. In this report, inspired by the excellent gravimetric performance and rate performance of the MXCF electrodes, we developed supercapacitive electrodes with mass loading as high as 73.4 mg cm^{-2}. Such electrodes of ultrahigh mass loading not only provide excellent areal capacitance of above 16 F cm^{-2} but also delivers a volumetric and gravimetric capacitance of 1548 F cm^{-3} and 221 F g^{-1} respectively (Fig. 5.8.a). In order to achieve such high mass loadings, instead of developing a single thick electrode, we stacked one electrode over other to create a stacked assembly. The benefits of such approach are multifold: Firstly, assembly of a single continuous macrostructure increases the diffusion resistance immensely which severely effects the rate performance. On the other hand, the comparatively thinner electrodes are immune to such restacking which provides better surface accessibility and porous structure in the electrodes. Furthermore, due to the stacked assembly of individual electrodes, the macrochannels in-between two stacked films

provides greater access to the bulk of the electrode and thus can show significant improvement compared to the former. Secondly, as the electric field guided co-assembly of MXene and CNF is highly scalable, the thinner electrodes can be developed rapidly and can be immediately restacked to achieve desired mass loadings whereas development of single high mass loading macrostructure requires much longer time in gelation which increases the synthesis complexity. This makes the physical one over another assembly process far more commercially viable than development of single electrode devices. We developed MXCF electrodes upto 18.35 mg cm^{-2} with upto 45 mins of gelation and it was then further stacked to achieve the other higher mass loadings reported in this chapter. As seen from Fig. 5.8.a, the low mass loading electrodes have a maximum capacitance of 326 F g^{-1} for 0.64 mg cm^{-2} which still maintains upto 221 F g^{-1} for an ultrahigh loading of 73.4 mg cm^{-2}. On the other hand, the areal capacitance increases from 0.21 F cm^{-2} to an outstanding 16.2 F cm^{-2} (Fig. 5.8.b). Interestingly, the compact nature of these electrodes allows a stable volumetric performance of the electrodes. Fig. 5.8.c shows the volumetric capacitance of electrodes that have more than 1.5 F cm^{-2} of areal capacitance. As seen from the figure, all the electrodes maintain an excellent volumetric capacitance irrespective of the thickness. Further, as the electrode thickness increases by 20 fold, the volumetric capacitance is still maintained upto 88% of the initial 1548 F cm^{-3}. Thus, in a nutshell the MXCF electrode with a mass loading of 73.4 mg cm^{-2} delivers an areal and volumetric capacitance of 16.2 F cm^{-2} and 1356.9 F cm^{-3} while still providing a gravimetric capacitance of 221 F g^{-1}. Such combination of energy storage metrics is rarely reported in literature for any MXene or other 2D material based electrodes which establishes the importance of such restacking controlled assembly of MXene for commercial scale energy storage device development.[28–37]

5.3.4.2. Electrochemical analysis of rGO/PANI/CNT//MXCF asymmetric capacitor

As MXene based materials are better used as negative electrodes, development of a similarly capable positive electrode is highly required in order to truly utilize the full potential of MXCF films in a full device. Further, development of an asymmetric supercapacitive device with two different anode and cathode allows extension of the operational window of a device beyond the thermodynamic limit of 1.23 V with water based electrolytes which greatly enhances the energy density of a device. Polyaniline (PANI), a conductive polymer with prominent pseudocapacitive properties, is a prime candidate in this regard as the pseudocapacitive response of this material lies within 0 - 0.8V vs Ag/AgCl. However, the inferior conducting properties of PANI restricts its application at lower scan rates due to resistive losses. To

overcome this limitation, we incorporated reduced graphene oxide (rGO) as conducting base for the electrode. However, the large sheets of graphene are well known for severe face-to-face restacking during vacuum filtration process and thus the rate performance of such electrode often remains the major bottleneck. In order to restrict such phenomenon, two strategies are introduced. First, instead of vacuum filtering graphene oxide (GO) and then reducing the film,

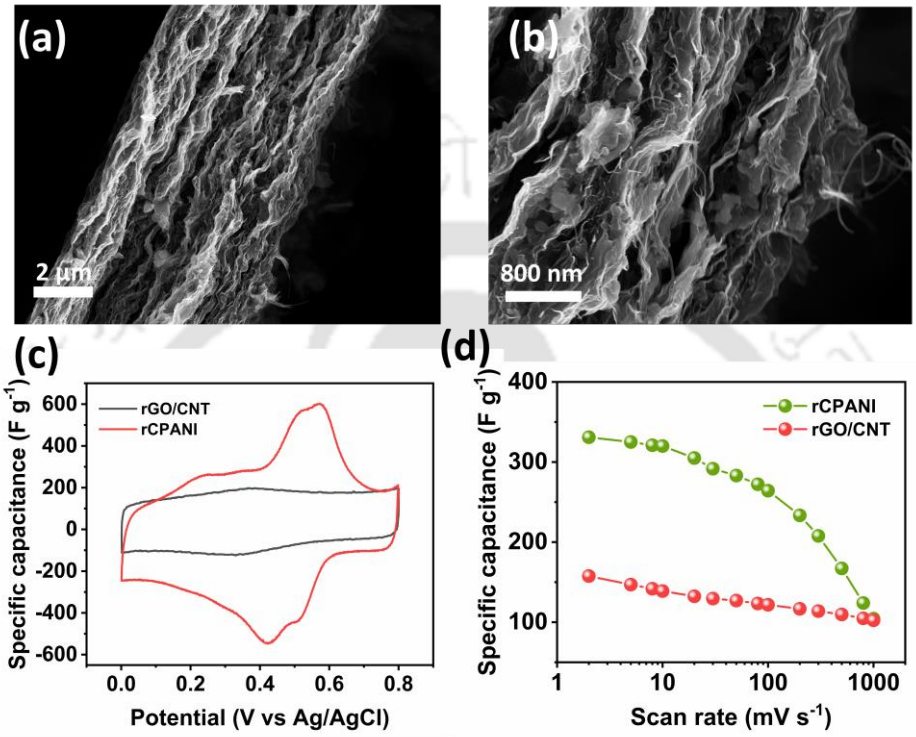

Figure 5.9. Structural and electrochemical characteristics of rCPANI electrode: (a) cross sectional FESEM image of rCPANI and (b) its corresponding higher resolution image showing the incorporation of CNT in the structure; (c) difference in the area under CV curve before and after incorporation of PANI; (d) change of specific capacitance with scan rate in rCPANI and rGO/CNT electrode.

we incorporated a previously reported method to synthesize solution dispersible rGO. During reduction, the individual sheets of graphene gets crumpled which restricts the complete restacking during vacuum filtration process. Secondly, to further increase the conductivity while maintaining proper separation between 2D sheets, we introduced CNT during vacuum filtration. Fig. 5.9.a-b shows the cross-section of rGO_CNT_PANI (rCPANI) where numerous CNT fibers can be seen. The presence of PANI in the rCPANI electrode can be confirmed from the CV curves due to the pseudocapacitive nature if the polymer. To investigate the pseudocapacitive properties of rCPANI, first the three-electrode performance of the electrodes

are investigated. The pseudocapacitive response and the presence of PANI in rCPANI electrode is clearly evident from the redox peaks in the range 0.4-0.6V vs Ag/AgCl (Fig. 5.9.c). The gravimetric capacitance of rCPANI is measured to be 331 F g^{-1} at 2 mV s^{-1}. The significant effect of PANI on the gravimetric performance of positive electrode is clearly evident from the large difference in CV curve area of rCPANI and rGO/CNT electrode. Compared to the 331 F g^{-1} of gravimetric capacitance, the rGO/PANI electrode shows only 157.8 F g^{-1} which is almost half of capacitance of the former. In spite of the presence of PANI in rCPANI, the positive composite electrode retains 32% of initial capacitance at 1000 mV s^{-1} whereas the rGO/PANI electrode retains almost 65% of its capacitance at same potentials (Fig. 5.9.d). This consolidates the importance of conducting rGO/CNT base in rCPANI electrode to effectively counter the low conductivity induced capacitance loss of PANI. Thus, with the synergy of rGO, CNT and PANI, the rCPANI composite possess the combination of pseudocapacity with improved conductive properties, making rCPANI a proper positive counterpart for supercapacitive electrode with MXene.

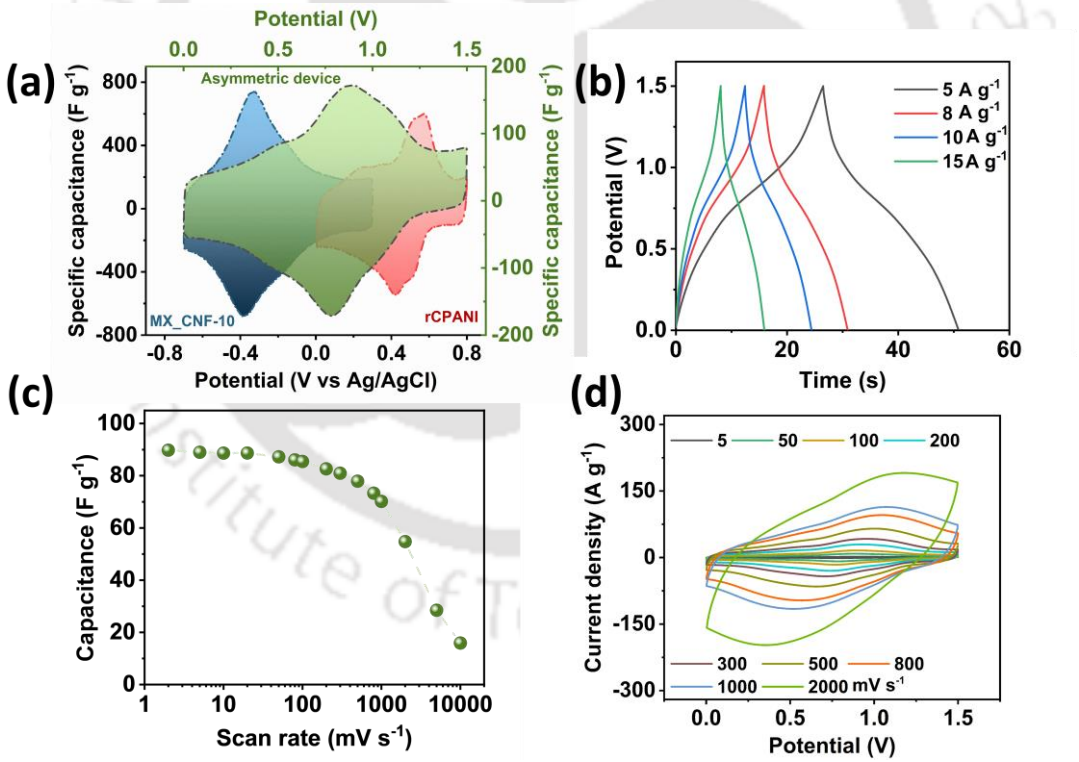

Figure 5.10. Electrochemical performance of rCPANI//MXCF asymmetric device: (a) CV curves of the device overlapping over rCPANI and MXCF electrodes at 50 mV s^{-1} showing the extended operational voltage window of the device; (b) GCD curves (c) rate performance and (d) CV curves at different scan rates for the rCPANI//MXCF device.

With the excellent performance of rCPANI as positive electrodes, it was then paired with MXCF_20 due to similar specific capacitance offered by these composite materials. However, before the development of asymmetric capacitors these two electrodes were first charge balanced using the Eq. 2. As mentioned before, the rCPANI operates at 0-0.8 V vs Ag/AgCl whereas the negative MXCF_20 electrodes are suitable at a potential range of -0.7-0.3 V vs Ag/AgCl. Fig. 5.10.a shows the operational windows of the two electrodes in their respective positive and negative regions which allows the asymmetric capacitor to have a potential window of 1.5 V. The CV profile of the asymmetric device in Fig. 5.10.a shows broad redox peaks contributing from both the pseudocapacitive type materials resulting in a total specific device capacitance of 89.8 F g^{-1} at 2 mV s^{-1}. The GCD curves also indicate towards the pseudocapacitive nature of the device with its deviated triangular curves recorded at different current densities (Fig. 5.10.b) Due to the excellent conductivity and restacking controlled development, the asymmetric device shows excellent capacitance even in high scan rates. The rate performance of the device is shown in Fig. 5.10.c where an excellent capacitance retention of 79% at 1000 mV s^{-1} and 32% at 5000 mV s^{-1} is observed. Such excellent rate performance is also evident from the CV curves of the device at different scan rates as shown in Fig. 5.10.d where the shape of the curve is excellently maintained even in the higher scan rates.

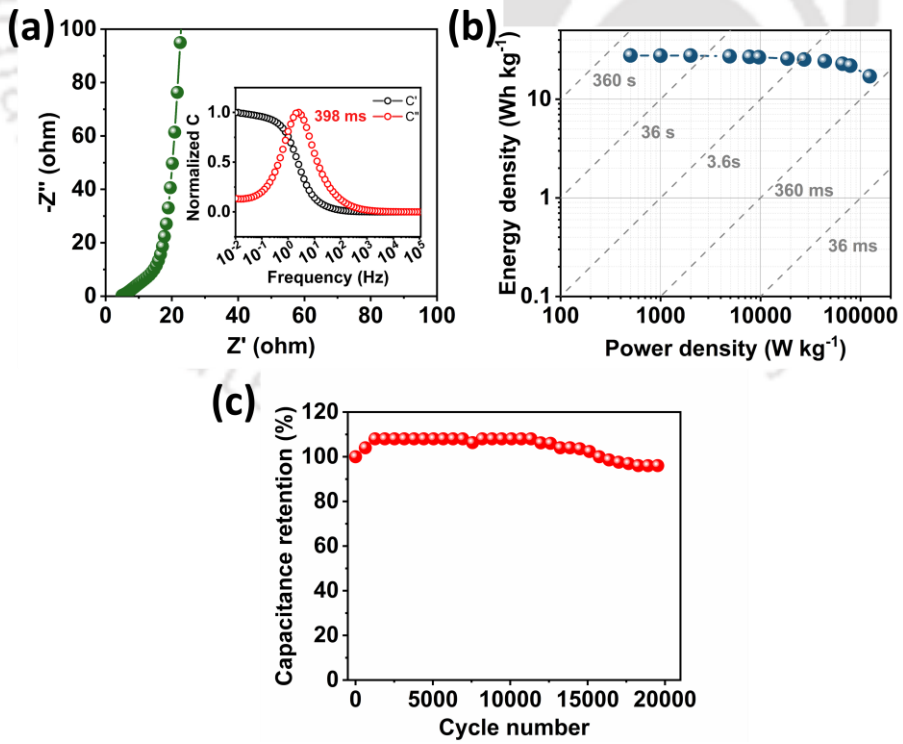

Figure 5.11. (a) Nyquist plot of rCPANI//MXCF asymmetric device with inset showing the relaxation time estimated from complex modelling of capacitance; (b) Regone plot and (c) stability test for 20000 cycles at 5 A g^{-1} showing excellent stability over long term operation.

The Nyquist plot of the device indicate extremely low series resistance (0.23 Ω) due to the excellent conducting properties of both the electrodes. Furthermore, the small 45° representing the Warburg region indicates the negligible charge-transfer resistance of the material (Fig. 5.11.a). The high ion transport efficiency of the device is also evident from the relaxation time estimated through complex capacitance modelling by real and imaginary capacitance analysis.[38] The asymmetric device exhibits a minimum characteristic relaxation time constant (τ_o) of 398 ms which denotes the minimum time required for the device to discharge all its capacity with an efficiency higher than 50% (Fig. 5.11.a inset). The excellent rate performance paired with the extended operational window of the device allows MXCF//rCPANI device to achieve high energy and power densities simultaneously. For example, the device can provide maximum 27.8 Wh kg^{-1} energy density at a power density of 501 W kg^{-1} and continues to provide 123 k W kg^{-1} while maintaining a 17.1 Wh kg^{-1} energy density which is better than previously reported MXene based asymmetric devices (Fig. 5.11.b).[39–42] Furthermore, we tested the device for 20000 charge-discharge cycles where it maintained 96% of initial capacitance, which establishes the long term operational stability of the device which is an important requisite for any commercially viable research prototype (Fig. 5.11.c).

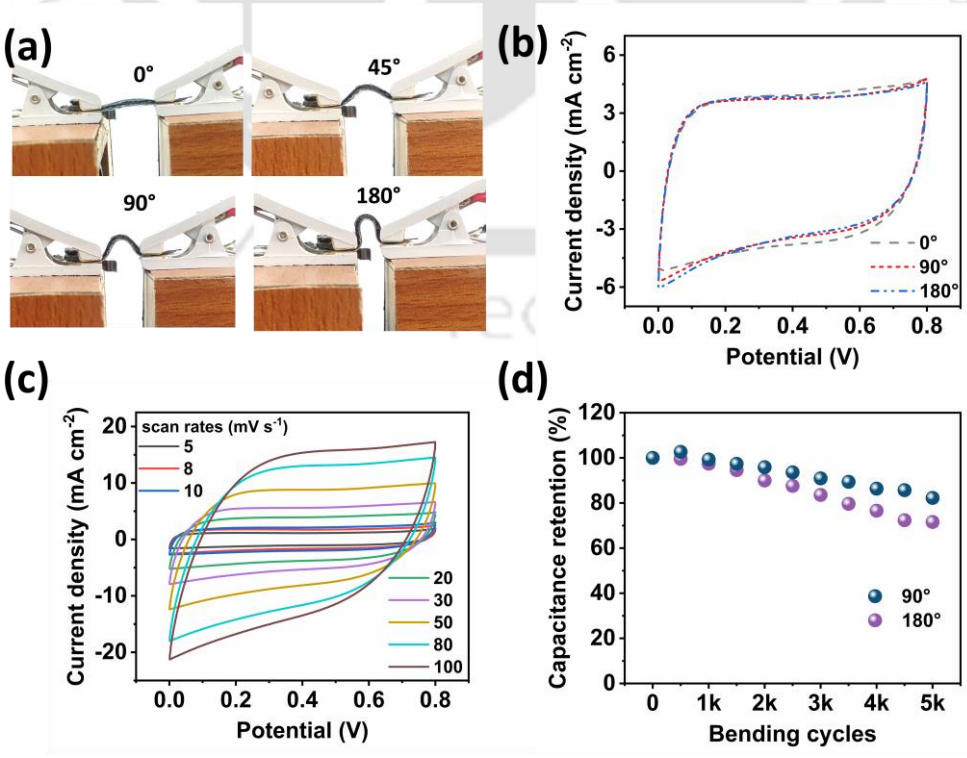

Figure 5.12. Supercapacitive performance of MXCF wearable device under different conditions: (a) MXCF wearable device in different bending state; the corresponding CV profiles in (b) bending angles of 0º, 90º and 180º and (c) different scan rates; (d) retention of device capacitance after 5000 bending cycle test at 90º and 180º angles.

5.3.4.3. Analyses of MXCF based wearable solid-state supercapacitor:

One major aspect of flexible electrodes lies in the development of next generation solid state energy storage devices. Further as discussed earlier, the electric field guided co-assembly of MXene and CNF can be performed over any ion-permeable conducting or non-conducting surface. As a proof-of-concept, we developed the MXCF films over CC and utilized the same in developing solid state wearable devices. Two such MXCF electrodes were first developed over carbon cloth and then assembled in a symmetric capacitor mode with PVA/H_2SO_4 solid electrolyte. For any wearable energy storage device, one of the prime prerequisites lies in the ability to deliver stable and uninterrupted power during bending. To investigate the above, the CV of the MXCF@CC wearable device was recorded at different bending angles of the device.

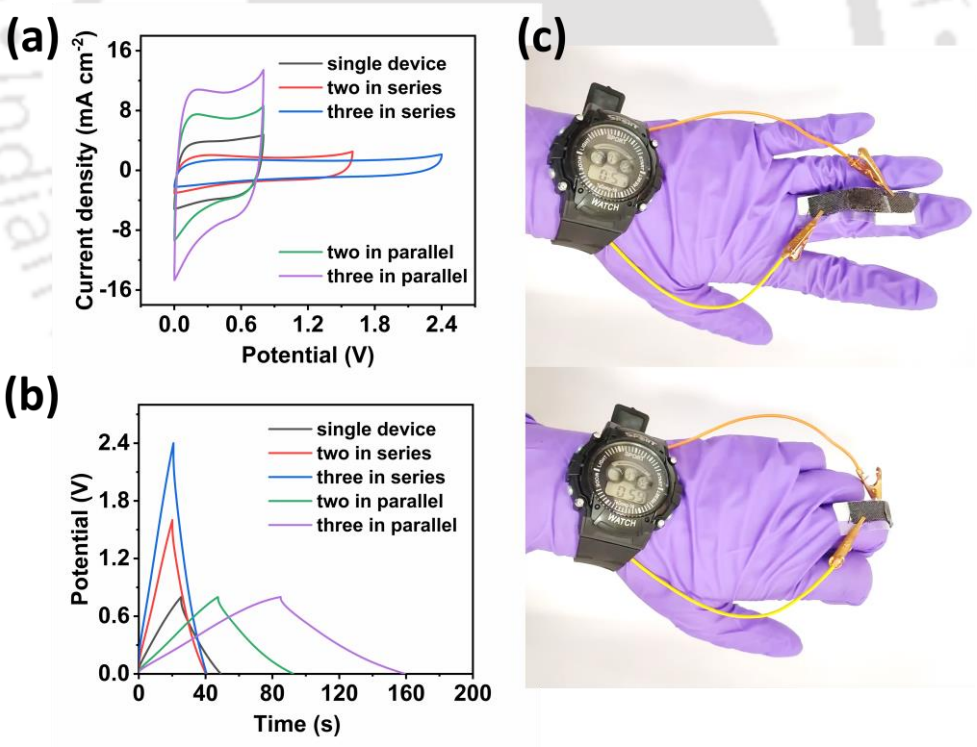

Figure 5.13. (a) CV and (b) GCD curves of up to three MXCF wearable device connected in series and parallel to achieve the desired voltage or capacitance output; (c) one MXCF wearable device powering a digital wrist watch while being continuously bent.

Fig. 5.12.a shows the bending angles of 0º, 90º and 180º while their corresponding CV curves are shown in Fig. 5.12.b. As seen from the figure, the CV curves shows deviation neither in shape nor in enclosed area under the CV curves even at high bending angles of 180º which confirms their ability to perform at extreme bending state. The areal capacitance of these wearables, as calculated from the CV curves is 216 mF cm^{-2} which is higher that many such symmetric wearable MXene based capacitors.[43–46] The excellent rate performance of the wearable devices is evident from the retention of the shape in the CV curves of wearable device at different scan rates (Fig. 5.12.c). Further, to investigate the robustness of the MXCF wearable devices, these devices were continuously bended at 90º and 180º for 5000 cycles while their CV was recorded at every 500 cycle. After the end of the experiment, the device retains 82% and 72% of initial capacitance indicating the excellent durability of the device (Fig. 5.12.d).

The MXCF wearables can be paired with multiple such devices to output either the application specific voltage or required capacitance. For example, in Fig. 5.13.a shows series and parallel arrangement of up to three such devices reaching a potential up to 2.4 V. Further, in parallel connections, the increase in current represents the increase in capacitance of the devices. This can be further understood from the corresponding GCD curves where for parallel connection the discharge time increases representing the increase in capacity of the arrangement (Fig.5.13.b). It is important to note that even after multiple devices connected in such combinations, the CV curves are well maintained which indicates the low resistance of the materials. As a demonstration of the practical applicability of the wearable supercapacitive

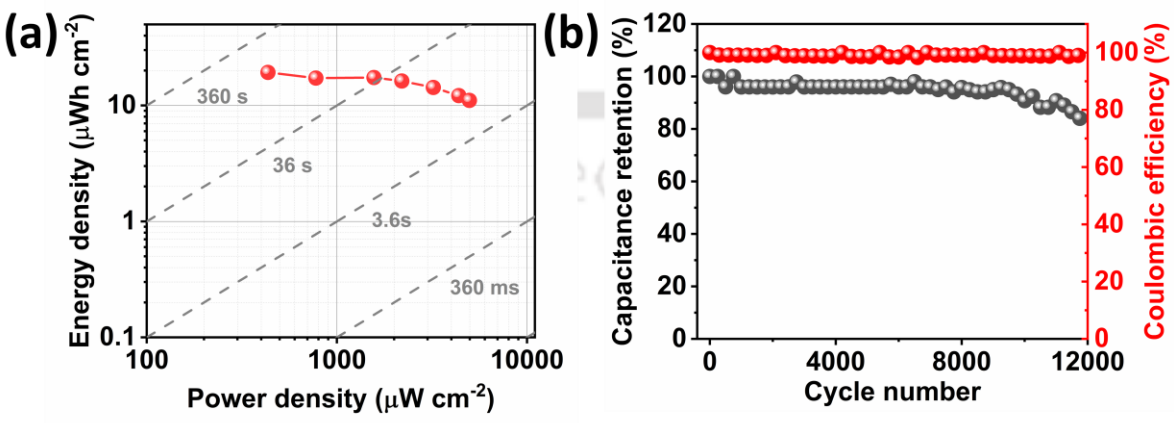

Figure 5.14. (a) Regone plot of MXCF wearable device; (b) stability test of wearable device after 12000 charge-discharge cycles at 100 mA cm^{-2} current density showing the excellent capacitance retention with high coulombic efficiency.

device, in Fig. 5.13.c, a digital watch is being powered with the MXCF@CC wearable under continuous bending. The wearable devices exhibit an energy density of 19.3 μWh cm^{-2} with a power density of 433.9 μW cm^{-2}. At increased energy densities the device can provide 4976 μW cm^{-2} while securing an energy density of 11 μWh cm^{-2} (Fig. 5.14.a). The long term charge-discharge test is also performed to confirm the stability of the device under operation where the device maintains a retention of 84% of initial capacitance which establishes its long term usability (Fig. 5.14.b). Furthermore, the high coulombic efficiency throughout the experiment indicates its low resistive losses in the process. Thus the unmatched performance of our MXCF electrodes throughout the wide range of supercapacitive energy storage domain can inspire the development of such versatile electrodes in a scalable and sustainable fashion.

5.4. Conclusion

In summary, electric-field guided layer-by-layer interfacial assembly of MXene and CNF has been implemented to develop a hydrogel derived field. Mutual interaction between negatively charged MXene and surface modified CNF aids the co-assembly of the two materials to address the restacking challenge in electrodes. Further, the optimized wrinkled structure allows a gravimetric capacitance of 358 F g^{-1} at 2 mV s^{-1} with 63% retention at 1000 mV s^{-1} for an electrode with 10% CNF. Due to the controlled face-to-face restacking, the mass loading of the electrodes can be increased upto 73.4 mg cm^{-2} via physical stacking which provides 16 F cm^{-2} areal capacitance paired with a volumetric capacitance of 1356 F cm^{-3}. When paired with a pseudocapacitive rCPANI positive electrode, the asymmetric supercapacitive devices deliver an impressive 27.8 Wh kg^{-1} energy density with a power density of 501 W kg^{-1}. In terms of stability, the all pseudocapacitive supercapacitive device maintains an excellent 96% capacitance after 20,000 charge-discharge cycles which establishes the long term operational stability of these electrodes. Further, due to the versatility of fabricating MXene composite film over other substrates, the MXCF films were developed over carbon cloths to develop solid state wearable devices with an areal capacitance of 216 mF cm^{-2} which remains unchanged even under extreme bending angles. The low-cost, highly scalable field guided assembly derived MXene films with such design and operational flexibility can truly lead the road for MXene lead energy storage research and commercialization.

References

1. Guo, W., Yu, C., Li, S. & Qiu, J. Toward commercial-level mass-loading electrodes for supercapacitors: opportunities, challenges and perspectives. *Energy Environ. Sci.* **14**, 576–601 (2021).
2. Huang, S., Zhu, X., Sarkar, S. & Zhao, Y. Challenges and opportunities for supercapacitors. *APL Mater.* **7**, 100901 (2019).
3. Dong, Y. *et al.* Carbon materials for high mass-loading supercapacitors: filling the gap between new materials and practical applications. *J. Mater. Chem. A* **8**, 21930–21946 (2020).
4. Wu, F. *et al.* High-Mass-Loading Electrodes for Advanced Secondary Batteries and Supercapacitors. *Electrochem. Energy Rev. 2021 42* **4**, 382–446 (2021).
5. Chang, L. & Hu, Y. H. Breakthroughs in Designing Commercial-Level Mass-Loading Graphene Electrodes for Electrochemical Double-Layer Capacitors. *Matter* **1**, 596–620 (2019).
6. Li, W., Wu, M., Yang, W., Zhao, M. & Lu, X. Effects of electrode mass loading on the self-discharge of supercapacitors. *Electrochim. Acta* **438**, 141550 (2023).
7. Anasori, B. *et al.* Two-Dimensional, Ordered, Double Transition Metals Carbides (MXenes). **12**, 34 (2021).
8. Lukatskaya, M. R. *et al.* Cation Intercalation and High Volumetric Capacitance of Two-Dimensional Titanium Carbide. *Science (80-.).* **341**, 1502–1505 (2013).
9. Ghidiu, M., Lukatskaya, M. R., Zhao, M.-Q., Gogotsi, Y. & Barsoum, M. W. Conductive two-dimensional titanium carbide 'clay' with high volumetric capacitance. *Nat. 2014 5167529* **516**, 78–81 (2014).
10. Cui, Z. *et al.* Lightweight MXene/Cellulose Nanofiber Composite Film for Electromagnetic Interference Shielding. *J. Electron. Mater.* **50**, 2101–2110 (2021).
11. Yang, W. *et al.* Ultrathin flexible reduced graphene oxide/cellulose nanofiber composite films with strongly anisotropic thermal conductivity and efficient electromagnetic interference shielding. *J. Mater. Chem. C* **5**, 3748–3756 (2017).
12. Kim, S. J. *et al.* Metallic Ti3C2Tx MXene Gas Sensors with Ultrahigh Signal-to-Noise Ratio. *ACS Nano* **12**, 986–993 (2018).
13. Zhang, Y.-Z. *et al.* MXenes stretch hydrogel sensor performance to new limits. *Sci. Adv.* **4**, eaat0098 (2018).
14. Dutta, P. *et al.* Electric Field Guided Fast and Oriented Assembly of MXene into Scalable Pristine Hydrogels for Customized Energy Storage and Water Evaporation Applications. *Adv. Funct. Mater.* **2204622**, 2204622 (2022).
15. Ran, J. *et al.* Ti3C2 MXene co-catalyst on metal sulfide photo-absorbers for enhanced visible-light photocatalytic hydrogen production. *Nat. Commun.* **8**, (2017).
16. Wu, Z., Shang, T., Deng, Y., Tao, Y. & Yang, Q. H. The Assembly of MXenes from 2D to 3D. *Advanced Science* vol. 7 1903077 (2020).
17. Fan, Z. *et al.* Modified MXene/Holey Graphene Films for Advanced Supercapacitor

Electrodes with Superior Energy Storage. *Adv. Sci.* **5**, 1800750 (2018).

18. Chen, J. *et al.* Integrating MXene nanosheets with cobalt-tipped carbon nanotubes for an efficient oxygen reduction reaction. *J. Mater. Chem. A* **7**, 1281–1286 (2019).
19. Liu, Y. T. *et al.* Self-Assembly of Transition Metal Oxide Nanostructures on MXene Nanosheets for Fast and Stable Lithium Storage. *Adv. Mater.* **30**, 1707334 (2018).
20. Javed, M. S. *et al.* Recent progress in the design of advanced MXene/metal oxides-hybrid materials for energy storage devices. *Energy Storage Mater.* **53**, 827–872 (2022).
21. Zhao, M.-Q. *et al.* Flexible MXene/Carbon Nanotube Composite Paper with High Volumetric Capacitance. *Adv. Mater.* **27**, 339–345 (2015).
22. Li, X., Ran, F., Yang, F., Long, J. & Shao, L. Advances in MXene Films: Synthesis, Assembly, and Applications. *Trans. Tianjin Univ. 2021 273* **27**, 217–247 (2021).
23. Alhabeb, M. *et al.* Guidelines for Synthesis and Processing of Two-Dimensional Titanium Carbide (Ti3C2Tx MXene). *Chem. Mater.* **29**, 7633–7644 (2017).
24. Sikdar, A. *et al.* Ultra-large area graphene hybrid hydrogel for customized performance supercapacitors: High volumetric, areal energy density and potential wearability. *Electrochim. Acta* **332**, 135492 (2020).
25. Hummers, W. S. & Offeman, R. E. Preparation of Graphitic Oxide. *J. Am. Chem. Soc.* **80**, 1339 (1958).
26. Li, D., Müller, M. B., Gilje, S., Kaner, R. B. & Wallace, G. G. Processable aqueous dispersions of graphene nanosheets. *Nat. Nanotechnol.* **3**, 101–5 (2008).
27. Halim, J. *et al.* X-ray photoelectron spectroscopy of select multi-layered transition metal carbides (MXenes). *Appl. Surf. Sci.* **362**, 406–417 (2016).
28. Tang, J. *et al.* Optimizing Ion Pathway in Titanium Carbide MXene for Practical High-Rate Supercapacitor. *Adv. Energy Mater.* **11**, 2003025 (2021).
29. Wang, H. *et al.* Enhanced Rate Capability of Ion-Accessible Ti3C2Tx-NbN Hybrid Electrodes. *Adv. Energy Mater.* **10**, 2001411 (2020).
30. Vahidmohammadi, A. *et al.* Thick and freestanding MXene/PANI pseudocapacitive electrodes with ultrahigh specific capacitance. *J. Mater. Chem. A* **6**, 22123–22133 (2018).
31. Li, J. *et al.* Achieving High Pseudocapacitance of 2D Titanium Carbide (MXene) by Cation Intercalation and Surface Modification. *Adv. Energy Mater.* **7**, 1602725 (2017).
32. Xia, Y. *et al.* Thickness-independent capacitance of vertically aligned liquid-crystalline MXenes. *Nat. 2018 5577705* **557**, 409–412 (2018).
33. Lukatskaya, M. R. *et al.* Ultra-high-rate pseudocapacitive energy storage in two-dimensional transition metal carbides. *Nat. Energy 2017 28* **2**, 1–6 (2017).
34. Mashtalir, O. *et al.* The effect of hydrazine intercalation on the structure and capacitance of 2D titanium carbide (MXene). *Nanoscale* **8**, 9128–9133 (2016).
35. Boota, M. *et al.* Interaction of Polar and Nonpolar Polyfluorenes with Layers of Two-Dimensional Titanium Carbide (MXene): Intercalation and Pseudocapacitance. *Chem.*

Mater. **29**, 2731–2738 (2017).

36. Boota, M. *et al.* Understanding Functionalization of Titanium Carbide (MXene) with Quinones and Their Pseudocapacitance. *ACS Appl. Energy Mater.* **3**, 4127–4133 (2020).

37. Yang, W. *et al.* Freeze-assisted Tape Casting of Vertically Aligned MXene Films for High Rate Performance Supercapacitors. *Energy Environ. Mater.* **3**, 380–388 (2020).

38. Yan, J. *et al.* Flexible MXene/Graphene Films for Ultrafast Supercapacitors with Outstanding Volumetric Capacitance. *Adv. Funct. Mater.* **27**, 1701264 (2017).

39. Li, K. *et al.* All-pseudocapacitive asymmetric MXene-carbon-conducting polymer supercapacitors. *Nano Energy* **75**, 104971 (2020).

40. Li, Y., Kamdem, P. & Jin, X. J. Hierarchical architecture of MXene/PANI hybrid electrode for advanced asymmetric supercapacitors. *J. Alloys Compd.* **850**, 156608 (2021).

41. Navarro-Suárez, A. M. *et al.* Development of asymmetric supercapacitors with titanium carbide-reduced graphene oxide couples as electrodes. *Electrochim. Acta* **259**, 752–761 (2018).

42. Li, K. *et al.* An Ultrafast Conducting Polymer@MXene Positive Electrode with High Volumetric Capacitance for Advanced Asymmetric Supercapacitors. *Small* **16**, 1906851 (2020).

43. Lee, H. *et al.* A Textile-Based Temperature-Tolerant Stretchable Supercapacitor for Wearable Electronics. *Adv. Funct. Mater.* **31**, 2106491 (2021).

44. Yang, L., Lin, F., Zabihi, F., Yang, S. & Zhu, M. High specific capacitance cotton fiber electrode enhanced with PPy and MXene by in situ hybrid polymerization. *Int. J. Biol. Macromol.* **181**, 1063–1071 (2021).

45. Wang, Q., Fang, Y. & Cao, M. Tailoring surface capacitance of Ti3C2Tx-PANI@CNTs nanoarchitecture for tunable energy storage and high-performance micro-supercapacitor. *Ceram. Int.* **48**, 21935–21944 (2022).

46. Zhang, C., Guo, R., Wang, H., Xie, X. & Du, C. Composite electrodes with NiCoAl-LDH coated Ti3C2Tx MXene and incorporated Ag nanowires for screen-printable in-plane hybrid supercapacitors on textiles. *Appl. Surf. Sci.* **598**, 153796 (2022).

Chapter 6

Summary and Outlook

Chapter 6

Summary and Outlook

6.1. Summary of the thesis

A brief summary and the key findings of this thesis is discussed in this chapter. This thesis focuses on the development of pristine MXene and MXene based macrostructures while addressing the key challenges in supercapacitive energy storage systems. Development of low cost highly scalable synthesis strategy, achieving state-of-the-art energy storage metrics with high mass loading electrodes while simultaneously achieving excellent gravimetric, areal and volumetric capacitance are some of the prime motives behind all the works. The key findings of this thesis have been categorized in six different points, namely, i) Development of MXene-graphene hybrid hydrogels via layer by layer interfacial assembly; ii) introduction of critical density controlled interfacial assembly method to develop pristine MXene hydrogels; iii) introduction of electric field guided forced assembly for dispersion density independent MXene hydrogel development; iv) realisation of a highly modular synthesis strategy to develop application specific customised hydrogels with controlled sheet orientation; v) bio-inspired co-assembly of cellulose nanofiber and MXene for restacking controlled highly scalable flexible electrode development; vi) achievement of state-of-the-art energy storage metrics with MXene and MXene based electrodes at commercial mass-loadings and scalability.

i) Development of MXene-graphene hybrid hydrogels via layer-by-layer interfacial assembly:

In chapter 2, we introduced a layer-by-layer co assembly of MXene and graphene into a porous hydrogel structure. Simultaneous gelation of MXene and graphene was induced by spontaneous release of Zn ions from metal Zn plate upon interaction with MXene-graphene dispersion. As the reduction potential of Zn is lower than that of graphene, Zn^{2+} ions were released from the metal plate to attract the negatively charged graphene and MXene sheets to assemble in a layer-by-layer fashion. Successively, electrons were transferred from Zn to graphene which reduced the graphene sheets. In the hydrogel structure, the complete restacking was prohibited by the intercalated water molecules that restricted the severe face-to-face restacking in MXene and graphene sheets. Finally, the hybrid hydrogel structure of MXene and graphene was stabilised by van der Waals interaction among MXene, MXene-graphene and π-π interaction among the large graphene sheets. The compactness of the electrodes was also

controlled by mechanically compressing the MXene/graphene hydrogel electrodes for high volumetric capacitance. The restacking of sheets during compression was countered by introducing electrolyte assisted compression, where large H_2SO_4 electrolyte ions preserved the ion-transport channels. The as developed electrodes delivered state-of-the art energy storage metrics with excellent stability and efficiency. The importance of the work lies in the development of MXene graphene hydrogels through an ambient condition, scalable assembly method where not only the restacking was controlled trough the introduction of graphene, but the ambient condition gelation was also able to disregard the synthesis induced degradation in MXene which is often reported for any temperature induced synthesis protocol.

ii) Introduction of critical density controlled interfacial assembly method to develop pristine MXene hydrogels:

The development of MXene/graphene hybrid hydrogels was introduced in chapter 2 where graphene acted as gelator to form the hydrogel network with MXene. However, a natural question remains on whether the development of pristine MXene hydrogel without the incorporation of any additional gelator or binder is possible or not. Due to excellent pseudocapacitive properties, superior conductivity, hydrophilicity and high light to heat thermal conversion efficiency, development of pristine MXene hydrogels is a natural choice for optimum performance in several fields of research. Despite many attempts, the relatively smaller sheet size and intrinsic stiffness in MXene sheets imposed numerous challenges in realising the same, which was also reported by many research groups. To develop pristine MXene hydrogels, we optimised the relative orientation of MXene sheets during assembly and increased the van der Waals interaction between them by incorporating the liquid crystalline properties in MXene. Thus, in order to develop self-supporting pristine MXene hydrogels, in chapter 3, we introduced critical density-controlled layer-by-layer assembly of MXene over metal plate. We proposed that the self-supporting hydrogels of MXene can only be developed above a certain dispersion concentration which is dependent on the sheet size of MXene in dispersion. The critical dispersion density for large MXene sheets (average sheet size 1370 nm) and small MXenes (337 nm) was found to be 40 mg mL^{-1} and 60 mg mL^{-1} respectively. The increased relative orientation in dispersion by increasing the concentration was confirmed by the presence of liquid crystalline properties in MXene. The porous structure and water intercalated network provided state-of-the art capacitance for pristine MXene hydrogels. This work provided a first-hand guideline to develop freestanding MXene hydrogels with ambient condition layer-by-layer assembly method.

iii) Introduction of electric field guided forced assembly for dispersion density independent MXene hydrogel development:

Although the previous critical density-controlled gelation strategy was successful in developing self-supporting hydrogels of pristine MXene, its dependence over such high dispersion concentrations introduced a critical synthesis cost induced scalability challenge. However, in order to increase the relative orientation and van der Waals interaction of MXene sheets without relying on the liquid crystalline properties, an alternative external influencer was required. By utilising the fact that functionalised MXene are negatively charged in dispersion, we introduced an electric-field guided forced assembly method in chapter 4. Upon application of an electric field, the negatively charged sheets of MXene get attracted towards the positive electrode and assemble over the anode in a layer-by-layer fashion. We proposed that such field-assisted assembly is not simple electrodeposition and rather highly depends on the standard reduction potential of the metal used as electrode. Interestingly, with such forced assembly, the pristine hydrogels of MXene were now possible with dispersion concentration as low as 5 mg mL^{-1} in 30 seconds gelation time compared to the previously required 60 mg mL^{-1} and hours of gelation in critical density controlled spontaneous assembly method. Further, the anodic environment in which the hydrogel was developed also showed no signs of oxidation which was confirmed from density functional theory (DFT) calculations. This field assisted forced assembly was a huge advancement from the previous spontaneous assembly method and provided a guideline on the effect of electric field, choice of anodic potential and material to truly attain the low-cost scalability for widespread practical adoptability of MXene hydrogels.

iv) Realisation of a highly modular synthesis strategy to develop application specific customised hydrogels with controlled sheet orientation:

On demand controlling over the relative orientation of nanosheets in a hydrogel structure adds a whole new dimension in microstructural synthesis from nanomaterials. In chapter 4, simple modification in electrode arrangement can change the electric field orientation which results in different macrostructures with varied nanosheet arrangement. As an example, we demonstrated a parallel arrangement of electrodes resulting in sheet-like hydrogels where the MXene sheets are oriented perpendicular to the surface normal, i.e. parallel to the basal plane of the hydrogel. On the other hand, a concentric arrangement of electrodes with the positive anode being the thin central wire, a monolith of MXene can be developed where the nanosheets are oriented in

a vertical manner, i.e. parallel to the surface normal or vertical to the basal plane. Furthermore, the electrodes can be designed in any shape to develop hydrogels of defined structure and can be developed over any ion-permeable conducting or non-conducting surfaces. In chapter 5, we have demonstrated the possibility of developing MXene based hydrogel or hydrogel derived dried films over commercial non-conducting cotton and also over conducting carbon cloth. Development of such electroactive material over these flexible substrates allows the development of wearables as we demonstrated in chapter 5. Such controllability and versatility over nanosheets arrangement, structural independence and a wide range of substrate choice in hydrogel or film development is rarely reported and extremely beneficial for a number of applications including energy storage, solar-water-evaporation, catalysis to name a few.

v) Bio-inspired co-assembly of cellulose nanofiber and MXene for restacking controlled highly scalable flexible electrode development:

In chapter 5, we introduced co-assembly of MXene and cellulose nanofibers (CNF) into a hydrogel structure to subsequently develop hydrogel derived film electrodes. The functional groups over MXene and surface modified CNFs develop mutual interaction with the presence of hydrogen bonds. As a result, under the application of electric field-guided forced gelation, the MXene sheets drags the nanowires into a hydrogel network and gets interlinked. These hydrogels were subsequently dried to develop flexible MXene/CNF dried films. The garlic-husk derived CNFs prevents the complete restacking of nanosheets during drying and bends the MXene sheets around it to create valleys in structure which then act as ion transport channels. Such incorporation of MXene and CNF significantly improves the rate performance of the material and allows reaching ultrahigh mass loading of electrodes without sacrificing the energy storage metrics. The MXene/CNF films were also incorporated over carbon cloths to develop wearable devices. Realization of co-gelation of MXene and CNF into a hydrogel network opens a much larger possibility of several other nanomaterials to be co-assembled with MXene into composite hydrogels or dried films to cater a much larger domain of application.

vi) Achievement of state-of-the-art energy storage metrics with MXene and MXene based electrodes at commercial mass-loadings and scalability:

Although many nanomaterials have been researched for state-of-the-art energy storage performance, the wide spread adoptability of these materials is still to be realised. One important aspect in this regard is the significant decrease in performance of materials at high commercial scale mass loadings (~ 10 mg cm^{-2}). Throughout the entire thesis, we have kept

our focus on the mass loading of the electrodes to be at par with commercial requirements while ensuring scalability and sustainability of the synthesis methods.

In chapter 2, we developed MXene/graphene hybrid hydrogels where the interfacial layer-by-layer assembly gave rise to porous hydrated network of the two nanomaterials. Aided by a small quantity (5 wt%) of MXene, the as developed hydrogels delivered a gravimetric capacitance of 653.7 F g^{-1} at 2 mV s^{-1} in three-electrode test. Furthermore, in symmetric two-electrode setup, a gravimetric capacitance of 460 F g^{-1} was achieved at 2 mV s^{-1} for a 1.93 mg cm^{-2} mass loading electrode. However, the porous structure and greater surface accessibility in MXene/graphene hydrogels allowed an excellent capacitance retention of 320 F g^{-1} even at high mass loadings of 9.3 mg cm^{-2}. Such high gravimetric capacitance established the importance of a porous architecture for MXene macroscopic structure design. To further examine the volumetric performance of these hybrid electrodes, the hydrogels were mechanically pressed with electrolyte assisted compression to prevent the complete restacking of sheets in the compact electrode. An electrode of 2.44 g cm^{-3} density provided a volumetric capacitance of 1522 F cm^{-3} (at 2 mV s^{-1}) with 50% retention of capacitance at 100 mV s^{-1} which is at par or better than most of MXene-graphene based electrodes. We reported this work in Carbon, 2020, 169, 225.

In chapter 3, we developed pristine MXene hydrogels from critical density-controlled layer-by-layer assembly of MXene from liquid crystalline MXene dispersions. The pristine MXene hydrogels delivered a specific capacitance of 391 F g^{-1} at 2 mV s^{-1} with an electrode mass loading of 3.1 mg cm^{-2} developed with large MXene sheets. On the other hand, although the specific capacitance of MXene hydrogels with smaller MXene sheets were lower, it had higher rate performance due to the shorter ion-diffusion paths. Inspired by this, we developed MXene hydrogels of mass loading 14.9 mg cm^{-2} where we achieved an areal capacitance of 5043 mF cm^{-2} (2 mV s^{-1}) while retaining a gravimetric capacitance of 337 F g^{-1}. Interestingly, we compared the electrochemical performance of hydrogels with commonly used MXene aerogels where we found 321 F g^{-1} compared to 391 F g^{-1} gravimetric capacitance in hydrogels. This established the importance of hydrogels over conventionally used aerogel electrodes. Further, the pristine MXene hydrogels were also made compact with electrolyte assisted mechanical compression to achieve a volumetric density of 3.6 g cm^{-3}. These compact MXene hydrogel films delivered a volumetric capacitance of 1101.6 F cm^{-3} at 2 mV s^{-1} and retained up to 73% of its capacitance at 1000 mV s^{-1}, making it highly suitable for high-rate applications. These MXene hydrogels also showed stable performance in long term operation where they retained

87% of their capacitance after 10,000 charge-discharge cycles at a current density of 5 A g^{-1}. We reported this work in Journal of Materials Chemistry A, 2021, 9, 25013-25023. This work provides important insights over the pristine MXene hydrogel development, its dependence over critical density and MXene sheet size. This work also extensively studied the electrochemical properties of pristine hydrogels and its dependence over sheet dimensions.

In chapter 4, we employed the electric-field guided assembly of MXene nanosheets. This forced assembly method provided a big leap over the spontaneous assembly as self-supporting MXene hydrogels were now possible with minimal dispersion concentrations and the gelation can take place in seconds. The as developed hydrogel electrodes delivered a maximum capacitance of 395.2 F g^{-1} at 2 mV s^{-1} with an outstanding rate performance of 42% at 5000 mV s^{-1}, which is primarily due to the facile ion-transport channels in the hydrogel structure. Further, a logarithmic plot between peak current and scan rate indicated that all the electric field guided hydrogels had a highest *b* value of 0.91 up to 1000 mVs^{-1} which direct towards their surface-controlled storage behaviour. The scalability of the process was also demonstrated with a 7 cm×9cm hydrogel. The electric-field guided assembly can be used to develop film electrodes through ambient drying. The as developed films were found to have higher tensile strength compared to films developed from vacuum filtered process. The compact films have a volumetric capacitance of 1251 F cm^{-3} at 2 mV s^{-1} while simultaneously having a gravimetric capacitance of 357 F g^{-1} at similar scan rates which shows the potential of such field-assisted films in range of electrode development. The electric-field guided forced assembly not only provided a highly scalable approach to develop electrodes with customised nanosheets assembly but also overcame a series of previous challenges in MXene hydrogel development. This work is published in Adv. Funct. Mater. 2022, 2204622.

In chapter 5, with electric field guided co-assembly of MXene and biological waste derived cellulose nanofibers, a compact hybrid film was developed where the nanofibers acted as spacers to preserve the ion-transport channels in the compact structure. With 10% addition of cellulose during synthesis, the co-assembled films provided a gravimetric capacitance of 358 F g^{-1} at 2 mV s^{-1} with 63% retention at 1000 mV s^{-1}. Interestingly, the ability to simply increase the gelation time to have higher mass loading electrodes allows facile upscaling of electrode mass loadings with such a field-assisted approach. Furthermore, instead of single high mass loading electrode development, stacking of several high electrodes was done to achieve an outstanding mass loading of 73.4 mg cm^{-2}. Even at such high loadings, the composite stacked film electrode provided a rare combination of volumetric, gravimetric and areal capacitance of

1356 F cm^{-3}, 216 F g^{-1} and 16 F cm^{-2} respectively. Such combination of capacitive performance solves one of the fundamental challenges in supercapacitive research and beats most of the reported performance metrics on MXene and other 2D materials. Furthermore, a suitable rGO/PANI/CNT composite positive electrode was developed to fabricate an asymmetric supercapacitor device which provided 27.8 Wh kg^{-1} at a power density of 501 W kg^{-1}. The ability to co-assemble different 2D materials along with MXene in a hybrid film structure opens a plethora of possibilities in the field of MXene energy storage.

6.2. Future scope

The focus of this thesis is tunable assembly of MXene and MXene like two-dimensional materials into a macrostructure suitable for high performance energy storage applications. In this regard, hydrogels and dried films of MXene, MXene/graphene and MXene/cellulose nanofibers have been developed along with reduced graphene based positive electrodes. The porous hydrated network of hydrogels can immediately find their application in any process where a solid-liquid interface is involved like energy storage, catalysis, oil adsorption and removal of water contaminants. Further, MXene materials have shown excellent H_2 storage potential in the delaminated layers. The possibility of such storage of the gas can be optimised with the hydrogel derived aerogel structures which can effectively utilize the entire surface area of the MXene. The aerogels derived from MXene hydrogels, in conjunction with flexible polymeric materials can be utilised to develop flexible materials for electromagnetic interface shielding. Here, the conductive property of MXene is expected to give higher reflection of electromagnetic waves whereas the porous surface can give rise to multiple reflection and thus increasing the absorption efficiency.

The field-assisted forced assembly of MXene provides a general methodology to derive a number of MXene based heterostructure with materials that either have interaction with MXene via hydrogen bond or gets effected by the applied electric field. This opens a wide possibility of MXene heterostructure for energy storage applications. The facile controllability of MXene sheet orientation can be further explored to develop vertically oriented MXene macrostructures where multiple reflection of light can result in an optimal light to heat converter and an efficient solar water evaporator.

The as developed hydrogels itself can provide a starting point from which the possibility of metal ion batteries can be explored. Theoretical studies predict that the halide functionalization over MXene provides lesser diffusion resistance and higher capacity to a number of metal-ion

batteries like Zn and Na. Such functionalization along with the hydrogel derived porous structure can be investigated for metal-ion battery development.